

UNIVERSITY OF CALIFORNIA
Los Angeles

Infrared Observations of Exoplanet Atmospheres

A dissertation submitted in partial satisfaction
of the requirements for the degree
Doctor of Philosophy in Astronomy

by

Ian James Mills Crossfield

2012

© Copyright by
Ian James Mills Crossfield
2012

ABSTRACT OF THE DISSERTATION

Infrared Observations of Exoplanet Atmospheres

by

Ian James Mills Crossfield

Doctor of Philosophy in Astronomy

University of California, Los Angeles, 2012

Professor Brad M. S. Hansen, Chair

The study of extrasolar planet atmospheres elucidates the formation and migration history of planets and places the origin and evolution of Earth and the Solar System in a broader context. The last several years have seen rapid strides in this direction via routine detections of planetary transits, thermal emission, atmospheric circulation, and transmission spectroscopy using both broadband photometry and spectroscopy. My dissertation employs all these techniques in an effort to investigate the atmospheric composition, structure, and dynamics of a broad range of exoplanet atmospheres. These observations focus on the infrared wavelengths where planet emission is strongest and molecular features are most prominent. I present transit, eclipse, and phase curve photometry of several hot Jupiters (*v* And b, HD 209458b, and WASP-12b), and present spectroscopy for both WASP-12b (emission, observed at low resolution) and the cool, low-mass planet GJ 1214b (transmission at high resolution). This work will guide future observations and inform the next generation of models in preparation for future spectroscopy of ever smaller, cooler, and more Earthlike planets.

The dissertation of Ian James Mills Crossfield is approved.

Ian McLean

Jonathan Mitchell

Michael Jura

Brad M. S. Hansen, Committee Chair

University of California, Los Angeles

2012

To Betsy.

TABLE OF CONTENTS

Abstract	ii
Table of Contents	v
List of Figures	xii
List of Tables	xv
1 Introduction	1
1.1 Introduction	1
1.2 Probing Exoplanet Interiors and Atmospheres	4
1.2.1 The Uncertain Nature of Exoplanet Atmospheres	4
1.2.2 Circulation	6
1.2.3 Atmospheric Probes of Interior Compositions	8
1.3 Observing Exoplanet Atmospheres	10
1.3.1 Eclipse Spectroscopy	11
1.3.2 Transmission Spectroscopy	11
1.4 Dissertation Outline	12
2 Energy Balance and Atmospheric Circulation in upsilon An- dromedae b	14
2.1 Abstract	14
2.2 Introduction	15

2.3	Observations and Analysis	18
2.3.1	The v Andromedae System	18
2.3.2	Observations	19
2.3.3	Data Reduction	19
2.3.4	Calibration and instrument stability	23
2.4	Results	25
2.4.1	System flux	25
2.4.2	A two-hemisphere model	25
2.4.3	Model fits	27
2.4.4	Phase curve amplitude	35
2.4.5	Phase offset	36
2.5	Discussion	37
2.6	Conclusions and Future Work	41
2.7	v And b: Post-publication Results	43
3	Eclipses and Transits of HD 209458b at 24 Microns	48
3.1	Abstract	48
3.2	Introduction	49
3.2.1	The HD 209458 system	50
3.2.2	Outline	53
3.3	Observations and Analysis	53
3.3.1	Observations	53
3.3.2	Data Reduction	54

3.3.3	Approach to Model Fitting	55
3.4	Calibration and Instrument Stability	56
3.4.1	The Ramp	56
3.4.2	The Fallback	61
3.4.3	Instrument Stability	64
3.5	Transits	65
3.5.1	Fitting Approach	65
3.5.2	Results	66
3.5.3	Discussion	69
3.6	Secondary Eclipses	74
3.6.1	Fitting Approach	74
3.6.2	Results	75
3.6.3	Discussion	76
3.7	Joint Orbital Constraints and System Flux	78
3.7.1	Timing and Eccentricity: Still a Chance for Winds	78
3.7.2	System Flux: No Excess Detected	80
3.8	Conclusions and Future Work	81
4	Tentative Emission from WASP-12b via Ground-based Spec-	
	troscopy	84
4.1	Abstract	84
4.2	Introduction	85
4.2.1	Ground-based Characterization of Exoplanet Atmospheres	85

4.2.2	The WASP-12 System	86
4.2.3	Outline	87
4.3	Observations and Initial Reduction	88
4.3.1	Summary of Observations	88
4.3.2	Initial Data Reduction	91
4.4	Characterization of Systematic Effects	93
4.4.1	Instrumental Sources	93
4.4.2	Slit Loss Effects	97
4.5	Searching for the Eclipse Spectrum	102
4.5.1	Fitting to the Data	102
4.5.2	Choice of Model	104
4.5.3	Estimating Coefficient Uncertainties	105
4.6	Systematic Errors in High-Precision Single-Slit Spectroscopy	106
4.6.1	Telluric Contamination	107
4.6.2	Chromatic Slit Losses	113
4.6.3	Result of Simulated Observations	115
4.7	Results: Thermal Emission from WASP-12b	117
4.7.1	Initial Presentation of Results	117
4.7.2	Comparison With Observations	119
4.7.3	Spectral Signatures: Still Unconstrained	122
4.7.4	Global Planetary Energy Budget	122
4.8	Lessons for Future Observations	126
4.9	Conclusions	128

5 Re-evaluating WASP-12b: Strong Emission at 2.315 μm, and Deeper Transits and Eclipses	130
5.1 Abstract	130
5.2 Introduction	131
5.2.1 Ground-based Characterization of Exoplanet Atmospheres	131
5.2.2 Paper Outline	134
5.3 Subaru/MOIRCS Narrowband Time-series Photometry	134
5.3.1 Summary of Observations	134
5.3.2 Initial Data Reduction	136
5.3.3 Instrumental Systematics	138
5.4 Searching for the 2.315 μm Narrowband Eclipse	140
5.4.1 Fitting to the Data	140
5.4.2 Initial Narrowband Eclipse Depth	142
5.4.3 Eclipse Duration and Timing: No Surprises	142
5.5 Bergfors-2: An Object Very Close to WASP-12	145
5.5.1 Planet Candidate Verification and Transit Dilution	145
5.5.2 Bergfors-2	147
5.5.3 Observations of Bergfors-2	148
5.5.4 The Spectral Type of Bergfors-2	155
5.5.5 Radial Velocities	159
5.5.6 Interpretation of Bergfors-2	160
5.6 Revising Past Eclipse and Transit Measurements of WASP-12b	160
5.7 Results: Thermal Emission from WASP-12b	163

5.7.1	Planetary Emission	163
5.7.2	Alternative Explanations for a Deep 2.315 μm Eclipse	166
5.8	Discussion	168
6	Transmission Spectroscopy of GJ 1214b	171
6.1	Abstract	171
6.2	Introduction	172
6.2.1	Characterizing Extrasolar Atmospheres	172
6.3	Observations and Atmospheric Models	174
6.3.1	The GJ 1214 System	174
6.3.2	Atmospheric Models of GJ 1214b	176
6.4	NIRSPEC Observations and Analysis	180
6.4.1	Summary of Observations	180
6.4.2	Initial Data Reduction	182
6.4.3	Measuring systematic effects	184
6.4.4	Identifying and Removing Systematic Effects	190
6.5	Needle in a Haystack: Searching for Transit Signatures	192
6.5.1	Fitting to the data	193
6.5.2	Comparing models to data	198
6.5.3	Sensitivity tests: injected models	204
6.6	Results and Discussion	209
6.6.1	Spectroscopic results	209
6.6.2	Constraints on GJ 1214b's atmosphere	210

6.6.3	Lessons for future ground-based spectroscopy	214
6.7	Conclusions	216
6.8	GJ 1214b: Post-publication Updates	217
7	Conclusion	220
7.1	Summary of Dissertation	220
7.2	Toward Multi-Object Exoplanet Spectroscopy	221
7.3	Selection of MOS Transit Targets	225
7.4	Final Thoughts	228
	Bibliography	229

LIST OF FIGURES

1.1	Census of known transiting planets.	2
1.2	Characterizing transiting exoplanet atmospheres.	3
1.3	Census of known super Earth.	9
2.1	<i>v</i> And b: Removal of pointing-correlated variability.	21
2.2	<i>v</i> And b: Fits to individual Spitzer/MIPS channels.	29
2.3	Thermal phase curve of the <i>v</i> And system.	30
2.4	Confidence intervals for <i>v</i> And b parameters.	34
2.5	<i>v</i> And b day-night contrast.	46
2.6	<i>v</i> And b composition.	47
3.1	MIPS/24 μ m photometry of HD 209458b.	57
3.2	MIPS pre-launch calibration data.	58
3.3	24 μ m transits of HD 209458b.	69
3.4	HD 209458b residual errors.	70
3.5	24 μ m eclipses of HD 209458b.	71
3.6	Transit parameter posterior distributions.	72
3.7	Current transmission spectrum of HD 209458b.	73
3.8	Theoretical T-P profiles of HD 209458b.	74
3.9	Current emission spectrum of HD 209458b.	79
4.1	WASP-12b: SpeX raw spectrophotometric data.	92
4.2	WASP-12b: SpeX systematic parameters (28 Dec 2009).	95

4.3	WASP-12b: SpeX systematic parameters (30 Dec 2009).	96
4.4	WASP-12b: Slitloss-corrected SpeX data.	99
4.5	WASP-12b: SpeX spectrophotometry (28 Dec 2009).	100
4.6	WASP-12b: SpeX spectrophotometry (30 Dec 2009).	101
4.7	WASP-12b: Best-fit eclipse parameters (28 Dec 2009).	108
4.8	WASP-12b: Best-fit eclipse parameters (30 Dec 2009).	109
4.9	Telluric water content during WASP-12b observations.	110
4.10	Spectral variability induced by telluric variations.	111
4.11	SpeX/WASP-12b forward modeling results.	117
4.12	SpeX/WASP-12b eclipse fit residuals.	118
4.13	SpeX spectra of WASP-12b.	119
4.14	WASP-12b: Tentative near-infrared spectrum.	123
4.15	Flux-calibrated spectral energy distribution of WASP-12b.	124
5.1	Instrumental trends during Subaru/MOIRCS narrowband photometry.	137
5.2	WASP-12b narrowband eclipse light curve.	143
5.3	RMS of the binned residuals to the WASP-12b eclipse fit.	144
5.4	Images used for astrometric analysis of Bergfors-2.	147
5.5	Constraints on the spectral type of Bergfors-2.	158
5.6	Corrected emission spectrum of WASP-12b.	164
6.1	Parameters of GJ 1214b atmospheric models.	177
6.2	Low-resolution, O/IR transmission models of GJ 1214b.	179

6.3	High-resolution, K-band transmission models of GJ 1214b.	179
6.4	Raw NIRSPEC spectrophotometry of the GJ 1214 system.	185
6.5	Representative spectrophotometry of the GJ 1214b system.	188
6.6	Keck/NIRSPEC systematic and telluric parameters.	189
6.7	Slitloss-calibrated spectrophotometric NIRSPEC data.	191
6.8	Transmission spectrum of GJ 1214b	197
6.9	Autocorrelation of high-resolution solar abundance model.	201
6.10	Template cross-correlation: solar abundance model.	202
6.11	Template cross-correlation: 10× solar abundance model.	203
6.12	Template cross-correlation: 30× solar abundance model.	204
6.13	Template cross-correlation: solar abundance (methane-free) model.	205
6.14	Template cross-correlation: solar abundance (low-carbon) model.	206
6.15	Photometric radius ratios of GJ 1214b: models and observations.	212
7.1	Sample multi-object slit mask.	222
7.2	Simulated results from MOS exoplanet spectroscopy.	223
7.3	Early results from MOS exoplanet spectroscopy.	224
7.4	Future targets for NIR MOS observations.	226

LIST OF TABLES

2.1	<i>v</i> And b Phase Curve and Calibration Parameters (2009 Data) ^a . . .	28
2.1	<i>v</i> And b Phase Curve and Calibration Parameters (2009 Data) ^a . . .	31
2.2	<i>v</i> And b Phase Curve and Calibration Parameters (2006 Data) ^a . . .	32
2.3	<i>v</i> And b Phase Curve: Astrophysical Parameters of Interest	33
2.4	<i>v</i> And b Phase Curve: Goodness-of-fit Statistics	33
3.1	HD 209458b: <i>Spitzer</i> /MIPS 24 μm Observations of	54
3.2	HD 209458b: Joint Transit Fits	67
3.3	HD 209458b: Semi-Joint Transit Fits	68
3.4	HD 209458b: Ramp/transit covariance matrix (cf. Figure 3.6). . . .	71
3.5	HD 209458b: Joint Eclipse Fits	76
3.6	HD 209458b: Independent Eclipse Fits	77
4.1	IRTF/SpeX Observations of WASP-12b	89
4.2	WASP-12b Calibrated Planet/Star Contrast Spectrum	121
5.1	WASP-12b: 2.315 μm Narrowband Eclipse Parameters	141
5.2	Bergfors-2 Astrometry	150
5.3	IRTF/SpeX Astrometric Calibrators ^a	151
5.4	WASP-12b Corrected Eclipse and Transit Depths	161
6.1	GJ 1214b Predicted Photometric Transit Radii (cf. Figure 6.2) . . .	180
6.2	Keck/NIRSPEC Observations of GJ 1214b	181

6.3	Telluric-free spectral regions from Hinkle et al. (2003)	186
6.3	Telluric-free spectral regions from Hinkle et al. (2003)	187
6.4	GJ 1214b Cross-Correlation Results	207
6.4	GJ 1214b Cross-Correlation Results	208

ACKNOWLEDGMENTS

My thanks go: to Brad Hansen for his support, tutelage, and advice during these many years; to my fellow graduate students, without whom my experience here would have been greatly diminished; and to Ned Wright and Alice Shapley for their support of and engagement with the department.

Ch. 2 is a version of [Crossfield et al. \(2010\)](#) and is reproduced by permission of the AAS. I thank J. Colbert, C. Engelbracht, and G. Rieke for help in interpreting MIPS systematics, and T. Loredó for helpful discussions of statistics.

Ch. 3 is a version of [Crossfield et al. \(2012b\)](#) and is reproduced by permission of the AAS. I thank Alberto Noriega-Crespo and James Colbert of the Spitzer Science Center for discussions about calibration of, and systematics in, the MIPS $24\ \mu\text{m}$ photometer.

Ch. 4 is a version of [Crossfield et al. \(2012a\)](#) and is reproduced by permission of the AAS. I thank S. Bus and J. Rayner for assistance in preparing and executing our observations, the IRTF Observatory for supporting my stay at Hale Pohaku, and the entire SpeX team for that rare achievement: a superb instrument that's a pleasure to use. Thanks also to A. Mandell for discussions about LBLRTM, to D. Feldman for his MATLAB wrapper scripts, to M. Swain for discussions about SpeX, and to S. Frewen, B. Croll, and N. Cowan for comments during manuscript preparation.

Ch. 5 is a version of a paper in preparation for submission to ApJ. For this work I thank M. Swain for the idea of using the sky background trend as a decorrelation vector in our analysis, and K. Stevenson and J. Harrington for reiterating the importance of partial pixels in high-precision aperture photometry.

Ch. 6 is a version of [Crossfield et al. \(2011\)](#) and is reproduced by permission of the AAS. I thank committee member I. McLean for useful discussions about the NIRSPEC instrument, D. Rodriguez for helpful comments during manuscript preparation, and B. Croll for useful feedback on the manuscript.

The data presented herein were obtained at the W.M. Keck, NASA IRTF, and Subaru Observatories on Mauna Kea, Hawai'i. I wish to recognize and acknowledge the very significant cultural role and reverence that the summit of Mauna Kea has always had within the indigenous Hawaiian community. The astronomical community is most fortunate to have the opportunity to conduct observations from this mountain. I also thank the many telescope operators and observatory support staff at Lick Observatory, the NASA Infrared Telescope Facility, Subaru Observatory, and Keck Observatory.

I received free software and services from SciPy, Matplotlib, and the Python Programming Language. In return I have made a large collection of my own code available on my website, and have received numerous inquiries over the years from people desirous of using my routines.

Finally, my research has made extensive use of the Exoplanet Orbit Database at <http://www.exoplanets.org> and the Extrasolar Planet Encyclopedia Explorer at <http://www.exoplanet.eu>.

VITA

- 2004 B.S. (Physics, concentration in Astrophysics)
University of California, Irvine
- 2004-2007 Optical & Systems Engineer
Jet Propulsion Laboratory, Pasadena, California.
- 2009 M.S. (Astronomy)
University of California, Los Angeles.

PUBLICATIONS

Crossfield, I. J. M.; Knutson, H.; Fortney, J.; Showman, A.; Cowan, N.B.; Deming, D.; “[Spitzer/MIPS 24 \$\mu\$ m Observations of HD 209458b: 3 eclipses, 2.5 transits, and a Phase Curve Corrupted by Instrumental Sensitivity Variations](#)”, ApJ accepted: April 2012.

Crossfield, I. J. M.; Hansen, B.M.S.; Barman, T.; “[Ground-based, Near-infrared Exospectroscopy. II. A Tentative Detection of Emission From the Extremely Hot Jupiter WASP-12b](#)”, 2011, ApJ, 746, 46

Crossfield, I. J. M.; Barman, T.; Hansen, B.M.S.; “[High Resolution, Differential, Near-infrared Transmission Spectroscopy of GJ 1214b](#)”, 2011, ApJ, 736, 132

Crossfield, I. J. M.; Hansen, B.M.S.; Harrington, J.; Cho, J.Y-K.; Deming, D.; Menou, K.; Seager, S.; “[A New 24 micron Phase Curve for upsilon Andromedae b](#)”, 2010, ApJ, 723, 1436

CHAPTER 1

Introduction

1.1 Introduction

We are in the midst of a revolution in our understanding of planetary systems. Missions studying planets in the Solar System (MESSENGER, Cassini, and soon Juno) and beyond (Hubble, Spitzer, and Kepler) are rapidly revealing new discoveries that challenge our conceptions of how planets form and evolve. The study of extrasolar planets, and especially of their atmospheres and all that these tell us, places the origin, formation, and evolution of Earth and the Solar System in a broader context. The last several years have seen rapid strides in this direction through the study of transiting planets (cf. Figure 1.1) – which pass in front of and behind their host stars (cf. Figure 1.2) – via routine photometric detection of ever-smaller planets (e.g., Batalha et al. 2011) as well as planetary thermal emission (Deming et al. 2005b; Charbonneau et al. 2005; Knutson et al. 2007b; de Mooij & Snellen 2009; Sing & López-Morales 2009) and atmospheric transmission (Charbonneau et al. 2002; Sing et al. 2009; Bean et al. 2010; Berta et al. 2012) with Spitzer, Hubble (HST), and ground-based telescopes.

The latest new frontier to emerge is the study of molecular chemistry in the atmospheres of the brightest nearby exoplanets, which is performed by looking at emission from the planet and/or at the transmission of starlight through the limb of the planet’s atmosphere (cf. Figure 1.2). Currently there are tight constraints

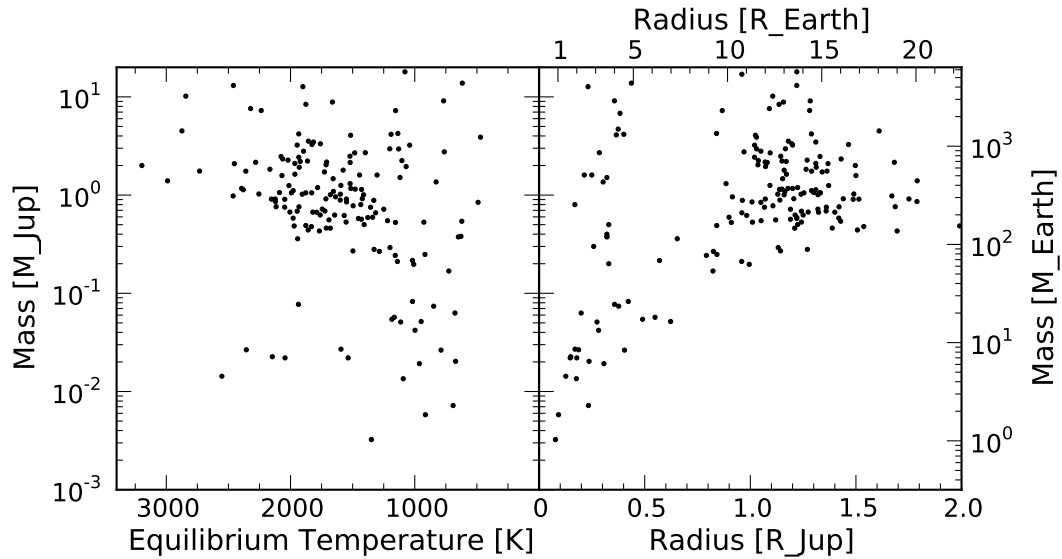


Figure 1.1 **Transiting planets with measured masses** plotted against radius (right) and equilibrium temperature (left, assuming zero albedo). Transiting planets are most easily discovered when they are large and close to their host stars, which causes the apparent pile-up of massive planets around 2000 K and $1.3 R_J$. Large, hot planets are also those whose atmospheres are most easily studied using methods depicted in Figure 1.2. Note that some transiting planets discovered by the Kepler mission lack mass measurements, and so do not appear here.

on the atmospheres of only a handful of planets, primarily based on Spitzer infrared photometry (e.g., [Knutson et al. 2008](#); [Stevenson et al. 2010](#); [Madhusudhan et al. 2011a](#)) but also using ground-based photometry ([de Mooij et al. 2012](#); [Croll et al. 2011a](#)), Hubble and ground-based optical spectroscopy ([Redfield et al. 2008](#); [Lecavelier Des Etangs et al. 2008a,b](#); [Bean et al. 2010, 2011](#)), and, more recently, ground-based near-infrared (NIR) spectroscopy ([Swain et al. 2010](#); [Snellen et al. 2010](#); [Bean et al. 2011](#)). Spectroscopic measurements of molecular features across multiple wavelength regions offer the best potential to constrain atmospheric structure and composition (e.g., [Fortney et al. 2010](#); [Madhusudhan et al.](#)

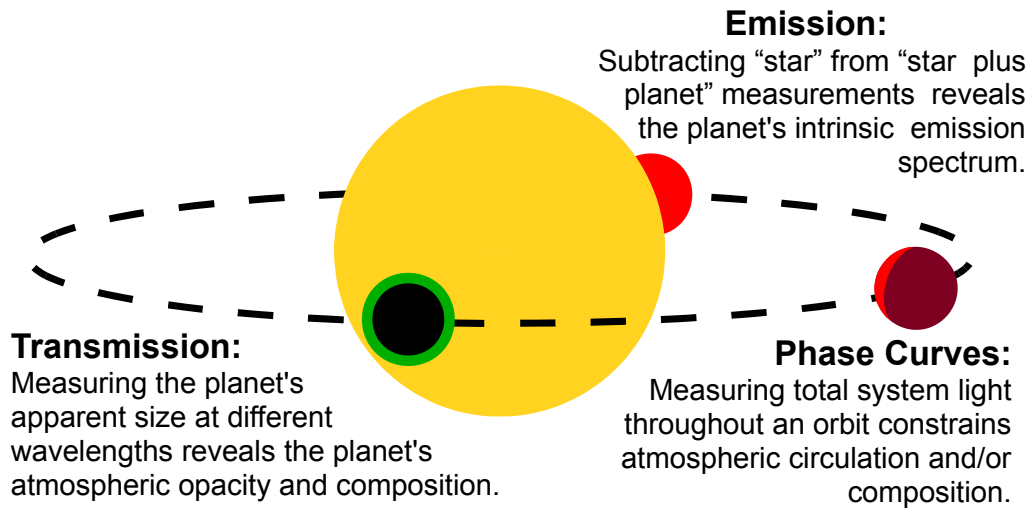


Figure 1.2 **Characterizing transiting exoplanet atmospheres.** A transiting planet’s emission can be measured by subtracting “star only” observations taken during eclipse from combined-light “star plus planet” flux measurements, whereas transmission observations measure how the size of a planet varies with wavelength due to absorption by the planet’s atmosphere. The techniques are complementary: emission measurements mostly constrain the brightness temperature of a planet and its atmospheric structure, while transmission measurements are better suited to constrain the abundances of atomic and molecular species. Phase curve observations require much longer observational baselines but provide crucial, longitudinally resolved measurements of planetary emission (infrared) or scattering (optical), and can be obtained for even non-transiting systems.

2011a), and to probe the planet’s formation and evolution (e.g., Öberg et al. 2011; Madhusudhan et al. 2011b; Lopez et al. 2012).

1.2 Probing Exoplanet Interiors and Atmospheres

1.2.1 The Uncertain Nature of Exoplanet Atmospheres

Ever since the first discovery of transits by the large planet orbiting around the star HD 209458 (Henry et al. 2000b; Charbonneau et al. 2000), hot Jupiters – massive planets located close to their host stars – have been the most common type of confirmed transiting planet, as can be seen in Figure 1.1. Although models of planetary interiors strongly suggest that these planets are H₂-dominated gas giants (Fortney et al. 2007), substantial uncertainties remain as to the detailed composition and structure of these planets’ atmospheres. This is especially frustrating because by virtue of their large sizes and high temperatures, hot Jupiters are the most easily studied type of transiting planet. The atmospheric ambiguities are greatest when (as in the majority of cases) observations remain dominated by broad band photometric measurements. Broad band photometry averages over features caused by separate opacity sources, and in most cases atmospheric models have more free parameters than there are observational constraints. Even for those planets with the highest-quality photometry, significant degeneracies remain both in atmospheric composition and planetary structure (e.g., Madhusudhan & Seager 2010). Thus although this dissertation begins with a discussion of broad band photometric observations in Chs. 2 and 3, the desire for resolved spectroscopic measurements motivates the chapters that follow.

1.2.1.1 Composition and Structure

Some hot Jupiters exhibit high-altitude temperature inversions at roughly 100 mbar (e.g., [Knutson et al. 2008](#)) while others do not (e.g., [Charbonneau et al. 2008](#)). We do not know why. One early theory predicted that TiO, an optical absorber prevalent in M dwarfs, could be the culprit ([Hubeny et al. 2003](#); [Fortney et al. 2008](#); [Burrows et al. 2008](#)). Hotter, more intensely irradiated planets would exhibit inversions because TiO would remain gaseous and absorb the incident stellar irradiation at altitude, while in less intensely irradiated planets temperatures would be low enough for TiO to condense and rain out of the atmosphere. Subsequent work has suggested that even on the hottest planets, extremely vigorous mixing is required to keep TiO from settling out of the atmosphere on the planets' colder night sides ([Spiegel et al. 2009](#)). In addition, subsequent analysis of inverted and non-inverted atmospheres show no clear correlation with irradiation ([Madhusudhan & Seager 2010](#)). Another theory suggests that planets should not have inversions around chromospherically active stars, because the high-energy radiation environment would dissociate the high-altitude compounds responsible for temperature inversions ([Knutson et al. 2010](#)) – but this theory, too, does not seem to adequately explain recent observations (e.g., [Madhusudhan et al. 2011a](#)).

A recently proposed paradigm posits that deviations from a solar carbon to oxygen (C/O) ratio could explain the dichotomous Hot Jupiter atmospheres ([Madhusudhan et al. 2011b](#)). If O-bearing compounds (e.g., water ice) migrated through the natal protoplanetary disk and left a C-enhanced gas disk for subsequent accretion, or alternatively if gas giants form from oxygen-depleted planetesimals between the H₂O and CO snow lines ([Öberg et al. 2011](#)), the resulting planet would be substantially enhanced in C and depleted in O relative to the Sun. Because the O content of carbon-rich giant planetary atmospheres is pri-

marily locked into CO, they are substantially depleted in O-bearing compounds – including H₂O and the TiO often invoked to explain thermal inversions (Madhusudhan et al. 2011b). Thus it may be that Hot Jupiters without inversions are carbon-rich. Even Jupiter’s C/O ratio is not known (Atreya et al. 2003), though it will be measured by the recently launched Juno mission (Bolton & Bolton 2010). Spectroscopy of hot Jupiters has the potential to tell us whether or not supersolar C/O ratios are common in gas giants, and to place Juno’s future results in an appropriate interstellar context. This paradigm of enhanced C/O motivated the observations of the extremely hot Jupiter WASP-12b described in Chs. 4 and 5, which detect the planet’s emission and place important new constraints on its atmospheric structure and composition.

1.2.2 Circulation

Hot Jupiter atmospheres are expected to display a diversity of atmospheric circulation behaviors. Large-scale super-rotating jets are a ubiquitous prediction of general circulation models of these planets’ atmospheres (e.g., Rauscher et al. 2008; Showman et al. 2009). In some cases these jets efficiently transport heat around the planet, resulting in fairly homogeneous circumplanetary temperature distributions. However, absorption of the incident stellar flux high in the atmosphere (where radiative timescales are short and advection is inefficient; Cowan & Agol 2011a), can result in large day/night temperature contrasts and low global energy redistribution factors even in the presence of these rapid winds (e.g., Showman et al. 2009).

Eclipse measurements determine planets’ dayside luminosities and can constrain atmospheric circulation (Cowan & Agol 2011b), but a more direct probe of circulation is the observation of these planets’ thermal phase curves; cf. Fig-

ure 1.2. Planets with little recirculation of incident stellar flux (and thus with high day/night temperature contrasts) are expected to exhibit high-amplitude phase curves centered close to the time of eclipse, while planets with efficient circulation should exhibit thermal phase curves offset that do not peak at eclipse and have lower amplitudes (e.g., [Showman et al. 2009](#); [Burrows et al. 2010](#)). In Ch. 2 I describe my analysis of Spitzer/MIPS $24\ \mu\text{m}$ observations of the non-transiting planet *v* And b’s thermal phase curve. The data exhibit a phase offset of nearly 80 deg, which is much greater than predicted by any atmospheric circulation models and remains unexplained.

An alternative method to constrain atmospheric circulation is through high-resolution spectroscopy of a planetary system during transit ([Snellen et al. 2010](#)). A planetary atmosphere manifests itself in such observations as a set of absorption features being Doppler shifted with the planet’s known radial velocity. When the orbital parameters are well-constrained, any difference between the expected and observed atmospheric radial velocities can be attributed to winds in the atmosphere: e.g., a net blueshift of the planetary spectrum as winds flow from the day side to the night side ([Snellen et al. 2010](#); [Fortney et al. 2010](#); [Rauscher & Menou 2012](#)). Eclipse observations are also essential to this analysis: they tightly constrain the planet’s orbital eccentricity, which can masquerade as a spurious velocity offset in such data ([Montalto et al. 2011](#)). My eclipse observations of HD 209458b (in Ch. 3) and of WASP-12b (in Ch. 4) are of direct utility to such observations. My NIRSPEC observations of GJ 1214b, described in Ch. 6, have a precision and spectral resolution that are too low to detect this effect, and were instead designed to provide insight in this planet’s atmospheric (and interior) composition.

1.2.3 Atmospheric Probes of Interior Compositions

Though hot Jupiters are the most plentiful transiting planets known, radial velocity surveys (e.g., [Howard et al. 2010](#)) and initial results from the Kepler mission ([Howard et al. 2011](#)) demonstrate that smaller, less massive planets are at least an order of magnitude more plentiful, at least for short (< 50 d) orbits. The transiting subset of these planets, intermediate in mass and/or radius between Earth and Neptune, is shown in [Figure 1.3](#).

The scatter in [Figure 1.3](#) suggests that planets in this intermediate (sub-Neptune, super-Earth) mass range have a variety of interior compositions. A Monte Carlo analysis of simulated radial velocity data (which measures planet masses) and simulated Kepler-like transit photometry (which measures precise planet radii) suggests that the results of these complementary surveys can be reconciled by invoking a rock fraction that increases from Neptune mass to Earth mass ([Wolfgang & Laughlin 2011](#)). Because of the large number of possible constituents (e.g., iron, rock, ice, gas), mass and radius measurements alone cannot uniquely determine these planets' compositions ([Valencia 2011](#)). Indeed, in some cases the planetary surface may be unobservable: in this case atmospheric studies are the only means of probing planetary composition.

At present we know even less about the makeup of these lower-mass planets than we do about Hot Jupiters. Some are denser than the bulk Earth (CoRoT-7b and Kepler-10b; [Ferraz-Mello et al. 2011](#); [Batalha et al. 2011](#), respectively) and so presumably have little or no atmosphere ([Schaefer & Fegley 2009](#); [Valencia 2011](#)), but a growing number have densities $\gtrsim 2$ g cm⁻³ and so probably have substantial complements of both volatiles and refractory elements ([Rogers & Seager 2010](#)) including, perhaps, detectable atmospheres. Uranus and Neptune have substantially enhanced heavy element abundances in their atmospheres ([En-](#)

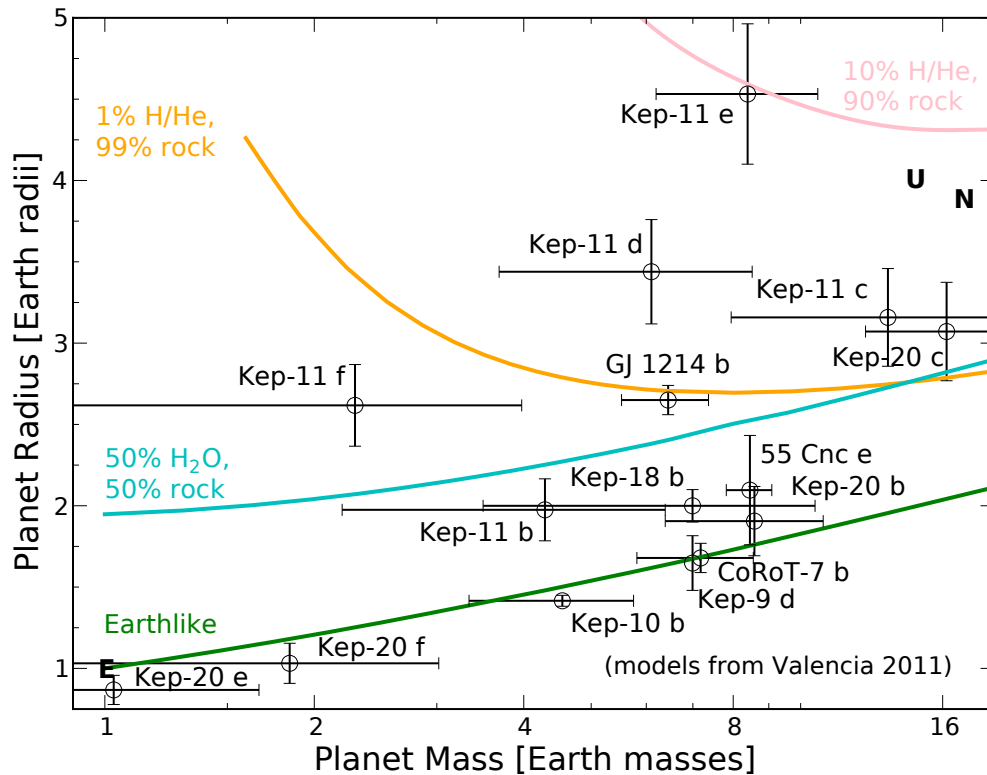


Figure 1.3 Mass-radius diagram for the smallest known transiting planets with confirmed masses. Many planets’ bulk parameters can be matched with a wide range of compositions, ranging from iron/rock (green, bottom; Earthlike), to H₂O dominated (blue, middle; Ganymede-like), to substantial H/He envelopes (orange and pink; Neptune-like). **Only atmospheric characterization can reveal the true compositions of these worlds.** Bulk composition models (solid lines) are from Valencia (2011), and planets denoted “Kep” are from the Kepler space telescope.

renaz 2005), which is interpreted as consistent with their bulk composition and taken as evidence for their formation via core accretion (Pollack et al. 1996). Similarly, atmospheric spectroscopy of exoplanets can provide clues to these planets’ formations, and thus to the origins of their atmospheres and to their history and evolution.

We cannot typically probe the interiors of extrasolar planets, but spectro-

spectroscopic atmospheric characterization can reveal much about these planet’s origins and compositions. For example, a planet with a large H₂/He envelope presumably accreted its gas from the protoplanetary disk in which it formed, but a small H₂/He envelope could form via outgassing as the planet cools (Rogers & Seager 2010). Spectroscopy can determine the heavy element abundances (especially C and O) of the atmosphere and constrain the planet’s formation history. A planet rich in H₂O would most likely have formed beyond the H₂O snow line and later migrated closer in (sub-Neptune sized planets known today are all hotter than Earth). A denser world could form via any of these scenarios and have had its primordial atmosphere subsequently ablated away in close proximity to its star – or, like the Earth, it may have formed in situ without an especially large gas envelope. In all cases spectroscopy is the best method to characterize the planet’s atmosphere. Ch. 6 describes my high-resolution Keck/NIRSPEC spectroscopy of the low-mass planet GJ 1214b, which rules out H₂-dominated atmospheres in chemical equilibrium but leaves the primary atmospheric constituent unconstrained.

1.3 Observing Exoplanet Atmospheres

Spectroscopy, properly calibrated, can provide the high-fidelity data necessary to resolve the degeneracies of current photometric data sets. The two complementary techniques outlined in Figure 1.2 – observations of a transiting planet’s intrinsic emission, and of its atmospheric transmission – allow insight into the nature of the planet’s atmosphere.

1.3.1 Eclipse Spectroscopy

Thermal emission from the hottest planets can be measured using eclipse spectroscopy. By subtracting a star-only spectrum taken when a transiting planet is occulted by its host star from a combined (star plus planet) spectrum taken just before or after eclipse, one obtains a measure of the intrinsic emission of the planet relative to that of the star. By comparing to stellar models or flux-calibrated stellar observations the observed planet/star contrast ratio can be converted into a planetary flux. A rough but useful estimate of the contrast observed can be obtained by assuming star and planet emission to be that of blackbodies, which gives an eclipse depth of $E = \left(\frac{R_P}{R_*}\right)^2 \frac{B_\lambda(T_P)}{B_\lambda(T_*)}$, where R is a radius, T a temperature, B_λ the Planck function, and the subscripts P and “*” refer to the planet and star, respectively. Since planets are not true blackbody radiators, it is the deviations from blackbody emission that constrain planetary albedos, atmospheric circulation, and the redistribution of incident stellar flux. Eclipse measurements have largely fueled the debate about Hot Jupiter high-altitude temperature inversions discussed in Section 1.2. I present my analyses of planetary eclipses of the hot Jupiters HD 209458b (using photometry) and WASP-12b (using both photometry and spectroscopy) in Chs. 3–5.

1.3.2 Transmission Spectroscopy

Many planets are too cool for their emission to be easily detected, and even a hot – but isothermal – atmosphere will exhibit a featureless emission spectrum that precludes detailed studies of its composition. However, atmospheres of cool planets can still be studied via transmission spectroscopy: as the planet transits its host star the $\tau = 1$ surface – and thus the apparent size of the planet – changes with wavelength. The amplitude of the resulting, spectrum-like signal depends

on the atmospheric scale height, $H = k_B T_P / (\mu g_P)$, where μ is the mean molecular weight of the planet’s atmosphere and g_P the surface gravity. The relative amplitude of spectral features is then proportional to H , viz.: $D \approx 2HR_P/R_*^2$ (Miller-Ricci et al. 2009). Because both T_P and g_P can be estimated for transiting planets (whose mass, radius, semimajor axis, and host star properties are all well-determined), to zeroth order multiwavelength transit observations constrain μ by determining the relative amplitude of variations in the transmission spectrum. Higher-precision measurements can also constrain the abundances of individual molecular and atomic species.

Thus transmission (like emission) observations favor hotter planets because their atmospheres are more puffed up and provide a larger translucent annulus during transit. One advantage of the transmission approach over emission measurements is that in the former, abundances can be determined even in the presence of an isothermal atmospheric temperature profile. In addition, transmission studies can be used to study substantially cooler planetary atmospheres and may be the primary technique by which planets with Earthlike temperatures are studied in the near future (Deming et al. 2009; Kaltenegger & Traub 2009). In Ch. 3 I present the most precise $24\mu\text{m}$ transit measurement of HD 209458b to date – however, the future of transmission spectroscopy lies in the direction of Ch. 6, which presents my spectroscopic analysis of transits of the cool, low-mass planet GJ 1214b.

1.4 Dissertation Outline

The remainder of this dissertation describes my infrared observations of a number of extrasolar planetary systems, which aim to inform our understanding of these bodies’ atmospheric structure and composition. Chs. 2 and 3 describe

Spitzer/MIPS 24 μm photometry of two hot Jupiters: *v* And b, a non-transiting planet orbiting a bright, nearby star, and HD 209458b, one of two canonical transiting hot Jupiters and the first discovered transiting planet. Photometry is the simplest and most straightforward method of characterizing transiting planets, so these initial analyses offer a gradual introduction to the more complicated spectroscopic results that follow. Narrowband Subaru/MOIRCS photometry follows, along with some first efforts at low-resolution, ground-based, near-infrared spectroscopy, with an examination of the thermal emission of the extremely Hot Jupiter WASP-12b in Chs. 4 and 5. In Ch. 6 I describe my attempt to detect the atmospheric signature of the cool, low-mass planet GJ 1214b using Keck/NIRSPEC high-resolution spectroscopy. Finally, I conclude and discuss future prospects for the study of exoplanet atmospheres in Ch. 7.

CHAPTER 2

Energy Balance and Atmospheric Circulation in upsilon Andromedae b

2.1 Abstract

We report the detection of $24\ \mu\text{m}$ variations from the planet-hosting upsilon Andromeda system consistent with the orbital periodicity of the system's innermost planet, υ And b. We find a peak-to-valley phase curve amplitude of 0.130%. Using a simple model with two hemispheres of constant surface brightness and assuming a planetary radius of $1.3 R_J$ gives a planetary temperature contrast of $\gtrsim 900$ K and an orbital inclination of $\gtrsim 28^\circ$. We further report the largest phase offset yet observed for an extrasolar planet: the flux maximum occurs $\sim 80^\circ$ before phase 0.5. Such a large phase offset is difficult to reconcile with most current atmospheric circulation models. We improve on earlier observations of this system in several important ways: (1) observations of a flux calibrator star demonstrate the MIPS detector is stable to 10^{-4} on long timescales, (2) we note that the background light varies systematically due to spacecraft operations, precluding use of this background as a flux calibrator (stellar flux measured above the background is not similarly affected), and (3) we calibrate for flux variability correlated with motion of the star on the MIPS detector. A reanalysis of our earlier observations of this system is consistent with our new result.

2.2 Introduction

The first thermal characterizations of highly irradiated extrasolar planetary atmospheres were made by measuring the flux decrement that occurs during secondary eclipse, when an extrasolar planet passes behind its host star (Deming et al. 2005a; Charbonneau et al. 2005). This decrement gives an estimate of the (hemisphere-averaged) temperature of a planet’s star-facing side at the time of eclipse and provides insight into the energy budgets of these hot worlds. Secondary eclipse (or, occultation) observations have been widely interpreted as indicating two types of planetary atmospheres, namely planets with and without high-altitude temperature inversions (Burrows et al. 2008; Fortney et al. 2008). However, the number of free parameters in current models is such that in many cases it is still difficult to place strong constraints on a planet’s atmospheric structure with the few data points available for most systems (Madhusudhan & Seager 2009).

Burrows et al. (2008) and Fortney et al. (2008) suggested that sufficiently high levels of irradiation prevent strong optically absorbing species from condensing and “raining out” of the upper atmosphere of hot Jupiters, thus directly linking high levels of incident stellar flux to the presence of a temperature inversion. However, subsequent secondary eclipse measurements with Spitzer/IRAC have complicated the picture and a straightforward connection between irradiation and inversions now seems untenable. For example, TrES-3b receives substantially more flux than does HD 209458b, yet the latter has an atmospheric inversion (Knutson et al. 2008) while the former does not (Fressin et al. 2010). Thus, planetary classification will require more subtlety than a simple critical-flux level model can provide. Knutson et al. (2010) have recently suggested a correlation between stellar activity and the absence of a temperature inversion: in this hy-

pothesis high-altitude absorbing species are photodissociated by the ultraviolet flux from an active star. It remains to be seen how this theory addresses the issue of temporally variable stellar activity (Shkolnik et al. 2008).

Phase curves provide complementary insights into planetary atmospheres. If a system’s total (star plus planet) infrared flux varies periodically and in phase with the planet’s orbit, the variation can be attributed to spatially nonuniform radiation emitted by the planet. Such measurements have the potential to constrain the planet’s circulation and heat redistribution patterns. If incident stellar flux were instantaneously re-radiated by the planet, the hottest region on the planet would be at the substellar point; such a phase curve is said to have zero phase offset. Nonzero phase offsets thus imply heat transport around the planet; for example, by advection of absorbed stellar energy by global winds (Showman et al. 2009), or by heating induced by atmospheric gravity waves (Watkins & Cho 2010). Interpreting phase curves can be challenging because the brightest atmospheric region will also depend on the opacity structure of the atmosphere and the wavelength at which one observes the system.

The extrasolar planet upsilon Andromeda b (υ And b) is the first exoplanet for which a phase curve was reported. Harrington et al. (2006; hereafter H06) used Spitzer/MIPS to measure the $24\ \mu\text{m}$ system flux at five epochs over one orbit and reported a finite amplitude phase curve consistent with zero phase offset, though here we report a new analysis and interpretation of our H06 data based on a better understanding of MIPS systematics. The $8\ \mu\text{m}$ observations of Cowan et al. (2007) also found variations with zero phase offset for HD 179949b. Observations of the less intensely irradiated planet HD 189733b at $8\ \mu\text{m}$ and $24\ \mu\text{m}$ (Knutson et al. 2007a, 2009b) revealed a relatively small temperature contrast between the planet’s day and night sides and a $30^\circ - 40^\circ$ phase offset, indicating a moderate

level of eastward heat redistribution from the warm dayside to the cool night side. It is important to note a possible observational bias: the first two phase curves were sparsely sampled and are for non-transiting systems with unknown orbital inclinations. Though simulations suggest inclination should not substantially affect a planet’s observed phase offset, the flux amplitude will be directly affected by inclination (Rauscher et al. 2008); furthermore, phase curve interpretations are more ambiguous without the absolute calibration provided by a secondary eclipse (Burrows et al. 2008).

Several groups have hypothesized a connection between temperature inversions and the magnitude of a system’s phase offset (e.g., Burrows et al. 2008; Fortney et al. 2008). The favored (though unproven) cause of inversions is a species residing at high altitude that absorbs optically but is transparent to infrared radiation. In this scenario an inverted atmosphere absorbs stellar energy at lower pressures where it should quickly re-radiate to space; in a non-inverted atmosphere the energy is absorbed much deeper, where it may circulate farther around the planet and cause a measurable phase offset. Showman et al. (2009) do a fair job of reproducing the HD 189733b phase curves, but they predict secondary eclipse depths for the more highly irradiated HD 209458b that do not match the observations of Knutson et al. (2008); Burrows et al. (2010) also model HD 209458b and they, too, do not match the observed eclipse depths especially well. Thus, our current understanding of the atmospheric structure and dynamics of even the best-characterized planets still appears to be incomplete.

This is the context in which we obtained the high-cadence $24\ \mu\text{m}$ phase curve of v And b described below. We introduce the upsilon Andromeda system, and discuss our observations and data analysis, in Sec. 3.3. In Sec. 2.4 we describe the planetary temperature contrast and heat redistribution implied by our analysis.

We discuss possible interpretations of our results in Sec. 2.5, and conclude in Sec. 3.8. Finally, in Sec. 2.7 we discuss results relevant to the study of ν And b presented here that occurred after publication of this chapter’s material (Crossfield et al. 2010).

2.3 Observations and Analysis

2.3.1 The ν Andromedae System

The planet ν And b was one of the earliest reported hot Jupiters (Butler et al. 1997), and the three-planet ν And system has been observed numerous times in the years since (Butler et al. 2006; Naef et al. 2004; Wittenmyer et al. 2007; McArthur et al. 2010). The host star has a spectroscopic effective temperature of 6212 ± 64 K (Santos et al. 2004) and a directly-measured diameter of $1.631 \pm 0.014 R_{\odot}$ (Baines et al. 2008). Spectroscopic and isochronal mass estimates generally agree on a mass of $\sim 1.3 M_{\odot}$ (Fuhrmann et al. 1998; Ford et al. 1999; Valenti & Fischer 2005; Takeda et al. 2007). Because this system’s planets do not transit we do not know their physical sizes; however, if we assume ν And b is a typical hot Jupiter we can estimate its radius to be $\sim 1.3 R_J$ ¹.

Using a combination of radial velocity and astrometry McArthur et al. (2010) recently determined the orbits of the second and third planets in the ν And system to be mutually inclined by 30° . They suggest this non-planar system may result from planet-planet scattering that could also have moved the innermost planet, ν And b, into its current orbit at 0.059 AU. The small stellar reflex motion induced by ν And b precluded a direct measurement of its orbital inclination, but their preliminary numerical simulations extending 10^5 yr suggest ν And b’s

¹Taken from the Extrasolar Planets Encyclopedia at <http://exoplanet.eu>

inclination may lie in the range $\sim 20\text{-}45^\circ$ (implying a planetary mass of $2\text{-}3 M_J$). Though their simulations did not fully explore the available parameter space, the inclination range [McArthur et al. \(2010\)](#) suggest for v And b is broadly consistent with the constraints we place on its inclination in [Sec. 2.4](#).

2.3.2 Observations

We observed the v And system with Spitzer’s MIPS $24\ \mu\text{m}$ channel ([Rieke et al. 2004](#)) with observations spread across 1.2 orbits of v And b (~ 5 days) during February 2009. The observations consist of seven brief (~ 3000 seconds on target) observational epochs and one long, near-continuous observation ~ 28 hours in length and centered at phase 0.5 (secondary eclipse for transiting systems in circular orbits, and the predicted time of flux maximum based on H06). Our integrations total 18.5 hours. Spitzer breaks up observations into blocks of time called astronomical observation requests (AORs) for instrument scheduling purposes: our short observations consist of three sequential AORs, and the long observing sequence consists of 71 AORs. Altogether our data consist of 25 488 frames, each with an integration time of 1.57 seconds. We also observe a flux calibrator star, HD 9712, in three two-AOR epochs, for a total of 1.3 hours of integration. The observations of v And by H06, which we reanalyze, consist of five AORs spaced over ~ 5 days.

2.3.3 Data Reduction

We use the basic calibrated data (BCD) files generated by version 18.14 of the MIPS data reduction pipeline ([Masci et al. 2005](#)). During MIPS observations the instrument and spacecraft dither the target star between fourteen positions on the detector ([Colbert, J. 2011](#), Section 8.2.1.2). As noted previously ([Deming](#)

et al. 2005; H06; Knutson et al. 2009b) the MIPS detector response is spatially nonuniform and so we treat the observations as consisting of fourteen separate time series, modeling their systematics separately in the final fit. In each frame we measure the system flux and the position of the star on the detector by fitting a $100\times$ super-sampled model MIPS PSF² generated using a 6200 K blackbody spectrum. We shift and scale the model PSF to determine the best-fitting combination of background, stellar flux, and PSF position. Using position-dependent model PSFs does not significantly change our results, so in all our photometry we use a single model PSF generated at the center of the MIPS field of view. We exclude hot pixels from the PSF fit by setting to zero the weight of any frame’s pixel that is more than 5σ discrepant from the median value of that pixel for all frames taken at that particular dither position, and also exclude bad pixels flagged by the MIPS reduction pipeline.

In each set of ~ 40 frames, the first frame has $\sim 3\%$ higher stellar flux, and the first several frames have a lower background, than the rest of the frames in the set. These effects may be related to the MIPS “first-frame” chip reset effect, though the effect we see is qualitatively different from the one described in the MIPS Instrument Handbook (Colbert, J. 2011). We exclude the first frame in each set from the remainder of our analysis, removing 708 frames. We further exclude the first three contiguous AORs (700 frames, ~ 40 minutes), which are markedly discrepant from the final time series. These first data were taken soon after a thermal anneal of the MIPS detector, and during these observations we see anomalous readings in the $24\mu\text{m}$ detector anneal current, the scan mirror temperature, and the MIPS B side temperature sensor.

The initial extracted photometry reveals a clear sinusoidal flux variation, but

²Generated using Tiny Tim; available at <http://ssc.spitzer.caltech.edu/>

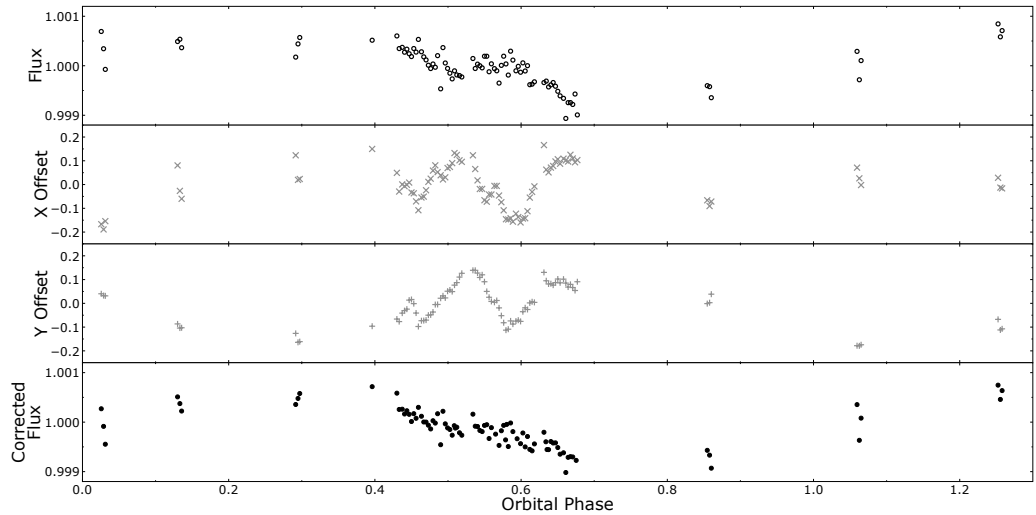


Figure 2.1 Removal of pointing-correlated photometric variability. The top panel shows photometry after bringing all fourteen individual time series to a common level. A large-scale sinusoidal flux variation is evident, but so is a shorter-scale “ripple” (near phase 0.5); this ripple is correlated with the motion of ν And on the MIPS detector, plotted as X and Y in the middle two panels. The bottom plot shows the final, cleaned photometry after removing this correlation. For display purposes the full data set has been averaged over each AOR in this figure. Uncertainties on the X and Y points are typically $\sim 10^{-3}$ pixel, while the uncertainties of the photometric points (not plotted for clarity) is typically $\sim 1.5 \times 10^{-4}$.

with additional variability correlated with the subpixel motion of the star on the detector, as shown in Figures 2.1 and 2.2. This effect is likely from imperfect flat fielding rather than an intrapixel sensitivity variation as seen in the Infrared Array Camera’s 3.6 and 4.5 μm channels (Reach et al. 2005; Charbonneau et al. 2005), because several time series with similar intrapixel locations exhibit anticorrelated flux variations. We tried creating a flat field by median-stacking all the BCD frames after masking the region containing the target star, but applying this flat field to the data before computing photometry did not reduce the amplitude of the position-correlated photometric variability. As we describe below, we suspect intermittent, low levels of scattered light interfere with our ability to construct a sufficiently accurate flat field

Instead, we treat this variability by removing a linear function of position from the computed photometry at each of the fourteen dither positions. Fitting functions with a higher-order dependence on position, or including cross terms, does not change our final results and increases the Bayesian Information Criterion ($\text{BIC} = \chi^2 + k \ln N$, where k is the number of free parameters and N is the number of points). We remove the systematic effects, and assess possible phase functions, by fitting the j^{th} data point at the i^{th} dither position (f_{ij}) with the following equation:

$$f_{ij} = (a + b \sin [\Omega_{\text{orb}} t - \Phi_0]) (1 + c_i + d_i x_{ij} + e_i y_{ij}) \quad (2.1)$$

This equation contains three astrophysical parameters and 42 instrumental parameters that account for the nonuniform detector response. The astrophysical parameters of interest are the average system flux a and a time (t)-dependent sinusoidal phase function with known planetary orbital frequency Ω_{orb} but unknown amplitude b and phase offset Φ_0 . The remaining parameters represent systematic effects to be removed: residual sensitivity corrections c_i and linear dependence on detector position (d_i, e_i) for each of the fourteen time series.

To prevent parameters a and b from floating we artificially set c_1 to satisfy the relation $\prod_i (1 + c_i) = 1$. Ignoring the (d_i, e_i) factors does not change our final result for the 2009 data set but increases the BIC, indicating a poorer fit to the data. For the purposes of backwards comparison, we also apply our analysis to the observations of H06. Due to the limited temporal coverage of this data set including the (d_i, e_i) does not improve the fit; therefore we use only 17 parameters when reanalyzing this earlier data set. We otherwise apply the same data reduction steps as described above.

In this work we consider only a sinusoidal phase function. Although we recognize that the phase curve will not be truly sinusoidal in shape, such a model is

simple to work with and has a straightforward interpretation as a two-hemisphere “orange slice” model (Cowan et al. 2007; Cowan & Agol 2008, see also Sec. 2.4.2 below). Since the motion-correlated flux variation only depends on relative motion (rather than on absolute detector position) we normalized the (x_{ij}, y_{ij}) in Eq. (2.1) by subtracting the mean position in each of the fourteen time series.

2.3.4 Calibration and instrument stability

Our continuous photometry reveals that the MIPS background flux changes discontinuously from one AOR to the next. Stellar photometry is not similarly affected. The background flux varies at the level of 0.1%, comparable in amplitude to the expected planetary signal. We also see these discontinuities in background flux during MIPS observations of HD 189733b (Knutson et al. 2009b) and HD 209458b (unpublished; Spitzer Program ID 40280).

Because the measured background level varies with the Spitzer AORs it is extremely unlikely that this variability is of astrophysical origin. It is also unlikely that the background variability results from the calibration process because we see the same effect in both the raw and calibrated data products. We observe no correlation between the background variability and the various reported instrumental parameters, though we cannot rule out either intermittent scatter from other sources or slight changes in the detector bias. A global sensitivity drift does not seem to be the culprit because the changes in background flux are uncorrelated with stellar photometry.

Although we were unable to determine the cause of the background variations, we suspect that they are due to small changes in the amount of scattered light reaching the MIPS detector. Variable scattered light could also explain our inability to remove the motion-correlated photometric jitter with an empirical flat

field. Stellar photometry was substantially more stable on short timescales than was the background in all of the extended MIPS $24\mu\text{m}$ observations we examined, so we use this photometry in our subsequent analysis.

Our observations include a flux calibrator star to check MIPS’s long-term photometric stability. MIPS $24\mu\text{m}$ photometry is known to be stable at the 0.4% level over several years (Engelbracht et al. 2007); if it were this variable on short timescales we would be unable to discern the expected planetary emission. We observed the K1 III star HD 9712, taken from a catalog of bright interferometric calibrator stars (Mérand et al. 2005), during six AORs. In our reduction of these data we do not apply a correction for pixel motions and we achieve a repeatability of $\sim 10^{-4}$. These observations, shown as the red triangles in Figure 2.3, imply that the MIPS $24\mu\text{m}$ detector was stable over the course of our observations, and so we rule out detector sensitivity drifts as the source of the observed flux variations.

The level of MIPS photometric stability was not well known early in the Spitzer mission, so H06 used the background, attributed to smoothly-varying zodiacal emission, as a calibrator to adjust the photometry (see H06 Figure 1B). As we now suspect the MIPS background variations to result from scattered light in the instrument, there is no longer any need, nor possibility, to use the zodiacal light as a calibrator. The H06 data were part of a preliminary Spitzer program to assess variability of several systems for subsequent study in programs such as ours. Its five v And AORs were taken at separate epochs and there was no calibrator star, so it was impossible to make the assessment described above. We have reanalyzed the H06 data using our new procedure and find values consistent with those plotted in H06 Figure 1A (see our Figure 2.3) and also with our new data. Thus, H06 did still present the first orbital phase variation for an exoplanet.

The phase curve fit here to the H06 data provides accurate parameters for that data set.

2.4 Results

2.4.1 System flux

Although our primary science result – the planetary phase curve described below – is inherently a relative measurement, our observations also allow us to measure precise, absolute $24\mu\text{m}$ photometry for the v And system. We measure $F_\nu = 0.488$ Jy and 0.490 Jy for the 2009 and 2006 data sets, respectively. These fluxes differ by 0.4% , which is at the limit of the MIPS $24\mu\text{m}$ precision; we therefore report the mean system flux as 0.489 ± 0.002 Jy. This value is significantly discrepant from the IRAS $25\mu\text{m}$ flux of 0.73 ± 0.05 Jy (Moshir 1989), but it is consistent with a Kurucz (1979) stellar spectrum tied to optical and near-infrared photometry of v And from the Tycho-2 (Høg et al. 2000) and 2MASS (Skrutskie et al. 2006) catalogs.

2.4.2 A two-hemisphere model

As shown in Figure 2.3 and discussed below, we detect a flux variation consistent with the orbital period of v And b. This measurement allows us to put tight constraints on the temperature contrast and phase offset of the planet. We interpret the observed flux variation in the context of a planet composed of two blackbody hemispheres of constant temperature – i.e., a two-wedge “orange slice” model (cf. Cowan et al. 2007). Sufficiently precise observations of such a bifurcated planet

will reveal a flux variation with peak-to-trough amplitude

$$\frac{\Delta F_P}{\langle F \rangle} = \frac{B_\nu(T_{P1}) - B_\nu(T_{P2})}{B_\nu(\gamma T_{\text{eff}})} \left(\frac{R_P}{R_*} \right)^2 \sin i, \quad (2.2)$$

which normalizes the full amplitude of the planetary flux variation ΔF_P by the mean flux from the system $\langle F \rangle$; in Eq. (2.1) $\Delta F_P / \langle F \rangle = 2b/a$. The quantity γ accounts for the star being fainter in the mid-infrared than a blackbody with temperature T_{eff} ; at $24 \mu\text{m}$ we set $\gamma = 0.8$ based on the models of Kurucz (1979). Thus, measuring $\Delta F_P / \langle F \rangle$ gives the hemispheres' brightness temperature contrast relative to the stellar flux, modulo a $\sin i$ ambiguity. By assuming a planetary albedo A_B and assuming all emitted radiation is reprocessed starlight, a second (bolometric) relation obtains:

$$(1 - A_B) \frac{R_*^2}{2a^2} T_{\text{eff}}^4 = T_{P1}^4 + T_{P2}^4. \quad (2.3)$$

Thus, we implicitly assume that each hemisphere of our model planet emits a bolometric flux equal to that of a blackbody with the $24 \mu\text{m}$ brightness temperature in Eq. (2.2). Subject to this assumption and given known or assumed values for the albedo A_B and planetary radius R_P , one can use Eqs. (2.2) and (2.3) to determine the hemispheric temperatures T_{P1} and T_{P2} at arbitrary orbital inclinations.

Setting $T_{P2} = 0$ and $T_{P1} = T_{P1,\text{max}}$ gives the minimum planetary radius capable of reproducing the observed flux variation, $\Delta F_P / \langle F \rangle$, as a function of the orbital inclination. Because this relation depends on inclination as $(\sin i)^{-1/2}$, measuring $\Delta F_P / \langle F \rangle$ gives an upper limit to the planet's surface gravity:

$$g \leq \frac{G(m \sin i)}{R_*^2} \frac{B_\nu(T_{P1,\text{max}})}{B_\nu(\gamma T_{\text{eff}})} \left(\frac{\Delta F_P}{\langle F \rangle} \right)^{-1}. \quad (2.4)$$

2.4.3 Model fits

We determine the best-fit parameters using Powell’s (1964) method for multivariate minimization (the SciPy function `optimize.fmin_powell`), and assess their uncertainties and correlations with a Metropolis-Hastings, Markov-chain Monte Carlo analysis (MCMC; see Section 15.8 of Press 2002). Table 2.1 (for the 2009 data) and Table 2.2 (for the 2006 data) report these results. Table 2.3 lists the astrophysical parameters of interest. We list the χ^2 and BIC values for the fits in Table 2.4. Parameter uncertainties are estimated from distributions generated using the kernel density method (KDE, implemented using the SciPy function `stats.gaussian_kde`) by determining the parameter values with equal KDE frequency that enclose 68% of the distribution.

Table 2.1. v And b Phase Curve and Calibration Parameters (2009 Data)^a

Parameter	Value		
a^b	0.488436	\pm	0.000011 Jy
b	0.000317	\pm	0.000017 Jy
Φ_0^c	84.5°	\pm	2.3°
c_1	0.005367	\pm	0.000054
c_2	0.012926	\pm	0.000055
c_3	0.001180	\pm	0.000055
c_4	0.009498	\pm	0.000055
c_5	0.001548	\pm	0.000054
c_6	0.014334	\pm	0.000027
c_7	-0.006333	\pm	0.000054
c_8	-0.004193	\pm	0.000054
c_9	-0.002129	\pm	0.000054
c_{10}	-0.007009	\pm	0.000055
c_{11}	-0.000549	\pm	0.000055
c_{12}	-0.009458	\pm	0.000054
c_{13}	-0.002757	\pm	0.000054
c_{14}	-0.012002	\pm	0.000054
d_1	-0.00429	\pm	0.00072
d_2	0.00146	\pm	0.00070
d_3	-0.00214	\pm	0.00071
d_4	-0.00428	\pm	0.00070
d_5	-0.00520	\pm	0.00071
d_6	-0.00177	\pm	0.00070
d_7	-0.00100	\pm	0.00078
d_8	-0.00049	\pm	0.00072
d_9	0.00196	\pm	0.00066
d_{10}	-0.00252	\pm	0.00067
d_{11}	-0.00029	\pm	0.00066
d_{12}	-0.00409	\pm	0.00067
d_{13}	0.00259	\pm	0.00068
d_{14}	-0.00152	\pm	0.00068
e_1	0.00066	\pm	0.00080
e_2	0.00031	\pm	0.00079

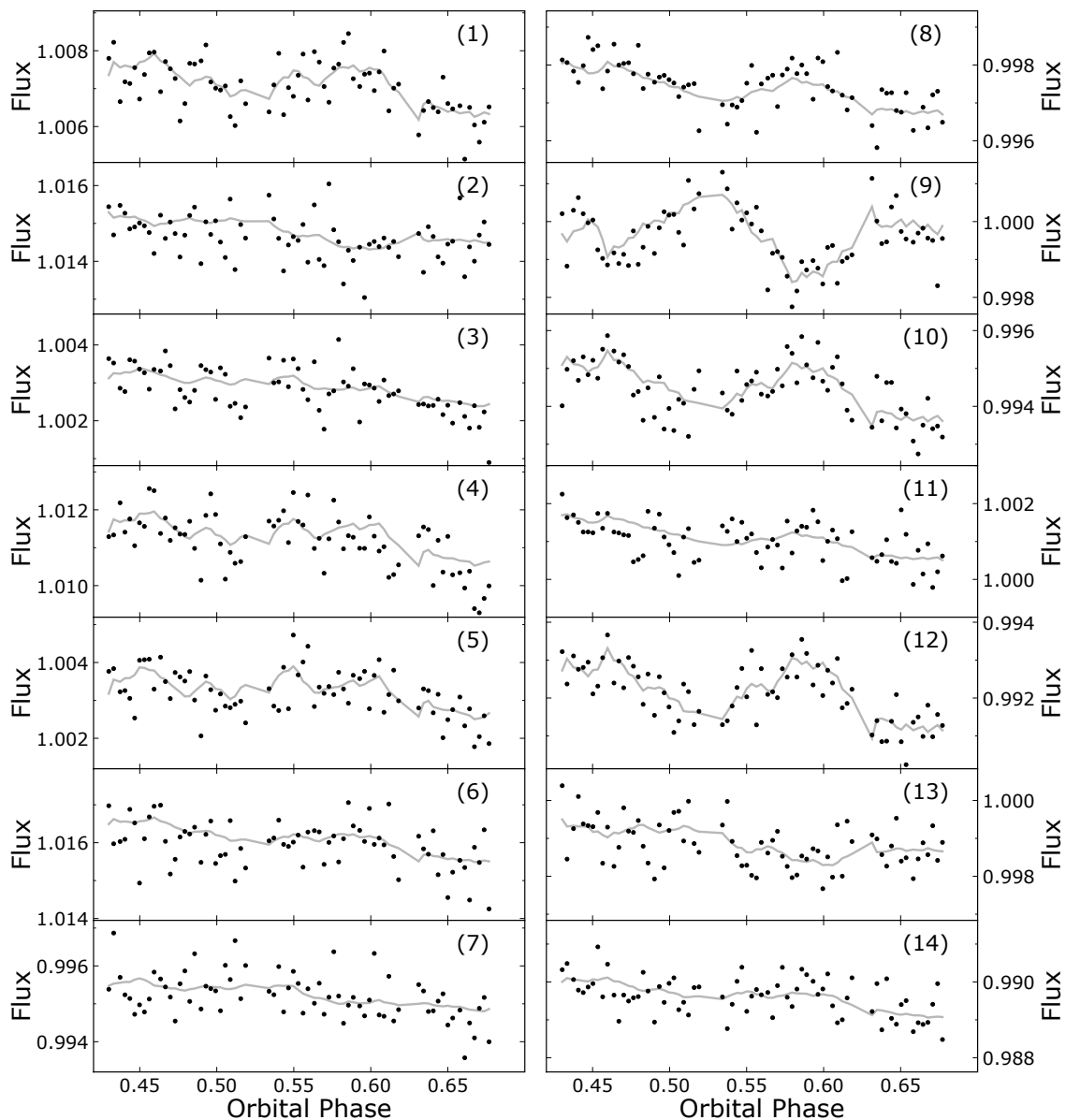


Figure 2.2 Raw photometry (dots) and the best-fit model (solid lines) at each of the fourteen dither positions. The measured flux varies by several percent from one position to another, as evidenced by the different scales in each panel. The downward trend evident in all panels is due to the decreasing flux from the system, shown more clearly in Figure 2.3. For display purposes the data have been averaged over each AOR and we plot only the continuous-observing segment of our observations. The precision of individual points (not plotted for clarity) is $\sim 5 \times 10^{-4}$.

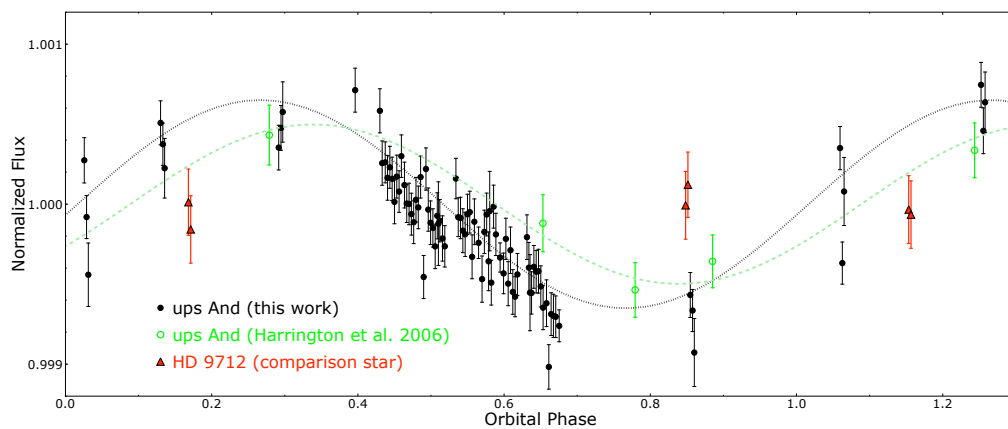


Figure 2.3 Phase curve of the υ And system, phased to the orbit of the innermost planet (black circles). Position-dependent sensitivity effects have been removed and for display purposes we have averaged the data over each AOR. The best-fit sinusoid (black dotted line) exhibits a phase offset of $\sim 80^\circ$, consistent with a planetary “hot spot” advected almost to the planet’s day-night terminator. The light green circles are our reanalysis of the data from [Harrington et al. \(2006\)](#), and the light green dashed line shows the best-fit sinusoid to these data; the phase coherence between the 2006 and 2009 data sets is consistent with flux modulated by the innermost planet’s orbit. The red triangles show our flux calibrator observations, which are consistent with a constant detector sensitivity.

Table 2.1—Continued

Parameter	Value		
e_3	0.00211	±	0.00040
e_4	0.00218	±	0.00078
e_5	0.00409	±	0.00080
e_6	0.00009	±	0.00080
e_7	0.00211	±	0.00081
e_8	-0.00259	±	0.00076
e_9	0.00628	±	0.00076
e_{10}	-0.00284	±	0.00039
e_{11}	-0.00168	±	0.00075
e_{12}	-0.0029	±	0.0011
e_{13}	-0.00061	±	0.00076
e_{14}	0.00025	±	0.00074

^a Errors quoted are the 68.3% confidence limits. The first three parameters are the mean system flux a , the phase curve half-amplitude b , and the phase offset Φ_0 . The other coefficients represent fits to the nonuniform detector response at each of the fourteen MIPS dither positions. The c_i are dimensionless, and the d_i and e_i are in units of pixel^{-1} .

^bThe absolute accuracy of the mean system flux a is 0.4% as discussed by [Engelbracht et al. \(2007\)](#).

^c Φ_0 is measured relative to our computed ephemeris, as discussed in [Sec. 2.4.5](#).

MCMC analysis evolves an initial set of parameters in a way that is ultimately representative of their underlying probability distributions. For our Markov chain we choose a step size to give approximately a 30% step acceptance rate. To adequately sample the full parameter space we found it necessary to run the Markov chains longer for the 2006 data set than for the 2009 data set. For the 2009 data set we first ran the chain for 10^6 burn-in steps and discarded these; we then ran the chain for 2×10^7 steps, saving every 1000th step. For the 2006 data set our procedure is the same but the burn-in phase lasted for 10^7 steps and the chain was then run for 5×10^7 steps, saving every 1000th step. We inspected correlation plots for all possible parameter pairs in both analyses to ensure adequate coverage of phase space and to assess parameter correlations.

Table 2.2. v And b Phase Curve and Calibration Parameters (2006 Data)^a

Parameter	Value		
a^b	0.490250	\pm	0.000039 Jy
b	0.000221	\pm	0.000053 Jy
Φ_0^c	57°	\pm	21°
c_1	0.00284	\pm	0.00030
c_2	0.01423	\pm	0.00028
c_3	0.00112	\pm	0.00030
c_4	0.01094	\pm	0.00028
c_5	0.00235	\pm	0.00029
c_6	0.01574	\pm	0.00028
c_7	-0.00757	\pm	0.00027
c_8	-0.00596	\pm	0.00030
c_9	-0.00086	\pm	0.00030
c_{10}	-0.00755	\pm	0.00029
c_{11}	-0.00097	\pm	0.00029
c_{12}	-0.00945	\pm	0.00029
c_{13}	-0.00299	\pm	0.00027
c_{14}	-0.01138	\pm	0.00027

^aErrors quoted are the 68.3% confidence limits. The first three parameters are the mean system flux a , the phase curve half-amplitude b , and the phase offset Φ_0 . The other coefficients represent fits to the nonuniform detector response at each of the fourteen MIPS dither positions. The c_i are dimensionless, and the d_i and e_i are in units of pixel^{-1} .

^bThe absolute accuracy of the mean system flux a is 0.4% as discussed by [Engelbracht et al. \(2007\)](#).

^c Φ_0 is measured relative to our computed ephemeris, as discussed in [Sec. 2.4.5](#).

Table 2.3 v And b Phase Curve: Astrophysical Parameters of Interest

	2006			2009		
$\Delta F/F$	0.00090	\pm	0.00022	0.001300	\pm	0.000074
Φ_0	57°	\pm	21°	84.5°	\pm	2.3°

Table 2.4 v And b Phase Curve: Goodness-of-fit Statistics

	2006	2009
χ^2	814.1	38422.7
k	17	45
N	838	23884
BIC	928.6	38876.4

All the one-dimensional parameter distributions are unimodal and approximately Gaussian in shape. We see some correlations between the d_i and e_i , which is unsurprising given the degree of correlation between the X and Y components of motion as shown in the middle panels of Figure 2.1. More surprising is a correlation between the mean system flux, a , and the phase offset, Φ_0 , as shown in Figure 2.4. Using a simulated data set with white noise, we confirmed that when forcing a fit to a sinusoid of known period, a slightly higher mean value be counteracted by a slightly lower phase offset; however, we observe the opposite correlation. In any case no significant correlation is apparent between the phase curve amplitude $\Delta F_P/\langle F \rangle$ and the phase offset, which are the primary quantities of interest for our analysis. The best χ^2 from the MCMC is consistent to within a small fraction of the uncertainties with the optimizer values.

The model in Eq. (2.1) provides a good fit to both the astrophysical flux modulation and the instrumental flux variations at each of the fourteen dither positions, as shown in Figure 2.2. We plot the photometry after removal of the

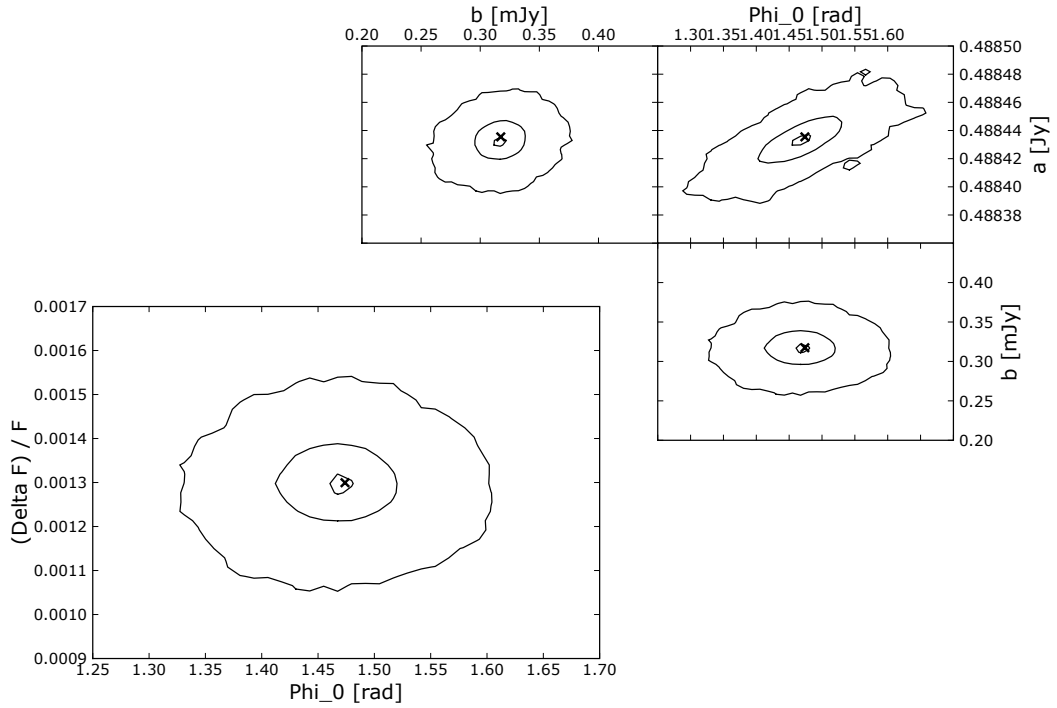


Figure 2.4 Two-dimensional confidence intervals on the astrophysical parameters of interest in Eq. (2.1): the relative phase curve amplitude $\Delta F_P/F$, the absolute mean system flux a , the phase curve half-amplitude b , and the phase offset Φ_0 . The solid lines are the contours that enclose 68.3%, 95.4%, and 99.7% of the parameter space from the 2009 data set. The ‘x’ in each panel marks the best-fit parameter listed in Tables 2.1 and 2.3.

systematic effects in Figure 2.3, along with the best-fitting sinusoidal phase curve, for both the 2006 and 2009 data sets. Both data sets appear to vary approximately in phase; this coherence is a strong argument that the flux modulation we see is due to the planet v And b. The goodness-of-fit statistics (χ^2 and BIC) for both data sets are listed in Table 2.4. The high χ^2 for the 2009 data set probably results from a somewhat non-sinusoidal phase curve and from the residual systematics apparent in Figure 2.3.

2.4.4 Phase curve amplitude

We measure values of $\Delta F_P/\langle F \rangle$ of $\Delta F_P/\langle F \rangle = 0.001300 \pm 0.000074$ for the 2009 data and 0.00090 ± 0.00022 for our reanalysis of the 2006 data, as shown in Table 2.3. Using the absolute calibration from Sec. 2.4.1, we find absolute peak-to-trough phase curve amplitudes of 0.636 ± 0.036 mJy and 0.44 ± 0.11 mJy for the 2009 and 2006 data sets, respectively. Thus the detection of the phase curve amplitude at both epochs is statistically significant at the $> 4\sigma$ level and is substantially smaller than reported by H06 (due to the calibration issues discussed above). The two epochs' phase curve amplitudes are consistent at the 1.7σ level; thus there is no evidence that the planetary emission exhibits inter-epoch variability. The lack of variability is consistent with the recent results of Agol et al. (2010), who set an upper limit of 2.7% on HD 189733b's dayside flux variations.

As *v* And b's orbit is inclined toward face-on, a greater intrinsic temperature contrast is required to generate the observed flux variation. Using Eq. (2.2) and our measurement of the phase curve amplitude we determine the expected day/night contrast ratio and plot it in the upper panel of Figure 2.5. We also plot the upper limits on the day/night contrast assuming planetary radii of 1.3 (1.8) R_J ; the implication is that the planet's orbital inclination angle is likely $\gtrsim 28^\circ$ (14°). These limits complement the preliminary limits on *v* And b's orbital inclination from the stability modeling of McArthur et al. (2010), which suggest $i \sim 20^\circ - 45^\circ$.

Invoking Eq. (2.3) allows us to determine the brightness temperatures of the planetary hemispheres in our model at each inclination angle. We assume zero albedo (cf. Rowe et al. 2008) and a planetary radius of 1.3 R_J and plot the hemispheres' temperatures and 3σ limits in the lower panel of Figure 2.5. This sets a lower bound to the temperature contrast between the two hemispheres to

be $T_{P_1} - T_{P_2} \gtrsim 900$ K. The hotter hemisphere’s temperature remains in the range ~ 1700 - 1900 K as we vary the radius from $1.0 R_J$ to $1.8 R_J$; however larger radii result in higher temperatures for the cooler hemisphere to maintain the measured flux and thus decrease the temperature contrast.

Using Eq. (2.4) we find that v And b’s surface gravity is $< 2100 \text{ cm s}^{-2}$ with 3σ confidence: this result is independent of assumptions about the planet’s radius or orbital inclination. For a hot hemisphere temperature of ~ 1800 K (cf. Figure 2.5) this limit on the surface gravity implies an atmospheric scale height > 300 km. In Figure 2.6 we plot the allowed regions of mass-radius parameter space against the known population of transiting extrasolar planets. Thus, our measurements suggest that v And b has a lower surface gravity than Jupiter, HD 189733b, and a number of other transiting extrasolar planets. This result demonstrates that v And b is indeed a gaseous Jovian planet, but we cannot determine whether it is a highly inflated planet or whether it is dominated by a sizable rocky core.

2.4.5 Phase offset

Because v And b does not transit its host star we know its orbital ephemeris less precisely than we do for transiting planets. We used the Systemic Console³ (Meschiari et al. 2009) to reanalyze the published radial velocity data of v And (Butler et al. 1997; Naef et al. 2004; Butler et al. 2006; Wittenmyer et al. 2007; McArthur et al. 2010) using Systemic’s Levenberg-Marquardt algorithm and ignoring system stability constraints. We obtain orbital parameters consistent with those of McArthur et al. (2010). By providing the covariances between the various fit parameters, this reanalysis allows a substantially more precise estimate

³available from <http://oklo.org/downloadable-console/>

of the planetary ephemeris than is available from the literature. We compute a time of zero relative radial velocity (phase 0.5, or secondary eclipse in a circular transiting system) of $\text{JD} = 2\,454\,868.78 \pm 0.07$ (1σ), which corresponds to an uncertainty of $\sim 6^\circ$ in determining the phase offset.

Assuming a two-hemisphere model, we find a phase offset of $84.5^\circ \pm 2.3^\circ$ relative to the computed ephemeris. This uncertainty may be an underestimate since we artificially constrain our phase curve to be sinusoidal. [Knutson et al. \(2009b\)](#) discuss the artificially low uncertainties obtained from fitting to an arbitrarily chosen model, though here we have substantially broader phase coverage than was available in that study. The system flux reaches a maximum before phase 0.5, indicating that the brighter hemisphere is offset to the east of the substellar point, as observed for HD 189733b ([Knutson et al. 2007a, 2009b](#); [Agol et al. 2010](#)).

This large phase offset is strikingly different from the near-zero phase offset reported by H06; this difference is due to the choice of system calibration as discussed above. From our reanalysis of the 2006 data we find a phase offset of $57^\circ \pm 21^\circ$ relative to our ephemeris. The phase offsets at the two epochs are consistent at the 1.3σ level, and thus there is no evidence for inter-epoch variability in the phase offset.

2.5 Discussion

The most striking result of our analysis is the large phase offset evident in the light curve. The direction of the phase offset is broadly consistent with the prediction by many circulation models of a large-scale, high-velocity, eastward-flowing jet on hot Jupiters ([Cho et al. 2003](#); [Cooper & Showman 2005](#); [Cho et al. 2008](#); [Showman](#)

et al. 2009; Burrows et al. 2010; Rauscher & Menou 2010; Thrastarson & Cho 2010) and as seen on HD 189733b (Knutson et al. 2007a, 2009b). However, the magnitude of the phase offset is far larger than is predicted at the low pressures characteristic of the $24\ \mu\text{m}$ photosphere (Showman et al. 2009).

A partial explanation for such a large phase offset could be that v And b’s atmosphere is substantially transparent to the incident stellar flux, with the result that the insolation is deposited at sufficient depth for substantial advection to occur. In this case, the planet might lack an atmospheric temperature inversion. Indeed, the large phase offset is more consistent with expectations for a planet lacking a temperature inversion than with expectations for a planet with an inverted atmosphere (cf. HD 189733b vs. HD 209458b; Showman et al. 2009). Cooper & Showman (2005, 2006) predicted maximum hemisphere-averaged temperatures to be offset by $\gtrsim 60^\circ$ for an irradiated planet with no high-altitude absorbers, but it is unlikely that this would translate into high phase offsets at $24\ \mu\text{m}$ due to the high altitude of the photosphere at this wavelength. The absence of a temperature inversion is at odds with the recent proposal by Knutson et al. (2010) that, due to the lack of activity apparent in optical spectra of v Andone would expect v And b to have a temperature inversion. Thrastarson & Cho (2010) also show clear shifted hot regions at higher pressure; the deep vortices produced by their simulations are several hundreds of degrees hotter than the surroundings.

Setting aside the phase offset for a moment, the phase curve amplitude we measure could be directly interpreted in the context of the models of Showman et al. (2009) as a typical phase curve for a planet with orbital inclination of 50° - 60° . However, simulations with greater phase offsets tend to show lower phase curve amplitudes (e.g. Showman et al. 2009; Burrows et al. 2010); thus it is

difficult to simultaneously explain both amplitude and offset and it is difficult to reconcile current theory with our observations.

Alternatively, the large phase offset we see could represent re-radiation of thermal energy deposited in shock fronts in the planet’s atmosphere. Many simulations predict supersonic equatorial jets on hot Jupiters that carry substantial kinetic energy; shocks could manifest themselves where the jet transitions to subsonic speeds. [Rauscher & Menou \(2010\)](#) note that their simulations, as well as those of [Showman et al. \(2009\)](#), exhibit structures which could be interpreted as shocks – however, these models do not explicitly treat shock physics. [Dobbs-Dixon et al. \(2010\)](#) observe similar features in their models using an additional artificial viscosity factor to simulate shock behavior, and note that in high-altitude, high-velocity regions the energy carried by kinetic energy becomes comparable to the enthalpic energy. [Watkins & Cho \(2010\)](#) have recently suggested that gravity waves in the atmosphere of a hot Jupiter can also heat the planet’s upper atmosphere. It is unclear whether either shocks or gravity waves can deposit sufficient energy in the $24\ \mu\text{m}$ photosphere to cause the large phase offset we see. We look forward to further research into these topics to determine whether these or other phenomena can explain our observations.

We must also consider the possibility that the periodic flux modulation we see is intrinsic to the star rather than emanating from the planet. [Shkolnik et al. \(2005, 2008\)](#) report evidence for intermittently periodic stellar activity in this system correlated with v And b’s orbital period. They interpret this periodicity as a possible magnetospheric star-planet interaction, but they detect this periodicity at only some of their observational epochs. The consistency between our analysis of the 2006 and 2009 MIPS data suggests we are not seeing such a transient phenomenon, although analysis of additional activity measurements (e.g., from the

Keck Observatory Archive) spanning the time of our Spitzer observations would help solidify this claim. [Shkolnik et al. \(2005\)](#) also report variations consistent with zero phase offset, which disagree with our observed phase offset. In addition, $24\ \mu\text{m}$ stellar variability at the level we observe would imply much greater variability at optical wavelengths: this is not observed ([Henry et al. 2000a](#)). Finally, as discussed by H06, energy considerations indicate that such an intense star-planet interaction would cause the planet to spiral into the star in $\lesssim 10^7$ yr. Thus, the $24\ \mu\text{m}$ flux variations are likely to be of planetary origin.

Although a general framework exists within which to interpret observations of exoplanetary atmospheres, our understanding is still extremely limited. [Madhusudhan & Seager \(2009\)](#) demonstrate that some planets with claimed inversions can also be fit by non-inverted atmospheric models due to much greater number of free model parameters versus the limited number of observational constraints. In addition, there may be reason to question the reliability of some of the circulation models currently in use. [Thrastarson & Cho \(2010\)](#), in their extensive exploration of initial condition parameter space, have recently shown the extreme susceptibility of at least one circulation model to minute variations in initial conditions, resulting in substantial variability in final “steady-state” temperature contrasts and phase offsets. This chaotic behavior calls into question the ability of at least some models to make accurate, qualitative predictions about any of the quantities we are interested in. Other models (e.g., [Dobbs-Dixon et al. 2010](#)) exclude planets’ polar regions from their simulations, where large vortices are often seen to form ([Cho et al. 2003, 2008](#); [Rauscher et al. 2008](#)). While the polar regions present a small cross-sectional area in transiting systems, for non-transiting systems such as *v* And b polar emission will constitute a larger component of the observed system flux. A fully consistent three-dimensional circulation geometry is essential for comparison to our observations. Nevertheless, it is important to

remember that general circulation models have trouble predicting global weather patterns even for relatively well-studied solar system planets; thus, a comprehensive, quantitative understanding of extrasolar planetary atmospheric dynamics will likely remain elusive for some time to come.

2.6 Conclusions and Future Work

We have described a new $24\ \mu\text{m}$ phase curve, which we interpret as being due to emission from the planet ϵ Andromeda b modulated by the planet’s orbit. Using a simple two-hemisphere model we determine the peak-to-trough phase curve amplitude to be 0.001300 ± 0.000074 . This result suggests an average “hot side” temperature of ~ 1800 K; for an average-sized hot Jupiter ($1.3 R_J$) this implies a hemisphere-averaged planetary temperature contrast of ~ 900 K and an orbital inclination $i \gtrsim 28^\circ$.

We find a phase offset of $84^\circ \pm 2^\circ \pm 6^\circ$, where we break the uncertainty into the error relative to our ephemeris and the error in our ephemeris, respectively. Such a large phase offset is difficult to reconcile with most current models. The phase curve is hotter hemisphere is offset to the east, as previously observed for HD 189733b (Knutson et al. 2007a, 2009b).

We reanalyze our earlier (H06) observations of this system and find a phase curve amplitude of 0.00090 ± 0.00022 and a phase offset of $57^\circ \pm 21^\circ \pm 6^\circ$. There is no evidence for inter-epoch variability in the planetary phase curve. This is primarily due to the large uncertainties from the 2006 data set and demonstrates the difficulty in measuring such variability with sparsely-sampled phase curves.

There are substantial challenges in interpreting a phase curve observed at only a single wavelength due to the degeneracies between planetary radius, orbital

inclination, and atmospheric composition and structure (Burrows et al. 2008). Some of these difficulties could be mitigated with phase curve measurements at additional wavelengths – ideally from space (i.e., warm Spitzer) but also potentially from ground-based near-infrared observations (e.g., Barnes et al. 2010). For example, commensurate phase curve amplitudes at both $3.6\ \mu\text{m}$ and $4.5\ \mu\text{m}$ would suggest that *v* And b does indeed lack a temperature inversion. On the other hand, differing phase curve amplitudes at these wavelengths could suggest an inversion and be more difficult to reconcile with the large phase offset at $24\ \mu\text{m}$. Phase offsets in these or other scenarios would also depend on the particular atmospheric temperature structure of the planet. Phase curves at $24\ \mu\text{m}$ currently exist for only two planets, *v* And b and HD 189733b (though unpublished data exist for HD 209458b). Cool, inversionless HD 189733b is probably the best-characterized extrasolar planet, and additional phase curves are already being observed for this object at $3.6\ \mu\text{m}$ and $4.5\ \mu\text{m}$. Phase curves of additional planets at multiple wavelengths are essential to ensure that our evolving views of the atmospheres of hot Jupiters are not biased by unbalanced data sets.

Whatever the cause of the substantial energy transport implied by the large phase offset we measure, if this phenomenon occurs in other (transiting) systems there are important implications for transmission spectroscopy. Line-of-sight effects cause optical transmission spectra to probe pressures comparable to those probed by mid-infrared emission; temperatures near the planetary terminator of $\sim 1800\ \text{K}$ (as we observe) should easily be detectable with ground- or space-based spectra. Sing et al. (2008) and Lecavelier Des Etangs et al. (2008c) infer a terminator temperature on HD 209458b of $2200 \pm 260\ \text{K}$ at $33 \pm 5\ \text{mbar}$ – roughly at the expected $24\ \mu\text{m}$ photosphere – which is not dissimilar from the hot terminator-centered hemisphere we observe on *v* And b. Further phase curve and transmission spectra of additional systems are needed to determine whether

this hot, high-altitude terminator measurement results from a mechanism similar to what we observe on *v* And b.

We note that *v* And b is too bright to be observed photometrically at shorter wavelengths with the planned James Webb Space Telescope (though spectroscopy may be feasible). Given JWST’s magnitude limits and the expected high demand for its observing time, the community should consider a dedicated space-based mid-infrared photometry and spectroscopy mission (Vasisht et al. 2008). Such a mission would allow uninterrupted long-term monitoring of nearby hot Jupiter systems. This would provide high-precision measurements of these systems’ thermal emission and energy distributions, and possibly provide the first definitive evidence of dynamical meteorological processes – weather – on extrasolar planets.

2.7 *v* And b: Post-publication Results

Several years have passed since the publication of the results presented in this chapter (Crossfield et al. 2010). Though some progress has been made toward understanding the atmospheric circulation and energy budgets of Hot Jupiters, their true natures remain somewhat murky. In this section I discuss a subset of recent pertinent results.

Of direct relevance to this chapter is the claimed detection of reflected visible light from *v* And b via polarization-based methods (Berdyugina et al. 2011). Combining U, B, and V band polarization data this study claims to resolve the planet’s orbital inclination and radius ambiguities, finding $i = 111 \text{ deg} \pm 11 \text{ deg}$ (consistent with the analysis of McArthur et al. 2010) and $R_p = 1.36 \pm 0.20 R_J$. This radius value is quite consistent with the value of $1.3 R_J$ assumed above, so my published results are still directly applicable. If confirmed, this measurement

would collapse the parameter space in Figure 2.5 to a set of straightforward, one-dimensional confidence intervals on the effective temperature of v And b’s two hemispheres: roughly 1850 ± 80 K and 850 ± 200 K. This near edge-on configuration is fortuitous, because (by requiring a relatively high temperature for the cooler hemisphere) it maximizes the level of atmospheric recirculation of the incident stellar flux and thereby lessens the difficulty in explaining v And b’s large phase offset with atmospheric advection.

Thermal measurements (all with Spitzer/IRAC) of several additional planets have also been reported. A comprehensive reanalysis of all IRAC $8\ \mu\text{m}$ data for HD 189733b (comprising fourteen transits and eclipses [Agol et al. 2010](#)) confirmed the prior detection of a small ($16\ \text{deg} \pm 6\ \text{deg}$) phase offset in this system ([Knutson et al. 2007a](#)), indicative of efficient atmospheric circulation. These same IRAC data were also used to reconstruct the first two-dimensional thermal map of an extrasolar planet via eclipse mapping ([Rauscher et al. 2007](#); [Majeau et al. 2012](#)); the results are consistent with previous analyses. Phase curves of the extremely hot Jupiter WASP-12b (a planet I discuss further in Chs. 4 and 5) at 3.6 and $4.5\ \mu\text{m}$ detect this planet’s thermal emission and ellipsoidal variations ([Cowan et al. 2012](#)). Any phase curve offset is quite small, but interpretation of these data are hampered to some extent by low S/N (WASP-12 is a much fainter star than HD 189733 or v And b) and by lingering systematics. Analysis is underway for additional systems with the short-wavelength IRAC channels (e.g. HAT-P-7b, [Knutson et al. in preparation](#)).

The Kepler satellite has produced optical phase curves of HAT-P-7b ([Welsh et al. 2010](#)) and TrES-2b ([Kipping & Spiegel 2011](#)). Though such measurements (and other numerous optical secondary eclipses) cannot always distinguish between thermal emission and reflected light, they still place tight constraints on

the planets' optical albedos: a key factor mediating their global energy budgets. These observations have revealed a wide diversity of hot Jupiter albedos, from $< 1\%$ (Kipping & Spiegel 2011) to as high as 30% (Demory et al. 2011). Kepler will provide significantly more data in this vein before the end of its mission, but observations at additional wavelengths will be necessary to understand the observed diversity of systems.

Kepler and Spitzer's missions will almost certainly have ended by 2015, but the James Webb Space Telescope is expected to launch no earlier than 2018. Unless the proposed Explorer-class mission FINESSE (Swain 2010) is selected for development (with a projected launch date of ~ 2016), there will be no space-based platform with which to characterize exoplanet phase curves. Ground-based, high-resolution, near-infrared phase curve spectroscopy (e.g., Barnes et al. 2007) has thus far resulted in no detections, but in the near-term it may be the only feasible technique for such observations.

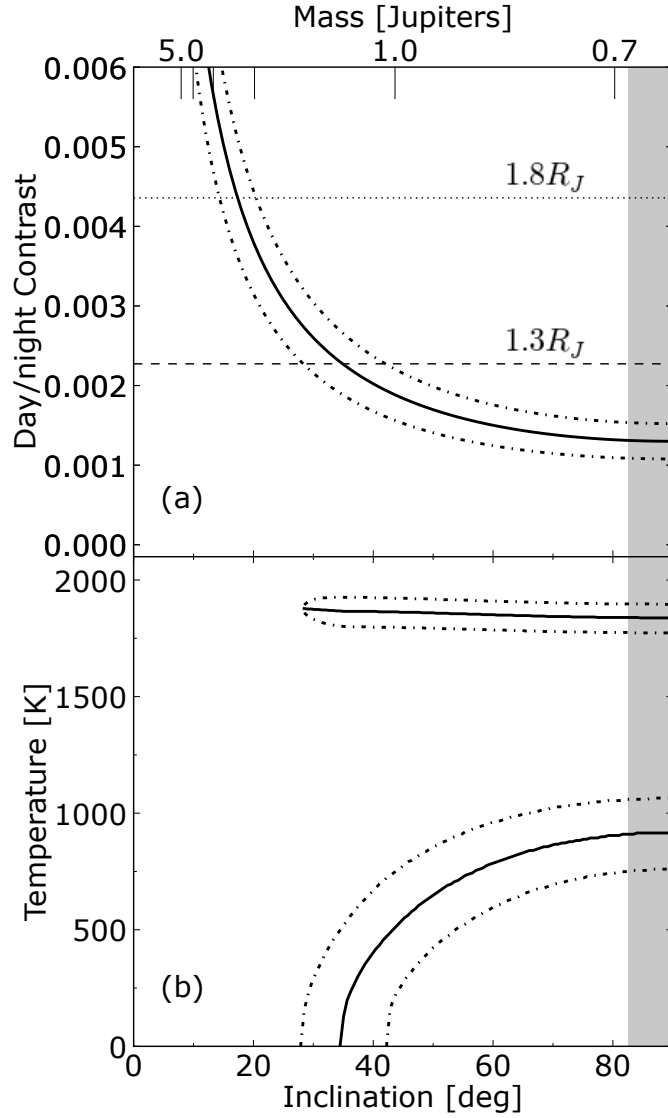


Figure 2.5 Day-night temperature contrast as a function of orbital inclination angle, assuming a planet with zero albedo. (a) Our measurement of the phase curve amplitude and Eq. (2.2) constrain the allowed day/night contrast to lie between the dot-dashed 3σ limits. The maximum allowable contrast for a planet of 1.3 (1.8) R_J is shown as the dashed (dotted) lines, suggesting a lower limit on the inclination angle of 25° (15°). (b) Considering Eq. (2.3) and assuming a radius of $1.3R_J$ allows us to determine the temperature of both hemispheres as a function of inclination (solid lines, with dot-dashed 3σ limits). This radius implies a planetary temperature contrast of $\gtrsim 900$ K. The cooler hemisphere is more sensitive to changes in planetary radius, though both temperatures increase as radius increases.

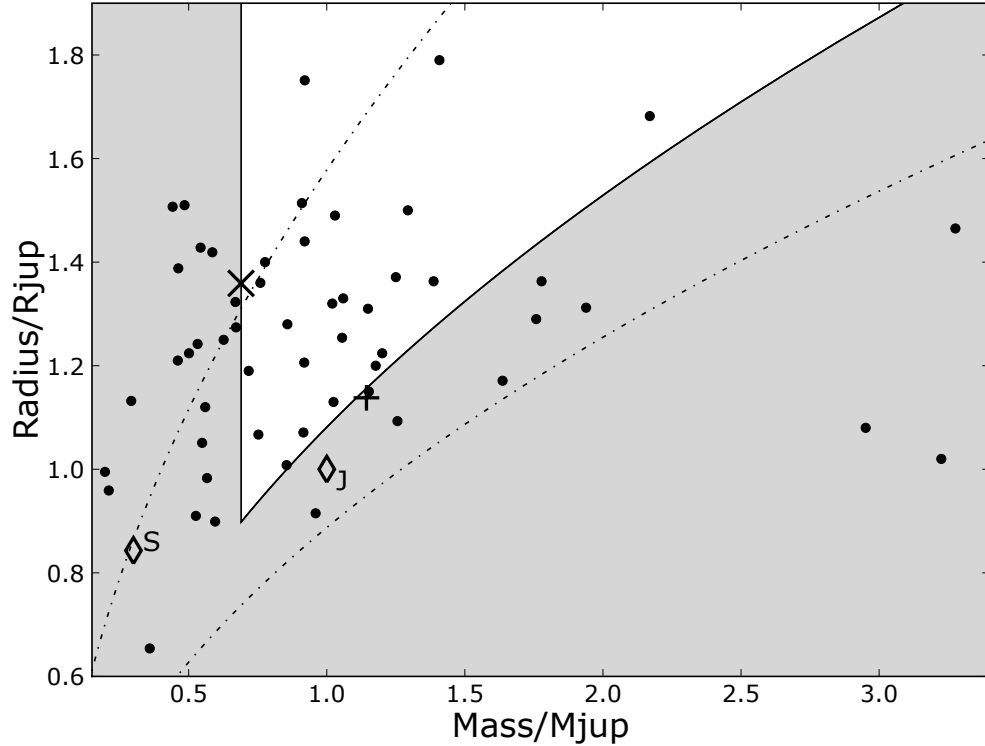


Figure 2.6 Mass/radius constraints for v and b from Eq. (2.4). The shaded area is the portion of mass-radius space excluded at the 3σ level. Points are known transiting extrasolar planets; measurement uncertainties have been omitted for clarity. Extrasolar planets that have been observed with MIPS are indicated by a ‘+’ (HD 189733b) and a ‘x’ (HD 209458b), while Jupiter and Saturn are marked with a ‘J’ and ‘S,’ respectively. The dot-dashed lines represent lines of constant surface gravity with $g = 10^3 \text{ cm s}^{-2}$ and $3.2 \times 10^3 \text{ cm s}^{-2}$. Our model and phase curve measurement constrain $g < 2100 \text{ cm s}^{-2}$ at the 3σ level.

CHAPTER 3

Eclipses and Transits of HD 209458b at 24 Microns

3.1 Abstract

We report the results of an analysis of all Spitzer/MIPS 24 μm observations of HD 209458b, one of the touchstone objects in the study of irradiated giant planet atmospheres. Altogether we analyze two and a half transits, three eclipses, and a 58-hour near-continuous observation designed to detect the planet's thermal phase curve. The results of our analysis are: (1) A mean transit depth of $1.484\% \pm 0.033\%$, consistent with previous measurements and showing no evidence of variability in transit depth at the 3% level. (2) A mean eclipse depth of $0.338\% \pm 0.026\%$, somewhat higher than that previously reported for this system; this new value brings observations into better agreement with models. From this eclipse depth we estimate an average dayside brightness temperature of $1320 \text{ K} \pm 80 \text{ K}$; the dayside flux shows no evidence of variability at the 12% level. (3) Eclipses in the system occur $32 \pm 129 \text{ s}$ earlier than would be expected from a circular orbit, which constrains the orbital quantity $e \cos \omega$ to be 0.00004 ± 0.00033 . This result is fully consistent with a circular orbit and sets an upper limit of 140 m s^{-1} (3σ) on any eccentricity-induced velocity offset during transit. The phase curve observations (including one of the transits) exhibits

an anomalous trend similar to the detector ramp seen in previous Spitzer/IRAC observations; by modeling this ramp we recover the system parameters for this transit. The long-duration photometry which follows the ramp and transit exhibits a gradual $\sim 0.2\%$ decrease in flux over ~ 30 hr. This effect is similar to that seen in pre-launch calibration data taken with the $24\ \mu\text{m}$ array and is better fit by an instrumental model than a model invoking planetary emission. The large uncertainties associated with this poorly-understood, likely instrumental effect prevent us from usefully constraining the planet’s thermal phase curve. Our observations highlight the need for a thorough understanding of detector-related instrumental effects on long time scales when making the high-precision mid-infrared measurements planned for future missions such as EChO, SPICA, and JWST.

3.2 Introduction

Most known extrasolar planets were discovered via the radial velocity technique – in which the Doppler wobble of a star indicates an orbiting planet – and/or by the transit method – in which periodic dimming of a star indicates a planet that crosses in front of the stellar disk. Owing to the observational biases of these techniques, the first planets thus discovered were the large, massive objects on few-day orbits commonly known as hot Jupiters (Mayor & Queloz 1995; Henry et al. 2000b; Charbonneau et al. 2000). Their large sizes and high temperatures make these objects excellent candidates for the study of their dayside emission when the planet is occulted by the star (Deming et al. 2005b; Charbonneau et al. 2005), of their longitudinally-averaged global emission (Harrington et al. 2006; Cowan et al. 2007; Knutson et al. 2007a), and of their atmospheric opacity via the wavelength-dependent flux diminution during transit (Seager & Sasselov

2000; Charbonneau et al. 2002). These observations have led to measurements of atmospheric abundances of key molecular species (Madhusudhan et al. 2011a), possible non-equilibrium chemistry (Stevenson et al. 2010), high-altitude hazes (Sing et al. 2009), and atmospheric circulation (Cowan & Agol 2011b).

Any discussion of hot Jupiter atmospheres must necessarily mention two systems in particular. One, HD 189733, is the brightest star known to host a hot Jupiter (Bouchy et al. 2005). The other is HD 209458, the first known transiting planet (Charbonneau et al. 2000; Henry et al. 2000b) and the focus of this study. These are the two touchstone objects in the study of irradiated giant exoplanets, both because they were discovered relatively early on and because they orbit especially bright (as seen from Earth) host stars. This last point in particular allows for especially precise characterization of these planets' atmospheres and permits observations which would provide unacceptably low signal to noise ratios for fainter systems.

3.2.1 The HD 209458 system

The star HD 209458 is an F8 star roughly 15 % more massive than the Sun (Mazeh et al. 2000; Brown et al. 2001; Baines et al. 2008), with an equivalent metallicity and slightly higher temperature (Schuler et al. 2011). It is orbited by HD 209458b, a roughly $1.4 R_J$, $0.7 M_J$ planet in a 3.5-day, near-circular orbit (Southworth 2008; Torres et al. 2008). The planet's parameters have been substantially improved upon since its initial discovery (Charbonneau et al. 2000; Henry et al. 2000b; Mazeh et al. 2000). Two sets of more recent values (Torres et al. 2008; Southworth 2008) do not differ significantly, and we use the former's system parameters in our analysis when not making our own measurements.

Infrared photometry during eclipses of HD 209458b measured from the ground

(Richardson et al. 2003a) and with Spitzer (Deming et al. 2005b; Knutson et al. 2008) determines the planet’s intrinsic emission spectrum, and is best fit by atmospheric models in which the planet’s atmospheric temperature increases above $\sim 0.1 - 1$ bar (Burrows et al. 2007, 2008; Fortney et al. 2008; Madhusudhan & Seager 2010). Such temperature inversions are common on hot Jupiters, and a popular explanation requires the presence of a high-altitude absorber (e.g., Fortney et al. 2008; Burrows et al. 2008). The nature of any such absorber is currently unknown and the subject remains a topic of active research (Désert et al. 2008; Spiegel et al. 2009; Knutson et al. 2010; Madhusudhan et al. 2011b).

If present, a high-altitude optical absorber is expected to absorb the incident stellar flux high in the atmosphere where radiative timescales are short and advection is inefficient (Cowan & Agol 2011a). Consequently, such planets are expected to exhibit large day/night temperature contrasts and low global energy redistribution despite circulation models’ ubiquitous predictions of large-scale super-rotating jets on these planets (Showman & Guillot 2002; Cooper & Showman 2005; Cho et al. 2008; Rauscher et al. 2008; Showman et al. 2009; Dobbs-Dixon et al. 2010; Burrows et al. 2010; Rauscher & Menou 2010; Thrastarson & Cho 2010; Heng et al. 2011b,a). Spitzer/IRAC observations of HD 209458b at $8\ \mu\text{m}$ place an upper limit on the planet’s thermal phase variation of 0.0022 (3σ ; Cowan et al. 2007). Given the planet’s demonstrably low albedo (Rowe et al. 2008) this limit is substantially lower expected if the planet has a low recirculation efficiency. In hot Jupiter atmospheres the dominant $24\ \mu\text{m}$ molecular opacity source is expected to be H_2O , but there is some tension between models and past observations at this wavelength (cf. Madhusudhan & Seager 2010). Thus our understanding of these planets’ atmospheres remains incomplete.

Recent spectroscopic observations of HD 209458b during transit show a hint

of a systematic velocity offset ($2 \pm 1 \text{ km s}^{-1}$) of planetary CO lines during planetary transit (Snellen et al. 2010). If confirmed, this offset would be diagnostic of high-altitude winds averaged over the planet’s day/night terminator, and similar measurements at higher precision could one day hope to spatially resolve terminator circulation patterns and constrain atmospheric drag properties (Rauscher & Menou 2012). However, small orbital eccentricities (specifically, nonzero $e \cos \omega$, where ω is the longitude of periastron) can also induce a velocity offset in a planetary transmission spectrum (Montalto et al. 2011). It is thus convenient that precise timing of planetary transits and eclipses directly constrains $e \cos \omega$ (Seager 2011, chapter by J. Winn). This provides a further motivation for our work: to more tightly constrain HD 209458b’s orbit via a homogeneous analysis of a single, comprehensive data set.

In this paper we analyze the full complement of data for the HD 209458 system taken with the MIPS $24 \mu\text{m}$ camera (which we hereafter refer to simply as MIPS; Rieke et al. 2004) on the Spitzer Space Telescope. MIPS has taken previous $24 \mu\text{m}$ observations of exoplanetary transits (Richardson et al. 2006; Knutson et al. 2009a), eclipses (Deming et al. 2005b; Charbonneau et al. 2008; Knutson et al. 2008, 2009b; Stevenson et al. 2010), and thermal phase curves (Harrington et al. 2006; Knutson et al. 2009b, Ch. 2). MIPS operations depended on cryogenic temperatures; since Spitzer’s complement of cryogen has been exhausted there may be no further exoplanet measurements at wavelengths $> 10 \mu\text{m}$ until the eventual launch of missions such as EChO, SPICA, or the James Webb Space Telescope (JWST). Our work here describes some of the last unpublished $24 \mu\text{m}$ exoplanet observations, and a further motivation for our work is to inform the calibration, reduction, and observational methodologies of future missions’ mid-infrared (MIR) observations.

3.2.2 Outline

This report is organized as follows: in Section 3.3 we describe the MIPS observations and our approach to measuring precise system photometry. In Section 3.4 we describe our efforts to understand the origin of instrumental sensitivity variations apparent in the long-duration phase curve observations; these effects ultimately prevent any measurement of HD 209458b’s thermal phase curve. However, we are able to recover the parameters of the observed transits and eclipses, and we present these results in Sec. 3.5 and 3.6, respectively. Combining the results of these two analyses allows us to constrain the planet’s orbit (i.e., $e \cos \omega$), and we discuss the implications of this, and of the total system flux, in Section 3.7. We summarize our conclusions and present some thoughts for future high-precision MIR observations in Section 3.8.

3.3 Observations and Analysis

3.3.1 Observations

We reanalyzed all observations of the HD 209458 system taken with Spitzer’s MIPS 24 μm channel: analysis of one transit, two eclipses, and the long-duration phase curve observations have remained unpublished until now. Altogether, we used the data from Spitzer Program IDs 3405 (PI Seager; published in Deming et al. 2005b), 20605 (PI Harrington; published in Richardson et al. 2006), and 40280 (PI Knutson). Table 5.1 lists the observatory parameters used for each set of observations. Collectively these data comprise 2.5 transits, three eclipses, and a 58-hour set of near-continuous observations designed to detect the planet’s thermal phase curve.

Table 3.1. HD 209458b: *Spitzer*/MIPS 24 μm Observations of

UT Date	Event	Duration (hr)	t_{int} (s)	$N_{exposures}$	Bkd (MJy Sr $^{-1}$) ^a	Δt (s) ^b
UT 2004 Dec 5	Half transit	2.8	8.91	840	28.8	-544
UT 2004 Dec 6	Eclipse	5.8	9.96	1680	29.2	-531
UT 2005 Jun 27	Transit	5.6	9.96	1680	28.9	-612
UT 2005 Dec 1	Eclipse	5.6	9.96	1680	26.7	+183
UT 2008 Jul 25 ^c	Transit ^d	14.2	9.96	4060	28.3	-649
UT 2008 Jul 27 ^c	Eclipse	6.9	9.96	2072	27.9	-663

^aAverage sky backgrounds as reported by DRIBKGND keyword.

^bFor each event, $\Delta t \equiv \langle \text{HJD} \rangle - \langle \text{BJD}_{TDB} \rangle$

^cThese events were observed as part of a single, continuous phase curve observation with a duration of 58 hours spanning one transit and one secondary eclipses.

^dThis transit was corrupted by an apparent ramp in detector sensitivity, so we used a longer section of data to better constrain the ramp parameters in the joint fit.

3.3.2 Data Reduction

Unless stated otherwise we use the same methodology to reduce our data as described in Sec. 2.3.3, performing PSF-fitting photometry using a $100\times$ super-sampled MIPS PSF¹ modeled using a 6070 K blackbody spectrum simulated at the center of the MIPS field of view. We vary the size of the synthetic aperture used to calculate our PSF-fitting photometry, and find that a square, 21×21 pixel aperture minimizes photometric variations. During MIPS observations the target star is dithered between fourteen positions on the detector (Colbert, J. 2011, Section 8.2.1.2), and we fit the data from all dither positions simultaneously as described below.

As noted in Sec. 2.3.4, the MIPS 24 μm detector appears to suffer from low-amplitude temporal variations in the diffuse background, presumably owing to small amounts of scattered light in the instrument. Because this could affect the flat-fielding performed by the MIPS reduction pipeline, we create an empirical flat

¹Generated using Tiny Tim; available at <http://ssc.spitzer.caltech.edu/>

field by taking a pixel-by-pixel median of all the individual frames after masking the region containing the target star. After constructing this flat field we extract photometry (a) after subtracting the master flat field from each frame, and (b) after dividing each frame by the normalized-to-unity master flat field. Both of these give photometry that is very slightly less noisy (RMS reduced by $\lesssim 1\%$) than photometry that does not use an additional flat field correction. Subtracting by the empirical flat-field prior to computing PSF-fitting photometry results in a lower residual RMS and so we use this approach for all our data; ultimately our choice of flat field does not change our final results.

We extract the heliocentric Julian Date (HJD) from the timing tags in each BCD data file, and then convert the HJD values to BJD_{TDB} using the IDL routine `hjd2bjd`² (Eastman et al. 2010). These new time stamps have an estimated accuracy of one second (Eastman et al. 2010), which is small compared to our final ephemeris uncertainties of roughly one and four minutes for transits and eclipses, respectively.

3.3.3 Approach to Model Fitting

The MIPS dither pattern introduces systematic offsets of $\lesssim 1\%$ (Deming et al. 2005b) in the photometry at each dither position. We follow the methodology of Sec. 2.3.3 and explicitly fit for this effect by multiplying the modelled flux for each visit at dither position i by the factor $(1 + c_i)$. We further impose the constraint that these corrections do not change the absolute flux level, and so define c_0 such that the quantity $\prod_i (1 + c_i)$ is equal to unity. We ultimately find that the c_i are similar, but not constant, from one epoch to the next.

In all cases we determine best-fit model parameters using the Python simplex

²Available at <http://astrutils.astronomy.ohio-state.edu/time/>

minimization routine `scipy.optimize.fmin`³. We assess parameter uncertainties using a Markov Chain Monte Carlo implementation of the Metropolis-Hastings algorithm (`analysis.generic_mcmc`⁴), then take as uncertainties the range of values (centered on the best-fit value) that enclose 68.3% of the posterior distribution. We verify by eye that the Markov chains are well-mixed; the resulting one-dimensional posterior distributions are unimodal, symmetric, and approximately Gaussian unless stated otherwise.

3.4 Calibration and Instrument Stability

3.4.1 The Ramp

Before we present the results of our model fits, we discuss two photometric variations that we conclude to be of instrumental origin. The HD 209458 system flux measured from our 2008 observations, shown in Figure 3.1, exhibits a steep rise during the first 10-12 hours in which the measured system flux increases by $\sim 2\%$. This ramp appears similar to that seen in photometric observations taken with Spitzer/IRAC and Spitzer/IRS (Charbonneau et al. 2005; Deming et al. 2006; Knutson et al. 2007a). The IRAC ramp is the better studied, and is thought to result from charge-trapping in the detector (cf. Knutson et al. 2007a; Agol et al. 2010). According to this explanation, a substantial fraction of photoelectrons liberated early in the observations become trapped by detector impurities, resulting in a lower effective gain for the detector. Eventually all charge-trapping sites become populated and the detector response asymptotes to a constant level. As the IRAC $8\ \mu\text{m}$, IRS $16\ \mu\text{m}$, and MIPS detectors are all constructed of Si:As it is conceivable that the MIPS ramp we observe has a similar origin in charge-

³Available at <http://scipy.org/>

⁴Currently available at <http://www.astro.ucla.edu/~ianc/python/>

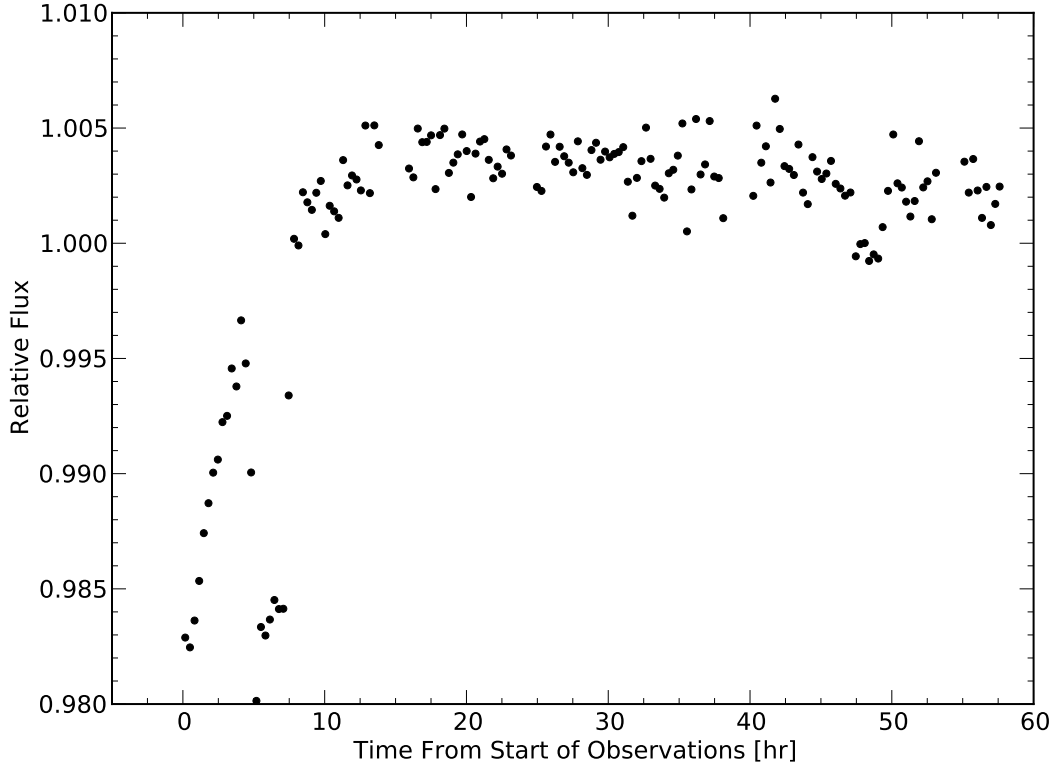


Figure 3.1 MIPS $24\ \mu\text{m}$ photometry of the HD 209458 system, showing the detector ramp (0–10 h), transit (5 h), and eclipse (48 h). For plotting purposes the data have been binned to lower temporal resolution. A slight ($\sim 0.2\%$) flux decrease is apparent from 10–58 h. This could be influenced by planetary phase variations, but the similarity to the purely instrumental effects seen in Figure 3.2 precludes an unambiguous distinction between the two effects.

trapping.

To test this hypothesis, we look for evidence of persistence in our data. Using all frames taken at the second dither position we compute the median image from each of several Astronomical Observing Requests (AORs). An AOR is a Spitzer logistical unit comprising some dozens of frames; in our data set each AOR lasts approximately 3 hr. We see faint afterimages at the other thirteen dither positions when we subtract the first median AOR frame from the final

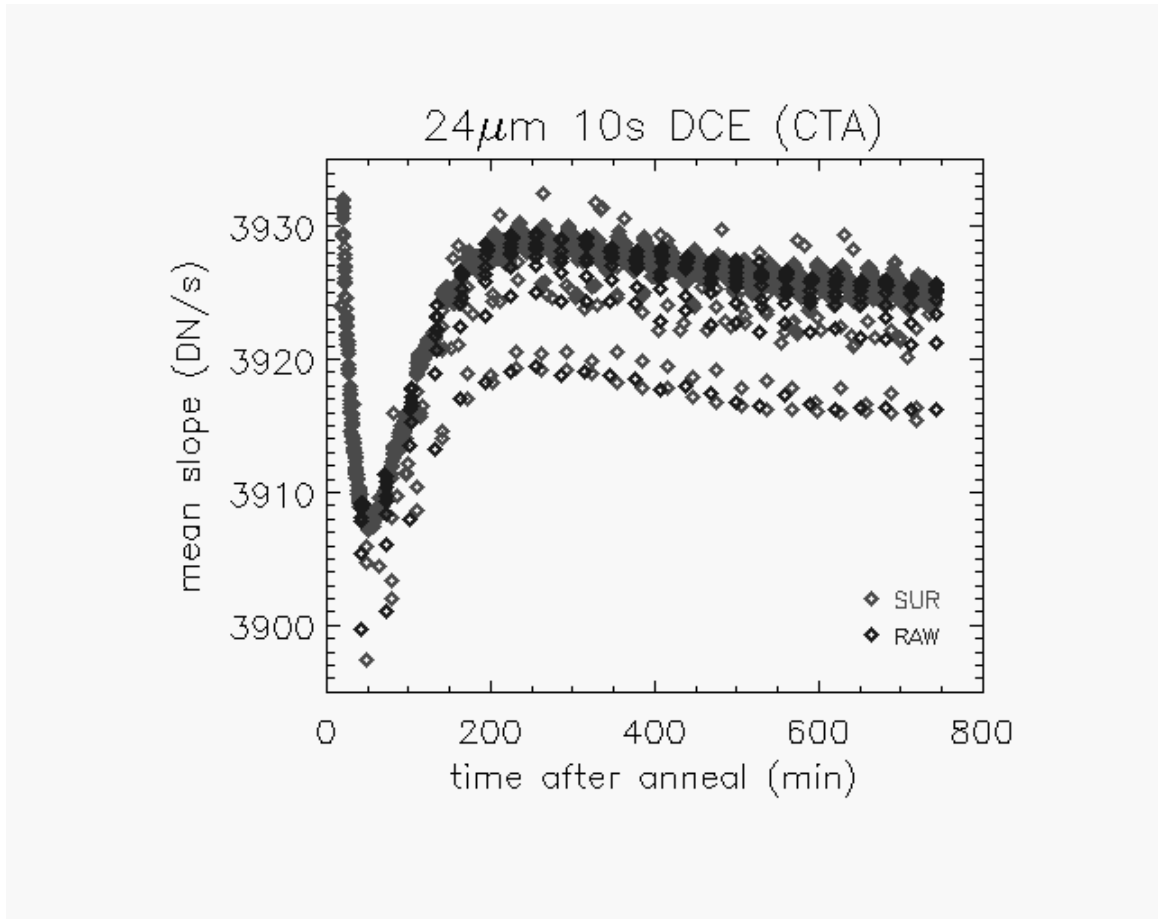


Figure 3.2 Lab calibration data for the MIPS 24 μm array, taken from [Young et al. \(2003; their Figure 7\)](#). The relevant data for comparison with Spitzer/MIPS observations are the gray diamonds labeled SUR (Sample Up the Ramp, the algorithm used to compute MIPS data numbers from pixel slopes). [Young et al. \(2003\)](#) suggest that the initial sensitivity decrease (0–50 minutes) is related to detector response variations related to a thermal anneal immediately preceding the data; as we describe in Sec. 3.4, our data should not be affected by any anneal operations. The rest of the observations appear strikingly similar to our photometry of HD 209458, shown in Figure 3.1. For comparison with Figure 3.1 the peak pixel fluxes in the HD 209458 data frames are roughly 1000 DN/s.

median AOR frame (taken ~ 56 hr later; cf. Figure 3.1), which suggests that the level of persistence (a byproduct of charge trapping) increases over the course of the observations. These afterimages are much fainter when comparing data from the first and second AORs (separated by 3.6 hr), consistent with the conclusion

that the level of persistence does not saturate to a constant value on these short time scales. The afterimages are not apparent by eye when comparing the last and penultimate AORs (again separated by 3.6 hr), which suggests that the charge trapping persistence has saturated by this time, as expected from the much-flattened data ramp seen in Figure 3.1.

The IRAC ramp is known to exhibit a behavior which depends on the level of illumination, with more intensely illuminated pixels exhibiting a steeper initial ramp and saturating more quickly (these pixels' charge traps are filled more quickly because more free photoelectrons are available). We see a hint of this behavior in our data. Though pointing variations prevent us from tracking the response of individual pixels, we extract photometry (again via PSF fitting) using both 3- and 5-pixel-wide square apertures. The 3-pixel photometry – which is weighted somewhat more heavily by the most intensely illuminated pixels than is the 5-pixel photometry – shows a hint of a steeper ramp. We take this as further tentative support for our hypothesis that our ramp has a common origin with the IRAC ramp. The ramp behavior remains unchanged when we use a wider aperture, but this may not be diagnostic since the gradient in illumination level quickly flattens out beyond a few pixels.

We would like to know why we see this ramp, especially considering that no previous MIPS observations detected this effect. However, we can find no consistent discriminant between the presence or absence of a ramp in MIPS data and the state of either instrument or observatory. The first set of AORs in the *v* and *b* observations in Ch. 2 (the first ~ 10 hr; not shown in Figure 2.3) were anomalously low ($\sim 0.3\%$) compared to subsequent observations, which they attributed to a thermal anneal of the $24\mu\text{m}$ detector conducted < 1 h before

these observations⁵. No ramp was observed in the continuous, long-duration MIPS observations of either [Knutson et al. \(2009b\)](#) or in my own (cf. Ch. 2 and Figure 2.3), which were taken $\gtrsim 1$ day after the last $24\ \mu\text{m}$ anneal. The photometry shown in Figure 3.1 also occurred > 1 day after the last $24\ \mu\text{m}$ anneal, so annealing seems unlikely to explain the presence of the ramp in our data.

We investigated whether preflashing could explain the absence of any ramp in other MIPS phase curve observations. To preflash is to conduct a set of brief (< 1 hr) observations of a bright target before observing a fainter exoplanet system ([Seager & Deming 2009](#); [Knutson et al. 2011](#)); experience shows that this tends to reduce the amplitude of the ramp, presumably by partially saturating the detector’s charge traps. HD 209458 is the faintest of the three exoplanet systems with long-duration MIPS $24\ \mu\text{m}$ observations, but the flux difference (~ 20 mJy for HD 209458 vs. ~ 60 mJy for HD 189733) does not seem sufficiently large for only one of our five observations of HD 209458 to fail to pre-flash the detector. If the difference were due to the increased flux from HD 189733, we should still see a shorter, steeper ramp at the start of these observations. That no ramp has been reported previously, and that we see a ramp in the HD 209458 data only intermittently, suggests that some other phenomenon may be at work here.

The phase curve observations of both HD 189733 and HD 209458 began immediately after a data downlink to Earth, so this factor also does not distinguish between the cases. Prior to the data downlinks, our 2008 observations of HD 209458 were preceded by $24\ \mu\text{m}$ observations of the faint RXCJ0145.2-6033 (~ 4 mJy), but no $24\ \mu\text{m}$ observations whatsoever were made in the \sim day leading up to [Knutson et al. \(2009b\)](#)’s observations of HD 189733. While MIPS was oper-

⁵As recorded in the Spitzer observing logs, available at <http://ssc.spitzer.caltech.edu/warmmission/scheduling/observinglogs/>

ational all its arrays were continuously exposed to the sky: although the Spitzer operations staff planned observations so as to avoid placing bright sources on the $24\ \mu\text{m}$ array (using IRAS $25\ \mu\text{m}$ images as a guide; A. Noriega-Crespo, private communication) we cannot dismiss the possibility that occasionally some bright sources may have been missed.

Thus we cannot conclusively determine why the MIPS observations we present here show the detector ramp while previous, comparable observations have not shown such an effect. Nonetheless, the similarity between our photometry in Figure 3.1 and raw IRAC $8\ \mu\text{m}$ photometry (e.g., Agol et al. 2010) strongly suggests that the most likely explanation involves detector response variations due to charge-trapping.

3.4.2 The Fallback

After the detector ramp, the photometry in Figure 3.1 decreases over the rest of the observations by $\sim 0.2\%$; we term this flux diminution the “fallback.” The amplitude of this effect is of the approximate amplitude expected for a $24\ \mu\text{m}$ planetary thermal phase curve (Showman et al. 2009; Burrows et al. 2010), so our first inclination was to ascribe a planetary origin to this flux decrease. However, there is a distinct qualitative similarity between the phase curve photometry and pre-launch calibration data taken with the MIPS $24\ \mu\text{m}$ detector under bright ($170\ \text{MJy sr}^{-1}$) illumination, shown in Figure 3.2 (reproduced from Young et al. 2003). A comparison of this figure and Figure 3.1 reveals that both display the same qualitative signature of an early, steep ramp followed by a slow, gradual fallback in measured flux. The only differences are (1) an initial steep decrease in flux in the calibration data not seen in our stellar photometry (attributed by Young et al. 2003, to the response of the detector to a thermal anneal immediately

preceding the data shown), and (2) longer ramp and fallback time constants in our data set.

The brightest pixels in the HD 209458 MIPS observations reach a flux of 45 MJy sr⁻¹ (corresponding to 1000 DN s⁻¹). Perhaps, like in some preflashed IRAC observations (cf. [Knutson et al. 2011](#)), the lower illumination level in the HD 209458 photometry (relative to the stimulation response curve from [Young et al. 2003](#)) is responsible for the different timescales evident in the two 24 μm time series. However, the brightest pixels in the observations of *v* And b described in [Ch. 2](#) reached a flux of 9000 DN s⁻¹ and no fallback is apparent in the continuous portion of those observations (though the continuous photometry of *v* And b described in [Ch. 2](#) did decrease monotonically by ~ 0.1 % (cf. [Figure 2.3](#)), they demonstrated a coherent planetary phase curve in two data sets spanning several years: thus planetary emission, rather than an instrumental sensitivity variation, seems a more likely interpretation of their results). Similarly, no fallback is seen in MIPS observations of HD 189733b (peak pixel flux ~ 1200 DN s⁻¹; [Knutson et al. 2009b](#)) or of the fainter eclipsing M binary GU Boo (≲ 500 DN s⁻¹; [von Braun et al. 2008](#)). Thus it seems possible that the fallback is linked to the presence of the detector ramp, which also appears only in our MIPS data set.

We try a number of different functional forms to fit to the ~ 0.2% post-ramp fallback, which we fit simultaneously with the ramp. These include a flat model (i.e., no decrease), sinusoidal and Lambertian profiles with arbitrary amplitude and phase (representative of a planetary phase curve), and a double-exponential of the form $(1 - \alpha e^{-t/\tau_1}) \times e^{-t/\tau_2}$, with $\tau_2 \gg \tau_1$, motivated by the detector response variations seen in [Figure 3.2](#). We decide which of these models is the most appropriate on the basis of the Bayesian Information Criterion (BIC⁶). The

⁶BIC = $\chi^2 + k \ln N$, where k is the number of parameters to be fit and N the number of data points. A fit that gives a lower BIC is preferred over a fit with a higher BIC, and thus the

model consisting of a ramp plus a decaying exponential gives the lowest BIC: ~ 15 units lower than obtained with the sinusoidal or Lambertian models. Thus the data prefer an instrumental explanation for the low-level flux variations that we see.

When using a sinusoidal or Lambertian model, the best-fit phase curve parameters describe a thermal phase variation which peaks well before secondary eclipse, suggesting a planetary hot spot eastward of the substellar point. Qualitatively, such a shift is consistent with observations of both HD 189733b (Knutson et al. 2009b) and ν And b (Ch. 2 and Figures 2.3 and 2.4). However, the phase offset determined by this fitting process is surprisingly large: $136 \text{ deg} \pm 18 \text{ deg}$, a result which would seem to imply that the planet’s night side is hotter than its day side. Such a scenario has been predicted by some models (cf. Cho et al. 2003), but such a large phase offset is bigger than observed for either ν And b or HD 189733b, and larger still when compared to expectations for this planet from more recent simulations (e.g., Rauscher et al. 2008; Showman et al. 2009). We thus deem the phase curve fit with large offset to be an unlikely result, providing one more reason to doubt that the flux variation we see is of planetary origin.

We also inject into the data a sinusoidal phase curve with zero phase offset and a peak-to-valley amplitude equal to our best-fit secondary eclipse depth results and repeat our analysis: in this case the best-fit sinusoidal and Lambertian models have a lower BIC value (by 12 units) than the instrumental model, though the recovered amplitude and phase offset are still somewhat biased by the flux fallback. Although these results suggest that we are close to achieving the sensitivity required to constrain HD 209458b’s thermal phase variations, our ignorance of the detailed morphology of the flux fallback prevents us from reaching a conclusion.

BIC penalizes more complicated models.

ing a more quantitative conclusion. Thus, we can only conclude that the striking qualitative similarity between Figures 3.1 and 3.2 precludes us from making any definite claims as to the detection of planetary phase curve effects in our data.

3.4.3 Instrument Stability

As noted previously in Sec. 2.3.4, the background flux of continuous MIPS photometry exhibits a roughly linear trend with time, with smaller, abrupt changes from one AOR to the next. The linear trend can be explained by a variation in the thermal zodiacal light as Spitzer’s perspective of HD 209458 changes with respect to the solar system, and in Sec. 2.3.4 I attribute the discontinuous, AOR-by-AOR background fluctuations to scattered light. Whatever the cause, these discontinuities are removed by the sky background subtraction, and do not appear to affect the final stellar photometry.

During our 2008 observations we see a $0.5 \mu\text{A}$ increase in the $24 \mu\text{m}$ detector anneal current (MIPS data file keyword AD24ANLI), a decrease of 6 mK in the scan mirror temperature (keyword ACSMMTMP), and swings in the electronics box temperature (keyword ACEBOXTM) of up to 0.3 K. During sustained observations the electronics box appears to experience heating with some time lag, but with a much shorter cooling lag during observational breaks to transmit data to Earth. Upon reexamination of past observations, we find that these three parameters exhibit similar behavior during observations of HD 189733b (Knutson et al. 2009a) and of upsilon Andromeda b (Ch. 2). The MIPS optical train is cryogenically cooled and separated from the non-cryogenic instrument electronics (Heim et al. 1998), so it does not seem likely that the observed swings in the electronics box temperature should influence the photometry. Similarly, the anneal current and scan mirror temperature do not seem to correlate with either

the ramp or the post-ramp flux decrease, so we conclude that these instrumental variations do not affect our final photometry.

3.5 Transits

3.5.1 Fitting Approach

We fit transits using uniform-disk and linear limb-darkened transit models (Mandel & Agol 2002), but (consistent with the results of Richardson et al. 2006) we find the limb-darkened model offers no improvement over the uniform-disk model (as determined by the BIC). We fit the transit data for: the time of center transit $T_{c,t}$, the impact parameter b , the scaled stellar radius R_*/a , the planet/star radius ratio R_p/R_* , and the out-of-transit system flux F_* . We hold the period fixed at $3.52474550 \pm 0.00000018$ d (Torres et al. 2008), which is a more precise determination than our observations can provide. To extract useful information from our half-transit event we always require that b and R_*/a have the same value, determined jointly from all our transits. We therefore perform one fit in which these two parameters are jointly fit, and a second fit in which we additionally fit jointly to $T_{c,t}$ and R_p/R_* across all transit events.

We fit to the detector ramp in the 2008 transit by including a multiplicative factor of the form $1 - \alpha e^{-t/\tau}$, where t is measured from the start of the observations. This formulation of the ramp model is motivated by a physical model of the charge-trapping phenomenon thought to cause the IRAC $8 \mu\text{m}$ ramp (Agol et al. 2010). Agol et al. (2010) find a ramp based on two exponentials to be preferred for their high S/N observations, but we find that our data are not precise enough to constrain this more complicated model: when fitting a double-exponential ramp of the form $1 - \alpha_1 e^{-t/\tau_1} - \alpha_2 e^{-t/\tau_2}$ (Agol et al. 2010) the parameters for the two

exponential trends become degenerate, and the resulting fits are not preferred to the single ramp fit on the basis of the BIC. Finally, we include in all our fits the fourteen sensitivity correction terms (c_i) corresponding to the fourteen MIPS dither positions.

3.5.2 Results

Table 3.2 lists the results of the fit in which we assume a constant orbit and transit – holding b , R_*/a , R_p/R_* , and $T_{c,t}$ constant across all transits – while Table 3.3 lists the results of the fit in which R_p/R_* and $T_{c,t}$ (but not b or R_*/a) are allowed to vary between events. We plot the results of fits to each individual transit, and to the combined data set, in Figure 3.3. We show how the residuals to the combined fit bin down with increasing sample size in Figure 5.3: the curve shown tracks closely with the $N^{-1/2}$ expectation from uncorrelated noise on short time scales (< 20 min), but on longer time scales the residuals bin down more slowly than this. This indicates the presence of correlated (red) noise (cf. Pont et al. 2006) in these data, which is not surprising considering the ramp residuals apparent in Figure 3.3.

We examine the residuals to the fourteen individual channels and see some evidence for qualitatively different correlated noise at different dither positions. We do not think it likely that this behavior is related to an intrapixel effect (as observed in IRAC; cf. Charbonneau et al. 2005), because the residual behavior we see does not correlate with mean PSF position relative to the boundaries of individual pixels. Instead, it seems more likely to be a manifestation of the known position-dependent sensitivity effect previously attributed to residual flat-fielding errors (Sec. 2.3.3 and Figure 2.2).

The resulting posterior distributions are all unimodal (except for the impact

Table 3.2. HD 209458b: Joint Transit Fits

Parameter	2004	2005	2008
c_0	$+0.0009 \pm 0.0022$	$+0.00036 \pm 0.00086$	$+0.00274 \pm 0.00053$
c_1	$+0.0097 \pm 0.0027$	$+0.00881 \pm 0.00088$	$+0.01387 \pm 0.00055$
c_2	-0.0030 ± 0.0022	$+0.00101 \pm 0.00136$	$+0.00487 \pm 0.00053$
c_3	$+0.0106 \pm 0.0024$	$+0.00866 \pm 0.00079$	$+0.00858 \pm 0.00056$
c_4	-0.0034 ± 0.0024	$+0.00148 \pm 0.00115$	-0.00020 ± 0.00053
c_5	-0.0021 ± 0.0032	$+0.01006 \pm 0.00080$	$+0.01310 \pm 0.00052$
c_6	$+0.0017 \pm 0.0022$	-0.00574 ± 0.00078	-0.00502 ± 0.00057
c_7	-0.0023 ± 0.0033	$+0.00167 \pm 0.00081$	-0.00720 ± 0.00054
c_8	-0.0036 ± 0.0023	-0.00298 ± 0.00078	-0.00121 ± 0.00058
c_9	$+0.0098 \pm 0.0023$	-0.00324 ± 0.00135	-0.00919 ± 0.00060
c_{10}	-0.0032 ± 0.0028	$+0.00394 \pm 0.00111$	$+0.00210 \pm 0.00057$
c_{11}	-0.0126 ± 0.0032	-0.00974 ± 0.00103	-0.01016 ± 0.00057
c_{12}	$+0.0008 \pm 0.0028$	-0.00039 ± 0.00085	-0.00122 ± 0.00065
c_{13}	-0.0028 ± 0.0024	-0.01360 ± 0.00091	-0.01062 ± 0.00052
F_* [mJy]	$+18.845 \pm 0.012$	$+18.7784 \pm 0.0049$	$+18.696 \pm 0.010$
α	–	–	$+0.02437 \pm 0.00068$
τ [d]	–	–	$+0.174 \pm 0.016$
	$T_{c,t}$ [BJD _{TDB}]	$2453549.20852 \pm 0.00049$	
	b	$+0.590 \pm 0.062$	
	R_*/a	$+0.1205 \pm 0.0066$	
	R_p/R_*	$+0.1218 \pm 0.0014$	
	$(R_p/R_*)^{2a}$	$+0.01483 \pm 0.00033$	

^aComputed from the posterior MCMC distributions of R_p/R_* .

Table 3.3. HD 209458b: Semi-Joint Transit Fits

Parameter	2004	2005	2008
c_0	-0.0001 ± 0.0024	$+0.00043 \pm 0.00084$	$+0.00268 \pm 0.00054$
c_1	$+0.0091 \pm 0.0030$	$+0.00866 \pm 0.00095$	$+0.01368 \pm 0.00053$
c_2	-0.0032 ± 0.0022	$+0.00087 \pm 0.00149$	$+0.00524 \pm 0.00076$
c_3	$+0.0117 \pm 0.0023$	$+0.00872 \pm 0.00082$	$+0.00878 \pm 0.00066$
c_4	-0.0032 ± 0.0023	$+0.00146 \pm 0.00110$	-0.00016 ± 0.00053
c_5	-0.0021 ± 0.0029	$+0.01009 \pm 0.00078$	$+0.01316 \pm 0.00053$
c_6	$+0.0019 \pm 0.0022$	-0.00603 ± 0.00084	-0.00516 ± 0.00053
c_7	-0.0019 ± 0.0039	$+0.00157 \pm 0.00083$	-0.00686 ± 0.00058
c_8	-0.0039 ± 0.0023	-0.00301 ± 0.00078	-0.00110 ± 0.00063
c_9	$+0.0095 \pm 0.0022$	-0.00317 ± 0.00144	-0.00910 ± 0.00057
c_{10}	-0.0032 ± 0.0029	$+0.00378 \pm 0.00093$	$+0.00189 \pm 0.00052$
c_{11}	-0.0124 ± 0.0028	-0.00942 ± 0.00082	-0.00977 ± 0.00056
c_{12}	$+0.0007 \pm 0.0028$	-0.00035 ± 0.00086	-0.00189 ± 0.00129
c_{13}	-0.0026 ± 0.0022	-0.01330 ± 0.00078	-0.01096 ± 0.00061
$T_{c,t}$ [BJD _{TDB}]	2453344.7718 ± 0.0025	$2453549.20746 \pm 0.00065$	$2454673.60391 \pm 0.00074$
R_p/R_*	$+0.1227 \pm 0.0060$	$+0.1189 \pm 0.0020$	$+0.1238 \pm 0.0019$
F_* [mJy]	$+18.850 \pm 0.016$	$+18.7735 \pm 0.0056$	$+18.6947 \pm 0.0095$
$(R_p/R_*)^{2a}$	$+0.0151 \pm 0.0015$	$+0.01413 \pm 0.00046$	$+0.01531 \pm 0.00046$
α	–	–	$+0.02458 \pm 0.00071$
τ [d]	–	–	$+0.168 \pm 0.016$
	b	$+0.581 \pm 0.070$	
	R_*/a	$+0.1197 \pm 0.0069$	

^aComputed from the posterior MCMC distributions of R_p/R_* .

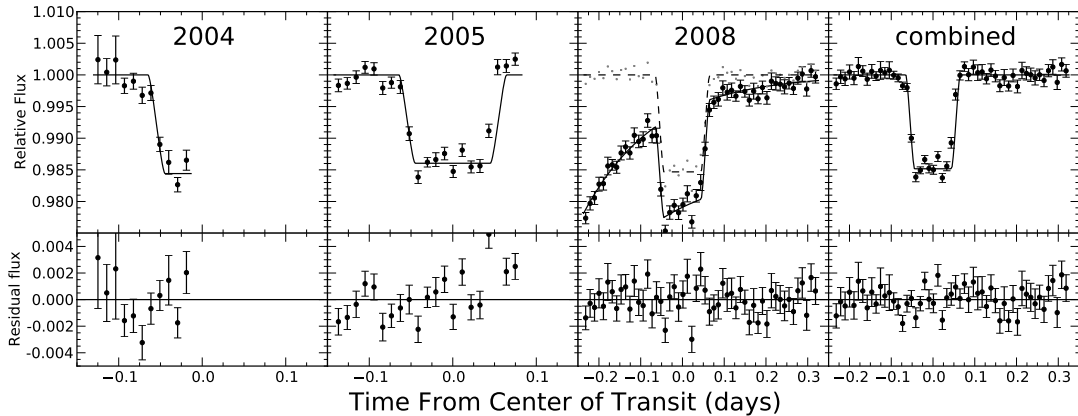


Figure 3.3 MIPS $24 \mu\text{m}$ transits of HD 209458b. The top panels show photometry and the best-fit model, and the lower panels show the residuals to the fits. For plotting purposes the data have been corrected for the MIPS 14-position sensitivity variations, normalized by the stellar flux, and binned by 70 points (for the individual transits) and by 210 points (for the combined data set). We also corrected for the ramp in the 2008 data set (corrected, binned data shown as small points) before combining the data to plot the data in the rightmost panel.

parameter b), and the usual correlations are apparent between b and R_*/a and between F_* and R_p/R_* (cf. [Burke et al. 2007](#)). As noted above, the 2008 transit data are strongly affected by the detector ramp, and we see correlations between the ramp parameters and the transit depth. We compute the two-dimensional posterior distributions of R_p/R_* , τ , and α (marginalized over all other parameters) from the MCMC chains using the kernel density estimate approach described in [Sec. 2.4.3](#); we show these distributions in [Figure 3.6](#) and list the elements of these parameters’ covariance matrix in [Table 3.4](#).

3.5.3 Discussion

The three independently-fit transit depths listed in [Table 3.3](#) have a fractional dispersion of 3%, consistent with our individual uncertainty estimates of 3-10%. We thus find no evidence for variations in transit depth, and our transit depths

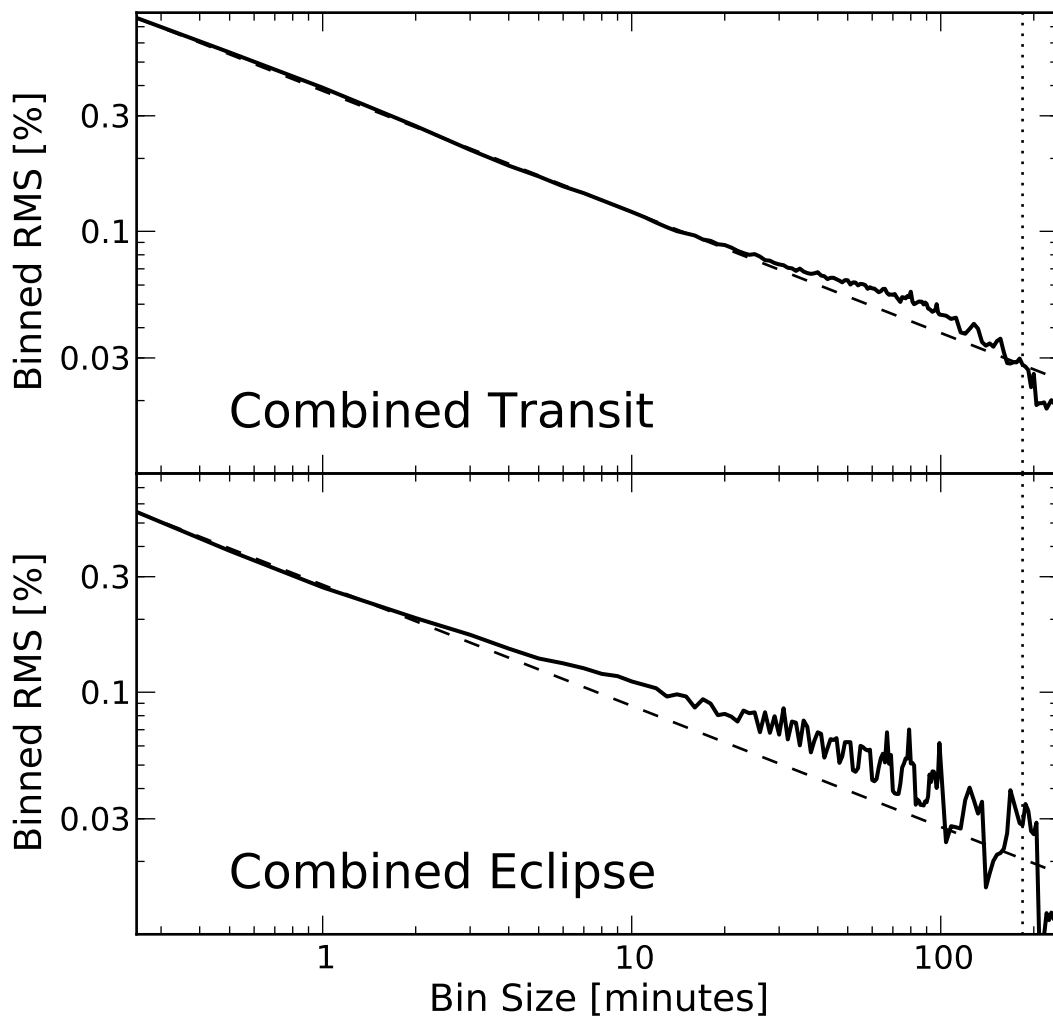


Figure 3.4 Dispersion of the binned residuals (solid lines) to the combined transit and eclipse light curve fits shown in Figure 3.3 and 3.5. On longer timescales both fits exhibit a binned dispersion 10-30% higher than expected from uncorrelated noise (dashed line). The dashed lines show the expectation for uncorrelated errors, which scale as $N^{-1/2}$. The vertical dotted line indicates the transit duration.

are consistent with the depth measured from the combination of our first two transit data sets (Richardson et al. 2006).

We plot the ensemble of HD 209458b’s transit depth measurements in Fig-

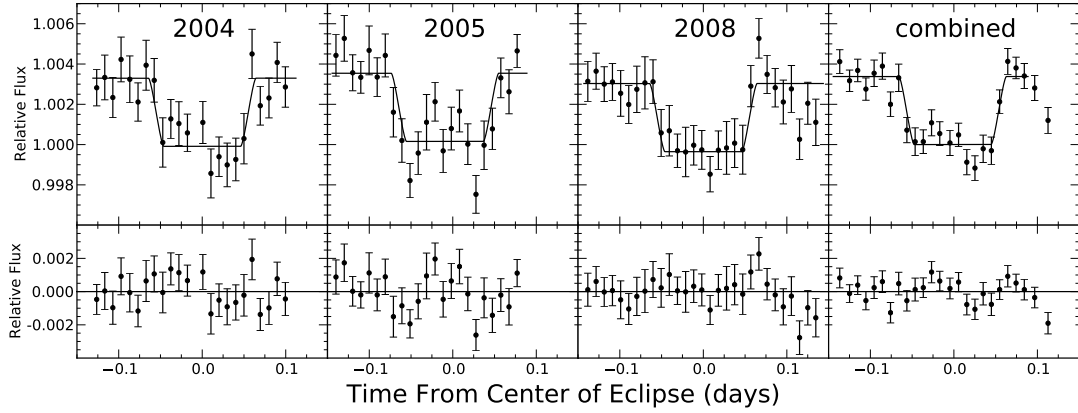


Figure 3.5 MIPS 24 μm eclipses of HD 209458b. The top panels show photometry and the best-fit models, and the lower panels show the residuals to the fits. For plotting purposes the data have been corrected for the MIPS 14-position sensitivity variations, normalized by the stellar flux, and binned by 70 points (for the individual eclipses) and by 210 points (for the combined data set).

Table 3.4. HD 209458b: Ramp/transit covariance matrix (cf. Figure 3.6).

Element	Value/ 10^6
σ_{α}^2	0.507
$\sigma_{\tau[d]}^2$	266 d ²
σ_{R_p/R_*}^2	3.49
$\sigma_{\alpha, \tau[d]}$	-5.03 d
$\sigma_{\alpha, R_p/R_*}$	0.379
$\sigma_{\tau[d], R_p/R_*}$	-16.3 d

ure 3.7 along with a model of transit depth vs. wavelength from Fortney et al. (2010). The model is consistent with the 24 μm measurement we present here and agrees fairly well with the optical measurements of Sing et al. (2008) and the IRAC 3.6 and 4.5 μm measurements of Beaulieu et al. (2010). However, our model strongly disagrees with the IRAC 5.8 and 8.0 μm , which was also shown for the same HD 209458b model in Fortney et al. (2010). The large discrepancy remains unclear. Given the known wavelength-dependent water vapor opacity, Shabram et al. (2011) showed that reaching all four 4 IRAC data points may be

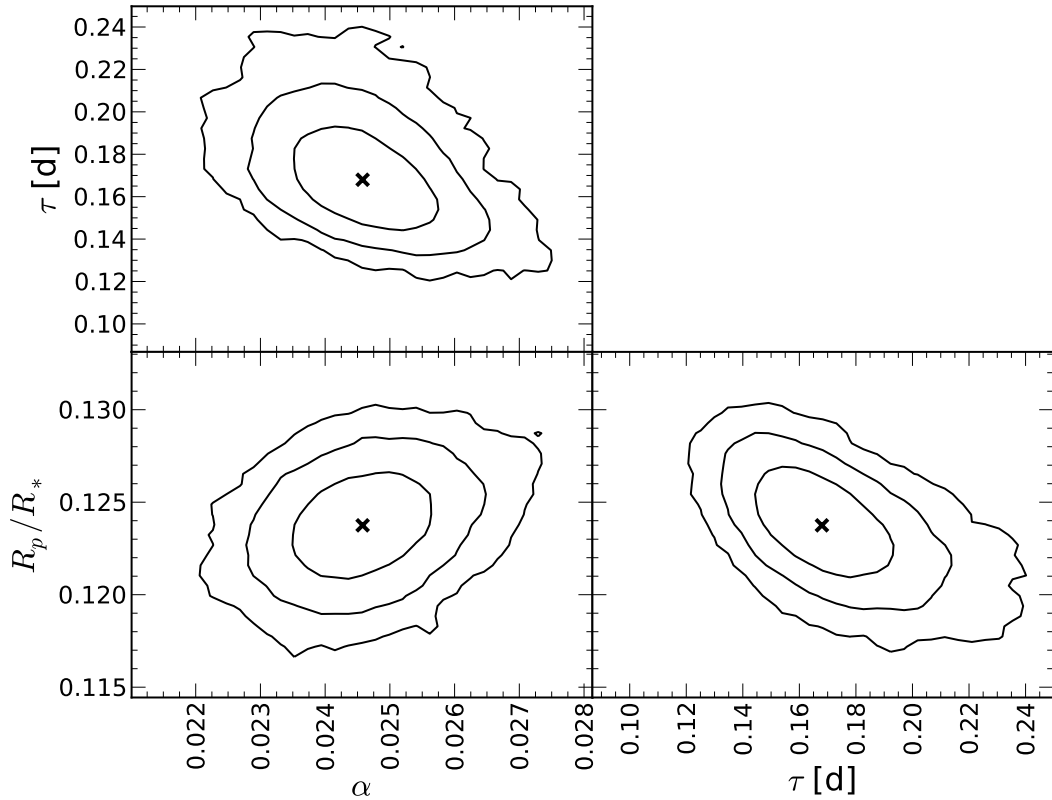


Figure 3.6 Posterior distributions of the ramp parameters (α, τ) and R_p/R_* , estimated from the MCMC analysis of the 2008 transit data. The ‘ \times ’ symbols indicate the best-fit parameters listed in Table 3.3, and the lines indicate the 68.27%, 95.45%, and 99.73% confidence intervals. The elements of these parameters’ covariance matrix are listed in Table 3.4.

impossible within the framework of a simple transmission spectrum model. Our transmission spectrum methods are described in these papers, and the atmospheric pressure-temperature profile is from a planet-wide average no-inversion model shown in Figure 3.8.

We resample the posterior distributions of the independent transit ephemerides shown in Table 3.3 to determine our own, independent constraint on the planet’s orbital period (assuming it is constant) using a linear relation. We compute the center-of-transit time and period to be 2453549.2075 ± 0.0013 d and $3.5247537 \pm$

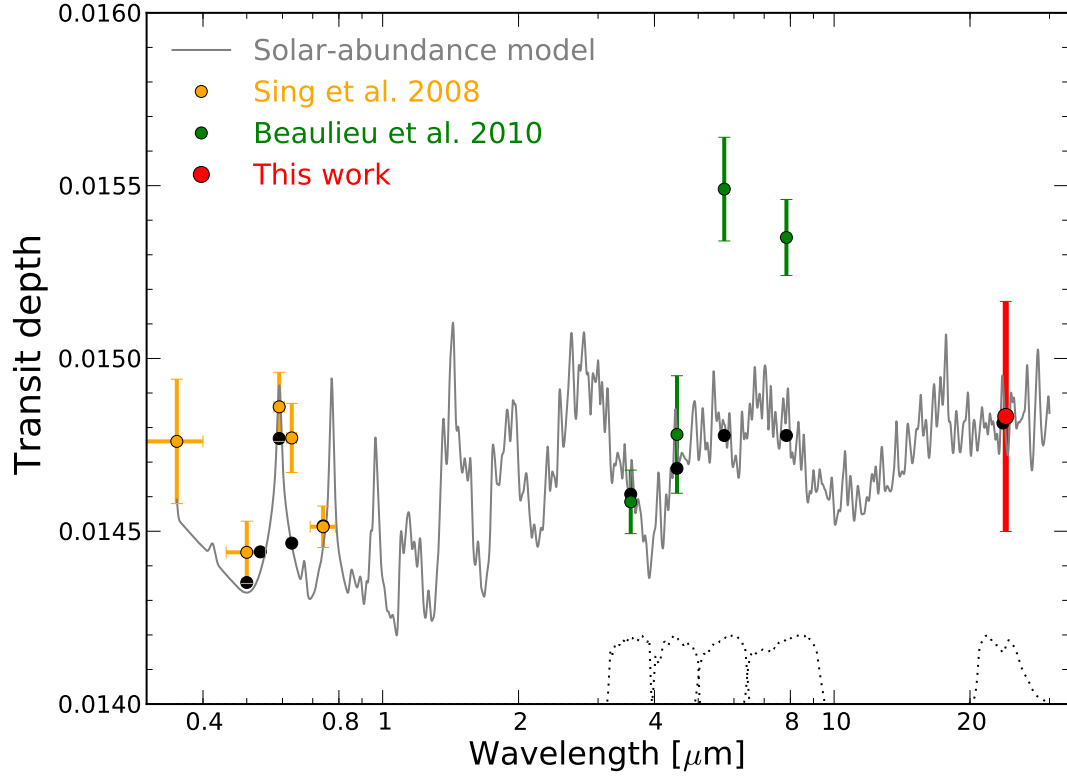


Figure 3.7 Measurements of the transit depth of HD 209458b: binned optical spectroscopy (Sing et al. 2008), previous mid-infrared photometry (Beaulieu et al. 2010), and our $24 \mu\text{m}$ measurement. The solid line is a model generated using the (dot-dashed) temperature-pressure profile shown in Figure 3.8. The solid black points without errorbars represent the weighted averages of the model over the corresponding bandpasses (indicated at bottom).

0.0000049 d, respectively; the covariance between these two parameters is $-5.652 \times 10^{-9} \text{ d}^2$. The period we obtain differs from the established period (Torres et al. 2008) by only $8.2 \times 10^{-6} \text{ d}$ (0.71 s), well within the uncertainties.

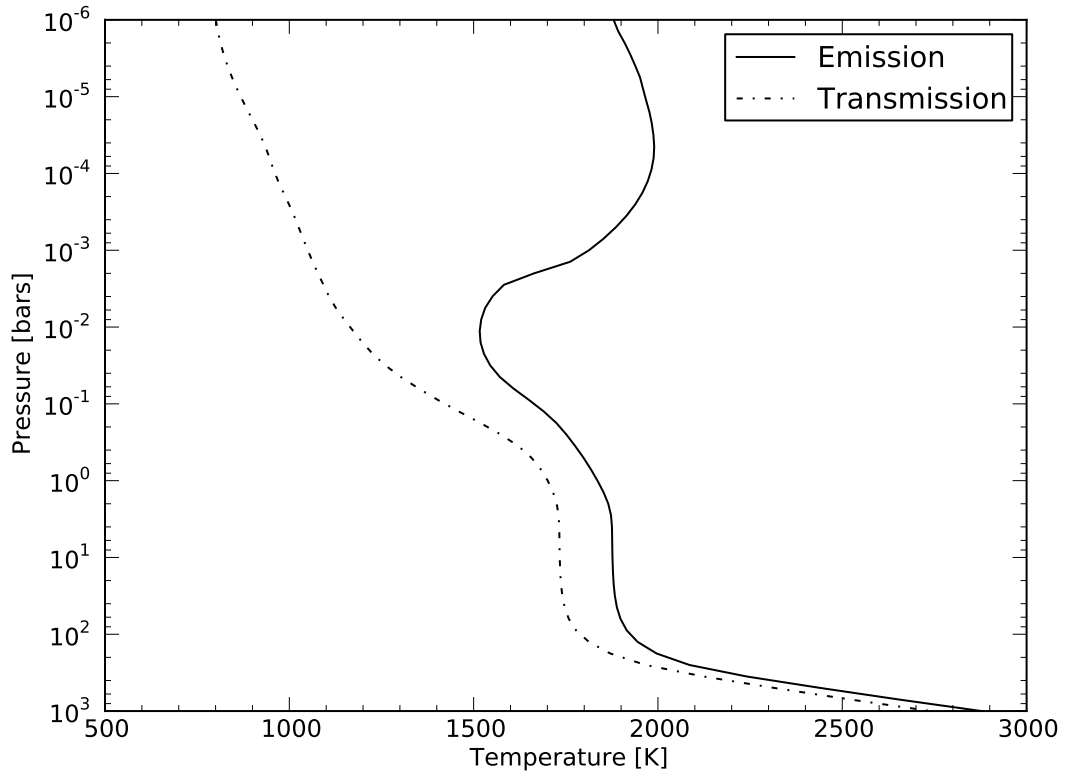


Figure 3.8 Temperature-pressure (T-P) profiles used to generate our model spectra. The dot-dashed curve is a planet-wide average T-P profile taken from a full (4π) redistribution model, and is used to model the transmission spectrum shown in Figure 3.7. It includes TiO/VO opacity, but these species have only a minor effect since nearly all of the Ti/V has condensed out of the gas phase at these cooler temperatures. The solid curve is from a model assuming no redistribution of absorbed energy (making it hotter), and includes TiO/VO to drive the temperature inversion seen in Figure 3.9. This figure was produced using data from collaborators J. Fortney and A. Showman.

3.6 Secondary Eclipses

3.6.1 Fitting Approach

We fit secondary eclipses using the uniform-disk occultation formulae of [Mandel & Agol \(2002\)](#), fitting each event for three astrophysical parameters: time of

center of eclipse $T_{c,e}$, stellar flux F_* , and eclipse depth F_p/F_* – as well as the fourteen sensitivity correction terms (c_i) discussed previously. We hold all other orbital parameters fixed at the values listed in [Torres et al. \(2008\)](#), which are more precise than our constraints based on the $24\ \mu\text{m}$ transit photometry. We perform four different fits: an independent fit of each eclipse taken in isolation, and a fit to the combined data set in which we fit for a single eclipse depth, but still allow $T_{c,e}$ and F_* to vary for each event. We use only a subset of the long-duration phase curve observations to fit the 2008 eclipse, as indicated in [Table 5.1](#). We tried including a linear slope in the combined eclipse fit, but this extra parameter is not justified because it gives a higher BIC than fits without such a slope.

3.6.2 Results

The parameters for the fit in which $T_{c,e}$ and F_p/F_* are fit jointly across all eclipses (but F_* remains independent) are shown in [Table 3.5](#), and parameters for the three wholly independent eclipse fits are shown in [Table 3.6](#). The data, best fit models, and residuals for all three eclipses and the combined data set are plotted in [Figure 3.5](#). The only strong correlations apparent in the resulting posterior distributions are between F_* and F_p/F_* – expected since we are making a relative measurement. We show how the residuals to the combined fit bin down with increasing sample size in [Figure 5.3](#): the residuals average down more slowly than the $N^{-1/2}$ expectation from uncorrelated errors. This indicates the presence of correlated (red) noise (cf. [Pont et al. 2006](#)) in these data, which is expected given the behavior of the eclipse residuals shown in [Figure 3.5](#).

Table 3.5. HD 209458b: Joint Eclipse Fits

Parameter	2004	2005	2008
c_0	$+0.00298 \pm 0.00080$	$+0.00048 \pm 0.00078$	$+0.00278 \pm 0.00073$
c_1	$+0.00793 \pm 0.00078$	$+0.01103 \pm 0.00080$	$+0.01331 \pm 0.00071$
c_2	$+0.00619 \pm 0.00079$	$+0.00349 \pm 0.00078$	$+0.00397 \pm 0.00074$
c_3	$+0.00943 \pm 0.00075$	$+0.00879 \pm 0.00078$	$+0.00887 \pm 0.00071$
c_4	$+0.00048 \pm 0.00108$	$+0.00186 \pm 0.00102$	-0.00002 ± 0.00074
c_5	$+0.01148 \pm 0.00080$	$+0.01151 \pm 0.00079$	$+0.01480 \pm 0.00069$
c_6	-0.00557 ± 0.00079	-0.00461 ± 0.00084	-0.00432 ± 0.00072
c_7	-0.00571 ± 0.00082	-0.00582 ± 0.00079	-0.00514 ± 0.00072
c_8	-0.00171 ± 0.00078	-0.00020 ± 0.00082	-0.00329 ± 0.00070
c_9	-0.00231 ± 0.00079	-0.00361 ± 0.00079	-0.00754 ± 0.00070
c_{10}	$+0.00052 \pm 0.00082$	$+0.00084 \pm 0.00093$	-0.00137 ± 0.00080
c_{11}	-0.00691 ± 0.00081	-0.00973 ± 0.00076	-0.00712 ± 0.00073
c_{12}	-0.00507 ± 0.00082	-0.00402 ± 0.00078	-0.00333 ± 0.00072
c_{13}	-0.01142 ± 0.00079	-0.00968 ± 0.00081	-0.01121 ± 0.00071
F_* [mJy]	$+18.78683 \pm 0.00486$	$+18.70529 \pm 0.00485$	$+18.60906 \pm 0.00472$
	F_p/F_*	$+0.00338 \pm 0.00026$	
	T_B [K]	$+1310 \pm 80$	
	F_p [μ Jy]	$+63.2 \pm 4.9$	
	$T_{c,e}$ [BJD T_{DB}] ^b	2453706.0595 ± 0.0014	

^aComputed from the posterior MCMC distributions of F_* and F_p/F_* .

^bJointly-fit ephemeris, assuming a period of 3.5247455 d (Torres et al. 2008).

3.6.3 Discussion

The three eclipse depths have a dispersion of 13%, consistent with our estimated measurement errors (12-18%). We thus find no evidence for variability of planetary emission, in good agreement with general circulation models which predict HD 209458b’s MIR dayside emission will vary by $< 5\%$ (e.g., Rauscher et al. 2008; Showman et al. 2009; Dobbs-Dixon et al. 2010) and consistent with the measurement that HD 189733b’s $8 \mu\text{m}$ dayside emission varies by $< 2.7\%$ (Agol et al. 2010). Our mean eclipse depth over all three epochs $-0.338\% \pm 0.026\%$ – is $\sim 1.3\sigma$ deeper than the initial measurement by Deming et al. (2005b) of $0.26\% \pm 0.046\%$. We convert this eclipse depth to a brightness temperature of $1320 \text{ K} \pm 80 \text{ K}$ using the method outlined in Sec. 2.4.4.

We plot the ensemble of HD 209458b’s secondary eclipse measurements in

Table 3.6. HD 209458b: Independent Eclipse Fits

Parameter	2004	2005	2008
c_0	0.00262 ± 0.00090	-0.00020 ± 0.00112	0.00044 ± 0.00264
c_1	0.00744 ± 0.00089	0.01028 ± 0.00124	0.01246 ± 0.00114
c_2	0.00500 ± 0.00169	0.00396 ± 0.00084	0.00449 ± 0.00106
c_3	0.00879 ± 0.00101	0.00879 ± 0.00077	0.00850 ± 0.00075
c_4	-0.00042 ± 0.00090	0.00198 ± 0.00111	0.00143 ± 0.00160
c_5	0.01090 ± 0.00104	0.01109 ± 0.00091	0.01392 ± 0.00115
c_6	-0.00488 ± 0.00106	-0.00502 ± 0.00109	-0.00351 ± 0.00120
c_7	-0.00453 ± 0.00138	-0.00331 ± 0.00284	-0.00561 ± 0.00086
c_8	-0.00248 ± 0.00109	-0.00078 ± 0.00089	-0.00249 ± 0.00105
c_9	-0.00230 ± 0.00082	-0.00239 ± 0.00142	-0.00744 ± 0.00073
c_{10}	0.00113 ± 0.00118	0.00086 ± 0.00093	0.00079 ± 0.00225
c_{11}	-0.00588 ± 0.00118	-0.01021 ± 0.00097	-0.01012 ± 0.00328
c_{12}	-0.00315 ± 0.00201	-0.00385 ± 0.00078	-0.00189 ± 0.00171
c_{13}	-0.01197 ± 0.00104	-0.01090 ± 0.00166	-0.01059 ± 0.00098
$T_{c,e}$ [BJD T_{DB}] ^a	2453346.5348 ± 0.0028	2453706.0600 ± 0.0029	2454675.3639 ± 0.0026
F_p/F_*	0.00325 ± 0.00053	0.00384 ± 0.00046	0.00281 ± 0.00051
T_B [K]	1270 ± 190	1450 ± 230	1130 ± 160
F_* [mJy]	18.7884 ± 0.0069	18.7023 ± 0.0064	18.6155 ± 0.0068
F_p [μ Jy]	61.1 ± 10.0	71.9 ± 8.6	52.3 ± 9.5

^aJointly-fit ephemeris, assuming a period of 3.5247455 d (Torres et al. 2008).

^bComputed from the posterior MCMC distributions of F_* and F_p/F_* .

Figure 3.9 along with a model of planet/star contrast ratio vs. wavelength. The modeling procedure is described in detail in Fortney et al. (2006) and Fortney et al. (2008). Using a stellar model for the incident flux and a solar metallicity atmosphere, we derive a radiative-convective pressure-temperature profile assuming chemical equilibrium mixing ratios. The model assumes no loss of absorbed energy to the night side, and redistribution of energy over the day side only (see Fortney et al. 2008). We show the pressure-temperature profile, which feature a temperature inversion due to the absorption of stellar flux by TiO and VO gasses, in Figure 3.8. Clearly a stronger temperature inversion is needed, as the contrast between the IRAC 3.6 and 4.5 μ m bands is not large enough. Since the 24 μ m photosphere is predicted to lie at 1 – 10 mbar on HD 209458b (Showman et al. 2009) our measurement indicates a somewhat cooler temperature than is expected for this planet given its atmospheric temperature inversion. The anoma-

lously low $24\ \mu\text{m}$ flux has been noted previously (e.g., [Madhusudhan & Seager 2010](#)); taken in concert with v And b’s large and still-unexplained $24\ \mu\text{m}$ phase offset (cf. [Sec. 2.4.4](#)) these results suggest that our current understanding of atmospheric opacity sources in this wavelength range may be incomplete. Alternatively, we can fit reasonably fit the 3.6, 8.0, and $24\ \mu\text{m}$ points with the dayside emission of the 3D general circulation model of [Showman et al. \(2009\)](#), which is cooler than the corresponding 1D model from [Fortney et al. \(2008\)](#). Clearly more work is needed to robustly fit the dayside photometry of the planet within the framework of a 1D or 3D self-consistent model.

We also fit a linear relation to the three eclipse times in the same manner as in [Sec. 3.5](#). We compute a period of 3.5247445 ± 0.0000097 d, which differs from the established period ([Torres et al. 2008](#)) by 0.99×10^{-6} d (0.086 s), well within the uncertainties. This value also agrees with our measurement of the period from the transit fits; the two periods differ by only 0.79 ± 0.94 s, which is (as expected) consistent with zero.

3.7 Joint Orbital Constraints and System Flux

3.7.1 Timing and Eccentricity: Still a Chance for Winds

Measuring the times of transit and secondary eclipse constrains the quantity $e \cos \omega$, where e is the planet’s orbital eccentricity and ω its longitude of periastron ([Seager 2011](#), chapter by J. Winn). We resample the posterior distributions of $T_{c,t}$ and $T_{c,e}$ from the fits shown in [Tables 3.2](#) and [3.5](#) and compute the difference between our transit and eclipse ephemerides (i.e., $[T_{c,e} - T_{c,t}] \bmod P - \frac{P}{2}$) to be 32 ± 129 s after also accounting for the 47 s light travel time from the planet’s location during eclipse to its location during transit ([Torres et al. 2008](#)). This

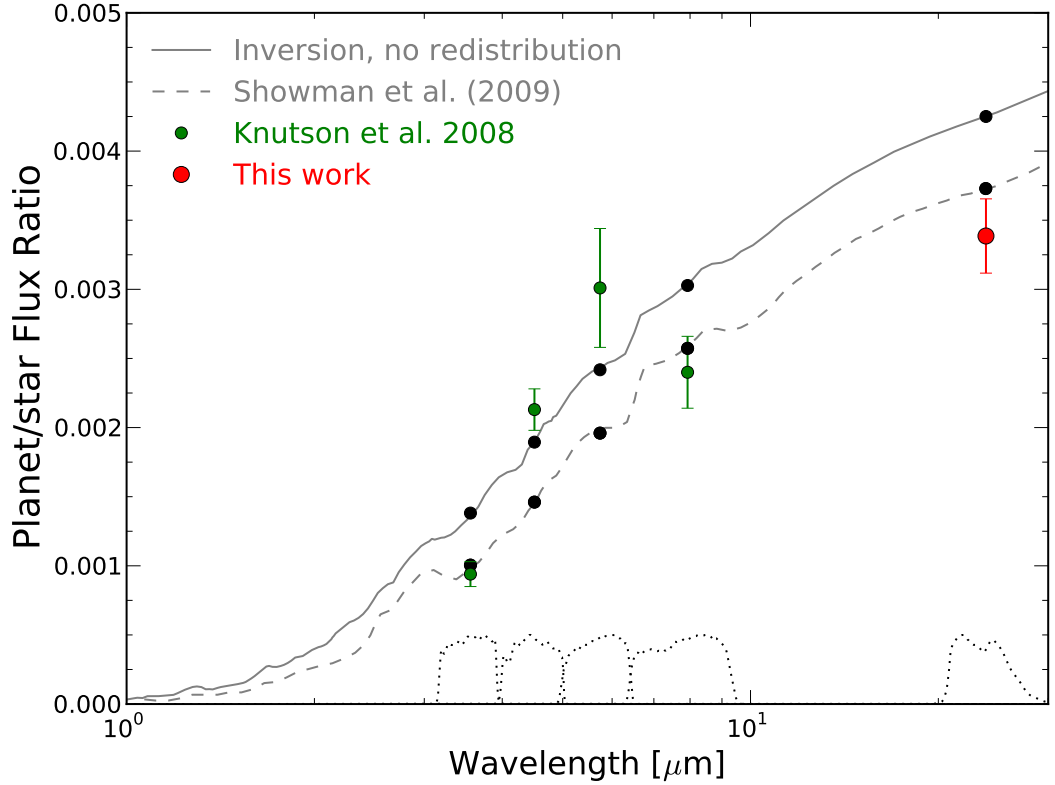


Figure 3.9 Measurements of the secondary eclipse depth of HD 209458b: previous Spitzer/IRAC photometry (Knutson et al. 2008) and our 24 μm measurement. The solid line is from a model assuming zero redistribution of incident flux and including gaseous TiO and VO to drive a temperature inversion; we show this model’s temperature-pressure profile in Figure 3.8. The dashed line is the emission spectrum from Showman et al. (2009). The solid black points without errorbars represent the weighted averages of the models over the corresponding bandpasses (indicated at bottom).

results constrains $e \cos \omega$ to be 0.00004 ± 0.00033 , consistent with zero and with previous constraints from radial velocity (Torres et al. 2008). We do not see the marginal timing offset previously reported (Knutson et al. 2008), which may have been biased by the higher level of correlated noise (due to the IRAC intrapixel effect) in the 3.6 and 4.5 μm IRAC data.

A measurement of $e \cos \omega$ directly constrains the apparent velocity offset that

can be induced in planetary absorption lines during transit (cf. [Montalto et al. 2011](#)); this provides an independent check as to whether the recent measurement of a velocity offset of $2 \pm 1 \text{ km s}^{-1}$ in HD 209458b ([Snellen et al. 2010](#)) can be attributed to a low, but nonzero, orbital eccentricity. Our timing measurements of HD 209458b set a 3σ upper limit on any velocity offset due to the planet’s orbital eccentricity of only $140 \text{ m s}^{-1}/\sqrt{1 - e^2}$. Thus the claimed velocity offset, though still of low significance, cannot be dismissed as resulting from the HD 209458b’s orbital eccentricity.

3.7.2 System Flux: No Excess Detected

Although our primary science results – the transit and eclipse depths – rely on relative flux measurements, our observations also allow us to measure absolute $24 \mu\text{m}$ photometry for the HD 209458 system. Our flux measurements for this system vary from epoch to epoch by much more than our quoted statistical uncertainties, but the variations are not large compared to the $\lesssim 1\%$ repeatability and 2% absolute calibration accuracy of the MIPS $24 \mu\text{m}$ array ([Engelbracht et al. 2007](#)). Our 21 pixel aperture encloses 99.2% of the starlight (as determined from our synthetic PSF), and we account for this small effect in the value quoted below.

We therefore report the $24 \mu\text{m}$ system flux as $18.7 \pm 0.4 \text{ mJy}$, consistent with the flux expected from the HD 209458 stellar photosphere (as reported by [Deming et al. 2005b](#)). HD 209458 was not detected by IRAS ([Beichman et al. 1988](#)), but is present in the Widefield Infrared Survey Explorer’s all-sky point source catalogue ([Wright et al. 2010](#)). The WISE photometry gives a W4 system flux of $25.74 \pm 0.12 \text{ mJy}$, which is higher than but marginally ($\sim 3\sigma$) consistent with the Spitzer-derived value after accounting for the different wavelengths of the

two instruments. We therefore conclude that HD 209458 does not have a strong $24\ \mu\text{m}$ infrared excess, as is typical of middle-aged F dwarfs (Moór et al. 2011).

3.8 Conclusions and Future Work

We have described a homogeneous analysis of all Spitzer MIPS observations of the hot Jupiter HD 209458b. The data comprise three eclipses, two and a half transits, and a long, continuous observation designed to observe the planet’s thermal phase curve; of these, analysis of two of the eclipses, one transit, and the phase curve observations have remained unpublished until now. The long-duration phase curve observation exhibits a detector ramp that appears similar to the ramp seen in Spitzer/IRAC $8\ \mu\text{m}$ photometry, and we model this effect using the exponential function proposed by Agol et al. (2010). We also see a $\sim -0.2\%$ flux decrease in the latter portion of the phase curve observations. This fallback is similar to a known (but poorly characterized) variation in the response of the MIPS detector when subjected to bright illumination (cf. Figure 3.2 and Young et al. 2003).

We are unable to determine why either the fallback or the ramp have not been seen in any prior MIPS observations. Despite this failure the correspondence between our photometry and the pre-launch array calibration data leads us to conclude that ramp and fallback are correlated and both are most likely of instrumental, rather than astrophysical, origin. This conclusion is strengthened by the result that fitting periodic phase functions to the data yields a planetary model hotter on its night side than its day side, strikingly at odds with theory (Rauscher et al. 2008; Showman et al. 2009; Dobbs-Dixon et al. 2010; Cowan & Agol 2011a) and inconsistent with other published observations of hot Jupiters (Harrington et al. 2006; Knutson et al. 2007a, 2009b, Ch. 2).

We see no evidence for variation in the three eclipse depths, and a joint fit of all three eclipses gives our best estimate of the $24\ \mu\text{m}$ planet/star contrast: $0.338\% \pm 0.026\%$. This value is more precise and higher than the previously published measurement (Deming et al. 2005b), and corresponds to an average dayside brightness temperature of $1320\ \text{K} \pm 80\ \text{K}$, consistent with models of this planet’s thermal atmospheric structure (Showman et al. 2009; Madhusudhan & Seager 2010; Moses et al. 2011). We note parenthetically that this new eclipse depth has already diffused into several papers (cf. Showman et al. 2009; Burrows et al. 2010; Madhusudhan & Seager 2009, 2010; Fortney et al. 2010; Moses et al. 2011); the value and uncertainty quoted in those works are close to those we report here, so their conclusions should be relatively unaffected.

We see no evidence for variations in our transit measurements, and a joint fit of our two and a half transits yields a $24\ \mu\text{m}$ transit depth of $1.484\% \pm 0.033\%$. The transit depth is less well-constrained than the eclipse depth because only half of the first transit was observed, and the last transit occurred during the detector ramp.

The ephemerides calculated from our analyses of the transits and eclipses allow us to compute orbital periods of 3.5247537 ± 0.0000049 d and 3.5247445 ± 0.0000097 d, respectively, which are consistent with but less precise than the orbital period of Torres et al. (2008). Eclipses occur 32 ± 129 s earlier than would be expected from a circular orbit, which constrains the orbital quantity $e \cos \omega$ to be 0.00004 ± 0.00033 . This suggests that HD 209458b’s inflated radius (larger than predicted by models of planetary interiors; Fortney et al. 2007) cannot be explained by interior heating from ongoing tidal circularization, and that the possible velocity offset reported by Snellen et al. (2010) cannot be explained by a nonzero orbital eccentricity.

Although we obtain improved estimates of the $24\ \mu\text{m}$ transit and secondary eclipse parameters, instrumental effects prevent a conclusive detection of the planet’s thermal phase curve. The phase curve signal is inextricably combined with the systematic fallback effect, despite estimates that the planet’s day/night contrast should be as large as a few parts per thousand (Showman et al. 2009). Such a large and intermittent systematic effect has profound implications for future mid-infrared exoplanet observations with EChO, SPICA, and JWST. Models of terrestrial planet phase curves predict phase amplitudes of $\lesssim 10^{-4}$ (Selsis et al. 2011; Maurin et al. 2012); such observations could be utterly confounded by the instrumental systematics seen in our observations, and so may be much more challenging than has been heretofore assumed (Kaltenegger & Traub 2009; Seager & Deming 2009). Although it may be possible to reduce the effect of the ramp with a pre-flash strategy similar to that adopted for the $8\ \mu\text{m}$ IRAC array, a further defense against these challenges would seem to be a more comprehensive campaign of array characterization. Specifically, a detailed characterization of the detector response to sustained levels of the high illumination expected from observations of terrestrial planets around the brightest nearby stars is highly desirable, and should be considered an essential requirement for all future infrared space telescopes.

CHAPTER 4

Tentative Emission from WASP-12b via Ground-based Spectroscopy

4.1 Abstract

We report the tentative detection of the near-infrared emission of the Hot Jupiter WASP-12b with the low-resolution prism on IRTF/SpeX. We find a $K - H$ contrast color of $0.137\% \pm 0.054\%$, corresponding to a blackbody of temperature 2400_{-500}^{+1500} K and consistent with previous, photometric observations. We also revisit WASP-12b's energy budget on the basis of secondary eclipse observations: the dayside luminosity is a relatively poorly constrained $(2.0 - 4.3) \times 10^{30}$ erg s⁻¹, but this still allows us to predict a day/night effective temperature contrast of 200 – 1,000 K (assuming $A_B = 0$). Thus we conclude that WASP-12b probably does not have both a low albedo and low recirculation efficiency. Our results show the promise and pitfalls of using single-slit spectrographs for characterization of extrasolar planet atmospheres, and we suggest future observing techniques and instruments which could lead to further progress. Limiting systematic effects include the use of a too-narrow slit on one night – which observers could avoid in the future – and chromatic slit losses (resulting from the variable size of the seeing disk) and variations in telluric transparency – which observers cannot control. Single-slit observations of the type we present remain the best option for obtaining

$\lambda > 1.7 \mu\text{m}$ spectra of transiting exoplanets in the brightest systems. Further and more precise spectroscopy is needed to better understand the atmospheric chemistry, structure, and energetics of this, and other, intensely irradiated planet.

4.2 Introduction

4.2.1 Ground-based Characterization of Exoplanet Atmospheres

Transiting extrasolar planets allow the exciting possibility of studying the intrinsic physical properties of these planets. The last several years have seen rapid strides in this direction, with measurements of precise masses and radii, detection of numerous secondary eclipses and phase curves, and the start of ground-based optical spectroscopy (Redfield et al. 2008; Snellen et al. 2008; Bean et al. 2010).

Though ground-based, near-infrared (NIR) photometry of exoplanets is becoming commonplace, until recently there were no successful detections via ground-based NIR spectroscopy (Brown et al. 2002; Richardson et al. 2003b; Deming et al. 2005a; Barnes et al. 2007; Knutson et al. 2007b). Several groups have employed high-resolution spectrographs with some form of template cross-correlation (Deming et al. 2005a; Snellen et al. 2010, Ch. 6) with varying degrees of success. Though cross-correlation provides a method to test for the detection of a particular model, it has the significant drawback that it does not provide a model-independent measurement. Furthermore, such observations require high-resolution cryogenic spectrographs on large-aperture telescopes.

The only published, model-independent, ground-based, NIR spectrum of an exoplanetary atmosphere (Swain et al. 2010) was obtained with a different approach: medium-resolution spectroscopy of HD 189733b with the 3 m NASA Infrared Telescope Facility (IRTF) covering the K and L bands. However, these

results are in dispute: the K band matches HST/NICMOS observations which have in turn been called into question (see [Swain et al. 2008](#); [Sing et al. 2009](#); [Gibson et al. 2011](#); [Deroo et al. 2010](#)), while the L band exhibits an extremely high flux peak attributed variously to non-LTE CH₄ emission ([Swain et al. 2010](#)) and to contamination by telluric water vapor ([Mandell et al. 2011](#)). In contrast, the tentative spectroscopic detection of WASP-12b we present in this paper reproduces previous, high S/N ground-based photometry ([Croll et al. 2011b](#)) and we demonstrate that our final result is not likely to be corrupted by telluric variations outside of well-defined spectral regions.

4.2.2 The WASP-12 System

The transiting Hot Jupiter WASP-12b has an orbital period of 1.1 days around its 6300 K host star, and the planet’s mass and radius give it a bulk density only 25% of Jupiter ([Hebb et al. 2009](#); [Chan et al. 2011](#)). The planet is one of the largest known and is significantly overinflated compared to standard interior models ([Fortney et al. 2007](#)). The planet is significantly distorted and may be undergoing Roche lobe overflow ([Li et al. 2010](#)), but tidal effects are not expected to be a significant energy source. Though the initial report suggested WASP-12b had a nonzero eccentricity, subsequent orbital characterization via timing of secondary eclipses ([Campo et al. 2011](#)) and further radial velocity measurements ([Husnoo et al. 2011](#)) suggest an eccentricity consistent with zero.

WASP-12b is intensely irradiated by its host star, making the planet one of the hottest known and giving it a favorable ($\gtrsim 10^{-3}$) NIR planet/star flux contrast ratio; it has quickly become one of the best-studied exoplanets. The planet’s large size, low density, and high temperature have motivated an ensemble of optical, ([López-Morales et al. 2010](#)), NIR ([Croll et al. 2011b](#)), and mid-infrared ([Campo](#)

[et al. 2011](#)) eclipse photometry which suggests this planet has an unusual carbon to oxygen (C/O) ratio greater than one ([Madhusudhan et al. 2011a](#)).

However, a wide range of fiducial atmospheric models fit WASP-12b’s photometric emission spectrum equally well despite differing significantly in atmospheric abundances and in their temperature-pressure profiles ([Madhusudhan et al. 2011a](#)). Many hot Jupiters appear to have high-altitude temperature inversions ([Knutson et al. 2010](#); [Madhusudhan & Seager 2010](#)), but even WASP-12b’s precise, well-sampled photometric spectrum does not constrain the presence or absence of such an inversion. Thus significant degeneracies remain; this is a common state of affairs in the field at present even for such relatively well-characterized systems ([Madhusudhan & Seager 2010](#)). This is because (a) broadband photometry averages over features caused by separate opacity sources and (b) atmospheric models have many more free parameters than there are observational constraints. Spectroscopy, properly calibrated, can break some of these degeneracies, test the interpretation of photometric observations at higher resolution, and ultimately has the potential to more precisely refine estimates of atmospheric abundances, constrain planetary temperature structures, and provide deeper insight into high-temperature exoplanetary atmospheres.

4.2.3 Outline

This paper presents our observations and analysis of two eclipses of WASP-12b in an attempt to detect and characterize the planet’s NIR emission spectrum. This is part of our ongoing effort to develop the methods necessary for robust, repeatable ground-based exoplanet spectroscopy, and we use many of the same techniques as those described subsequently in [Ch. 6](#).

We describe our spectroscopic observations and initial data reduction in [Sec-](#)

tion 4.3. The data exhibit substantial correlated variability, and we describe our measurements of various instrumental variations in Sec. 4.4. We fit a simple model that includes astrophysical, instrumental, and telluric effects to the data in Sec. 4.5. Chromatic slit losses (resulting from wavelength-dependent atmospheric dispersion and seeing) and telluric transmittance and radiance effects can confound ground-based NIR observations, so in Sec. 4.6 we investigate these systematic error sources in detail. We present our main result – a tentative detection of WASP-12b’s emission – in Sec. 4.7 and compare it to previous observations. Finally, we discuss the implications of our work for future ground-based, NIR spectroscopy in Sec. 4.8 and conclude in Sec. 4.9.

4.3 Observations and Initial Reduction

4.3.1 Summary of Observations

We observed the WASP-12 system with the SpeX near-infrared spectrograph (Rayner et al. 2003), mounted at the IRTF Cassegrain focus. Our observations during eclipses on 28 and 30 December 2009 (UT) comprise a total of 10.2 hours on target and 8.3 hours of integration time. We list the details of our observations and our instrumental setup in Table 4.1. One of our eclipses overlaps one of those observed by Croll et al. (2011b) with broadband photometry from the Canada-France-Hawaii Telescope (CFHT), also on Mauna Kea, on UT 27-29 December 2009. Our first night, 28 Dec, is the same night as their H band observation.

On both nights we observed the WASP-12 system continuously for as long as conditions permitted using SpeX’s low-resolution prism mode, which gives uninterrupted wavelength coverage from $< 1 - 2.5 \mu\text{m}$. We chose prism mode because it offers roughly twice the throughput of to SpeX’s echelle modes (Rayner et al.

Table 4.1. IRTF/SpeX Observations of WASP-12b

	2009 Dec 28	2010 Dec 30
UT date	2009 Dec 28	2010 Dec 30
Instrument Rotator Angle	225 deg	225 deg
Slit Position Angle	90 deg	90 deg
Slit	1.6" x 15"	3.0" x 15"
Grating	LowRes15	LowRes15
Guiding filter	J	K
OS filter	open	open
Dichroic	open	open
Integration Time (sec)	15	20
Non-destructive reads	4	4
Co-adds	2	2
Exposures	502	356 ^a
Airmass range	1.01 - 1.91	1.01 - 2.70 ^a
Wavelength coverage (μm)	< 1 - 2.5 μm	< 1 - 2.5 μm
WASP-12b phase coverage	0.42 - 0.61	0.41 - 0.61

^aWe limit the 30 Dec observations to airmass less than 2.326, which reduces the number of usable frames from 379 to 356.

2003, their Fig. 7), though it has a necessarily reduced capability to spectrally resolve, separate, and mitigate telluric features. We nodded the telescope along the slit to remove the sky background; as we discuss below, this induced substantial flux variations in our spectrophotometry at shorter wavelengths and we urge future exoplanet observers to eschew nodding at these wavelengths (the exception to this rule would be for instruments that suffer from time-varying scattered light, such as SpeX’s short-wavelength cross-dispersed mode). We deactivated the instrument’s field rotator to minimize instrumental flexure, but this meant the slit did not track the parallactic angle and atmospheric dispersion (coupled with variable seeing and telescope guiding errors) causes large-scale, time-dependent, chromatic gradients throughout the night. As we describe in Sec. 4.6.2 and 4.6.3, this effect is reduced (but not eliminated) by using a wider slit, and we strongly advise that future observations covering a large wavelength range (a) use as large a slit as possible and (b) keep the slit aligned to the parallactic angle.

On our first night, 28 Dec, we observed with the 1.6” slit to strike a balance between sky background and frame-to-frame variations in the amount of light entering the slit. After this run an initial analysis suggested we could further decrease spectrophotometric variability without incurring significant penalties from sky background, and so we used the 3.0” slit on the second night (30 Dec).

WASP-12 is sufficiently bright ($K=10.2$) that we were able to guide on the faint ghost reflected from the transmissive, CaF slit mask into the NIR slit-viewing guide camera. Guiding kept the K band relatively stationary but because SpeX covers such a wide wavelength range the spectra suffer from differential atmospheric refraction; this results in substantially larger motions over the course of the night at shorter wavelengths. We did not record guide camera frames, but we recommend that future observers save all such data to track guiding

errors, measure the morphology of the two-dimensional point spread function, and measure the amount of light falling outside the slit. Typical frames had maximum count rates of $\lesssim 2,000$ ADU $\text{pix}^{-1} \text{coadd}^{-1}$, safely within the 1024^2 Aladdin 3 InSb detector’s linear response range.

4.3.2 Initial Data Reduction

We reduce the raw echelleograms using the SpeXTool reduction package (Cushing et al. 2004), supplemented by our own set of Python analysis tools. SpeXTool dark-subtracts, flat-fields, and corrects the recorded data for detector nonlinearities, and we find it to be an altogether excellent reduction package that future instrument teams would do well to emulate. We used SpeXTool in optimal “A–B” point source extraction mode with extraction and aperture radii of $2.5''$, inner and outer background aperture radii of $2.8''$ and $3.5''$, respectively, and a linear polynomial to fit and remove the residual background in each column.

The extracted spectra have peak H and K band fluxes of roughly 5500 and 2000 $e^- \text{pix}^{-1} \text{s}^{-1}$, respectively. After removing observations rendered unusable for telescope or instrumental reasons (e.g., loss of guiding or server crashes), we are left with 502 and 356 usable frames from our two nights. The extracted spectra are shown in Fig. 4.1 and substantial variations are apparent; we discuss these in Sec. 4.4.

SpeX typically uses a set of arc lamps for wavelength calibration, but SpeXTool fails to process arcs taken with the $3''$ slit in prism mode. Instead, we calculate wavelength solutions by matching observed telluric absorption features with an empirical high-resolution telluric absorption spectrum (Hinkle et al. 2003) convolved to the approximate spectral resolution of our observations. We estimate a precision of 1.7 nm for the individual line positions and use this uncertainty to

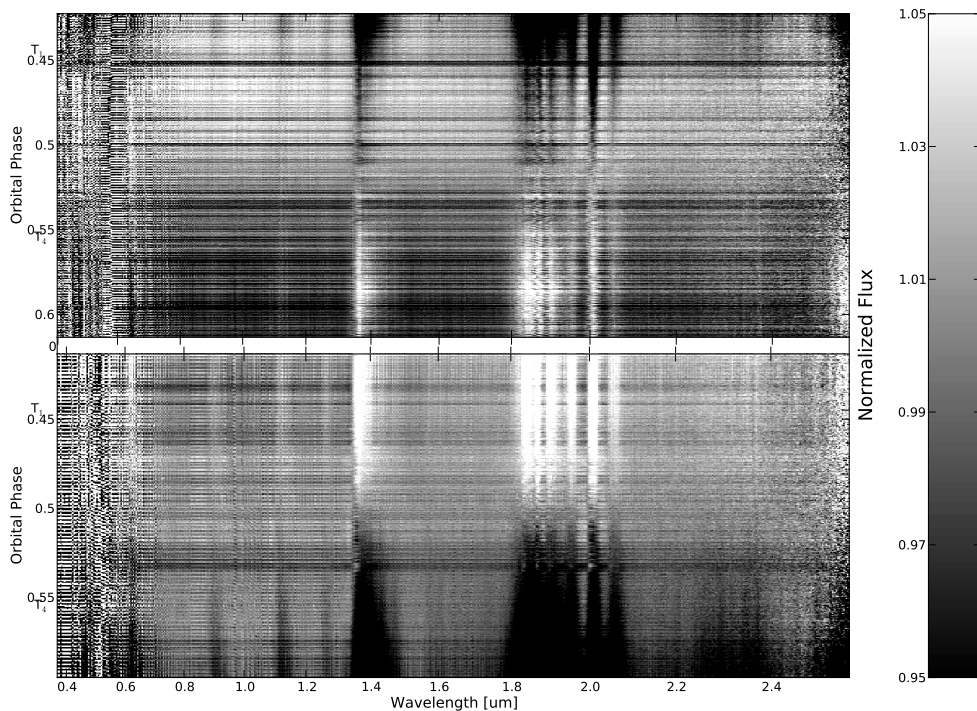


Figure 4.1 Spectrophotometric data for the nights of 28 Dec 2009 (*top*) and 30 Dec 2009 (*bottom*); each column has been normalized by its median value. The variations (due to a combination of airmass effects and instrumental slit loss) are largely common mode; variations are less on 30 Dec, probably because of the wider slit used then. The first (T_1) and fourth (T_4) points of contact of the eclipse are indicated, as calculated from the ephemeris of [Hebb et al. \(2009\)](#).

calculate the χ^2 and Bayesian Information Criterion¹ (BIC) for fits using successively higher degrees of polynomials: for both nights a fourth-order polynomial gives the lowest BIC, indicating this to be the preferred model. The RMS of the residuals to these fits are 1.3 and 1.6 nm for 28 Dec and 30 Dec, respectively, while maximum residuals for each night are 3.1 nm (at $2.35 \mu\text{m}$) and 2.9 nm (at 1.3, 1.85, and $2.32 \mu\text{m}$), respectively.

¹Bayesian Information Criterion (BIC) = $\chi^2 + k \ln N$, where k is the number of free parameters and N the number of data points.

Our wavelength solutions for 28 and 30 Dec are respectively

$$\begin{aligned}\lambda_{28}(p)/\mu m &= 6.77626638 \times 10^{-12}p^4 - 9.82847002 \times 10^{-9}p^3 + \\ &2.52383166 \times 10^{-6}p^2 + 4.26945216 \times 10^{-3}p + \\ &0.414989079\end{aligned}$$

and

$$\begin{aligned}\lambda_{30}(p)/\mu m &= 4.85652782 \times 10^{-12}p^4 - 6.49601098 \times 10^{-9}p^3 + \\ &4.97530220 \times 10^{-7}p^2 + 4.78270230 \times 10^{-3}p + \\ &0.371045967\end{aligned}$$

where p is the pixel number, an integer from 0 to 563, inclusive. We apply these wavelength solutions to all our spectra after shifting them to a common reference frame using the shift-and-fit technique described by [Deming et al. \(2005a\)](#) and implemented in [Sec. 6.4.3](#).

4.4 Characterization of Systematic Effects

4.4.1 Instrumental Sources

The initially extracted spectra shown in [Fig. 4.1](#) exhibit temporal variations due to a combination of telluric, instrumental, and astrophysical sources, with the last of these the weakest of the three effects. We wish to quantify and remove the instrumental and telluric effects to the extent that we can convincingly detect any astrophysical signature – i.e., a secondary eclipse. The strongest variations in [Fig. 4.1](#) are largely common-mode (i.e., they appear in all wavelength channels)

and are due to variations in light coupled into the spectrograph due to changes in seeing, pointing, and/or telluric transparency. Longer-term telluric variations are distinguishable by the manner in which they increase in severity in regions of known telluric absorption.

We approximate the amount of light coupled into the spectrograph slit by measuring the flux in regions clear of strong telluric absorption, as determined using our high-resolution telluric absorption spectrum (Hinkle et al. 2003) convolved to our approximate resolution. The flux in these channels should only depend on the frame-to-frame changes in starlight entering the spectrograph slit, which in turn depends on the (temperature- and pressure-dependent) atmospheric dispersion, the (wavelength-dependent) size and shape of the instrumental response, telescope guiding errors, and achromatic changes in telluric transparency. In the interests of simplicity we initially treat this as a wavelength-independent quantity; we return to address the validity and limitations of this assumption in Sec. 4.6.2.

At each time step we sum the flux in these telluric-free parts of each spectrum, creating a time series representative of the achromatic slit losses suffered by the instrument. Although we refer to this quantity as the slit loss, it is actually a combination of instrumental slit losses (spillover) and changing atmospheric transmission. The achromatic slit loss time series is plotted for each night in Figs. 4.2 and 4.3, along with other candidate systematic sources described below. We ultimately compute this quantity by summing the flux between $1.63\text{--}1.73\ \mu\text{m}$ and $2.10\text{--}2.21\ \mu\text{m}$, spectral regions we show in Sec. 4.6.1 to be mostly free of telluric contamination.

SpeX is a large instrument and is mounted at the IRTF's Cassegrain focus, where its spectra can exhibit several pixels of flexure due to changing gravity vector; similarly, atmospheric dispersion (Filippenko 1982) introduces many pix-

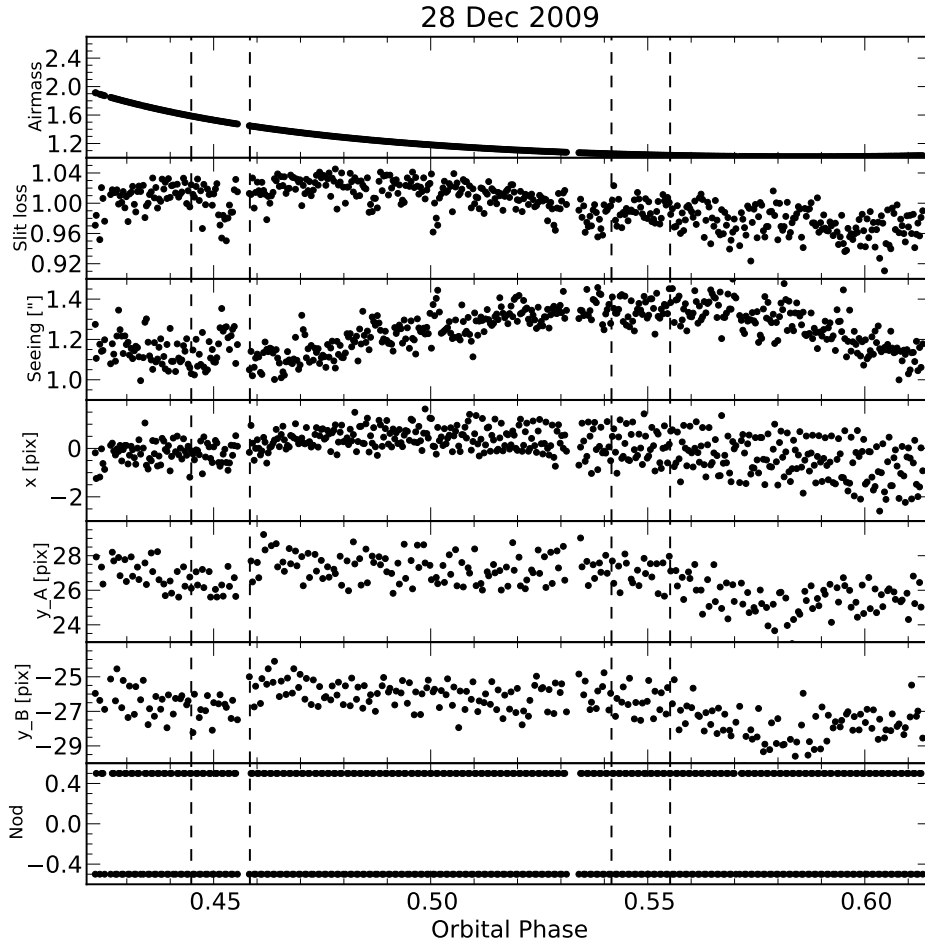


Figure 4.2 The observable quantities (described in Sec. 4.3.2) measured during the course of our observations on 28 Dec 2009. As described in the text, we ultimately detrend our observations with a combination the airmass reported by the telescope control system and the nod position vector. As noted in the text we measure the seeing FWHM and y position as a function of wavelength, but here we plot only the approximate K-band values of these quantities. The dashed lines indicate the four points of contact of the eclipse as calculated from the ephemeris of Hebb et al. (2009).

els of motion at shorter wavelengths (because we keep the star in the slit by guiding at K band). Apparent spectrophotometric variations can be induced by such instrumental changes (e.g., Knutson et al. 2007b, Paper I). We measure the motion of the spectral profiles in the raw frames perpendicular to (x) and par-

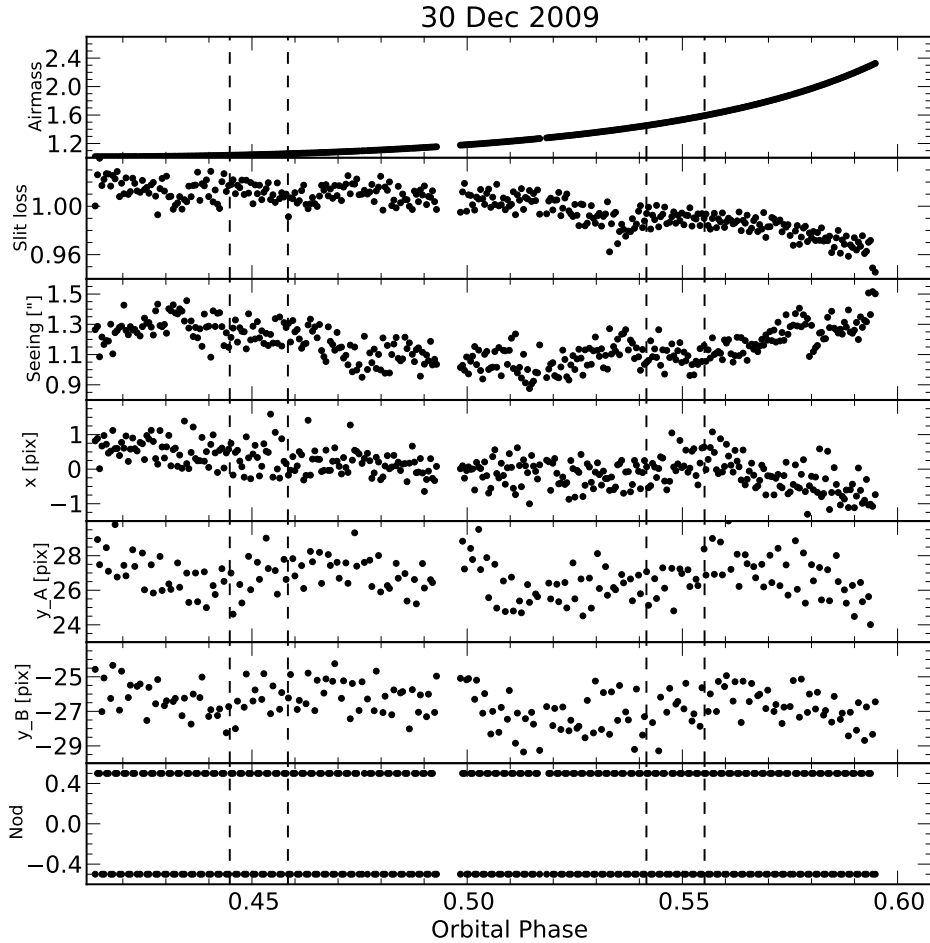


Figure 4.3 Same as Fig. 4.2, but for the night of 30 Dec 2009.

allel to (y) the long axis of the spectrograph slit as follows. We compute the x motion of the star on the slit while aligning the spectra to a common reference frame as described in Sec. 4.3.2 above. For y we fit Gaussian profiles to the raw spectral traces, then fit a low-order polynomial to the measured positions in each frame. The x and y motions are typically 2-4 pixels in K band and are plotted for both nights in Figs. 4.2 and 4.3. An independent method to measure the x and y motions would be to use images recorded by SpeX’s slit-viewing camera: since the slit is slightly reflective one would then be able to measure directly the

star’s position on the slit at the guiding wavelength. We recommend observers investigate this approach in the future.

We measure the full-width at half maximum (FWHM) of the spectral profiles during the spectral fitting and tracing described above. Again, we fit a low-order polynomial to the measured values to smoothly interpolate the compute values. The value we measure (which does not scale as $\lambda^{-1/5}$ as would be expected from atmospheric Kolmogorov turbulence; [Quirrenbach 2000](#)) presumably depends on a combination of atmospheric conditions, instrumental focus, and pointing jitter during an exposure, but we hereafter refer to it merely as seeing.

Previous studies ([Deming et al. 2005a](#), Ch. 6) report that an empirical measure of atmospheric absorption is preferable to the calculated airmass value when accounting for telluric extinction. We measured the flux in a number of telluric absorption lines for the species CO₂, CH₄, and H₂O in a manner similar to that in Sec. 6.4.3. However, in our empirical airmass terms we still see substantial contamination from both slit losses and A/B nodding, and so in our final analysis we use the airmass values reported by the telescope control system and plotted in Figs. 4.2 and 4.3.

4.4.2 Slit Loss Effects

Absolute spectrophotometry is difficult with narrow slits because guiding errors, seeing variations, and (when the slit is not aligned to the parallactic angle) atmospheric dispersion, all result in a time-varying amount of starlight coupled into the spectrograph slit (e.g., [Knutson et al. 2007b](#), Secs. 6.4.3 and 6.5.1). After extracting the spectra, our next step is to remove the large-scale flux variations present in the data.

As described in Sec. 4.6.2 we try to empirically calibrate the amount of light

entering the spectrograph slit. Despite considerable effort, we are only able to qualitatively match the variability in our observations. This could be because the PSF morphology (and especially the wavelength-dependent flux ratio between the core and wings) cannot be accurately modeled using a simple Gaussian function (perhaps due to alignment errors within SpeX and/or guiding errors), because our implementation of the simplified formulation of [Green \(1985\)](#) does not reflect reality with sufficient fidelity, or because variations due to telluric sources overwhelm those due to instrumental effects. An independent test could be performed in future efforts by recording images from the slit-viewing camera and directly measuring the light not entering the slit, the shape of the PSF, and its position.

Instead, following [Sec. 6.4.4](#) we divide the flux in every wavelength channel by a wavelength-independent slit loss time series. This step removes the absolute eclipse depth (the mean depth over the slit loss wavelength range) from all spectral channels, but the overall shape of the emission spectrum should remain the same. However, the quality of this correction will degrade rapidly at shorter wavelengths because air's refractive index increases rapidly at shorter wavelength. Especially with a narrow slit (as during our 28 Dec observations) or at high airmass (as on 30 Dec), this can cause a greater proportion of the short-wavelength flux to fall outside the slit. Nonetheless, we are unwilling to venture beyond removal of this simple achromatic trend, given our inability to accurately model the chromatic slit loss component.

Dividing the data by this time series substantially reduces the variability in regions clear of telluric absorption, as shown in [Figs. 4.4, 4.5, and 4.6](#). Note however that some correlated variability remains even after this correction step, as seen for example near orbital phase 0.45 on 28 Dec ([Figs. 4.4 and 4.5](#)). These residual variations are wavelength-dependent, and support our conclusion that

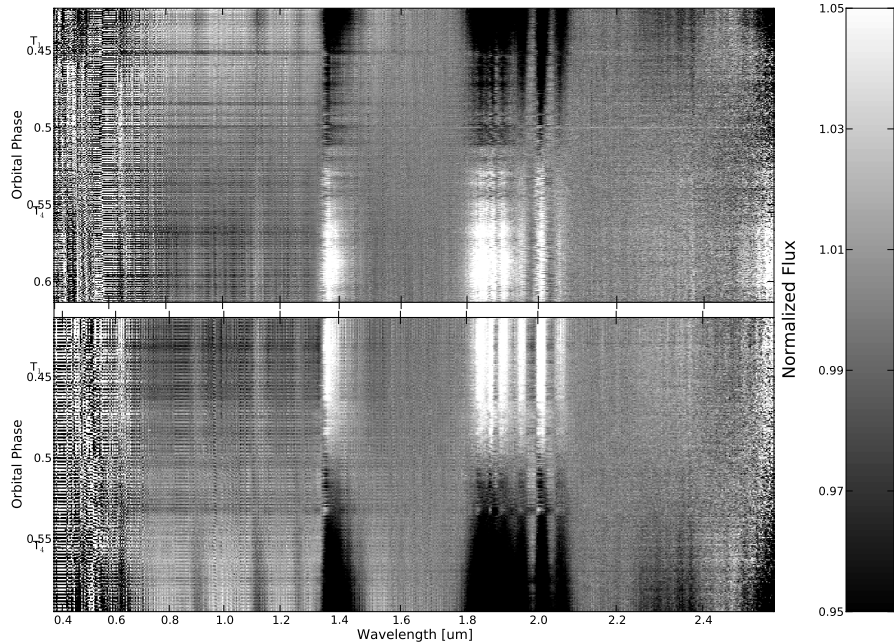


Figure 4.4 Spectrophotometric data for the nights of 28 Dec (*top*) and 30 Dec (*bottom*) after dividing all wavelength channels by the achromatic slit loss time series and normalized by the median flux in each wavelength channel. Still no eclipse is visible because dividing by the achromatic slit loss term has removed the mean eclipse signal from all wavelength channels, but variations have been strongly suppressed. The first (T_1) and fourth (T_4) points of contact of the eclipse are noted, as calculated from the ephemeris of [Hebb et al. \(2009\)](#).

chromatic slit losses are affecting our data. Wider slits should reduce this effect, and indeed such chromatic residuals are reduced by a factor of ~ 2 on 30 Dec (see Fig. 4.4), when we used the wider slit.

Our simple correction reveals a residual sawtooth-like pattern in the photometry in phase with the A/B nodding and especially prominent at shorter wavelengths ($< 1.4 \mu\text{m}$), as seen in Figs. 4.4, 4.5, and 4.6. The sawtooth has been previously noted with SpeX in echelle mode ([Swain et al. 2010](#)) and presumably results from an imperfect flat-field correction of the differential sensitivity be-

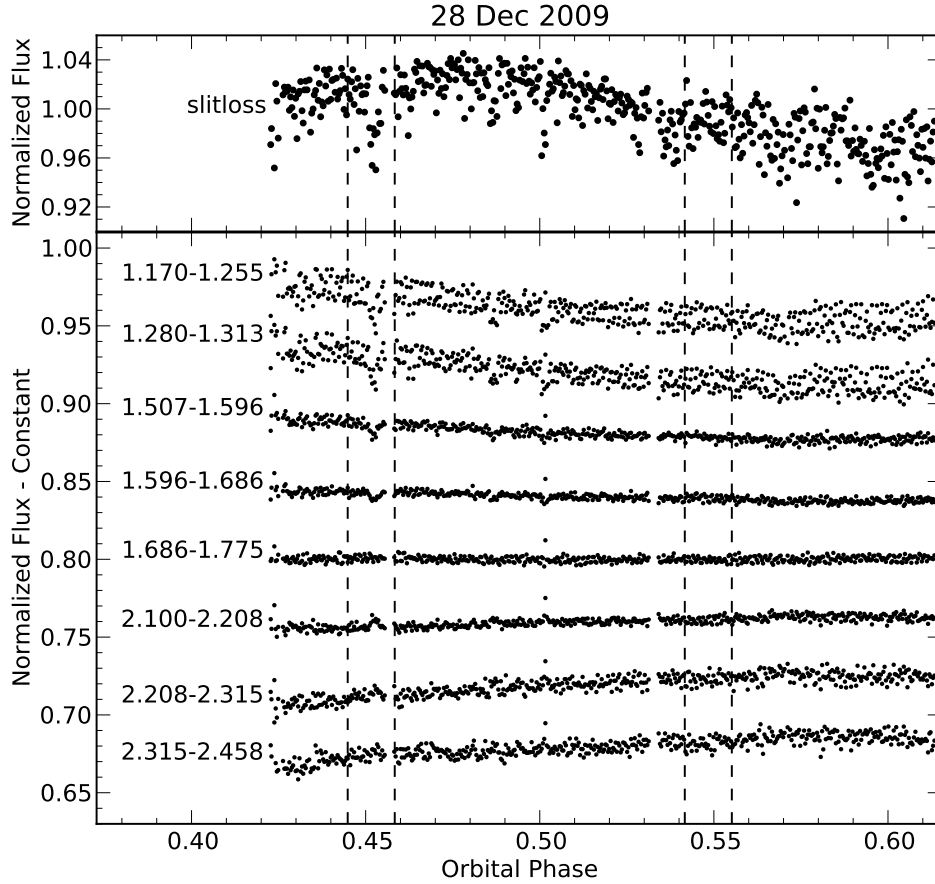


Figure 4.5 Several representative spectrophotometric time series for 28 Dec. The top panel shows the relative flux coupled into the spectrograph slit, as measured in regions free of deep telluric absorption lines; telluric continuum absorption, seeing variations, and guiding errors combine to produce large variations, wholly masking the $\lesssim 0.3\%$ eclipse signature. The bottom panel shows time series for several different wavelength ranges, after removal of the common mode slit loss term and binned over the wavelength range listed (in μm). The eclipse is still not visible because dividing out the common-mode slit loss term removes the mean eclipse signal from all the data. Dashed lines are as in the previous figures.

tween the two nod positions on the detector. We fit the data at both positions simultaneously by including a vector equal to 0.5 at the A nods and -0.5 at the B nods in our set of potential systematic-inducing observables (as described

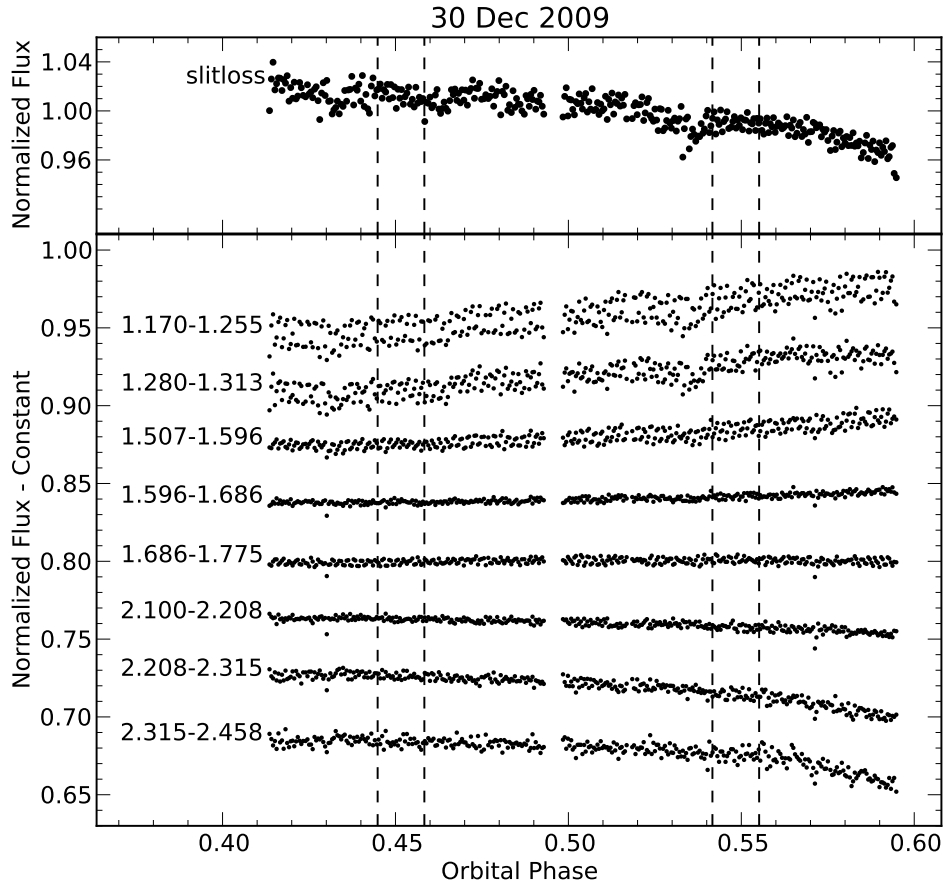


Figure 4.6 Same as Fig. 4.5, but for the night of 30 Dec. Note that these data are less noisy than those shown in the previous figure, probably because of the different slit sizes used.

in Sec. 4.5 below). That the sawtooth is stronger at shorter wavelengths may indicate that the fidelity of the SpeX internal flat fields is wavelength-dependent. Since in any case the eclipse signal is stronger at longer wavelengths (Croll et al. 2011b), and because the shorter-wavelength regions experience larger motions on the detector due to atmospheric refraction and larger systematic biases due to chromatic slit losses (described in Sec. 4.6.2), we ultimately discard the shortest-wavelength data.

4.5 Searching for the Eclipse Spectrum

4.5.1 Fitting to the Data

As noted previously, without external calibration we cannot accurately recover the absolute eclipse depth from the telluric-contaminated spectrophotometry. Instead, we self-calibrate as described in Sec. 4.4.2 above by dividing out a common time series, thereby largely removing systematic effects (such as variable slit loss); information about the absolute eclipse depth is lost, but the shape of the spectrum is largely unchanged (note however that systematic effects remain that will influence the extracted planetary spectrum; we quantify these effects in Sec. 4.6 below). We are then better able to look for the eclipse signature as a differential effect while relying on the precise NIR photometric eclipse depths (Croll et al. 2011b) to place our measurements on an absolute scale. However, even after removing the common-mode time series the eclipse signal is still masked by the photometric sawtooth, airmass dependencies, and general photometric noise.

We cannot use cross-correlation techniques (Deming et al. 2005a; Snellen et al. 2010, Sec. 6.5) in this analysis because of our low resolution. We investigated the use of the Fourier-based self-coherence spectrum technique (Swain et al. 2010) but did not find it to remove correlated variability or to otherwise improve the quality of our data. Instead, we follow Sec. 6.5.1 and search for differential eclipse signatures in our data by fitting a model that includes telluric, systematic, and eclipse effects to the slit loss-corrected time series in each wavelength channel; this approach also has the advantage of allowing an estimate of the covariances of the various determined parameters.

We fit each spectral time series (i.e., the flux in each wavelength bin) with the following relation, representing an eclipse light curve affected by systematic

and telluric effects:

$$F_i^\lambda = f_0^\lambda \left(e^{b^\lambda a_i} \right) (1 + d^\lambda \ell_i) \left(1 + \sum_{j=1}^J c_j^\lambda v_{ij} \right) \quad (4.1)$$

The symbols are: F_i^λ , the slit loss-corrected flux measured at timestep i in wavelength bin λ ; f_0^λ , the total (star plus planet day side) flux that would be measured above the Earth’s atmosphere; a_i , the airmass, which is modulated by the coefficient b^λ , an airmass-like extinction coefficient in which the airmass is proportional to the log of observed flux; ℓ_i , the flux in an eclipse light curve scaled to equal zero out of eclipse and -1 inside eclipse; d^λ , a scale parameter equal to the relative depth of eclipse; v_{ij} , the J state vectors (e.g., nod position, x_i or y_i) expected to have a small, linearly perturbative effect on the instrumental sensitivity; and c_j^λ , the coefficients for each state vector. To account for and remove the effect of any slow drifts we also tried including low-order Chebychev polynomials in orbital phase in the set of state vectors, but these did not improve our results. We thus obtain the set of coefficients $(f_0^\lambda, d^\lambda, c_j^\lambda)$ from our full set of observations; the d^λ represent our measured emission spectrum.

To fix the parameters of our model eclipse light curve we compared the orbital ephemerides from several different sources (Hebb et al. 2009; Campo et al. 2011; Croll et al. 2011b; Chan et al. 2011) and found them all to be consistent to within 1-2 minutes at our observational epoch, an uncertainty insignificant given the noise in our data and our sampling rates. We therefore use the parameters from Hebb et al. (2009), which we compute using our Python implementation² of the uniform-disk formulae of Mandel & Agol (2002).

²Available from the primary author’s website; currently <http://astro.ucla.edu/~ianc/python/transit.html>

4.5.2 Choice of Model

As in Sec. 6.5.1, we fit the data sets using many different combinations of state vectors and slit loss time series and use the BIC to choose which of these many models best fit our data. Calculating the BIC for each set of parameters involves computing χ^2 for each time series, which in turn requires us to assign uncertainties to each data point. We estimate the uncertainties as follows. We initially compute unweighted fits of Eq. 4.1 to the data using a multivariate minimization provided in the SciPy³ software distribution (the function `optimize.leastsq`). Decorrelating using only the A/B nod position and airmass calculated from the telescope’s zenith angle, we fit and compute the residuals for each time series. We scale the uncertainties in each time series such that the χ^2 in each wavelength channel equals unity. For each combination of state vectors we then compute another, weighted, fit and its associated χ^2 and BIC. Although this method of estimating uncertainties likely underestimates absolute parameter uncertainties (Andrae 2010, and see Sec. 4.5.3 below), we feel it still allows us to compute useful qualitative estimates of the relative merit of various models.

Our modeling approach is most successful in spectral regions largely clear of telluric absorption, which suggests telluric absorbers may be one of the primary factors limiting our analysis (as confirmed in Sec. 4.6.1 and 4.6.3). When restricting our analysis to the BIC values computed in regions largely clear of strong telluric effects (1.52 – 1.72 μm and 2.08 – 2.34 μm), the instrumental models which give the lowest BIC for our data use a slit loss term computed using telluric-free spectral regions in the H band, the airmass values reported by the telescope control system, and two state vectors: the A/B nod position and an airmass-corrected, mean-subtracted copy of the slit loss term. The BIC values

³Available at <http://www.scipy.org/>.

do not change significantly when we use slightly different wavelength ranges.

Although including these two decorrelation vectors appears warranted on statistical grounds, our modeling efforts (discussed in Sec. 4.6.3) demonstrate that decorrelating against the slit loss time series in the light curve fits systematically biases the extracted planetary spectrum. Because the slit loss effects removed by including this vector are chromatic, the coefficient associated with this vector increases at shorter wavelengths. Since our achromatic slit loss vector is not wholly orthogonal to the model eclipse light curve, as the slit loss vector’s amplitude increases the eclipse depth tries to compensate, and the extracted spectrum is corrupted. Our modeling of the 30 Dec observations (when the 3.0” slit was used) indicates that for these data this bias would mainly affect $\lambda < 1.4 \mu m$, but the bias is stronger for the 28 Dec data (when the 1.6” slit was used) and significantly affects the H band as well. Thus we again emphasize that similar observations in the future should use as large a slit as possible, and should guide at the parallactic angle, in order to mitigate the biases introduced by chromatic slit loss. For these reasons we include only the A/B nod vector in our list of decorrelation vectors

4.5.3 Estimating Coefficient Uncertainties

We assess the statistical uncertainties on the computed planetary spectra using several techniques. First, we fit to the data in each of the 564 wavelength channels as described above and compute the mean and standard deviation of the mean (SDOM) of the parameters in wavelength bins of specified width. The SDOM provides a measure of the purely statistical variations present in the planetary spectra.

After summing the data into wavelength channels 25 nm wide (to ease the

computational burden) we run both Markov Chain Monte Carlo (MCMC) and prayer bead (or residual permutation; [Gillon et al. 2007](#)) analyses for each time series. Since MCMC requires an estimate of the measurement uncertainties, we follow our earlier approach of setting the uncertainties in each wavelength channel such that the resultant χ^2 value equals unity. The residual permutation method fits multiple synthetic data sets constructed from the best-fit model and permutations of the residuals to that fit, and it is similar to bootstrapping but has the advantage of preserving correlated noise.

The posterior distributions of eclipse depth that result from the MCMC analysis are all much narrower than the uncertainties estimated from both the SDOM and from the prayer bead analysis. This suggests that artificially requiring that χ^2 equal unity has led to underestimated parameter uncertainties (cf. [Andrae 2010](#)). The prayer bead and SDOM uncertainties are comparable in magnitude, and to be conservative we use the larger of these two uncertainties in each wavelength bin as our statistical uncertainty.

Because we expect systematic uncertainties to play a large role in our data, in the following section we now pause to examine possible sources of bias and their impact on our planetary spectra.

4.6 Systematic Errors in High-Precision Single-Slit Spectroscopy

Our analysis is hampered by systematic biases arising from several sources. We discuss telluric contamination arising from variable transmittance and/or radiance (which affects only certain wavelength ranges) in [Sec. 4.6.1](#). In [Sec. 4.6.2](#) we discuss chromatic slit losses, which result from wavelength-dependent seeing and

atmospheric dispersion; this introduces a smoothly varying bias across the entire spectrum, increasing in severity toward shorter wavelengths. Then we combine these effects in Sec. 4.6.3 and use all available information to simulate our observations. Applying our standard reduction to these simulations demonstrates that we can hope to successfully recover a planetary signal within certain well-defined spectral regions.

4.6.1 Telluric Contamination

Increased levels of precipitable water vapor (PWV) lead to increased telluric emittance and decreased transmittance. If unaccounted for, such variations can mimic and/or contaminate the desired eclipse spectrum (Mandell et al. 2011, but see also Waldmann et al. 2012). The claim of a strong ground-based L band detection of HD 189733b in eclipse (Swain et al. 2010) was challenged partially by an appeal to changes in telluric water content (Mandell et al. 2011), so we investigate these effects in our observations.

As can be seen in Fig. 4.7, the 28 Dec eclipse spectrum is strongly biased toward larger eclipse depths in regions of greater telluric absorption. This does not seem to be the case for the 30 Dec results (cf. Fig. 4.8), in which we see variability (but no net deflection of the spectrum) in regions of high telluric absorption. This behavior suggests that our data are compromised by telluric effects in these wavelength ranges, and the regions of greatest spectral deflection suggest telluric water vapor is the prime culprit.

Telluric water content is measured on Mauna Kea by the 350 μm tipping photometer at the Caltech Submillimeter Observatory⁴. We convert its 350 μm

⁴Data taken from <http://ulu.submm.caltech.edu/csotau/2tau.pl>

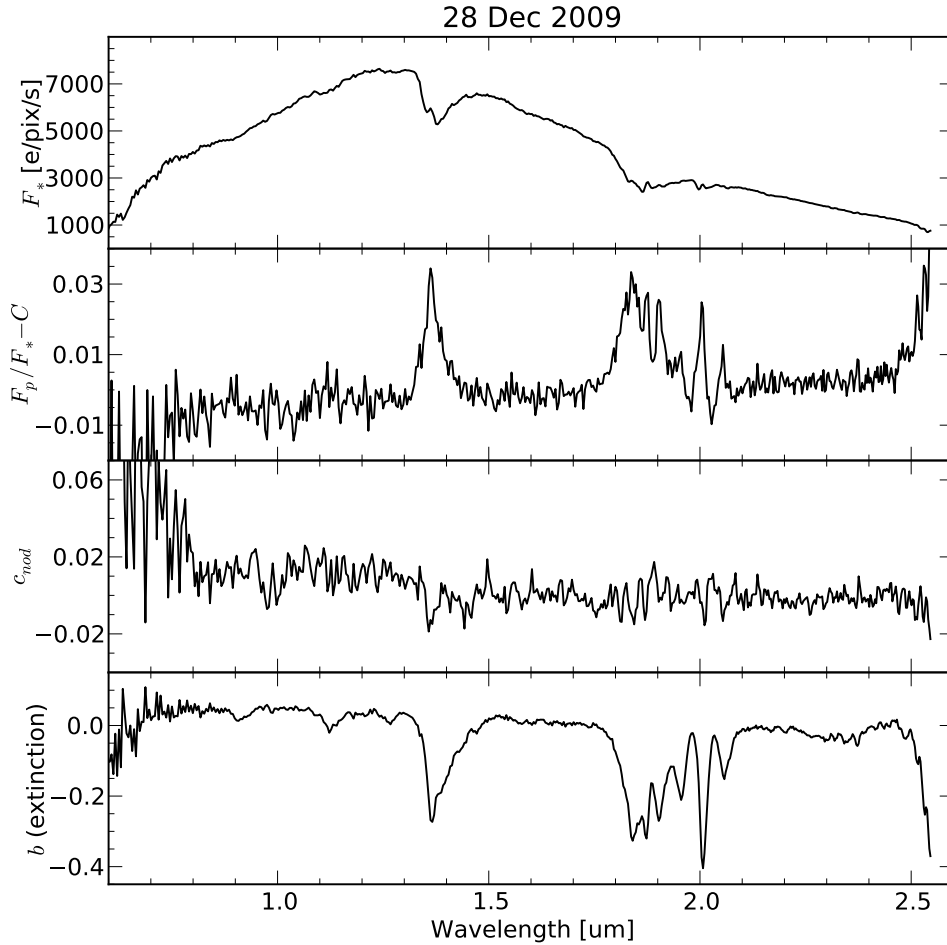


Figure 4.7 Best-fit coefficients from fitting Eq. 4.1 to the slit loss-corrected 28 Dec observations shown in Fig. 4.4. From top to bottom: stellar flux, eclipse depth, A/B nod sensitivity coefficient, and telluric extinction coefficient. Refer to Sec. 4.5 for a description of the fitting process.

opacity measurements to PWV using the relation from [Smith et al. \(2001\)](#):

$$PWV = 20(\tau_{350}/23 - 0.016) \text{ mm} \quad (4.2)$$

The PWV values for the two nights we observed are plotted in Fig. 4.9. Although the PWV along the telescope’s line of sight will scale with airmass, because our fitting approach removes airmass-correlated trends we consider only the water

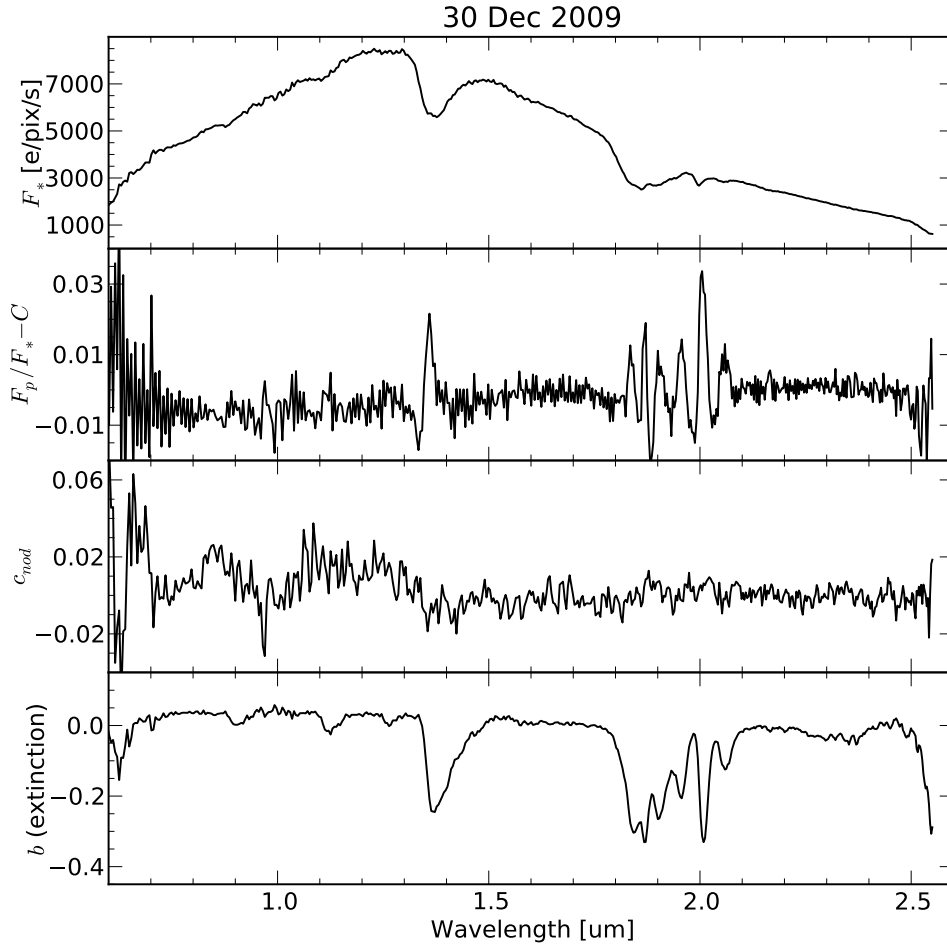


Figure 4.8 Same as Fig. 4.7, but for the night of 30 Dec.

burden at zenith. On 28 Dec the mean PWV values in and out of eclipse were 0.64 and 0.60 mm, respectively; on 30 Dec these values were 0.68 and 0.70 mm, respectively.

We used two independent telluric modeling codes, ATRAN (Lord 1992) and LBLRTM⁵ (Version 12.0; Clough et al. 2005), to generate NIR telluric spectra for the in- and out-of-eclipse PWV values; all spectra were computed using

⁵Run using MATLAB scripts made publicly available by D. Feldman and available at <http://www.mathworks.com/matlabcentral/fileexchange/6461-lblrtm-wrapper-version-0-2>

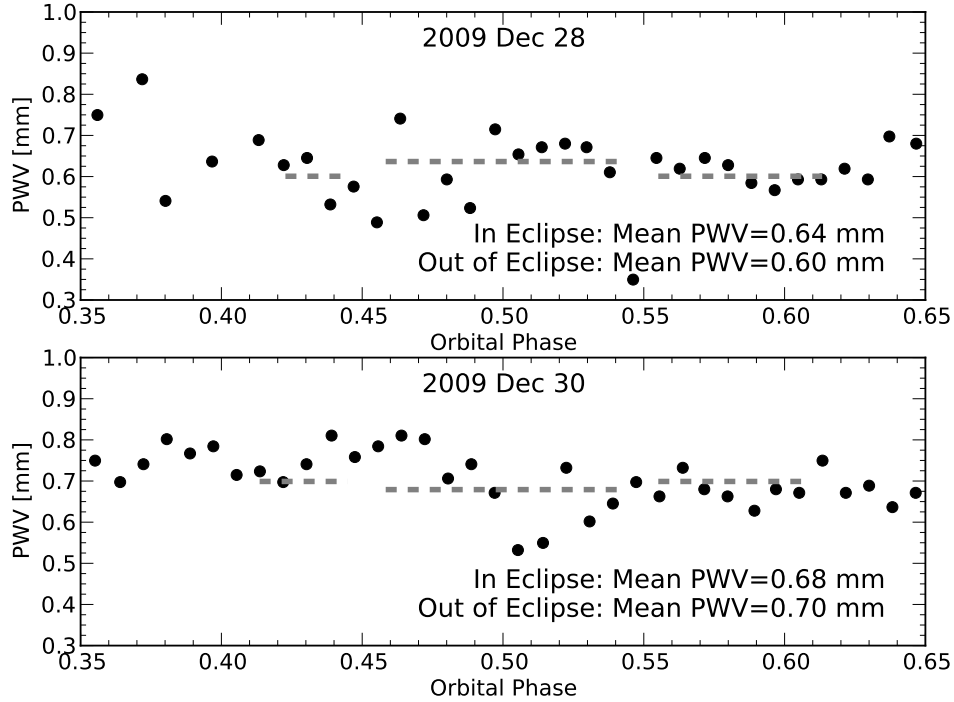


Figure 4.9 Telluric water content during our observations, as measured by the $350\ \mu\text{m}$ tipping photometer at the Caltech Submillimeter Observatory. The dashed lines represent the mean PWV values in and out of eclipse on each of the two nights, and also indicate the start and end of each nights' observations.

an airmass of unity. ATRAN simulates atmospheric transmission only, while LBLRTM simulates both transmission and emission. The apparent eclipse signal induced by transmission changes is $\Delta\text{Tran} = (t_{out} - t_{in})/t_{out}$, where t_{in} and t_{out} are the in- and out-of-eclipse transmission spectra; the radiance-induced signal is $\Delta\text{Rad} = \Omega(s_{out} - s_{in})/(s_* + \Omega s_{out})$, where s_{in} and s_{out} are the sky radiance spectra in and out of eclipse, s_* is the incident stellar flux, and Ω is the solid angle on the sky of the effective spectral extraction aperture. We validated our models against the study of [Mandell et al. \(2011\)](#) and match their results to within 15%, which we deem an acceptable match given the large number of user-specified parameters in such simulations. While we thus confirm that the $3 - 3.5\ \mu\text{m}$ L band spectrum

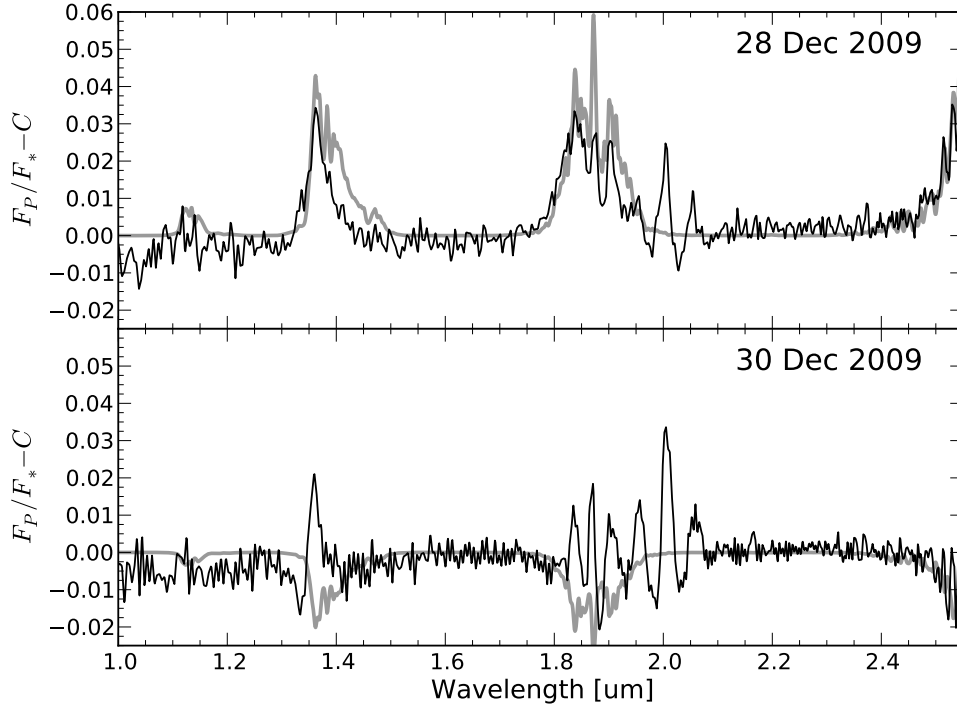


Figure 4.10 The effect of changes in telluric water absorption during our observations. The thin black line shows the measured residual eclipse spectrum, while the thick gray line represents the apparent eclipse signal (ΔTran) that would be inferred from the uncorrected changes in telluric PWV shown in Fig. 4.9. The 28 Dec spectrum appears strongly correlated with the ΔTran signal, but the 30 Dec spectrum does not. Neither ΔTran spectrum is significant far from telluric water absorption lines.

reported by [Swain et al. \(2010\)](#) for HD 189733b appears similar to the spectrum that would result from uncorrected variations in telluric water vapor emission, water vapor radiance effects do not match their spectrum from $3.5 - 4 \mu\text{m}$, where eclipse depths of 0.5% would be seen; nor do radiance effects match their K band spectrum. A complete explanation of the [Swain et al. \(2010\)](#) results must involve more than merely telluric effects.

Over our wavelength range we find that telluric thermal radiation is low enough that $|\Delta\text{Rad}| < |\Delta\text{Tran}|$ always, so we neglect radiance effects. We plot

the ΔTran signals with the observed eclipse spectra in Fig. 4.10, and the comparison is intriguing. The 28 Dec eclipse spectrum bears a striking resemblance to our calculated ΔTran spectrum, suggesting these observations are affected by variations in telluric water vapor transmission at some wavelengths. However, the 30 Dec observations show only a weak correlation with the ΔTran signal (in the wings of strong water bands), suggesting that the CSO data allow for only a crude estimate of the effects of atmospheric water on the extracted planetary spectrum.

For both nights, the ΔTran spectra do not capture the large spectral variations in the eclipse spectra from $2 - 2.07 \mu\text{m}$ where there are strong telluric CO_2 absorption bands. We generate several ATRAN atmospheric profiles with varying concentrations of CO_2 but find that the in- and out-of-eclipse CO_2 concentrations must differ by > 5 ppm to reproduce the features seen at these wavelengths. Such a change would be greater than any hour-to-hour change recorded at Mauna Loa by the National Oceanic and Atmospheric Administration Earth System Research Laboratory (NOAA ESRL) during all of 2009 (Thoning et al. 2010). Thus the telluric residuals in this wavelength range, though clearly correlated with the telluric CO_2 bands, are more likely attributable to the non-logarithmic relationship between flux and airmass in near-saturating lines and not to time-variable concentration.

As noted, ΔRad is negligible across most of our passband, reaching $< 2 \times 10^{-4}$ by $2.4 \mu\text{m}$ for our PWV values. The magnitude of ΔTran shown in Fig. 4.10 is $< 2 \times 10^{-4}$ for our observations in the wavelength ranges $1 - 1.1 \mu\text{m}$, $1.22 - 1.30 \mu\text{m}$, $1.52 - 1.72 \mu\text{m}$, and $2.03 - 2.34 \mu\text{m}$. We further exclude the spectral regions affected by CO_2 ($2.00 - 2.08 \mu\text{m}$). So long as we restrict our analysis to these regions we consider it unlikely that telluric water or CO_2 significantly affect our

results on either night.

Methane is another species whose abundance we are interested in measuring but whose telluric concentration can vary on short timescales. The NOAA ESRL also measures atmospheric CH_4 content (Dlugokencky et al. 2011), so we examined the hourly logs. The largest hour-to-hour change during our observations was $\sim 0.5\%$, with typical hourly changes smaller by a factor of several. We again use ATRAN (Lord 1992) to simulate two atmospheric transmission spectra with methane amounts varying by 0.5% (PWV was set to 1 mm and we simulated observations at zenith), and we then calculate ΔTran as before. At our spectral resolution we find that ΔTran reaches a maximum of about 0.04% near $2.36\ \mu\text{m}$ and is $< 10^{-4}$ outside of $2.23 - 2.4\ \mu\text{m}$. We include this ΔTran spectrum as a wavelength-dependent systematic uncertainty in our final measurements.

4.6.2 Chromatic Slit Losses

We quantify the impact of chromatic slit loss on our data by modeling this effect and then trying to extract spectroscopic information from the simulation. For this modeling we use an implementation based on `lightloss.pro` in the SpeXTool (Cushing et al. 2004) distribution; this in turn is based on the discussion of atmospheric dispersion in Green (1985; their Eq. 4.31). A crucial factor in these simulations is the refractive index of air, which we model following Boensch & Potulski (1998) assuming air temperature, pressure, and composition that are constant but otherwise consistent with values typical for Mauna Kea. We also used our empirical measurements of the wavelength-dependent seeing FWHM and the positions of the spectra along the slit. We cannot measure atmospheric dispersion perpendicular to the slit’s long axis, so we calculate this wavelength-dependent quantity and then shift it by the spectral offsets measured in Sec. 4.3.2.

The result is a model of our chromatic slit loss which is based almost wholly on empirical data. We see some agreement between this model and our spectrophotometric throughput – e.g., less flux and chromatic tilt of the spectrum during brief periods of poor seeing. Though our modeling can qualitatively reproduce the types of variations seen, in detail the data are highly resistant to accurate modeling and we suspect additional dispersion and/or optical misalignments in SpeX may be to blame.

We suspect that our modeling is also limited by an imperfect knowledge of the (variable) instrument point spread function: the slit loss is most dependent on the distribution of energy along the dispersion direction, but we can only measure this shape perpendicular to the dispersion direction. We see 10% variations in the seeing from one frame to the next (as measured by the standard deviation of the frame-to-frame change in seeing FWHM) – whether this represents our fundamental measurement precision or the level of fluctuations in the instrument response, this level of variation prevents accurate and precise modeling of the chromatic slit loss.

Whatever the cause of the disagreement, our model appears qualitatively similar to the spectrophotometric variations apparent in our observations. We therefore proceed to extract a planetary spectrum after removing an achromatic slit loss term as described in Sec. 4.4.2. Although we input no planetary signal the spectrum extracted is nonzero because, in general, the projection of the achromatic slit loss vector onto the model eclipse light curve is nonzero. As the chromatic slit losses become more severe at shorter wavelengths, so too is the extracted planetary signal progressively more biased in those same regions. We then perform a pseudo-bootstrap analysis of the chromatic slit loss: we re-order the modeled slit transmission series – i.e., we move the first frame’s modeled slit

transmission to the end of the data set and re-fit, then move the second frame’s transmission to the end, and repeat – and each time extract a planetary spectrum.

The variations in the extracted spectrum represent a systematic bias introduced by our wavelength-dependent slit losses. As expected observations taken with a wider slit fare better: for the 30 Dec observations the apparent variations in planetary emission (as measured by the standard deviation in each wavelength channel) are low in the H and K bands, reaching $\gtrsim 0.1\%$ (the approximate magnitude of the expected signal) in J band and rising shortward. However, our model of the 28 Dec observations indicates a substantially higher level of systematics: still low in the K band (where atmospheric dispersion is lessened; this is also our guiding wavelength, so variations are low here) but rising steeply with decreasing wavelength, reaching $\sim 0.5\%$ by the H band. We apply these noise spectra to our final measurement uncertainties to account for the possibility of systematic bias.

We also find that the induced spectral variations tend to depend more on changes in seeing than on atmospheric dispersion when using a 3.0” slit. This result suggests that our 30 Dec observations were not significantly compromised by our decision to lock down the instrument rotator.

4.6.3 Result of Simulated Observations

For completeness, we also combine our two dominant sources of systematic uncertainties – telluric absorption and chromatic slit loss effects – in a comprehensive model of our observations, using all empirical data available to us. We use a stellar template for the star (Castelli & Kurucz 2004) and inject a model planetary spectrum (Madhusudhan et al. 2011a, the purple curve in their Fig. 1, in which temperature decreases monotonically with decreasing pressure and with

the largest predicted $2.36\ \mu\text{m}$ CH_4 bandhead) and modulated by an analytical eclipse light curve (Hebb et al. 2009). For each frame we simulate the telluric transmission for each observation with LBLRTM (Clough et al. 2005), using the appropriate zenith angle and atmospheric water content (determined by interpolating the CSO observations in Sec. 4.6.1 to the time of the observation). We model the chromatic slit loss as described in the previous section and do not introduce any measurement noise into these simulated observations; this is because our goal is only to investigate the systematic biases the aforementioned effects have on our spectral extraction procedures. We also assume the detector response and instrumental throughput (excluding slit losses) are constant in time and wavelength. Any temporal variations in detector sensitivity will manifest themselves as increased scatter in the residuals and thus propagate to larger uncertainties in the prayer-bead analysis.

After generating these simulated spectra, we then send them through the analysis pipeline described in Sec. 4.5. We plot the extracted planetary spectra in Fig. 4.11. As expected, our analysis performs poorly in regions of strong telluric absorption due to a combination of changing abundances and the more complicated behavior of partially saturated absorption lines; the telluric-induced errors are qualitatively similar to those seen in our simpler analysis of Sec. 4.6.1, confirming our decision to avoid these wavelengths.

Fig. 4.11 also demonstrates the large systematic bias introduced by chromatic slit losses. The effect is especially pronounced at short wavelengths and, in the case of the narrower ($1.6''$) slit, the bias is so large as to prevent this data set from setting any useful constraints on WASP-12b’s emission. This finding agrees with our estimate of the systematic uncertainties induced by chromatic slit losses in the previous section.

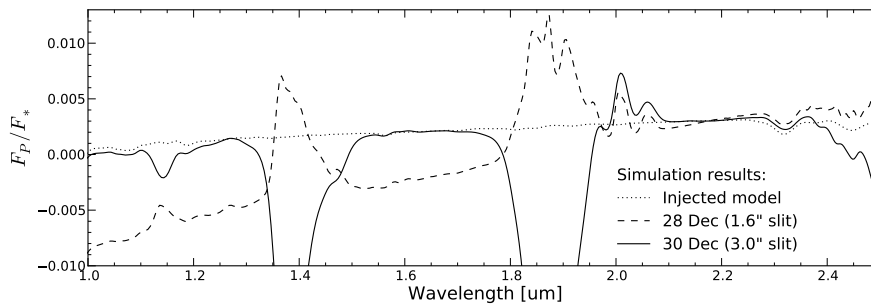


Figure 4.11 Planetary spectra extracted from our simulated observations (solid and dashed lines); the difference between these and the injected model (dotted line, from Madhusudhan et al. 2011a) demonstrates the systematic biases present in our data. Changes in telluric water content introduce biases in particular spectral regions, while chromatic slit losses introduce gradients across all wavelengths, especially with a narrow slit and/or at short wavelengths. See Sec. 4.6.3 for a complete description.

Having developed at least a rough understanding of our data’s expected biases, we are now well-equipped to interpret the results of our spectroscopic analysis.

4.7 Results: Thermal Emission from WASP-12b

4.7.1 Initial Presentation of Results

The parameters d^λ that result from the fitting process represent a modified emission spectrum of WASP-12b, specifically $d^\lambda = F_P^\lambda / F_*^\lambda - C$. The constant C results from our correction for common-mode photometric variations, and we set it using photometric eclipse measurements as described in Sec. 4.7. The individual channel (i.e., unbinned) best-fit coefficients for 28 Dec and 30 Dec are plotted in Figs. 4.7 and 4.8, respectively, and we show the fit residuals in Fig. 4.12. We plot the binned eclipse spectra and their uncertainties (the quadrature sum of statistical and systematic errors) in Fig. 4.13.

Our measurement errors generally increase toward shorter wavelengths owing

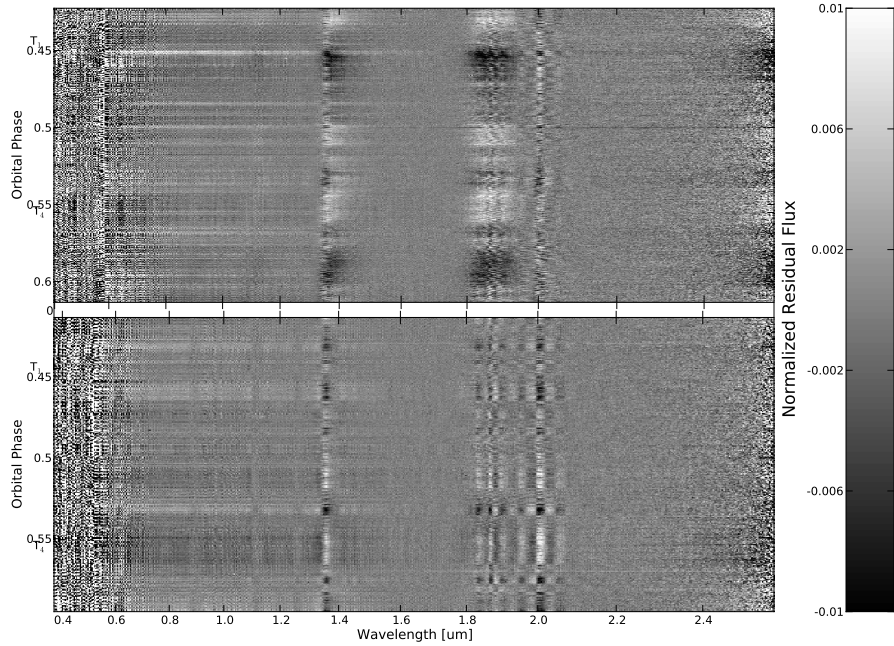


Figure 4.12 Residuals to the data for the nights of 28 Dec (*top*) and 30 Dec (*bottom*) after fitting Eq. 4.1 to the data in each wavelength channel, normalized by the median flux value in each wavelength channel. Residual correlated errors remain at shorter wavelengths and in regions of strong telluric absorption. The first (T_1) and fourth (T_4) points of contact of the eclipse are noted, as calculated from the ephemeris of Hebb et al. (2009).

to the systematic biases discussed in Sec. 4.6.2. Our performance also worsens in regions of high telluric absorption; this is either because our simple modeling does not accurately capture the behavior of saturating absorption lines, or because the abundances of the absorbing telluric species are changing with time. As we describe in Sec. 4.6.1 above we believe the latter description applies to the behavior of the 28 Dec eclipse spectrum in water absorption bands, while the former applies to the strong CO_2 absorption bands (around $2 - 2.07 \mu\text{m}$) on both nights.

As expected from Secs. 4.6.2 and 4.6.3 and Fig. 4.11, the large uncertainties

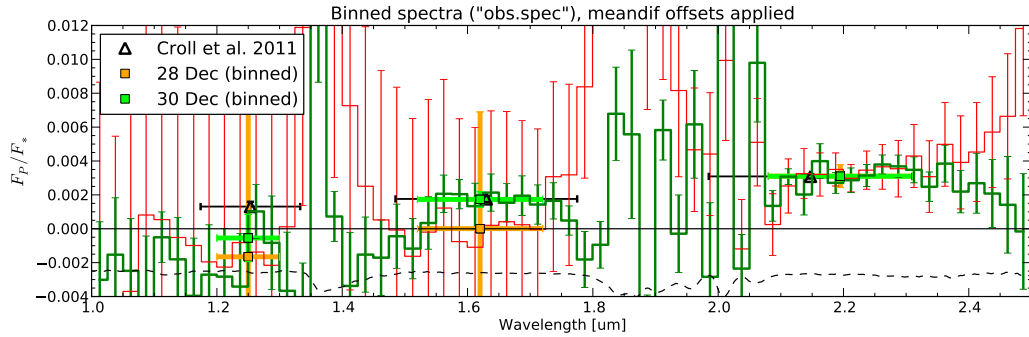


Figure 4.13 Emission spectra (solid lines, binned to squares) after calibrating our relative measurement with the absolute photometry of [Croll et al. \(2011b\)](#) (black triangles). The 28 Dec observations (red) suffer from extremely large systematic uncertainties at shorter wavelengths (cf. Fig. 4.11), and uncertainties are also large in the J band for the 30 Dec observations (green). The K–H color we measure on 30 Dec agrees with the previous photometric value. The dashed line at bottom shows the observed telluric extinction coefficient.

for the 28 Dec data (deriving from our use of a narrow slit and our decision not to guide along the parallactic angle) prevent the 28 Dec data from usefully constraining WASP-12b’s emission. In our final analysis we thus use only the wide-slit (30 Dec) data, which our modeling suggests are the most reliable.

4.7.2 Comparison With Observations

As we have noted throughout, we make only a relative eclipse measurement because division by the slit loss term removes a mean eclipse signature from all channels. Precise photometric eclipse measurements ([Croll et al. 2011b](#)) allow us to tie our observations to an absolute scale. From our investigation of systematic effects in Sec. 4.6.1 we expect our measurements to be robust in telluric-free regions of the H and K bands, but we expect systematics to limit our precision at shorter wavelengths and in any region of strong telluric absorption.

The H and Ks filters used by [Croll et al. \(2011b\)](#) cover part of the telluric absorption band from 1.78–1.98 μm , and without an independent calibration source we strongly mistrust our extracted spectra in these regions. We average our spec-

tra over wavelength ranges corresponding approximately to the CFHT/WIRCam filter responses, but modified as necessary to avoid strong telluric features where our analysis is compromised: we use ranges of $1.52 - 1.72 \mu\text{m}$ and $2.08 - 2.31 \mu\text{m}$ to correspond to the H and K bands, respectively. The regions we avoid have greater telluric absorption, so these wavelengths contribute relatively less to the photometric measurements. Though telluric contamination thus precludes a truly homogeneous comparison between our results and those of [Croll et al. \(2011b\)](#), using a blackbody model we estimate that the different wavelength ranges results in a difference of only 0.01 %, well beneath the precision we demonstrate below.

We compute K–H contrast colors (i.e., differential eclipse depths) on 28 Dec and 30 Dec of $0.31 \% \pm 0.69 \%$ and $0.137 \% \pm 0.054 \%$, respectively. The former value has a much larger uncertainty for the reasons discussed above in [Sec. 4.6.3](#): the 28 Dec observations used a narrow (1.6”) slit and so are much more susceptible to systematic errors. We thus discard the 28 Dec spectrum and adopt the 30 Dec spectrum as our best estimate of WASP-12b’s emission. We thus have a K–H contrast color ($0.137 \% \pm 0.054 \%$) fully consistent with, though of a lower precision than, the photometric value of $0.133\% \pm 0.022 \%$ ([Croll et al. 2011b](#)). WASP-12b’s broadband NIR emission closely approximates that of a 3,000 K blackbody ([Croll et al. 2011b](#); [Madhusudhan et al. 2011a](#)); our contrast color is consistent with a blackbody of temperature 2400_{-500}^{+1500} K, confirming this result. The 30 Dec K–J contrast color is $0.36 \% \pm 0.14 \%$, which is also consistent with the photometric value of $0.178\% \pm 0.031\%$ ([Croll et al. 2011b](#)) but is more uncertain: this large uncertainty exists because chromatic slit losses could substantially bias our measurement at these shorter wavelengths even with a 3.0” slit. Since the J-band uncertainties are dominated by the seeing-dependent component of chromatic slit losses, it may be difficult to improve on the short-wavelength performance we demonstrate here.

Table 4.2. WASP-12b Calibrated Planet/Star Contrast Spectrum

Wavelength Range (μm)	F_P/F_* (10^{-3}) ^a
1.525 – 1.550	0.34 ± 1.55
1.550 – 1.575	2.06 ± 1.10
1.575 – 1.600	2.04 ± 0.86
1.600 – 1.625	1.33 ± 1.35
1.625 – 1.650	2.13 ± 1.10
1.650 – 1.675	1.53 ± 1.13
1.675 – 1.700	1.95 ± 1.17
1.700 – 1.725	1.43 ± 1.16
1.725 – 1.750	1.65 ± 1.07
2.075 – 2.100	1.35 ± 0.90
2.100 – 2.125	3.08 ± 0.46
2.125 – 2.150	2.02 ± 1.21
2.150 – 2.175	3.99 ± 1.03
2.175 – 2.200	2.71 ± 0.62
2.200 – 2.225	2.86 ± 0.73
2.225 – 2.250	3.14 ± 0.65
2.250 – 2.275	3.79 ± 0.56
2.275 – 2.300	3.68 ± 0.67
2.300 – 2.325	3.48 ± 0.77
2.325 – 2.350	2.48 ± 0.87

^aQuoted uncertainties refer to the relative measurements made by our analysis. The uncertainties of an absolute contrast ratio is the quadrature sum of the value listed here and 0.029 %.

The weighted mean difference between our H and K measurements and those of [Croll et al. \(2011b\)](#) is $0.236\% \pm 0.029\%$, consistent with the offset of 0.215% expected from spectral models ([Madhusudhan et al. 2011a](#)) given the wavelengths used in our initial correction with the achromatic slit loss time series. We adjust our relative spectra by this offset and thus place our measurements on an absolute scale. The calibrated spectra from each individual night are plotted in [Fig. 4.13](#) and we show our final planet/star contrast spectrum, plotted over the wavelengths we consider to be uncorrupted by telluric effects, in [Fig. 4.14](#) and list the contrast ratios in each wavelength bin in [Table 4.2](#).

4.7.3 Spectral Signatures: Still Unconstrained

The most prominent spectral signature predicted to lie in our spectral range is the $2.32\ \mu\text{m}$ CH_4 absorption bandhead (Madhusudhan et al. 2011a). We consider the model from Madhusudhan et al. (2011a) in which temperature decreases monotonically with decreasing pressure (the purple curve in their Fig. 1), which is the model with the largest predicted CH_4 bandhead equivalent width. Estimating the continuum using wavelengths from $2.1\ \mu\text{m} - 2.25\ \mu\text{m}$ and measuring the equivalent width from $2.25\ \mu\text{m} - 2.34\ \mu\text{m}$, we calculate this feature’s equivalent width (calculated as a planet/star contrast) to be 16 nm in the model; with our spectrum we can set a 3σ upper limit of 27 nm.

We therefore come within a factor of two of being able to measure the strength of a specific spectral feature, and thus of spectroscopically constraining atmospheric abundances. However, because the uncertainties at these wavelengths are dominated by systematics relating to telluric absorption (cf. Sec. 4.6.1), a convincing detection would require many eclipses and a more complete understanding of the effects of telluric methane absorption.

4.7.4 Global Planetary Energy Budget

In light of our confirmation that WASP-12b’s NIR contrast color matches that of a 3,000 K blackbody, we revisit the published eclipse depths for WASP-12b with an eye toward examining the planet’s global energy budget. Since the orbital eccentricity is consistent with zero (Campo et al. 2011; Husnoo et al. 2011) we neglect tidal effects as a possible energy source and focus only on reprocessed stellar energy.

We convert eclipse depths (López-Morales et al. 2010; Croll et al. 2011b;

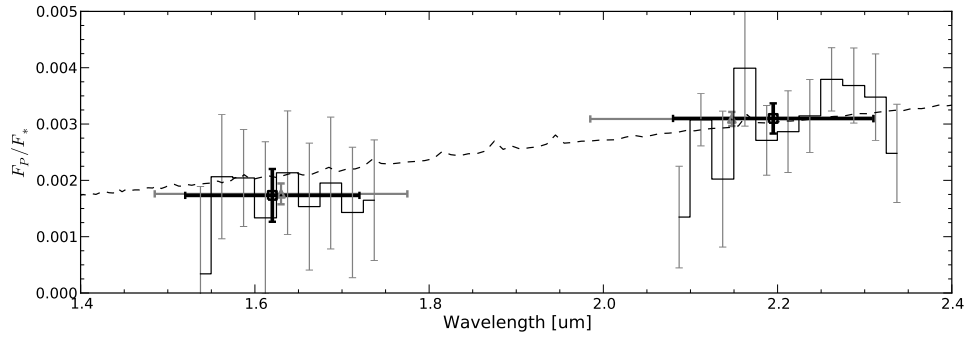


Figure 4.14 Tentative planet/star contrast spectrum of the WASP-12 system from our 30 Dec observations. We have calibrated our relative spectroscopic measurements (thin black curve, binned to thick black squares) with photometric data points (gray triangles; Croll et al. 2011b). Horizontal errorbars represent the effective widths of the photometric bandpasses; the ranges differ to prevent telluric variations from corrupting our single-slit observations. The dashed line shows the flux expected from a 3,000 K blackbody divided by the stellar flux model described in Sec. 4.7.4. Systematic uncertainties are larger at shorter wavelengths due to chromatic slit losses, so we do not plot those data here.

Campo et al. 2011) into surface fluxes using the known system parameters (Hebb et al. 2009), propagating the uncertainties in these parameters throughout our subsequent analysis. We use Castelli & Kurucz (2004) models with $T_{eff} = 6250$ and 6500 K, $\log g = 4.0$ and 4.5 (cgs units), and $[M/H] = +0.2$ and $+0.5$, and interpolate linearly in each of these quantities to the WASP-12 parameters of 6300 K, 4.16, and 0.3. Using the known WASP-12 system parameters we then convert to planetary fluxes using appropriate filter transmission profiles in each waveband (z' , J, H, and Ks from the ground, and all four IRAC channels on the Spitzer Space Telescope)⁶. In the same manner we convert our contrast ratio spectrum in Fig. 4.14 into a surface flux spectrum. We plot the full set of flux-calibrated eclipse measurements for this system in Fig. 4.15.

We use the filter profiles and WASP-12b's known size to then compute the

⁶We take the effective z' profile to be the product of the SPICAM CCD quantum efficiency and the z' filter transmission, obtained from the Apache Point Observatory website: <http://www.apo.nmsu.edu/>. CFHT/WIRCam profiles are taken from the WIRCam website: <http://www.cfht.hawaii.edu/Instruments/Filters/wircam.html>. Spitzer/IRAC filters are the full array spectral response curves, found at the IRAC website: <http://irsa.ipac.caltech.edu/data/SPITZER/docs/irac/calibrationfiles/spectralresponse/>

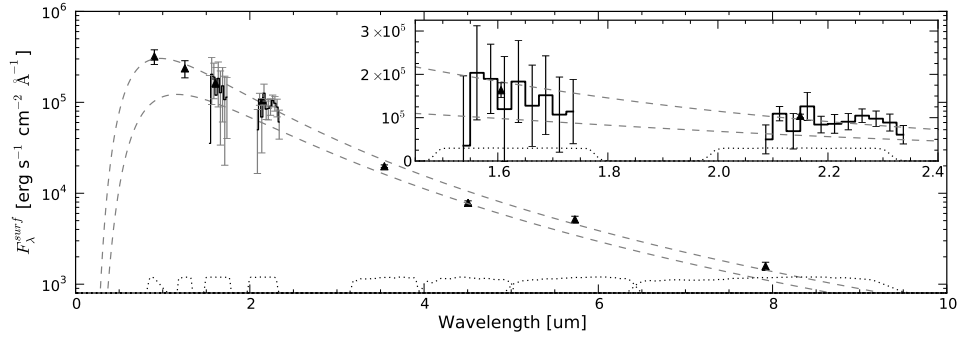


Figure 4.15 Flux-calibrated spectral energy distribution of WASP-12b. Triangles are from previous optical (López-Morales et al. 2010), NIR (Croll et al. 2011b), and mid-infrared (Campo et al. 2011) photometry, and the solid line (magnified in the inset) shows our measurements. The dashed lines show the surface flux of blackbodies with temperatures of 3,000 K and 2,500 K. The dotted lines at bottom show the filter transmission profiles described in Sec. 4.7.4.

dayside luminosity density. The current set of measurements puts a lower limit on the dayside luminosity of 2.0×10^{30} erg s⁻¹. This value is a lower limit because it assumes zero flux outside the filter bandpasses, which is improbable. Modeling the planet’s spectrum between filters as a piecewise linear function increases the measured luminosity to 3.6×10^{30} erg s⁻¹. As noted previously, the planet’s broadband spectrum closely approximates a 3,000 K blackbody (Madhusudhan et al. 2011a); such a spectrum would emit an additional 0.7×10^{30} erg s⁻¹ shortward of the z’ band. The presence of any optical absorbers (as has been observed on some planets: e.g., Charbonneau et al. 2002; Sing et al. 2011a) would tend to decrease this optical emission. We thus estimate the planet’s total dayside luminosity to lie in the range $(2.0 - 4.3) \times 10^{30}$ erg s⁻¹.

On the other hand, WASP-12b absorbs $(1 - A_B)(5.1 \pm 0.8) \times 10^{30}$ erg s⁻¹ of stellar energy, where A_B is the planet’s Bond albedo. Cowan & Agol (2011b) have suggested that the hottest of the Hot Jupiters (including the 3,000 K WASP-12b) have low albedos and low energy recirculation efficiencies; assuming zero albedo, our calculations limit the nightside luminosity to $(0.8 - 3.1) \times 10^{30}$ erg s⁻¹.

Approximating the nightside as a blackbody of uniform temperature, these

values correspond to a nightside effective temperature of 2,000–2,800 K or a day-night effective temperature contrast of 200–1,000 K. Temperature contrasts of this magnitude would correspond to a planetary energy recirculation efficiency (Cowan & Agol 2011a) of $\epsilon = 2–10$, which suggests that the planet’s recirculation efficiency may not be as low as predicted if the planet also has a low albedo (cf. Cowan & Agol 2011b). This result should be relatively easy to test, since these temperature contrasts imply IRAC1 & 2 phase curve contrasts ($\Delta F/\langle F \rangle$), cf. Cowan et al. 2007) of as much as 0.25 % and a Ks-band phase curve contrast of $\lesssim 0.15\%$. Warm Spitzer can easily reach this precision, and the results will help constrain WASP-12b’s recirculation efficiency and Bond albedo. After referral of this manuscript we became aware of just such a set of IRAC observations (Cowan et al. 2012). Though of limited precision, these Spitzer observations support our predictions above and suggest that WASP-12b has a nonzero albedo and low recirculation efficiency.

Eclipse observations still do not bracket the flux peak of WASP-12b’s emission: F_λ increases monotonically from $8\ \mu\text{m}$ (IRAC4) to $0.9\ \mu\text{m}$ (z’ band). We therefore strongly encourage efforts to detect the planet’s emission and/or reflection at shorter wavelengths (e.g., in the I and R bands) to further refine the planet’s albedo and flesh out its energy budget. The optical planet/star contrast ratios are challenging ($< 0.08\%$) but should be attainable on modest-sized (3–4 m) ground-based telescopes or with the Hubble Space Telescope (HST). HST observations at wavelengths inaccessible from the ground would also help fill the gaps in the planet’s spectral energy distribution and so decrease the uncertainty in the planet’s dayside luminosity.

4.8 Lessons for Future Observations

Our primary, but ultimately tentative result is WASP-12b’s K–H contrast color of $0.137\% \pm 0.054\%$. This result is a factor of 2.5 less precise than that determined by wide-field, relative eclipse photometry (Croll et al. 2011b) with a comparable amount of observing time. Nonetheless, we are heartened by our ability to self-calibrate out correlated noise in pursuit of precise relative measurement and to come within a factor of two of constraining the strengths of specific molecular features. This suggests that many repeated observations with SpeX or similar wide-slit spectrograph might describe spectral signatures. However, more progress must be demonstrated for single-slit observations to be competitive with photometry. The field is only now developing the beginnings of an understanding of telluric effects on such observations (Mandell et al. 2011), and there is still no consensus explanation for the full set of observations of Swain et al. (2010).

Our analysis in Sec. 4.6 demonstrates that telluric variations can imprint spurious features on our planetary spectrum, and chromatic slit losses can induce broad spectral gradients. Certainly, future observations should guide the slit along the parallactic angle and use as large a slit as possible. Future SpeX observations should make use of MORIS (Gulbis et al. 2011), a camera allowing simultaneous NIR spectroscopy and optical imaging, to distinguish between telluric transparency effects and instrumental throughput variations coupled to variable seeing, pointing, and PSF morphology. It could be possible to improve future performance by modeling the evolution of telluric features using high-resolution spectra, but we suspect this will not be feasible for very low-resolution observations such as those presented here. In any event, we would prefer to eschew telluric modeling and the many additional complications such analyses must entail. At this point we cannot say whether the increase in throughput afforded

by prism mode was worth the cost in lower resolution, but we have SpeX echelle data in hand (and more pending) that may allow us to answer this question. In any case higher resolution will not substantially improve the resolution of our final planetary spectrum, because substantial binning is still required to achieve a useful S/N.

As we stated in Sec. 6.6.3, we believe that near-infrared, multi-object spectrographs (MOS) will be the key technology that will enable detailed spectroscopic studies of exoplanet atmospheres. As the high precision achieved with optical and NIR MOS units (Bean et al. 2010, 2011) demonstrates, these instruments may well prove transformative for such studies. Slits can be made large enough to avoid all pointing error-induced slit loss effects, and simultaneous spectra of multiple calibrator stars allow all the advantages enjoyed by relative photometric techniques to be transferred to the field of spectroscopy. The spectroscopic calibrator stars provided by a MOS largely eliminates spectral contamination due to changes in telluric water transmission (i.e., ΔTran) since the calibrator observations remove telluric transmission effects in the same manner as is done in relative transit photometry. This should largely obviate the need to model evolving air-mass extinction effects. Because the large majority of multi-object spectrographs work at wavelengths where ΔRad effects are negligible, with multi-object observations neither telluric radiance nor transmittance should prove a confounding factor.

However, a large fraction of the currently known transiting systems will remain off-limits to the multi-object technique. This can result either from systems which lack comparison stars of adequate brightness within several arc minutes of the exoplanet host star, or from host stars that are too bright to observe with the large-aperture telescopes currently hosting MOS units. Transiting planets

in these systems can be observed spectroscopically at $\lambda < 1.7 \mu m$ with Hubble/WFC3 (cf. [Berta et al. 2012](#)), but spectroscopy in the K and L bands (where CH₄ and CO bands are prominent) will remain the domain of ground-based, single-slit spectroscopy for the near future.

Whatever the observing technique used, we emphasize the importance of observing multiple transit or eclipse events with ground-based observations. There are many subtle confounding factors in such analyses, and repeated observations are essential to discriminate between intermittent systematic effects and a true planetary signal. Many nights of observations would be required with SpeX to build up a useful spectroscopic S/N for most systems, but it does seem feasible. Nonetheless even with large-aperture telescopes single-epoch observations – including the results we present here – may well be treated with some skepticism.

4.9 Conclusions

We have presented evidence for a tentative spectroscopic detection of near-infrared emission from the extremely Hot Jupiter WASP-12b. Our data are compromised by correlated noise: spectrophotometric variations induced by telluric variations (owing to changing airmass and telluric abundances) and instrumental instabilities (caused mainly by fluctuations in the instrument PSF, but also by atmospheric dispersion) that are largely, but not wholly, common-mode across our wavelength range. By removing a common time series from all our data we self-calibrate and remove much of this variability, but biases remain. Though this calibration subtracts an unknown constant offset from our measured spectrum we renormalize using contemporaneous eclipse photometry ([Croll et al. 2011b](#)).

Although we present a possible emission spectrum of the planet in [Fig. 4.14](#),

uncertainties are still too large (by a factor of two) to constrain the existence of putative CH₄ absorption features. We measure a K–H contrast color of $0.137\% \pm 0.054\%$, consistent with a blackbody of temperature 2400_{-500}^{+1500} K; thus our results agree with (but are less precise than) previous photometric observations (Croll et al. 2011b). Our spectroscopic precision is limited by residual correlated noise and, due to our lack of external calibrators, by our extreme susceptibility to interference from telluric and instrumental sources outside a fairly narrow wavelength range. Modeling (described in Sec. 4.6) gives us confidence that within these regions our planetary spectrum is free of telluric contamination and (with a 3.0" slit) chromatic slit losses play a negligible role at $\lambda > 1.4 \mu\text{m}$.

Our primary result is methodological: to avoid biases from chromatic slit losses single-slit, NIR spectroscopy of transiting exoplanets should use slits as wide as possible and always keep the slit aligned to the parallactic angle. Instruments must be kept well-focused throughout such observations to minimize the effects of seeing variations. Substantially more attention must be paid to telluric variations if observations are to extend beyond the fairly narrow windows we describe in Sec. 4.6.1.

We predict that multi-object spectrographs will easily achieve better performance than what we have demonstrated here: wider slits and multiple simultaneous calibration stars will measure and remove instrumental and telluric systematics. These instruments are deployed on an ever-growing number of large-aperture telescopes and are beginning to be put to the test. In the meantime, we hope our descriptions of these first stumbling efforts will inform future studies so that the routine, detailed characterization of exoatmospheres can begin in earnest.

CHAPTER 5

Re-evaluating WASP-12b: Strong Emission at 2.315 μm , and Deeper Transits and Eclipses

5.1 Abstract

We detect unexpectedly strong emission from the extremely hot Jupiter WASP-12b at 2.315 μm using a narrowband filter at Subaru/MOIRCS. The planet/star contrast ratio ($0.455\% \pm 0.053\%$) corresponds to a brightness temperature of $3660\text{ K} \pm 210\text{ K}$, which is higher than predicted at this wavelength by published models used to infer a high C/O ratio in this planet’s atmosphere.

We also confirm the recent discovery of a fainter object located only 1” from WASP-12. This object has diluted previous eclipse and transit depth measurements, and its discovery necessitates a revision upward of these values. We find that this object has an effective temperature of $3660_{-60}^{+85}\text{ K}$ and surface gravity of $\log g\text{ (cgs)} = 0.488_{-0.167}^{+0.234}$, and conclude that it is most likely to be a foreground dwarf located $\sim 30\%$ closer to Earth than is WASP-12.

Finally, we correct past WASP-12 transit and eclipse measurements for the presence of this object, and we revisit the interpretation of WASP-12b’s photometric emission spectrum.

5.2 Introduction

5.2.1 Ground-based Characterization of Exoplanet Atmospheres

Transiting extrasolar planets allow the exciting possibility of studying the intrinsic physical properties of these planets. The latest new frontier to emerge is the detailed study of molecular chemistry in the atmospheres of these planets, many of which exist in intensely irradiated environments. The last several years have seen rapid strides in this direction, with measurements of precise masses and radii, detection of secondary eclipses and phase curves and the start of ground-based spectroscopy (Redfield et al. 2008; Swain et al. 2010; Bean et al. 2010). Based on observed day/night temperature contrasts (e.g., Cowan & Agol 2011b), atmospheric circulation patterns (Knutson et al. 2009b), and atmospheric chemistry (Stevenson et al. 2010; Madhusudhan et al. 2011a) these planets' atmospheres are likely to be quite different from anything previously known.

The transiting Hot Jupiter WASP-12b is one of the largest and hottest transiting planets known (Hebb et al. 2009; Chan et al. 2011; Maciejewski et al. 2011). The planet is significantly overinflated compared to standard interior models (Fortney et al. 2007), though its radius and age can be explained by an appropriate dynamical history involving an initially eccentric orbit and subsequent interior dissipation of tidal torques (Ibgui et al. 2011).

Due to its close proximity to its host star the planet is thought to be significantly distorted and may even be undergoing Roche lobe overflow (Li et al. 2010). Possible evidence for this scenario comes (1) from HST/COS UV spectra taken during transit (Fossati et al. 2010), which show tentative evidence of a deeper transit with earlier ingress than observed in the optical (Hebb et al. 2009), (2) from a tentative detection of an extended transit duration during a

Ks band eclipse (Croll et al. 2011b), which could be interpreted as an opaque accretion stream or disk, and (3) from Spitzer/IRAC phase curve observations of WASP-12b, which detect the planet’s ellipsoidal variations (i.e., its distortion from a spherical shape). If verified this could be the first evidence of the tidal inflation instability (Gu et al. 2003). However, there is no evidence for an extended eclipse duration in Spitzer/IRAC observations (Campo et al. 2011) or in the $2.315\ \mu\text{m}$ narrowband eclipse we describe here, and degeneracies between ellipsoidal variations and thermal phase variations prevent an unambiguous determination of WASP-12b’s geometry from the Spitzer observations (Cowan et al. 2012).

Both radial velocity measurements associated with the initial transit discovery and the first eclipse observation both suggested WASP-12b had a nonzero eccentricity (Hebb et al. 2009; López-Morales et al. 2010). However, subsequent orbital characterization via timing of secondary eclipses (Croll et al. 2011b; Campo et al. 2011; Cowan et al. 2012) and further radial velocity measurements (Husnoo et al. 2011) set an upper limit on the eccentricity of $\sim 0.03(1\sigma)$. Our $2.315\ \mu\text{m}$ narrowband eclipse is also consistent with a circular orbit.

As yet transmission spectroscopy (which determines atmospheric opacity at the planet’s limb via multiwavelength transit measurements) has been limited for this system. Optical transit measurements show some disagreement (Hebb et al. 2009; Chan et al. 2011; Maciejewski et al. 2011), which makes interpretation difficult. Spitzer/IRAC transit observations suggest that WASP-12b’s radius may be greater at $3.6\ \mu\text{m}$ than at $4.5\ \mu\text{m}$ (Cowan et al. 2012), but the significance of this result hinges on the uncertain interpretation of ellipsoidal variations in these data, which were found to be of much greater amplitude than expected at $4.5\ \mu\text{m}$. Nonetheless WASP-12b’s low density and high temperature make the planet an

excellent target for future efforts in this direction.

WASP-12b is intensely irradiated by its host star, making the planet one of the hottest known and giving it a favorable ($\gtrsim 10^{-3}$) NIR planet/star flux contrast ratio; it has quickly become one of the best-studied exoplanets. The planet's large size, low density, and high temperature motivated a flurry of optical, (López-Morales et al. 2010), NIR (Croll et al. 2011b), and mid-infrared (Campo et al. 2011) eclipse photometry which suggests this planet has an unusual carbon to oxygen (C/O) ratio greater than one (Madhusudhan et al. 2011a). Subsequent observations (Zhao et al. 2012; Cowan et al. 2012; Crossfield et al. 2012a) have been consistent with these earlier measurements and model, but the $2.315\ \mu\text{m}$ eclipse we present here is inconsistent with these models.

However, significant degeneracies remain in the theoretical interpretation of these broadband emission observations; this situation is typical even for the best-characterized systems (Madhusudhan & Seager 2010). This is the case because (a) broadband photometry averages over features caused by separate opacity sources and (b) atmospheric models have many more free parameters than there are observational constraints. Spectroscopy, properly calibrated, can break some of these degeneracies, test the interpretation of photometric observations at higher resolution, and ultimately has the potential to more precisely refine estimates of atmospheric abundances, constrain planetary temperature structures, and provide deeper insight into high-temperature exoplanetary atmospheres. This provided the motivation for our earlier ground-based spectroscopy of WASP-12b (Crossfield et al. 2011) and serves as the impetus for the analysis presented here.

5.2.2 Paper Outline

This paper presents our observations and analysis of WASP-12b’s emission in a narrow band centered at $2.315\ \mu\text{m}$, our detection and characterization of a cool star with high surface gravity near WASP-12, a correction of past eclipse and transit measurements, and our interpretation of WASP-12b’s atmospheric emission. In addition to our analysis of an eclipse of WASP-12b, we confirm the previous discovery (Bergfors et al. 2011) of an object (which we call Bergfors-2) located only $1''$ from WASP-12. We tightly constrain this object’s spectral type and correct past transit and eclipse measurements for the photometric dilution it causes.

We describe our eclipse observations and initial data reduction in Sec. 5.3. As described in Sec. 5.4 we fit numerous models to the data, select the statistically optimal combination of parameters to use, and present the results of this eclipse. In Sec. 5.5 we describe our analysis of Bergfors-2’s properties, and in Sec. 5.6 we use the results of this analysis to correct past transit and eclipse observations of WASP-12b. In Sec. 5.7 we compare WASP-12b’s emission to models and previous observations. Finally, we conclude and suggest relevant possibilities for followup in Sec. 5.8.

5.3 Subaru/MOIRCS Narrowband Time-series Photometry

5.3.1 Summary of Observations

We described recently the first tentative detection of emission from WASP-12b via spectroscopy at the 3m NASA Infrared Telescope Facility (IRTF) (Cross-

field et al. 2012a). However, our precision was limited by chromatic and time-dependent slit losses resulting from the use of a single, narrow (3") slit. We thus applied for time on the Multi-Object InfraRed Camera and Spectrograph (MOIRCS; Ichikawa et al. 2006; Suzuki et al. 2008) at Subaru Observatory to conduct multi-object eclipse spectroscopy (cf. Bean et al. 2010, 2011) of WASP-12b. A coolant leak at Subaru caused damage that prevented us from observing in multi-object mode, so we observed in imaging mode using a custom narrowband filter (NB2315). This filter is centered at approximately $2.315\ \mu\text{m}$ with a width at half maximum of $27\ \text{nm}$ ¹, and so is very well suited to probe the strong absorption feature predicted to lie at this wavelength (Madhusudhan et al. 2011a, their Figure 1).

We observed one eclipse of WASP-12b on 14 Dec 2011 (UT). The start of observations was delayed by instrument problems, but we managed to begin about half an hour before ingress and observed continuously thereafter. We observed at a position angle of 330 deg and read out frames in correlated double sampling (CDS) mode with a constant integration time of 21 s per frame, using a readout speed of 8 and two dummy reads. With faster readouts the detector exhibits higher levels of correlated noise, and with fewer dummy reads residual bias tilt remains. These readout parameters result in substantial overhead penalties, and we averaged only one frame per 61 s over our 6.5 hr of observations (which cover an airmass range of 1.6 – 1.02 – 1.3). We recorded 388 frames in total. Conditions were nearly photometric, with stellar flux variations of 1-2 % apparent (in addition to an airmass-dependent trend).

Following standard high-precision photometry practices (e.g., de Mooij & Snellen 2009; Rogers et al. 2009) we defocussed the telescope to spread the

¹A transmission profile of the NB2315 filter is available upon request.

starlight over more pixels, thereby increasing observing efficiency and reducing the effect of residual flat fielding errors. The instrumental seeing improved throughout the night, and to avoid any substantially nonlinear detector response we added defocus to the telescope several times. Because the Subaru autoguider was inoperative we had to periodically apply manual offsets to the telescope tracking. The tracking was rather poor and despite our corrections we observed image drifts as large as 1.2" (10 pixels); however, we note that subsequent software development at Subaru has resulted in improved tracking even without the telescope autoguider. The temperature of both detectors (as measured by the Chip Box FITS header keywords) increased from 76.2 K to a constant 77.0 K over the first 1.5 – 2 hr, as shown in Figure 5.1. However, we observe no correlation between these temperature trends and our photometry.

5.3.2 Initial Data Reduction

We calibrate the raw frames following the standard MOIRCS reduction prescription, which proceeds as follows. We dark-subtract each frame and divide the result by the stack median of a set of dark-subtracted dome flats. However, substantial scattered and/or background light remains: we remove this by scaling and subtracting a median-combined set of median-normalized, dithered, dark-subtracted sky images. MOIRCS splits its field of view across two detectors, and we follow these procedures independently for data from both channels. Requiring an identical level of sky subtraction in both channels does not significantly change our results.

We extract photometry using our own aperture photometry package², which uses bilinear interpolation to account for partial pixels while conserving flux. In

²Available from the primary author's website.

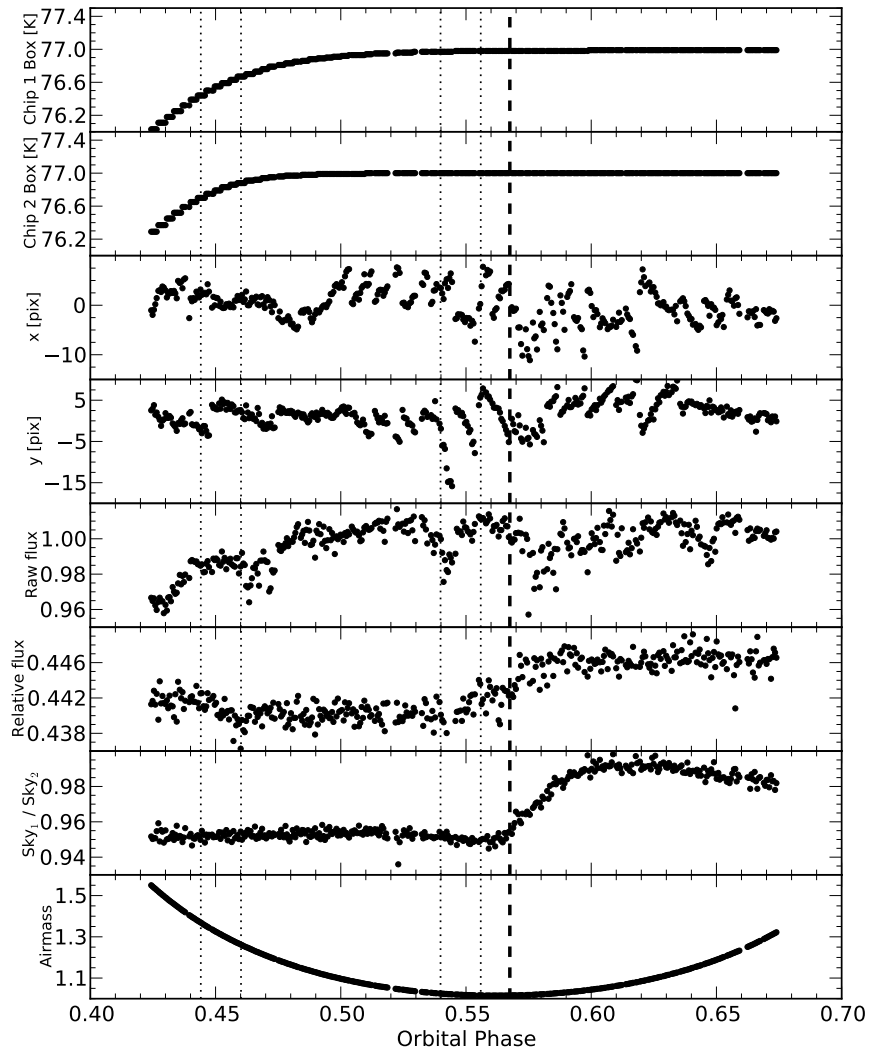


Figure 5.1 Instrumental trends during our observations. From top to bottom: Chip 1 and 2 electronics box temperatures, relative x and y motions, WASP-12 raw flux, WASP-12 relative flux, ratio of median sky background (pre-calibration) in Chips 1 and 2, and airmass. The dotted lines indicate the four points of contact corresponding to a circular orbit with our best-fit eclipse center. The vertical dashed line corresponds to the onset of the anomalous trend apparent in the sky background and relative photometry: we exclude all data after this in our final analysis.

each frame we extract subregions around each star, perform 1D cross-correlations to measure relative stellar motions, and interpolate over hot pixels, stuck pixels, and any pixels more than 6σ discrepant from their mean value. We then recenter the photometric apertures and perform standard aperture photometry.

In imaging mode MOIRCS offers a roughly $4' \times 7'$ field of view split equally over two 2048^2 HAWAII-2 detectors, which allows several comparison stars to be fit into the WASP-12 field of view. We find that using stars more than about 1.8 mag fainter than WASP-12 decreases our final precision. Our large photometric apertures also require us to avoid choosing comparison stars with nearby companions. This leaves six comparison stars: 2MASS 06303632+2937582, 06302437+2937293, and 06303222+2937347 (on Chip 1) and 2MASS 06302377+2939118, 06301801+2939204, and 06302280+2938338 (with WASP-12 on Chip 2). Our final results are consistent (though of lower precision) if we use fewer comparison stars or use stars falling only on a single detector. We examine the results from photometric apertures of various sizes and ultimately use apertures with diameters of 33, 39, and 64 pixels ($4.0''$, $4.7''$, and $7.7''$). This choice minimizes the root mean square (RMS) of the residuals to our model fits.

MOIRCS returns the UT date and time at the beginning and end of each exposure in its FITS header. We convert these to BJD_{TDB} for our subsequent analysis (Eastman et al. 2010).

5.3.3 Instrumental Systematics

We plot several variable instrumental parameters, along with the our absolute and relative photometry of WASP-12, in Figure 5.1. One variable dominates in terms of its impact on our photometry: the curious trend in the relative sky background measured in the two detectors, which begins an anomalous excursion

as WASP-12 crosses the meridian (only 10-15 min after egress). The relative photometry shows a qualitatively similar trend.

We also see this trend when dividing stellar photometry from Chip 2 (excluding WASP-12) by photometry from Chip 1, and we even see it (at a lower amplitude) when comparing multiple reference stars on Chip 2 against each other. Because the trend begins just as WASP-12 crosses the meridian, we hypothesize that some loose component in the telescope or instrument settled in response to the change from a westward-directed to an eastward-directed gravity vector.

One possible culprit in this scenario is our narrowband filter, which sits in the pupil plan and whose spectral transmission profile depends on the angle of incidence of incoming light. To first order, increasing the angle of incidence translates the transmission profile to shorter wavelengths. The filter profile intersects a particularly strong telluric absorption (CH_4) bandhead; from the vendor-supplied characterization data for our filter we estimate that a shift in the filter's angle of incidence of ~ 10 deg could induce a photometric variation of the magnitude observed. However, no strong sky emission features are seen at these wavelengths, so this scenario still has difficulty explaining the observed variation in the sky background. Future high-precision relative MOIRCS data (currently under analysis) will test the validity of our hypothesized explanation.

Whatever the cause of this trend, so long as we restrict our analysis to times before orbital phase 0.5675 (the vertical dashed bar in Figure 5.1) our results change by less than 1.5σ no matter which comparison stars we choose. We explored ways to use our entire data set by using the sky background trend as a decorrelation parameter (see Section 5.4 below), but such analyses resulted in larger fit residuals with substantially higher correlations on long timescales. We therefore proceed by excluding the later data, while acknowledging the existence

of this poorly-understood systematic effect in MOIRCS data.

5.4 Searching for the 2.315 μm Narrowband Eclipse

5.4.1 Fitting to the Data

We fit our photometric time series with the following relation, representing a relative eclipse light curve subjected to systematic effects:

$$F_i = f_0 (1 + d\ell_i) \left(1 + \sum_{j=1}^J c_j v_{ij} \right) \quad (5.1)$$

The symbols are: F_i , the relative flux measured at timestep i ; f_0 , the true relative flux; ℓ_i , the flux in an eclipse light curve scaled to equal zero out of eclipse and -1 inside eclipse; d , the normalized depth of eclipse; v_{ij} , the J state vectors (i.e., image motions, sky background, airmass, orbital phase, or low-order polynomials of these quantities) exhibiting a linearly perturbative effect on the instrumental sensitivity; and c_j , the coefficients for each state vector. We allow the time of eclipse center, duration, and depth of eclipse to vary while holding fixed the scaled semimajor axis (a/R_*) and the orbital inclination (and hence also the impact parameter) at the values listed in Table 5.1.

Experience shows that the choice of instrumental model is of crucial importance in extracting the most accurate system parameters from transit and eclipse observations (cf. Campo et al. 2011). We therefore explore a large region of model parameter space by fitting our photometry using many different combinations of state vectors and a fixed eclipse time and duration. We then use the Bayesian Information Criterion³ (BIC) to choose which of these many models best rep-

³Bayesian Information Criterion (BIC) = $\chi^2 + k \ln N$, where k is the number of free parameters and N the number of data points.

Table 5.1. WASP-12b: 2.315 μm Narrowband Eclipse Parameters

Parameter	Units	Value	Reference
P	days	1.091423	Hebb et al. (2009)
a/R_*	–	3.14	Hebb et al. (2009)
$T_{c,e}$	BJD _{TDB}	2455910.9098 ± 0.0012	This work
T_{offset}	s	71 ± 107 s	This work
T_{58}	min	183.0 ± 4.0 min	This work
$e \cos \omega$	–	$+0.00075 \pm 0.00085$	This work
$e \sin \omega$	–	0.020 ± 0.012	This work
F_P/F_* (observed)	–	$0.414\% \pm 0.048\%$	This work
F_P/F_* (corrected)	–	$0.455\% \pm 0.053\%$	This work
$T_{B,2.315}$	K	$3660 \text{ K} \pm 210 \text{ K}$	This work

resents our data. To do this we assign uncertainties to each data point equal to the RMS of the residuals to an eclipse fit with no additional decorrelation variables. We find this same simple model to be the one that minimizes the BIC. The models with the next-best BIC (2.2 units higher) also include linear or quadratic functions in time. This linear fit gives an eclipse depth consistent with our constant-baseline model; the quadratic fit gives a significantly deeper eclipse (0.6%), but we disfavor this model given our limited coverage out of eclipse.

We then again fit our preferred instrumental model to the data, but this time we allow the eclipse duration and eclipse center to vary. We assess the uncertainties on the best-fit parameters using both the Markov Chain Monte Carlo and prayer bead (or residual permutation, cf. Gillon et al. 2007) approaches. The two sets of distributions are quite consistent, which suggests correlated noise does not strongly affect our photometric subset of data. In both cases the resulting parameter distributions are unimodal, symmetric, and approximately normal. In the following we quote only the prayer bead results.

5.4.2 Initial Narrowband Eclipse Depth

We plot the data, our best-fit (constant baseline) model, and the residuals in Figure 5.2. The best-fit eclipse depth is $0.414\% \pm 0.048\%$, which is consistent with our previous (less precise) spectroscopy (Crossfield et al. 2012a); note that the true eclipse depth is $\sim 10\%$ greater, as we describe in Section 5.6. The residuals to the best fit have a relative RMS of 0.234% . Photon (target + sky) noise considerations predict a typical per-frame precision of 0.06% , so our residuals exhibit a scatter roughly four times greater than this prediction. This level of performance is comparable to that obtained with other NIR eclipse photometry (e.g., Croll et al. 2011b). Our residuals bin down approximately as $N^{-1/2}$, as shown in Figure 5.3: this behavior indicates a low level of temporally correlated noise despite the higher-than-expected scatter in the data, which is also consistent with previous work (e.g., Croll et al. 2011b).

An alternative model for our data set, which excludes no data and includes the sky background trend as a decorrelation state vector, gives a deeper eclipse ($0.53\% \pm 0.05\%$). This model has a higher residual RMS (0.261%) and exhibits substantially higher levels of correlated noise when averaging on long time scales, as shown in Figure 5.3. For these reasons believe our simpler model, and its consequently shallower eclipse measurement, to be more reliable.

5.4.3 Eclipse Duration and Timing: No Surprises

We find no evidence for significant deviations in eclipse duration or in the time of center eclipse, as compared to expectations from transit observations and a circular orbit. We find a best-fit eclipse duration of 183.0 ± 4.0 min, and the eclipse occurs later than predicted by 71 ± 107 s (accounting for the 23 s light travel time across the system). Again, the parameter distributions are unimodal and

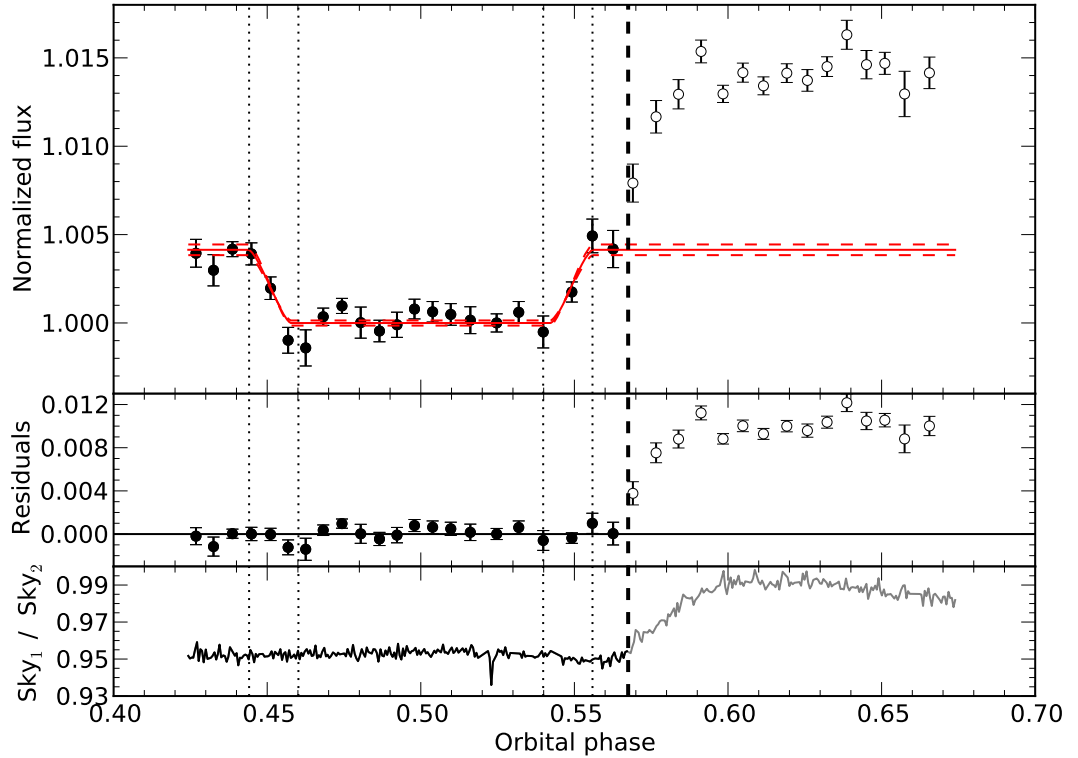


Figure 5.2 Top: relative $2.315\ \mu\text{m}$ narrowband photometry of WASP-12 (points; binned only for plotting purposes) and our best-fit model (solid line). The 1σ range of our model is also indicated by the dashed curves. Solid points are used in our analysis, while open points are excluded. Middle: Residuals to the fit. Bottom: differential sky background measured in the two MOIRCS detectors. The vertical dashed line indicates the onset of the photometric ramp apparent in sky and stellar photometry; we exclude this data from our analysis, though our results are unchanged if we use all data and include the use an additional decorrelation parameter. The dotted lines indicate the four points of contact corresponding to a circular orbit with our best-fit eclipse center.

approximately normal. An analysis of previous Ks band observations reported a marginally longer eclipse duration (Croll et al. 2011b). We find a shorter eclipse than this measurement, but our results are consistent with both the Ks eclipse measurement and the duration expected from a circular orbit at $< 2\sigma$. We thus see no evidence for evolution of the eclipse duration. Similarly, our measurement

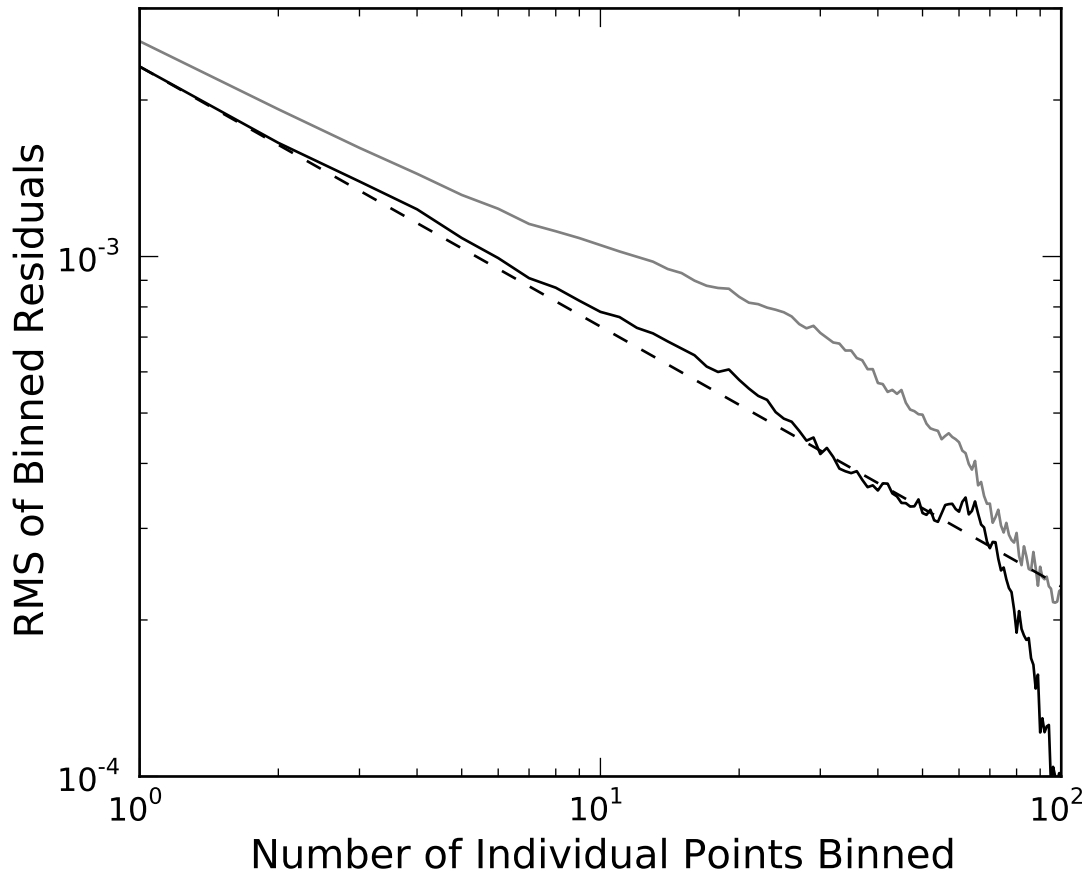


Figure 5.3 RMS from binning the residuals shown in Figure 5.2 over increasing numbers of datapoints (solid black line). This curve tracks with the $N^{-1/2}$ expectation from white noise (dashed line). The solid grey line shows the behavior of the residuals to a model using all photometric points in Figure 5.2 and including the background sky variation as an additional decorrelation parameter. This alternative model exhibits a higher per-point RMS and shows a higher level of correlated noise on longer timescales.

of the time of center eclipse agrees with both the expected (circular orbit) value and with the Ks band measurement of this quantity to within 2σ (Croll et al. 2011b). Thus our data provide no evidence for an offset or longer-duration eclipse.

Together, the eclipse timing and duration tightly constrain the orbital eccentricity and longitude of periastron (Winn 2010; Seager 2011). We determine

$e \cos \omega$ and $e \sin \omega$ to be $+0.00075 \pm 0.00085$ and 0.020 ± 0.012 , respectively: the orbit is within 2σ of being perfectly circular, consistent with previous results based on eclipse and radial velocity observations (Campo et al. 2011; Croll et al. 2011b; Husnoo et al. 2011). The time of eclipse also constrains the planetary velocity offset expected at transit center, which can mimic wind-induced velocity offsets measured with high-resolution spectroscopy (Snellen et al. 2010; Fortney et al. 2010; Montalto et al. 2011; Miller-Ricci Kempton & Rauscher 2011). Our eclipse sets a 3σ upper limit on any such orbit-induced velocity offset of $+0.67 \text{ km s}^{-1}$.

5.5 Bergfors-2: An Object Very Close to WASP-12

5.5.1 Planet Candidate Verification and Transit Dilution

A wide range of atmospheric models fit WASP-12b’s photometric emission spectrum equally well despite differing significantly in atmospheric abundances and in their temperature-pressure profiles (Madhusudhan et al. 2011a). However, the recent detection of a point source ~ 3 mag fainter than WASP-12 and only $1''$ away (Bergfors et al. 2011) requires us to revise upward these past measurements. This, along with the $2.315 \mu\text{m}$ eclipse analysis we present here, requires a re-evaluation of atmospheric models.

Because optical, ground-based transit surveys are sensitive only to relatively large (hence massive) planets, their discovery paradigm focuses largely on a careful analysis of high-precision radial velocity measurements, which admit as their explanation only an orbiting body of planetary mass. Because many astrophysical arrangements can mimic the signature of a transiting planet (Torres et al. 2004, 2005), candidates must undergo further, more rigorous analysis before being deemed planets. This is also true for candidates discovered by the Kepler

mission (Borucki et al. 2011), many of which have masses that are too low (or orbit stars too faint) for radial velocity measurements to be useful. One tool frequently employed in the Kepler validation battery is the use of high-resolution (adaptive optics or speckle) imaging to search for faint objects (possible eclipsing binaries) very close to the candidate transiting system (Howell et al. 2011). The photometric contribution of another, untransited, object dilutes the depth of the transit (Johnson et al. 2011) – or the background object may itself be an eclipsing binary whose deep eclipses are diluted by the brighter foreground object, giving a transit-like depth. Even in a confirmed transiting planet system, derived physical parameters must account for this contaminating light.

A number of systematic effort have been undertaken to uncover faint companions near systems with planets discovered by transits and/or radial velocity variations (e.g., Eggenberger et al. 2007). The first systematic survey to specifically target transit host stars found 3 faint, nearby objects around 14 surveyed systems Daemgen et al. (2009), which suggests that such objects are not rare; an extension of this survey brings the ratio to 6 in 30 (Bergfors et al. 2011). In these cases the planets have already been validated, but transit dilution can still change system parameters by greater than the initially reported uncertainties (Daemgen et al. 2009). If such objects are physically bound to the planet host star (which has yet to be demonstrated for many of these objects), they could then help to explain the dynamical history of these planets' migration (e.g., Fabrycky & Tremaine 2007; Nagasawa et al. 2008) and explain their inflated radii (e.g., Ibgui et al. 2011). (Another such effort has been undertaken for HAT-P-7; Narita et al. 2010, .)

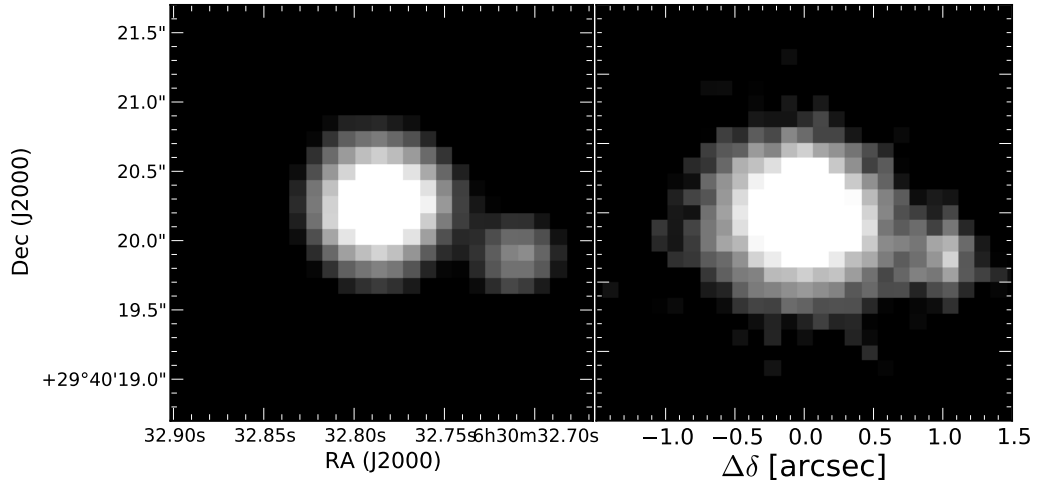


Figure 5.4 Images used for astrometric and relative flux measurements: at left, seeing-limited image from Subaru/MOIRCS ($2.315\ \mu\text{m}$ narrowband); at right, speckle image from IRTF/SpeX (K_{MKO}). Astrometric parameters derived from these images are listed in Table 5.2. Both images are displayed at the same orientation and scale; they have different (logarithmic) color stretches in order to highlight the fainter companion.

5.5.2 Bergfors-2

During our Subaru observations Dr. Ichi Tanaka (Subaru/NAOJ) noticed a slight elongation in our (defocused) images and motivated us to refocus the system at the end of the night, and we recorded the image shown in Figure 5.4. It clearly shows a point source roughly $1''$ from WASP-12.

This object was recently discovered (using i and z photometry; Bergfors et al. 2011) and assigned a preliminary spectral type of K4-M1 V. We refer to this object as Bergfors-2, because it is the second object reported by Bergfors et al. (2011). The existence of a bound companion at this projected separation ($\lesssim 300$ AU) would have potentially profound implications for the dynamical history of the system, and could provide a mechanism for Kozai-induced eccentricity and

subsequent tidal heating to inflate the planet’s radius to its present size (Fabrycky & Tremaine 2007; Nagasawa et al. 2008; Ibgui et al. 2011).

Bergfors-2 has not been remarked upon in previous optical and infrared transit and eclipse observations of the WASP-12 system (Hebb et al. 2009; López-Morales et al. 2010; Chan et al. 2011; Maciejewski et al. 2011; Campo et al. 2011; Croll et al. 2011b; Cowan et al. 2012; Crossfield et al. 2012a; Zhao et al. 2012). This is likely because with seeing-limited (or Spitzer/IRAC) resolution the two objects are at best only marginally resolved. The case is worse for most high-precision ground-based photometry, because standard practice is to substantially defocus the telescope; this practice clearly precludes detection of objects such as Bergfors-2.

This star falls within the photometric apertures used in most previous analyses and dilutes the transit and eclipse signals that have been measured (cf. Daemgen et al. 2009). In this work we confirm the previous detection of Bergfors-2, more tightly constrain its spectral type, and correct previous measurements for its photometric contamination.

5.5.3 Observations of Bergfors-2

5.5.3.1 Subaru/MOIRCS NB2315 Image

As described above, we recorded the single well-focused MOIRCS image shown in Figure 5.4. We register the image’s coordinate system using the 2MASS point source catalogue (Skrutskie et al. 2006) and confirm the MOIRCS plate scale to be $0.117 \pm 0.001'' \text{ pix}^{-1}$ (as listed in the instrument documentation). We conservatively adopt an uncertainty of 1 deg in the instrumental position angle.

Bergfors-2 sits in the wings of the WASP-12 point spread function (PSF), so

we perform a simultaneous fit to the two-dimensional PSFs of both stars. We use multiple elliptical Gaussian functions, holding the rotation and dispersion parameters fixed in each of the model PSFs and allowing only a single central location for each star. Thus for n Gaussian functions we have $(5 + 5n)$ free parameters. We set the pixel uncertainties equal to the expectation from photon and read noise.

We find that three elliptical Gaussians minimize the BIC, so we adopt this model and use Markov Chain Monte-Carlo (MCMC) techniques to explore the range of valid parameter space. We find the subsequent parameter distributions to be unimodal and approximately Gaussian. To conservatively account for the uncertainties inherent in estimating accurate photometry and astrometry from a single measurement, we inflate the parameter uncertainties estimated from our MCMC by a factor of two. Our final determination of the flux ratio, separation, and system position angle from the MOIRCS data are listed in Table 5.2. The separation is consistent with the initial discovery value (Bergfors et al. 2011). We confirm this $2.315 \mu\text{m}$ flux ratio by comparing aperture photometry of WASP-12 and (after subtraction of the best-fit WASP-12 PSF model) of Bergfors-2: this approach gives a consistent result. The estimates presented here are consistent with, but more precise than, estimates derived from several of our more poorly focused MOIRCS frames.

5.5.3.2 IRTF/SpeX K Band Lucky Imaging

The well-focused Subaru image described above, in addition to our discovery of the Bergfors et al. (2011) results, motivated us to acquire additional high-resolution imaging data. On 2012 Feb 25 (UT) we imaged the WASP-12 system with the IRTF/SpeX guide camera (Rayner et al. 2003), which uses a 512^2 Al-

Table 5.2. Bergfors-2 Astrometry

Parameter	Units	CA 2.2 m/AstraLux		Subaru/MOIRCS	IRTF/SpeX
Filter	—	i'	z'	NB2315	K_{MKO}
Flux ratio	—	0.0244 ± 0.0015	0.0305 ± 0.0028	0.108 ± 0.007	0.1048 ± 0.0059
Separation	arcsec	$1.047'' \pm 0.021''$		$1.055'' \pm 0.026''$	$1.078'' \pm 0.033''$
Position Angle	deg	$\sim 250 \text{ deg}^a$		$250 \text{ deg} \pm 1 \text{ deg}$	$249.4 \text{ deg} \pm 1.1 \text{ deg}$
Date	UT	not reported		2011 Dec 14	2012 Feb 25
Reference	—	Bergfors et al. (2011)		This work	This work

^aEstimated from their Figure 1.

addin 2 Insb array with a plate scale of $0.1185'' \text{ pix}^{-1}$. Observing through sometimes patchy clouds, we aquired 1,200 0.4 s K_{MKO} ([Tokunaga et al. 2002](#)) frames (from airmass 1.2 – 1.5) and 900 0.21 s J_{MKO} frames (from airmass 1.5 – 2.2). In all observations we held the SpeX instrument rotator at a position angle of 90 deg. The J band data were not sufficient to reliably detect Bergfors-2, so we discuss only the K band data.

We calibrate the SpeX images using a median stack of internal (thermal) flat fields and subsequently perform binlinear interpolation over a few noticeably bad pixels. We select the top 10% (118) of all frames on the basis of the peak pixel flux near the location of WASP-12, then use the “shift and add” algorithm to align and stack these frames (our data were too noisy to use more advanced algorithms; [Jefferies & Christou 1993](#); [Schoedel et al. 2011](#)). Changing the fraction of frames used in our analysis from 5% to 40% leaves our results unchanged within our estimated uncertainties. The final image derived from these data is shown in [Figure 5.4](#): the image exhibits an axisymmetric PSF with a Strehl ratio of roughly 8% and a full width at half maximum of $0.33''$, roughly a factor of 3 better than the seeing-limited resolution.

For astrometric reference we observed three known multiple systems taken from Version 2012-02-12 of the Washington Visual Double Star Catalog (WDS

Table 5.3. IRTF/SpeX Astrometric Calibrators^a

WDS identifier	Separation [arcsec]	Position Angle [degrees]
06295+3414	4.25 ± 0.14	256.8 ± 0.6
06051+3016	11.74 ± 0.40	177.3 ± 0.6
06508+2927	6.60 ± 0.22	23.7 ± 0.6

^aAll observations were made in the MKO K band on UT 2012 Feb 25.

06295+3414, 06051+3016, and 06508+2927 [Mason et al. 2001](#)) moderately near WASP-12, with comparable magnitudes to WASP-12, and with separations of 4-12". We took twenty 0.5-1 s frames of each system in the same region of the detector as our WASP-12 images, and in each frame we compute the centroids of both components using standard IRAF tasks. From these measurements and their dispersion we derive a SpeX guider plate scale of $0.116'' \pm 0.004''$ and an intrinsic field rotation (i.e., true position angle minus measured position angle) of $-0.5 \text{ deg} \pm 0.6 \text{ deg}$. We adopt these values in our subsequent analysis and list our astrometry of the WDS stars in [Table 5.3](#).

We determine the flux ratio of the two stars using aperture photometry. Bergfors-2 is again located in the PSF wings of WASP-12, so we must account for this contamination. Because our PSF is quite symmetric (though distinctly non-Gaussian) we compute an average radial profile for WASP-12 (after masking out the 90 deg wedge of sky directed toward Bergfors-2). We reinterpolate this one-dimensional profile into a two-dimensional model PSF. We estimate the uncertainty of the profile by taking the standard deviation on the mean in each annular bin, and propagate these uncertainties along with the combined photon and read noise. We then subtract the WASP-12 model PSF from the image and compute (partial-pixel) aperture photometry at the locations of Bergfors-2 and

WASP-12. Residuals are still apparent near the center of WASP-12, so we restrict our analysis to smaller apertures: an inner aperture radius of 2.5 pix provides the highest S/N (and least evidence for contamination) for Bergfors-2, so we use this aperture for both systems. Our final estimate of the K_{MKO} flux ratio is listed in Table 5.2, and it is consistent with our narrowband MOIRCS measurement.

We measure the relative astrometry of WASP-12 and Bergfors-2 by computing the centroid of WASP-12 in the speckle image, and of Bergfors-2 in the profile-subtracted image. We estimate the uncertainties in these measurements by bootstrap resampling (cf. Press 2002), in which we repeat our analysis many times using synthetic data sets, constructed by sampling (with replacement) our original set of 1,200 images. We list the separation and position angle derived from the IRTF speckle data in Table 5.2.

5.5.3.3 Spitzer/IRAC Imaging

We also examined Spitzer/IRAC subarray data (3.6 μm and 4.5 μm , from Cowan et al. 2012) to search for evidence of Bergfors-2. We performed a weighted least squares fit to each median stack of 64 subarray frames (using the pixel uncertainties provided by the IRAC calibration pipeline, Version 18.18.0) by linearly interpolating the appropriate $5\times$ oversampled point response functions⁴ (PRF) to account for subpixel motions.

We do see evidence for an additional point source in the IRAC data, located approximately 1-2 pixels west-southwest of WASP-12. However, we are unable to measure precise astrometry or relative photometry with these data for several reasons. First, the IRAC plate scale (1.09" pix^{-1}) is comparable to

⁴Available at <http://irsa.ipac.caltech.edu/data/SPITZER/docs/irac/calibrationfiles/psfprf/>

the WASP-12/Bergfors-2 separation; second, the IRAC PSF is undersampled at these wavelengths. Consequently, we see clear evidence for oversubtraction in the PRF fitting at the location of Bergfors-2, so we cannot reliably determine the system flux ratio (de-weighting the pixels closest to Bergfors-2, but offset from the WASP-12 core, does not change this result). From these measurements we estimate a flux ratio of $> 7\%$ in the two IRAC channels, consistent with our ultimate interpretation of Bergfors-2 as a cool stellar object.

5.5.3.4 Keck/NIRSPEC Spectroscopy

We searched online data archives for additional evidence of Bergfors-2, and found a set of high-resolution K band spectra taken with Keck/NIRSPEC (a high-resolution, cryogenic, echelle, NIR spectrograph; [McLean et al. 1998](#)) on UT 2010 Apr 22 (Keck Program ID C269NS, P.I. G. Blake). This data set consists of 16 four-minute integrations of WASP-12 taken using the $0.432' \times 24''$ slit. The WASP-12 observations were taken at a position angle of ~ 73 deg (roughly aligned with WASP-12 and Bergfors-2), and the seeing was sufficient to distinctly resolve the two components in the spectra. Our subsequent analysis focuses on the two most prominent gravity-sensitive features covered by these spectra: the ^{12}CO (2, 0) and (4, 2) bandheads located at $2.294 \mu\text{m}$ and $2.353 \mu\text{m}$ ([Kleinmann & Hall 1986](#)).

Using a high-resolution simulated telluric spectrum (generated using ATRAN; [Lord 1992](#)) we identify known telluric lines and compute a best-fit dispersion function in each echelle order. Estimating a line centroid precision of 0.5 pix, we find a cubic or quartic polynomial minimizes the BIC of these fits. The residuals to our dispersion solutions have RMS values $\lesssim 0.1\text{\AA}$ and maximum excursions of $< 0.2\text{\AA}$.

We extract our spectra using our own set of Python tools to trace the spectra in the dark-corrected and flat-fielded NIRSPEC frames. In each echelle order of each frame, we compute a high S/N mean spectral profile by collapsing the trace along the dispersion direction and fit two Gaussian functions to this profile: this provides an estimate of the projected separation of WASP-12 and Bergfors-2 in each frame. We then fit two Gaussian functions to each resolution element while holding constant the positions of the two sources: the amplitude of each Gaussian represents the flux in that wavelength element. We then compute weighted means from the individual extracted spectra and estimate uncertainties by measuring the variations in each pixel, after excluding points deviating by $> 3\sigma$.

In the raw NIRSPEC frames the spatial axis of the slit is not aligned with the NIRSPEC detector columns, so spectra taken at the A and B nod positions are offset from each other. We spline-interpolate the spectrum in each echelle order and cross-correlate it at sub-pixel increments with a high signal to noise (S/N) template spectrum (cf. [Deming et al. 2005a](#)). We construct our template by taking the temporal average, after removing outliers, of all our spectra. A parabolic fit to the peak of each spectrum's cross correlation provides the optimal offset value, and we then spline-interpolate all the spectra to a single, common reference frame. We then combine the resulting set of aligned spectra (excluding outlying points) and thereby provide a set of simultaneous high-resolution spectra of both WASP-12 and Bergfors-2. The spectra of WASP-12 and Bergfors-2 have median S/N values of 203 and 32 per pixel, respectively.

Because the two spectra are obtained simultaneously and the objects are separated by only $1''$ we expect the telluric absorption in the spectra to be indistinguishable. We therefore divide the spectrum of Bergfors-2 by that of WASP-12 to remove the effect of telluric absorption. Possible misalignment of the spectro-

graph slit prevent these data from usefully constraining the absolute flux ratio of these two objects, but the data place extremely strong constraints on the stars' relative flux densities. WASP-12's stellar parameters are already well-determined from high-resolution optical spectroscopy (Hebb et al. 2009); these NIR spectra place similarly strong constraints on the spectral type of Bergfors-2. As we describe in Section 5.5.4, we find that it is a hot M dwarf.

5.5.4 The Spectral Type of Bergfors-2

We considered that Bergfors-2 might be an extragalactic, rather than a stellar, contaminant (cf. Luhman & Mamajek 2010). However, a comparison of its photometric spectral energy distribution with low-resolution galactic spectral templates (Assef et al. 2010) suggests that this explanation is unlikely. Instead, with our four (i, z, K_{MKO}, K_{2315}) relative photometric measurements and the NIRSPEC spectrum we determine the spectral type of Bergfors-2, as described below.

5.5.4.1 Photometric Constraints

First, we apply the relationship between spectral type and absolute magnitude (Kraus & Hillenbrand 2007) using our photometry. This relationship is for main sequence stars, and WASP-12 is 25% larger than a zero-age main sequence star of the same mass (Torres et al. 2010). Accounting for this, and assuming $T_{eff} = 6300 \pm 100$ K, gives a distance modulus $\mu = 7.7 \pm 0.2$ mag (significantly nearer than the previous estimate; Chan et al. 2011). For Bergfors-2, our estimate of the $i - K$ color (after applying the color transformations of Carpenter 2001) implies a main-sequence spectral type of M0-M1 ($T_{eff} = 3700 \pm 100$ K). Assuming systematic uncertainties of 0.2 mag gives $\mu = 7.1 \pm 0.2$ mag, rather closer than WASP-12 if Bergfors-2 is a main sequence star. Note that this is the opposite

of the trend discussed by [Daemgen et al. \(2009\)](#), who uniformly estimated that their faint companions to planet host stars were more distant than the brighter component.

Next, we fit only the relative (Bergfors-2/ WASP-12) stellar photometry using low-resolution Castelli-Kurucz stellar atmosphere models ([Castelli & Kurucz 2004](#)). We interpolate to the effective temperature, [Fe/H], and surface gravity of WASP-12 and hold these values fixed in the modeling. For Bergfors-2 we assume a metallicity equal to that of WASP-12 and allow three free parameters: surface gravity, effective temperature, and a geometric factor (i.e., $\frac{R_X}{R_{W12}} \frac{d_{W12}}{d_X}$) relating the relative sizes and heliocentric distances of the two stars. A standard Pythonic minimizer and an MCMC analysis using the `emcee` affine-invariant sampler ([Foreman-Mackey et al. 2012](#)) provide the desired physical parameters and their uncertainties. The derived parameters for Bergfors-2 are 3840 ± 70 K and 0.452 ± 0.015 (which agrees well with our previous estimate of this object’s effective temperature); the covariance between these parameters is -1.73 K. The photometric data place an upper limit of $\log g(\text{cgs}) < 4.62$ (3σ limit) on Bergfors-2’s surface gravity.

5.5.4.2 Spectroscopic Constraints

However, spectroscopy is much better suited to constrain surface gravity. We now use both the NIRSPEC spectrum and the relative photometry described above to constrain Bergfors-2’s parameters, again using the `emcee` MCMC sampler ([Foreman-Mackey et al. 2012](#)). For this analysis we use the BT-Settl library⁵ ([Allard et al. 2010](#)) which provides high-resolution model spectra across a wide range of parameter space. We use the so-called “hot” models using abundances

⁵Available online at <http://phoenix.ens-lyon.fr/>

from [Asplund et al. \(2009\)](#) with no alpha enhancement. For simplicity and ease of computation we use only the two NIRSPEC echelle orders that cover CO bandhead features – the wavelengths from 2.273-2.308 μm and 2.344-2.380 μm .

We devise a model which, for a given set of input parameters, begins by logarithmically interpolating between BT-Settl models at the nearest values of T_{eff} , $\log g$, and $[M/H]$. The model then applies (a) a Doppler shift, (b) a quadratic continuum normalization (because the absolute slope and curvature of the spectrum is unknown owing to possible slit misalignments), and (c) a convolution with a Gaussian kernel of specified width. Finally, we bin the model spectrum onto our NIRSPEC pixel grid and compute relative broadband photometry as described in the preceding section – except that here we propagate the uncertainties in WASP-12’s parameters into the modeling by performing a random draw from normal distributions in T_{eff} , $\log g$, and $[M/H]$ at each step in the MCMC analysis that follows.

In our analysis the spectral type of Bergfors-2 is constrained almost entirely by the ~ 2000 spectroscopic data points, while the geometric ratio $\frac{R_X}{R_{W12}} \frac{d_{W12}}{d_X}$ is constrained only by the broadband photometry. The results of this analysis for Bergfors-2 are an effective temperature of 3660_{-60}^{+85} K and a $\log g$ (cgs) of $0.488_{-0.167}^{+0.234}$, and we show our best-fit model spectrum in [Figure 5.5](#). Our derived parameters are fully consistent with an M0 dwarf on the main sequence, which would imply a radius of $0.5 - 0.6R_{\odot}$ ([Torres et al. 2010](#)). The geometric ratio from our analysis is $0.520_{-0.037}^{+0.027}$, 50% larger than would be expected for a main-sequence dwarf lying at the same distance at WASP-12. Our spectral analysis therefore suggests that Bergfors-2 lies approximately 50% closer to Earth than does WASP-12 and that it represents a chance foreground alignment.

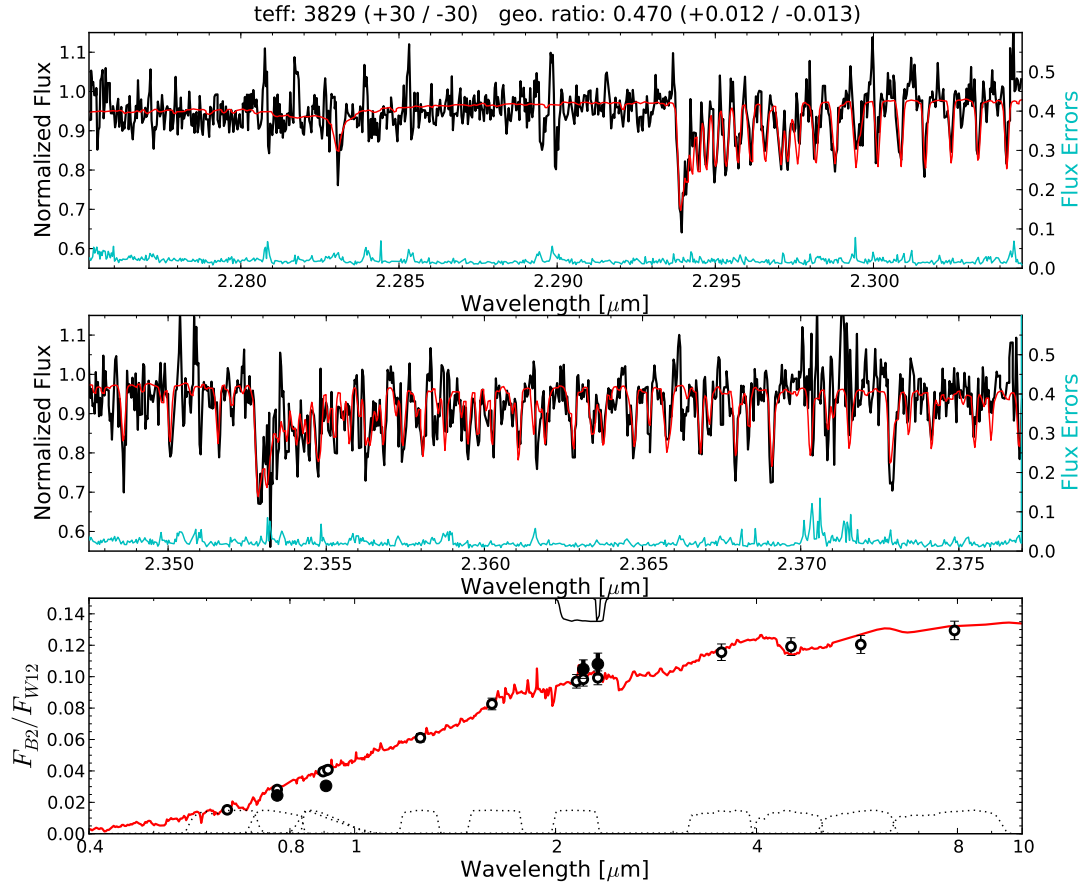


Figure 5.5 *Top*: Keck/NIRSPEC spectrum of Bergfors-2 (thick black curve, top and middle) and relative photometry of WASP-12 and Bergfors-2 (filled points, bottom), and our best-fit Phoenix/BT-Settl model (red curve). As discussed in Section 5.5.4, the ensemble of measurements suggests Bergfors-2 is a hot M dwarf located 50% closer to Earth than WASP-12. *Top and Middle*: The blue curves show our estimated spectroscopic measurement uncertainties; the vertical scale for these curves is indicated at right. *Bottom*: The open points at bottom are the inferred photometric dilutions of transits or eclipses measured in various bandpasses (tabulated in Table 5.4); we indicate filters used in this analysis with solid lines, while other filters are denoted with dashed lines. The error bars of the open points represent the 68.3% confidence intervals on these dilution estimates, taking into account the uncertainties in our fit.

5.5.5 Radial Velocities

We also use cross-correlation with BT-Settl models (Allard et al. 2010) to estimate the radial velocities of the two stellar components in our telluric-corrected Bergfors-2/WASP-12 ratio spectrum. We cross-correlate each echelle order of the ratio spectrum with models with effective temperatures of 6200 K and 3800 K. We also cross-correlate the spectra (before telluric correction) with the high-resolution atmospheric transmission profile of Hinkle et al. (2003) to establish our observational reference frame.

The radial velocity of Bergfors-2 is constrained mainly by the strong CO bands lying redward of $2.29 \mu\text{m}$, while WASP-12's is tightly constrained only by the broad (FWHM = 8.1\AA) Brackett γ line. After correcting for the Earth's velocity along the line of sight (using the Python routine `astrolib.baryvel`) we estimate radial velocities for WASP-12 and Bergfors-2 of $16.5 \pm 2.6 \text{ km s}^{-1}$ and $19.7 \pm 1.3 \text{ km s}^{-1}$, respectively. These values differ by $< 1.2\sigma$, and are both consistent with the radial velocity of 19.1 km s^{-1} derived from WASP-12b's initial radial velocity measurements (Hebb et al. 2009; Campo et al. 2011). This common velocity is consistent with a scenario in which WASP-12 and Bergfors-2 are gravitationally bound and share a common three-dimensional space motion.

We also find no evidence for multiple spectral line profiles that might indicate Bergfors-2 is an unresolved binary. The cross-correlation profiles of our data and spectral template have full-widths at half-maximum of approximately 14 km s^{-1} . All three echelle orders containing strong CO features (centered on 2.29 , 2.36 , and $2.44 \mu\text{m}$) show unimodal cross-correlation peaks and no evidence of the secondary peaks that would suggest an additional cool companion. Thus Bergfors-2 shows no spectroscopic evidence of binarity.

5.5.6 Interpretation of Bergfors-2

Thus we find that Bergfors-2 is a cool star with no luminous companions, and showing absorption features in its spectrum consistent with a high surface gravity. Our spectroscopy implies that Bergfors-2 is a main sequence star, and our relative photometry suggests that name lies 50% closer to Earth than does WASP-12. If Bergfors-2 were an unresolved binary this distance discrepancy would be relaxed and the objects could all lie at the same distance. There is a hint of North-South elongation in the [Bergfors et al. \(2011\)](#) discovery image and in our SpeX imaging (cf. Figure 5.4), but our NIRSPEC analysis shows no evidence of spectroscopic binarity.

High-resolution imaging will be required to determine whether WASP-12 and Bergfors-2 truly exhibit common proper motion and are gravitationally bound. Based on WASP-12's proper motion ($\sim 8 \text{ mas yr}^{-1}$; [Zacharias et al. 2004](#)), a two-year baseline of large-aperture adaptive optics imaging (cf. [Yelda et al. 2010](#)) could suffice to confirm or rule out common proper motion. Speckle or seeing-limited astrometry of the type presented here will not be sufficient for this purpose.

5.6 Revising Past Eclipse and Transit Measurements of WASP-12b

Because Bergfors-2 was not noted in previous transit and eclipse observations of WASP-12b, these flux diminutions were diluted by this faint star's constant baseline flux. This effect is largest in the infrared, but optical observations are significantly affected as well. Although a full re-evaluation of the WASP-12 system parameters is beyond the scope of this work, we correct the depth measurements

Table 5.4. WASP-12b Corrected Eclipse and Transit Depths

Filter	Reported Depth	Aperture Fraction	Dilution Fraction	Corrected Depth	Reference ^a
z	0.00082 ± 0.00015	1.000 ± 0.000	0.03973 ± 0.00172	0.00085 ± 0.00016	LM10
J	0.00131 ± 0.00028	1.000 ± 0.000	0.06057 ± 0.00292	0.00139 ± 0.00030	Cr11
H	0.00176 ± 0.00018	1.000 ± 0.000	0.08303 ± 0.00388	0.00191 ± 0.00020	Cr11
Ks	0.00309 ± 0.00013	1.000 ± 0.000	0.09806 ± 0.00466	0.00339 ± 0.00014	Cr11
Ks (MKO)	0.00281 ± 0.00085	1.000 ± 0.000	0.09937 ± 0.00471	0.00309 ± 0.00093	Z12
NB2315	0.00414 ± 0.00048	1.000 ± 0.000	0.10022 ± 0.00454	0.00455 ± 0.00053	This work
IRAC CH1	0.00379 ± 0.00013	0.902 ± 0.018	0.11677 ± 0.00548	0.00419 ± 0.00014	Ca11
IRAC CH2	0.00382 ± 0.00019	0.911 ± 0.016	0.12037 ± 0.00598	0.00424 ± 0.00021	Ca11
IRAC CH3	0.00629 ± 0.00052	0.855 ± 0.036	0.12166 ± 0.00600	0.00694 ± 0.00057	Ca11
IRAC CH4	0.00636 ± 0.00067	0.788 ± 0.068	0.13065 ± 0.00633	0.00701 ± 0.00074	Ca11
IRAC CH1	0.00330 ± 0.00040	0.827 ± 0.052	0.11677 ± 0.00548	0.00362 ± 0.00044	Co12
IRAC CH2	0.00390 ± 0.00030	0.850 ± 0.038	0.12037 ± 0.00598	0.00430 ± 0.00033	Co12
IRAC CH1	0.01250 ± 0.00030	0.827 ± 0.052	0.11677 ± 0.00548	0.01371 ± 0.00033	Co12
IRAC CH2	0.01120 ± 0.00040	0.850 ± 0.038	0.12037 ± 0.00598	0.01235 ± 0.00044	Co12
B/z'	0.01380 ± 0.00020	0.950 ± 0.100	0.03911 ± 0.00171	0.01431 ± 0.00021	H09
Johnson R	0.01380 ± 0.00016	1.000 ± 0.000	0.01571 ± 0.00096	0.01402 ± 0.00016	M11
V/i'	0.01252 ± 0.00045	0.230 ± 0.100	0.02806 ± 0.00143	0.01260 ± 0.00045	C11

^aLM10: [López-Morales et al. \(2010\)](#), Cr11: [Croll et al. \(2011b\)](#), Z12: [Zhao et al. \(2012\)](#), Ca11: [Campo et al. \(2011\)](#), Co12: [Cowan et al. \(2012\)](#), H09: [Hebb et al. \(2009\)](#), M11: [Maciejewski et al. \(2011\)](#), C11: [Chan et al. \(2011\)](#)

^bThese transit analyses average multiple photometric bands, so their correction factors may be less precise.

for the contamination effect and present revised transit and eclipse depths below. We propagate the uncertainties in Bergfors-2's effective temperature into our estimates of the photometric dilution caused by Bergfors-2, which we list in Table 5.4. In some eclipses, and in all transits, the corrections we apply change the previously reported depths by $> 1\sigma$.

Essentially all the light from Bergfors-2 lies within the apertures of ground-based observations ([Hebb et al. 2009](#); [López-Morales et al. 2010](#); [Croll et al. 2011b](#); [Chan et al. 2011](#); [Maciejewski et al. 2011](#); [Crossfield et al. 2012a](#)), but Spitzer/IRAC analyses use narrower apertures ([Campo et al. 2011](#); [Cowan et al. 2012](#)) and so only a portion of the starlight contaminates the eclipse measurement.

To estimate the IRAC contamination fraction we generate $10\times$ super-sampled

PSFs for all four IRAC channels⁶, using a 6300 K blackbody spectrum simulated at the center of the instrument field of view. We then compute aperture photometry using the reported photometric aperture diameters (Campo et al. 2011; Cowan et al. 2012) at a position offset by 1.05'' from the PSF center to estimate how much of Bergfors-2's flux fell into the WASP-12 aperture in these analyses. We ignore possible time-variable illumination caused by the intrapixel effect (Charbonneau et al. 2005), which is not significant for this analysis.

The correction of optical transit measurements is complicated by the standard but deplorable practice of averaging together transits observed in different bandpasses (Hebb et al. 2009; Chan et al. 2011). These analyses are not always clear about the relative weighting of data points from separate observations. A preferred practice would be for future analysis of multiple photometric data sets to report the transit depths measured in each bandpass in addition to the final averaged value. Nonetheless we attempt to estimate the relative weightings and derive appropriate correction factors for prior multi-band optical transit observations of WASP-12.

The discovery paper (Hebb et al. 2009) used two transit data sets: 227 B band and 614 z' band observations with residual RMS values of 7 and 2.5 mmag, respectively. From these quantities we estimate that the relative weighting of the z' and B data are 95% and 5%, respectively. The situation is similar for the recent report of Chan et al. (2011), who also analyze two data sets: 671 V band and 470 i' band⁷ observations with residual RMS values of 2.0 and 1.2 mmag, respectively. This work uses an additional multiplicative term to increase the per-point data uncertainties (1.48 and 1.57, respectively). In this case the two data sets constrain the transit parameters with roughly equal weight.

⁶Using Tiny Tim; available at <http://ssc.spitzer.caltech.edu/>

⁷The previous indication of z' was in error (J. Winn, private communication).

We use these weights to determine a weighted average of the correction factors for each bandpass. For simplicity we assume that the bluer filter contributes zero contaminating light from Bergfors-2. Because of this assumption, and because such a weighted average is only a rough approximation to the true correction factor, the correction factors for these analyses are less certain and for now we double the uncertainties in the corrected transit depths listed in Table 5.4. In contrast, the analysis of Maciejewski et al. (2011) used only a single bandpass (Johnson R) and so their Johnson R transit depth is the most reliable optical transit measurement in Table 5.4.

5.7 Results: Thermal Emission from WASP-12b

5.7.1 Planetary Emission

The first systematic effort to retrieve WASP-12b’s atmospheric parameters (using infrared broadband eclipse photometry) inferred a high C/O ratio and ruled out any strong temperature inversion at the pressures probed (0.01-2 bar; Madhusudhan et al. 2011a). That study determined an atmospheric C/O abundance ratio > 1 and published several representative models. All these models predict a strong absorption feature (depth $\lesssim 0.2\%$) at $2.315 \mu\text{m}$. Our eclipse measurement strongly rules out this absorption feature at $> 4\sigma$.

We plot WASP-12b’s corrected photometric emission spectrum in Figure 5.6, along with several blackbody spectra of different temperatures. Our eclipse depth corresponds to a brightness temperature of $3660 \text{ K} \pm 210 \text{ K}$: this value is $\sim 3\sigma$ higher than the planet’s equilibrium temperature (Cowan et al. 2012) and higher than inferred in any broad photometric bandpass (López-Morales et al. 2010; Croll et al. 2011b; Campo et al. 2011; Cowan et al. 2012). The CFHT/WIRCam

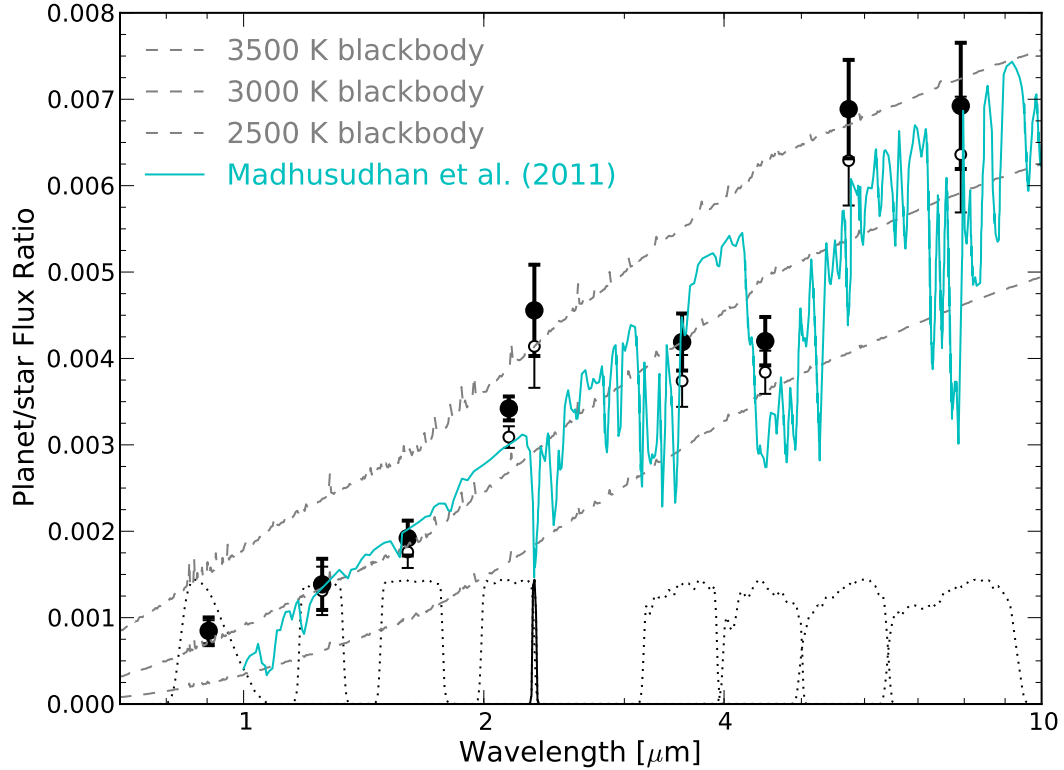


Figure 5.6 Emission spectrum of WASP-12b, expressed as the ratio of planet flux to stellar flux. Old values are shown as open points, and measurements corrected for Bergfors-2’s “Second Light” (as described in Table 5.4) are shown as solid points. Our new measurement is shown at $2.315\ \mu\text{m}$. The broadband measurements are those of López-Morales et al. (2010), Croll et al. (2011b), Campo et al. (2011), and Cowan et al. (2012); we taken the weighted average of the two sets of IRAC 3.6 and $4.5\ \mu\text{m}$ measurements to produce the values plotted here. The light blue curve is a representative model of WASP-12b from Madhusudhan et al. (2011a). Dashed gray lines indicate blackbodies of the temperatures noted.

Ks filter cuts off just where the NB2315 filter cuts in, so our measurement is not in conflict with this previous eclipse observation (Croll et al. 2011b).

There is some CO opacity at $2.315\ \mu\text{m}$, (as evidenced in spectra of cool giant stars; cf. Kleinmann & Hall 1986; Rayner et al. 2009), but our filter does not intersect the main CO band head opacity. In addition, it is not clear why we would

see CO in emission when Spitzer/IRAC2 eclipses have been used to infer strong CO absorption at $4.5\ \mu\text{m}$ (Campo et al. 2011; Madhusudhan et al. 2011a; Cowan et al. 2012). Perhaps both effects are due to CO but the different wavelengths are merely probing substantially different parts of the temperature-pressure regime.

While CH_4 has a strong band head at this wavelength, (as observed in the telluric transmission spectrum and in spectra of L dwarfs; cf. Hinkle et al. 2003; Cushing et al. 2005), but in chemical and thermodynamic equilibrium this species should not form prominent spectral features at the high temperature of WASP-12b (e.g., CH_4 is not observed in early M dwarf spectra; Cushing et al. 2005). Models do exist for WASP-12b (before correction of the eclipse depths) in which the CH_4 mixing ratio is greater than that for CO (Madhusudhan et al. 2011a, their Figure 2) – but in any case our measurement suggests emission, while Madhusudhan et al. (2011a) ruled out strong temperature inversion in WASP-12b’s atmosphere.

Thus if WASP-12b’s broadband emission spectrum has been accurately measured, our narrowband photometry may probe a qualitatively different pressure-temperature regime than does the IRAC2 point. If our narrowband observations probe sufficiently high in the atmosphere (above 1 mbar) we could be seeing the effect of a localized thermal inversion induced either by high-altitude absorption of the incident stellar irradiation (cf. Spiegel et al. 2009) or by planetary circulation (Hansen 2008) caused by the planet’s extreme (2000 K) day/night temperature contrast (Cowan et al. 2012). Further modeling, and above all high-fidelity spectroscopic observations, are needed to divine the nature of WASP-12b’s atmosphere.

5.7.2 Alternative Explanations for a Deep 2.315 μm Eclipse

5.7.2.1 Strange Stellar Spectrum: Rejected

An alternative interpretation of our 2.315 μm eclipse depth is that WASP-12b's emission is not excessive at this wavelength, but that instead WASP-12 is anomalously fainter (because we only measure the ratio F_P/F_*). We reject this hypothesis using both broadband photometry and IRTF/SpeX spectroscopy. We first compare the $Ks - [2.315 \mu\text{m}]$ colors of several stars with $Ks < 14.5$ using 2MASS photometry (Skrutskie et al. 2006) and our MOIRCS images. We find that the WASP-12+Bergfors-2 total flux has a net color offset of $\Delta(Ks - [2.315]) = -0.057 \pm 0.046$ compared to other stars in our field of view, suggesting a possible slight flux excess at 2.315 μm , rather than the flux dearth that would be required by this hypothesis.

We also obtained flux-calibrated, combined-light spectra of WASP-12 and Bergfors-2 with IRTF/SpeX. On 2012 Mar 15 (UT) we obtained ten 60 s AB nod pairs of the WASP-12 system in SXD mode. We aligned the slit along the line connecting the stars by setting the instrument rotator at a position angle of 72 deg. Comparison of the spectrum (extracted using the SpeXTool package; Cushing et al. 2004) to typical F8 stars from the IRTF Spectral Library (Rayner et al. 2009) demonstrates no unusual flux variations at 2.315 μm of greater amplitude than 1-2%. We therefore conclude that our large measurement of F_P/F_* indicates higher-than-expected planetary emission, rather than lower-than-expected stellar emission.

5.7.2.2 Telluric Variations: Rejected

The claim of strong, non-equilibrium CH₄ emission in HD 189733b (Swain et al. 2010) was disputed on the basis of contamination by telluric effects (Mandell et al. 2011). However, the types of spectral contamination discussed by Mandell et al. (2011) do not apply to relative photometry. Changes in telluric absorption are common mode and should be removed when we divide the flux from WASP-12 by the comparison star flux. Variable telluric emission should be removed by the combination of global sky frame subtraction and local background subtraction in the aperture photometry process (cf. Section 5.3.2).

As discussed in Section 5.3.3, our narrowband filter intersects a strong telluric (CH₄) absorption feature located at 2.317 μm . Though this absorption feature could explain the systematic photometric ramp (seen shortly after WASP-12 crosses the meridian; cf. Figure 5.2) when considered in concert with the wavelength dependence of our filter transmission profile on its orientation relative to incoming light, it seems unlikely that telluric variations could slip through the analysis and masquerade so perfectly as an eclipse with the expected duration and time of center.

5.7.2.3 WASP-12b is Not a Planet: Rejected

Though we were slightly unnerved to discover a 3800 K M dwarf very close to a system hosting a 3100 K hot Jupiter, we can nonetheless reject the hypothesis that WASP-12b is either a background eclipsing binary or a smaller, nonluminous object transiting Bergfors-2. First, the planet's discovery paper (Hebb et al. 2009) shows no evidence of a correlation between radial velocity and the bisector spans (a common diagnostic to guard against contamination by background stars; Torres et al. 2004).

A further argument that WASP-12b is, indeed, a planet is the achromaticity of the planet’s transit depth from 0.5-4.5 μm , as shown in Table 5.4. The eclipse depths of eclipsing binaries containing luminous objects (i.e., stars) exhibit a strong wavelength dependence, but this is not observed for WASP-12b. If WASP-12b were instead a nonluminous object transiting Bergfors-2, because of the wavelength-dependent transit dilution the optical transit depth would imply that Bergfors-2 was roughly half-obscured, while the infrared transit depth would imply that only one-tenth of Bergfors-2 was obscured. We predict that imminent HST/WFC3 grism spectroscopy of WASP-12 will definitively demonstrate that WASP-12, not Bergfors-2, is being transited.

5.8 Discussion

Our analysis suggests a deeper-than-expected eclipse ($0.455\% \pm 0.053\%$) of the very hot Jupiter WASP-12b in a narrow band centered at 2.315 μm . This feature has a brightness temperature of $3660\text{ K} \pm 210\text{ K}$, hotter than WASP-12b’s 3300 K equilibrium temperature (assuming $A_B = 0.25$ and zero heat redistribution; Cowan et al. 2012) and as hot as the planet’s substellar equilibrium temperature. Our precision is lower than expected because of an unanticipated systematic trend affecting both sky background and stellar photometry, but we are able to exclude data affected by this trend. The duration and timing of the eclipse we measure from these data are consistent with a circular orbit and with previous measurements (Hebb et al. 2009; Croll et al. 2011b; Campo et al. 2011; Cowan et al. 2012).

Using NIR photometry and high-resolution spectroscopy, we find that a previously identified object only 1” from WASP-12 (Bergfors et al. 2011) is a 3660^{+85}_{-60} K dwarf star, which we name Bergfors-2. If this object is an unresolved binary of

roughly equal mass it could lie at the same distance from Earth as does WASP-12. However, our Keck/NIRSPEC spectroscopy of this object shows no evidence for binarity. If single, it likely lies 50% closer to Earth than does WASP-12. Adaptive optics imaging on large-aperture telescopes will be necessary to conduct the proper motion studies necessary to discriminate between these two scenarios. If WASP-12 and Bergfors-2 are gravitationally bound, further simulations (along the lines of [Ibgui et al. 2011](#)) should be undertaken to determine whether Kozai interactions with an object with Bergfors-2's characteristics could have caused WASP-12b's inward migration and, through tidal pumping, have inflated the planet's radius ([Bodenheimer et al. 2001](#)).

The presence of Bergfors-2 so close to WASP-12 caused the former to pass unnoticed in previous transit and eclipse observations, which results in a dilution of the depths of these events. We use our constraints on Bergfors-2 to infer and correct for the dilution of these observations. In several cases this correction increases depths by $> 1\sigma$, with the result that WASP-12b is slightly larger and hotter than previously believed. These large changes emphasize the importance of high-resolution imaging surveys in the vicinity of newly discovered transiting planets.

Our $2.315\ \mu\text{m}$ narrowband measurement of the planet/star contrast ratio is $> 4\sigma$ higher than predicted by previous models of WASP-12b used to infer a high carbon to oxygen ratio for this planet ([Madhusudhan et al. 2011a](#)), as shown in [Figure 5.6](#). Both CO and CH₄ are strong absorbers at this wavelength, but in equilibrium conditions CH₄ is not expected to be abundant at the high temperature inferred for this planet. Thus it seems we are seeing CO emission from WASP-12b – but Spitzer/IRAC $4.5\ \mu\text{m}$ eclipse photometry suggest CO absorption, not emission ([Croll et al. 2011b](#); [Campo et al. 2011](#); [Madhusudhan et al.](#)

2011a).

The two wavebands could be sampling different parts of the atmospheric temperature profile; for example, models of emission from HD 189733b and HD 209458b estimate that observations at $2.30\ \mu\text{m}$ probe pressures roughly a factor of four greater than $4.5\ \mu\text{m}$ photometry (Moses et al. 2011) whether or not an inversion is present. Such a span of pressures corresponds to a temperature range of $\leq 1000\ \text{K}$, (depending on the pressure level being probed; Madhusudhan et al. 2011a), which would be sufficient to account for the different brightness temperatures observed from WASP-12b at $2.315\ \mu\text{m}$ and $4.5\ \mu\text{m}$. However, whether WASP-12b’s emission spectrum (shown in Figure 5.6) is more consistent with or without a temperature inversion remains to be seen.

Because of the systematic effects present in our data and our short out-of-eclipse baseline, our observations should be confirmed. Though additional narrowband photometry (from the ground or, if available, using HST/NICMOS) could accomplish this goal, single- or multi-object spectroscopy (cf. Bean et al. 2011; Berta et al. 2012; Crossfield et al. 2012a), or perhaps by high-resolution phase curve spectroscopy (e.g., Barnes et al. 2007), would be more amenable to interpretation and would avoid the degeneracies inherent in the interpretation of photometry. In addition, we suggest that the current set of one-dimensional, mean-dayside models of WASP-12b (Madhusudhan et al. 2011a) may not be adequate for such a distorted object with such a large day/night temperature gradient. Three-dimensional models, ideally coupled with a general circulation model of the planetary atmosphere’s dynamics, may hold the best hope for unraveling the mystery of WASP-12b’s atmospheric structure and composition.

CHAPTER 6

Transmission Spectroscopy of GJ 1214b

6.1 Abstract

The nearby star GJ 1214 hosts a planet intermediate in radius and mass between Earth and Neptune, resulting in some uncertainty as to its nature. We have observed this planet, GJ 1214b, during transit with the high-resolution, near-infrared NIRSPEC spectrograph on the Keck II telescope, in order to characterize the planet's atmosphere. By cross-correlating the spectral changes through transit with a suite of theoretical atmosphere models, we search for variations associated with absorption in the planet atmosphere. Our observations are sufficient to rule out tested model atmospheres with wavelength-dependent transit depth variations $\gtrsim 5 \times 10^{-4}$ over the wavelength range $2.1 - 2.4 \mu\text{m}$. Our sensitivity is limited by variable slit loss and telluric transmission effects.

We find no positive signatures but successfully rule out a number of plausible atmospheric models, including the default assumption of a gaseous, H-dominated atmosphere in chemical equilibrium. Such an atmosphere can be made consistent if the absorption due to methane is reduced. Clouds can also render such an atmosphere consistent with our observations, but only if they lie higher in the atmosphere than indicated by recent optical and infrared measurements.

When taken in concert with other observational constraints, our results support a model in which the atmosphere of GJ 1214b contains significant H and

He, but where CH_4 is depleted. If this depletion is the result of photochemical processes, it may also produce a haze that suppresses spectral features in the optical.

6.2 Introduction

6.2.1 Characterizing Extrasolar Atmospheres

Astronomers are poised to soon discover the first rocky, Earth-like exoplanets orbiting in the habitable zone – the region where water could be expected to be liquid on the planet’s surface. Already, ground-based exoplanet surveys are finding super Earths (planets several times Earth’s mass and radius) such as GJ 1214b with temperatures only a few hundred degrees hotter than Earth ([Charbonneau et al. 2009](#)) – much more hospitable than the more easily detected giant, highly irradiated Hot Jupiters. In addition, the *Kepler* spacecraft is currently searching for the subtle, periodic dip in a star’s brightness that will indicate an Earth-sized planet in an Earth-like orbit has passed in front of its Sun-like stellar host, and indeed a preliminary list of 54 habitable planet candidates has already been released ([Borucki et al. 2011](#)).

Transit and radial velocity measurements can constrain the radius and mass of a planet, but significant degeneracies remain in the determination of interior and atmospheric composition. From theoretical models of planetary interiors we know that any Jupiter-sized object is composed primarily of H_2 and He. A super Earth is more complicated and thus more interesting: it could be a small, rocky core with an extended H_2/He envelope (a mini-Neptune), a larger, icy core with a denser molecular atmosphere (a scaled-up Ganymede), or something in between ([Rogers & Seager 2010](#)). To determine the true makeup of such a planet we need

precise methods to characterize the atmospheres of these new worlds.

All else being equal, planets which transit small, low-mass stars are the most favorable targets for atmospheric characterization because the planet/star size ratio R_P/R_* is especially high. When the host star occults the planet one can measure the planet’s intrinsic emission spectrum; when the planet transits its star, the transit depth will vary with wavelength in a way that reflects absorption in the atmosphere at the limb of the planet. This quantity, $(R_P(\lambda)/R_*)^2$, is often called the transmission spectrum of the planet. The wavelength-dependent atmospheric signature during transit is a variable function of wavelength, but in general is proportional to the relative area of the atmospheric annulus probed, i.e. $HR_P(\lambda)/R_*^2$, where H is the standard atmospheric scale height (Miller-Ricci et al. 2009). In the most favorable cases the transmission spectrum’s features vary by a factor of (roughly) 10^{-3} relative to the flux from the planet’s host star – challenging to detect, but much more tractable than the expected planet/star flux contrast of $\lesssim 10^{-4}$ from a relatively temperate planet.

While numerous transit observations have been made from space, it is only in the last few years that ground-based infrared characterization has met with success. Ground-based infrared photometry is becoming almost commonplace (e.g., Rogers et al. 2009; Croll et al. 2011b), but ground-based spectroscopy remains challenging. Swain et al. (2010) reported the detection of the K and L band emission spectrum of HD 189733b, but these results are contested (Madhusudan & Seager 2009; Mandell et al. 2011). On a more optimistic note, the recently reported detection of CO on HD 209458b (Snellen et al. 2010) demonstrates the power of template cross-correlation techniques for ground-based spectroscopy. We will adopt a similar philosophy in this paper.

Recent observations of the low mass planet GJ 1214b represent some of the

most precise ground-based exoplanet spectroscopy to date (Bean et al. 2010), and show a flat transmission spectrum from $0.75 - 1 \mu\text{m}$. Our study aims to complement these results in the near-infrared. In this paper we describe our observations of GJ 1214b in an attempt to detect the differential transmission spectrum of the planet’s atmosphere. We describe the GJ 1214 system and the suite of atmospheric models we test in Section 6.3. We discuss our observations and data reduction in Section 6.4, and describe our methods for measuring relative spectrophotometry and performing model template cross-correlations in Section 6.5. We discuss our results and possible future work in Section 6.6 and conclude in Section 6.7. Finally, in Sec. 6.8 we briefly discuss observations of GJ 1214b that have occurred since the publication of the work presented in this chapter (Crossfield et al. 2011).

6.3 Observations and Atmospheric Models

6.3.1 The GJ 1214 System

GJ 1214b is the first planet discovered by the MEarth project (Irwin et al. 2009), a transit survey targeting the nearest red dwarfs. The planet orbits a 3000 K, M4.0-4.5 dwarf with high metallicity (+0.3 to +0.4; Schlafman & Laughlin 2010; Rojas-Ayala et al. 2010). The star displays a periodic, 1% variability in the red optical and evidence of spots is seen during planetary transits, but the star appears to be only weakly active and spot features should affect near-infrared transmission spectroscopy only at the < 0.0003 level (Berta et al. 2011) – beneath the sensitivity we achieve in this work. Because the star is so cool, the system is most amenable to characterization at infrared wavelengths. With a semimajor axis of 0.014 AU, the planet’s (albedo-dependent) equilibrium temperature is

400-550 K (Charbonneau et al. 2009).

GJ 1214b’s size and mass (2.65 and 6.45 times that of the Earth, respectively; Carter et al. 2011) give it a density intermediate to that of our solar system’s inner (rocky) and outer (gas-dominated) planets. GJ 1214b occupies an intriguing location in the planetary mass-radius diagram, inasmuch as these two bulk characteristics allow for substantial degeneracies in models of the planet’s interior composition. Nonetheless, models generally suggest that the planet has a substantial gas component, making it potentially amenable to atmospheric characterization (Rogers & Seager 2010; Nettelmann et al. 2011).

Though the present constraints on GJ 1214b’s bulk composition preclude any unique predictions of the planet’s atmospheric structure and composition, Miller-Ricci & Fortney (2010) predicted that the planet would show substantial ($\leq 10^{-3}$) variations in transit depth with wavelength if it hosts a cloudless, H₂/He-dominated atmosphere. They also predicted that the atmospheric signature would be an order of magnitude lower – essentially undetectable in the near-infrared – for a denser atmosphere dominated by heavier molecular species. Any clouds in GJ 1214b’s atmosphere would further mask the presence of any spectral signals.

The planet to star size ratio R_P/R_* of the GJ 1214 system has been measured photometrically in the optical (Charbonneau et al. 2009; Carter et al. 2011; Berta et al. 2011) and mid-infrared (Désert et al. 2011) and with optical spectroscopy (Bean et al. 2010). These measurements all agree to within $\lesssim 2\%$, and have been interpreted as evidence for a clear atmosphere dominated by heavy molecular species (Désert et al. 2011). An atmosphere obscured by clouds or haze would also be consistent with these observations, but a haze would need to be composed of rather large (several microns) particles to flatten the spectrum all the way into

the mid-infrared (Désert et al. 2011). On the other hand, recent measurements in the near infrared (Croll et al. 2011a) argue for a larger radius at Ks-band, indicative of a H-dominated atmosphere with large scale height. One way to make the observations consistent with one another is to postulate a methane-depleted atmosphere with a haze of small particles at $R_P/R_* \approx 0.1165$ to smooth out features in the optical (Désert et al. 2011; Croll et al. 2011a).

6.3.2 Atmospheric Models of GJ 1214b

We test our observations (described in Section 6.4) by comparing them to high-resolution model transmission spectra. Thus our detection method is only as good as the molecular line lists we use for our models: significant revision of the near-infrared opacities would require a recalculation of the constraints we ultimately present.

To explore a variety of atmospheric conditions in GJ 1214b we generated several irradiated planetary models using the PHOENIX code, assuming traditional H₂/He-rich atmospheres (Barman et al. 2005). The baseline models were taken to be cloud free with either solar (Asplund 2005), 10× solar, or 30× solar abundances (i.e., the abundance of all elements other than H and He enhanced by the specified factor), and we used the bulk planet and star parameters from Charbonneau et al. (2009).

We generated the following atmospheric models:

- Solar composition and equilibrium chemistry.
- 10× solar abundance and equilibrium chemistry. This model has a slightly smaller radius, and is hotter below 0.1 mbar, than the solar model.
- 30× solar abundance and equilibrium chemistry. This model has a slightly

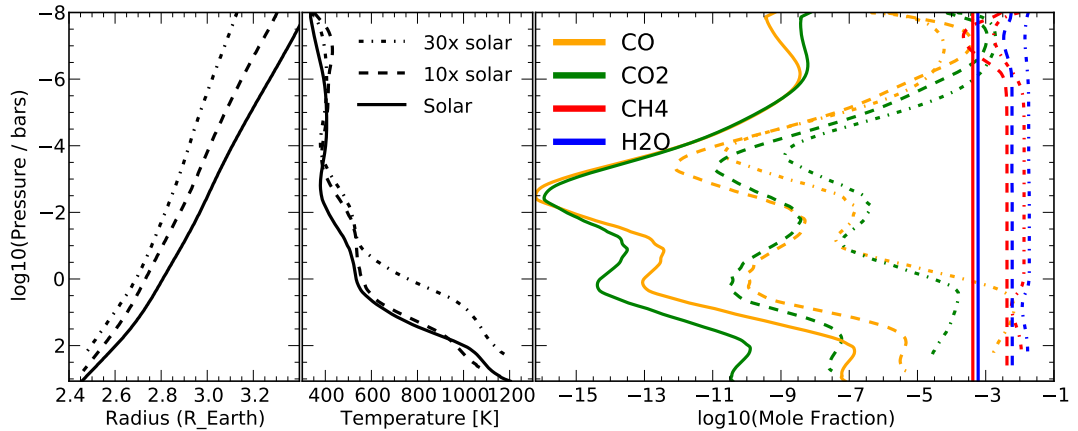


Figure 6.1 Atmospheric parameters for our solar (dot-dashed), $10\times$ solar (dashed), and $30\times$ solar (solid) abundance models. From left to right, the panels show as a function of pressure: the effective planetary radii, the atmospheric temperature profiles, and the abundances of several species. We discuss our models in Section 6.3.2, and show transmission spectra in Figure 6.2 and 6.3.

higher temperature and smaller radius than the solar and $10\times$ solar models.

- No methane. Solar composition, but with the concentration of CH_4 set to zero. We used this model to interpolate to various levels of atmospheric CH_4 . This allows us to test the hypothesis that CH_4 abundances may be substantially reduced in cooler atmospheres at the pressures probed by transmission spectroscopy (Zahnle et al. 2009; Désert et al. 2011).
- Low carbon abundance. This model assumes chemical equilibrium but with the carbon abundance set to 10^{-8} relative to solar; this factor is roughly comparable to the ratio of the lowest and highest carbon-containing compounds found in our solar abundance model. This model is similar to the methane-depleted model just described, but features from residual CH_4 are still visible from 2.2-2.35 μm .

We plot the atmospheric temperature profiles and the abundance of several molecular species as a function of pressure for several of these models in Figure 6.1.

For each model we compute the monochromatic planetary radii, $R_P(\lambda)$, with PHOENIX under the assumption of spherical symmetry (Barman 2007) and with a wavelength sampling of 0.05 \AA from $1 - 3 \text{ \mu m}$. Each radius spectrum is then convolved with a Gaussian kernel to the instrumental resolution and then interpolated onto the observed wavelengths. We also compute the quantity σ_{R_P} , defined as the standard deviation of the planet radius at our model resolution over the wavelength range used in our analysis. A completely flat spectrum would have $\sigma_{R_P} = 0$ and be undetectable by our methods, but models with sufficiently prominent spectral features – which we can detect – have larger values. To facilitate comparison of σ_{R_P} with our sensitivity limits we list these values in Table 6.4 with the final results of our analysis.

Note that all of our models are H_2/He -dominated. The small atmospheric scale height of an atmosphere dominated by heavier molecules results in a suppressed transmission spectrum with features undetectable at our precision (cf. Miller-Ricci & Fortney 2010). We list some of the models we test, and the $R_P(\lambda)$ they predict when observed with various broadband filters, in Table 6.1. We plot $R_P(\lambda)$ from a selection of our models in Figure 6.2 across the near-infrared, and in Figure 6.3 zoomed in on the spectral regions probed by our NIRSPEC observations.

In the infrared, as in the optical, clouds can alter the transit spectrum by blocking flux below a certain radius, establishing different minimum radii compared to cloud-free models. The impact of cloud opacity was tested for the cloud-free models described above by truncating the model radius spectrum at several different values, in effect inserting an opaque cloud deck at a desired level in the atmosphere. This means that in our cloudy cases we set all values of $R_P(\lambda)$ less than a given radius equal to that radius.

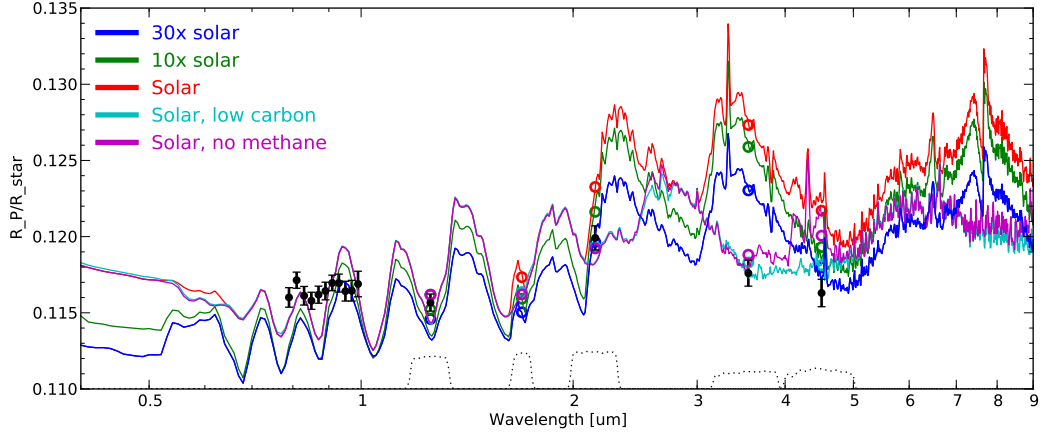


Figure 6.2 A selection of our model transmission spectra of GJ 1214b (solid lines; smoothed for display purposes). The dashed lines at bottom represents the effective throughput of the WIRCam J, CH4-on, and Ks and IRAC 1 & 2 filters. The open circles show the averages of our models over the several filters, and the solid points are the observations (Bean et al. 2010; Désert et al. 2011; Croll et al. 2011a). The spectroscopic analysis presented in this paper rules out all but the low carbon and no methane models (cf. Table 6.4). We describe these models in Section 6.3.2 and Table 6.1.

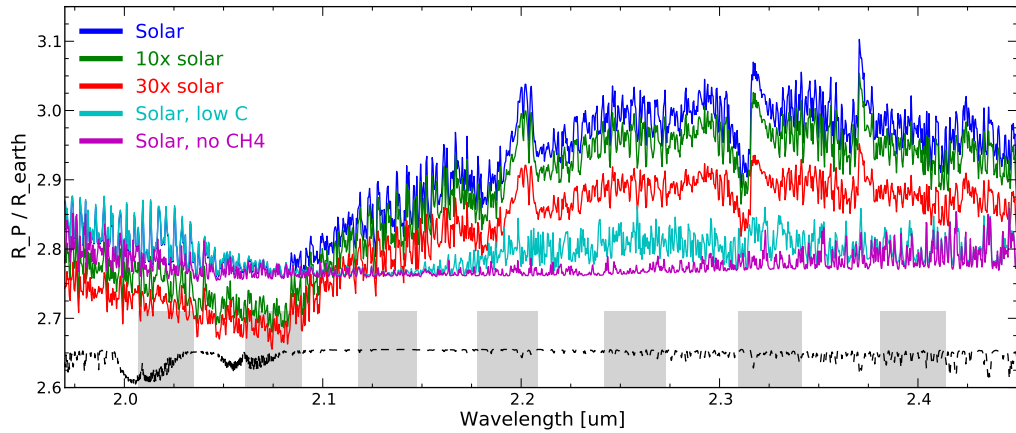


Figure 6.3 A selection of the same model transmission spectra shown in Figure 6.2, showing only the wavelength range covered by our observations and smoothed for display purposes. The shaded regions represents those wavelength we observed; the regions are discontinuous due to NIRSPEC’s echelle format. The dashed line represents the telluric transmission (Hinkle et al. 2003).

Table 6.1. GJ 1214b Predicted Photometric Transit Radii (cf. Figure 6.2)

Model	R_{min}^a / R_{\oplus}	J ^b	CH4-on ^b	Ks ^b	IRAC1 (3.6 μ m)	IRAC2 (4.5 μ m)
Solar	-	2.665	2.692	2.828	2.921	2.792
Solar	2.85	2.850	2.850	2.877	2.921	2.851
Solar	2.90	2.900	2.900	2.909	2.931	2.900
10x solar	-	2.643	2.659	2.790	2.888	2.737
10x solar	2.85	2.850	2.850	2.865	2.892	2.850
10x solar	2.90	2.900	2.900	2.901	2.911	2.900
30x solar	-	2.629	2.639	2.745	2.823	2.707
Solar, low carbon	-	2.665	2.669	2.737	2.714	2.710
Solar, no methane	-	2.665	2.666	2.735	2.726	2.754

^aPlanetocentric radius of artificially imposed near-infrared opaque cloud deck; cf. Section 6.3.2

^bNear-infrared radii computed using the CFHT/WIRCam filter profiles at <http://www.cfht.hawaii.edu/Instruments/Filters/wircam.html>

6.4 NIRSPEC Observations and Analysis

6.4.1 Summary of Observations

The temperature of GJ 1214b is such that we expect many prominent spectral features in the near infrared, and we therefore observed GJ 1214b using the NIRSPEC cryogenic near-infrared echelle spectrograph (McLean et al. 1998), located at the Nasymth focus of the Keck II telescope. Our observations covered one transit each in both the H and K near-infrared bands; we list the details of these observations and our instrumental setup in Table 6.2.

On both nights we observed the GJ 1214 system continuously for as long as conditions permitted. We designed our observations to minimize possible sources of systematic error, and thus did not nod the telescope. Our prior experience with NIRSPEC and with SpeX (a moderate-resolution spectrograph at the NASA Infrared Telescope Facility) has taught us that nodding induces an undesirable “sawtooth” pattern in the extracted spectrophotometry (presumably due to residual flat-field variations), while it does not provide a substantial im-

Table 6.2. Keck/NIRSPEC Observations of GJ 1214b

	2010 Aug 16	2010 Sep 04
Cross-disperser position	35.60	36.89
Echelle position	63.82	62.94
Slit	0.72" x 24"	0.72" x 12"
Filter	NIRSPEC-7	NIRSPEC-5
Wavelength coverage (μm)	2.007 - 2.414	1.514 - 1.783
Spectral grasp	52%	70%
Integration Time (sec)	60	60
Number of co-adds	1	1
Number of exposures	182	85
Airmass range	1.04 - 1.65	1.15 - 1.65
GJ 1214b phase coverage	-0.060 - +0.038	-0.021 - +0.025

provement in removing background emission. Instead, we kept the target star in a fixed position about 6" from the end of the spectrograph slit; this allowed us to squeeze an extra echelle order onto the detector. For the same reason, we deactivated the instrument's field rotator; differential atmospheric refraction did not appear to affect the relative tilt of our spectra over the course of the night. We used the widest possible slit (0.7") to maximize throughput and minimize the effects of sub-arcsecond guiding errors. Typical frames had maximum count rates of roughly 5,000 e^- per pixel, safely within the ALADDIN-3 detector's linear response range. We chose not to switch repeatedly between target and calibrator stars because (a) of the limited amount of observation time (GJ 1214b's transit only lasts about an hour), and (b) in our experience each re-acquisition of the target can induce substantial flux discontinuities in spectrophotometric time series. Although we did acquire a few observations of a telluric calibrator star (the A0V star HD 161289) at high airmass we do not use these in our analysis: due to the nature of our analysis dividing our spectra of GJ 1214 by a single, constant

telluric calibrator spectrum (as is typically done for such observations) will add noise into our data but will not otherwise affect our final results.

6.4.2 Initial Data Reduction

We reduce the raw echelleograms using a combination of standard IRAF routines (as implemented in PyRAF¹) and our own set of Python analysis tools²; we also draw on the experience of similar past observations (e.g., Deming et al. 2005a). We dark-subtract the frames and interpolate over cosmic rays and bad pixels. We performed flat-field correction for our data using the NIRSPEC internal calibration lamp, then using the IRAF task `apnormalize` to remove the lamp’s intrinsic continuum and correct small-scale flat-field variations.

The two left-hand (shorter-wavelength) quadrants of the NIRSPEC detector sometimes exhibit nonuniform readout characteristics in a pattern that repeats every eight detector rows. This manifests itself both as increased read noise and an apparent bias offset in affected rows. We remove the offset from each set of rows in each quadrant using linear least squares after excluding pixel values more than seven standard deviations from the median. Nonetheless the short-wavelength half of each extracted echelle order is detectably noisier.

We extract the spectra using the IRAF `apall` task with variance weighting and a third-order sky background fit. Our extraction ignores the slight tilt of the spectrograph slit in the raw spectral orders, but this does not seriously compromise our resolution ($R \approx 17,000$) when using the 0.7" slit. The extracted spectra have fluxes of roughly $16,000 \text{ e}^- \text{ pix}^{-1}$. After removing observations rendered

¹PyRAF is a command language for running IRAF tasks that is based on the Python scripting language, and is available at http://www.stsci.edu/resources/software_hardware/pyraf/

²Available at <http://www.astro.ucla.edu/~ianc/>

unusable for telescope or instrumental reasons (e.g., loss of guiding or server crashes), we are left with 182 K-band and 85 H-band spectra.

Our initial analysis reveals that the the H-band data are unable to constrain the presence of even the most easily detectable atmospheric models. The cause seems to be the relatively short duration of the H band data (cf. Table 6.2), and especially the paucity of out-of-transit observations. We repeated the analysis we describe below using only 80 of the 182 K-band frames (similar in length to the H band data set); under these conditions we achieve precision comparable to that from the H band data set. Therefore it seems likely that the limiting factor in the H band data set is an insufficient number of observations and/or insufficient pre- and post-transit coverage. We thus discard the H band data and focus solely on the K band data.

We calculate a wavelength solution for our spectra using the IRAF task `ecidentify` to identify isolated telluric absorption lines in each extracted spectrum. As our reference we use the high-resolution telluric absorption spectrum measured by [Hinkle et al. \(2003\)](#). We fit a third-order dispersion solution to all echelle orders simultaneously; our final wavelength solution has RMS residuals of 0.3 \AA (0.7 pixels). The largest residual we see is 0.6 \AA (2.2 pixels) in the $2.02\mu\text{m}$ echelle order, but as this order is heavily corrupted by absorption from telluric CO_2 we do not use data from this order in our final analysis: the largest residual we see that could directly affect our data is 0.45\AA (1.5 pixels) in the $2.13\mu\text{m}$ echelle order.

To convert observed wavelengths to wavelengths in the GJ 1214 system's rest frame we use a radial velocity of 48 km s^{-1} , which we estimate by cross-correlating a high-resolution model stellar spectrum with our spectra. Before cross-correlation we used the IDL package XTELLCORR ([Vacca et al. 2003](#)) to

correct our GJ 1214 spectra for telluric absorption using observations we took of the A0V star HD 161289. With the IDL routine `BARYVEL` we estimate a solar system barycentric correction of -23.8 km s^{-1} for the date of our K band observations; the resulting systemic velocity of 24 km s^{-1} is in decent agreement with the value of 21.0 km s^{-1} from [Berta et al. \(2011\)](#). Finally, we convert the UTC timestamps in our NIRSPEC files to heliocentric Julian dates (HJD) using the function `helio_jd` in the Python `astrolib` module.

6.4.3 Measuring systematic effects

Our spectra, shown in [Figure 6.4](#), exhibit substantial residual temporal variations due to a combination of instrumental, telluric, and astrophysical sources (i.e., the planetary transit), with the last the weakest of these effects. We wish to quantify and ultimately remove the instrumental and telluric effects to the extent that we can convincingly detect any wavelength-dependent variations in the transit depth.

The widest slit available on NIRSPEC is only $0.7''$ across, so even in excellent seeing significant light is lost and does not enter the slit. In $0.6''$ seeing (about the best we observed), guiding errors of $0.1''$ can cause the amount of light entering the spectrograph to vary by as much as 10% from one frame to the next. We see variations at this level in our spectrophotometric data, which we attribute to pointing jitter. These variations wholly overwhelm the 1.4% flux decrement from GJ 1214b's transit.

We quantify the amount of light coupled into the spectrograph slit by measuring the flux in spectral regions free of telluric absorption lines; we avoid these lines by referring to a high-resolution telluric absorption spectrum ([Hinkle et al. 2003](#)). We list the spectral regions we use in [Table 6.3](#). The flux in these channels

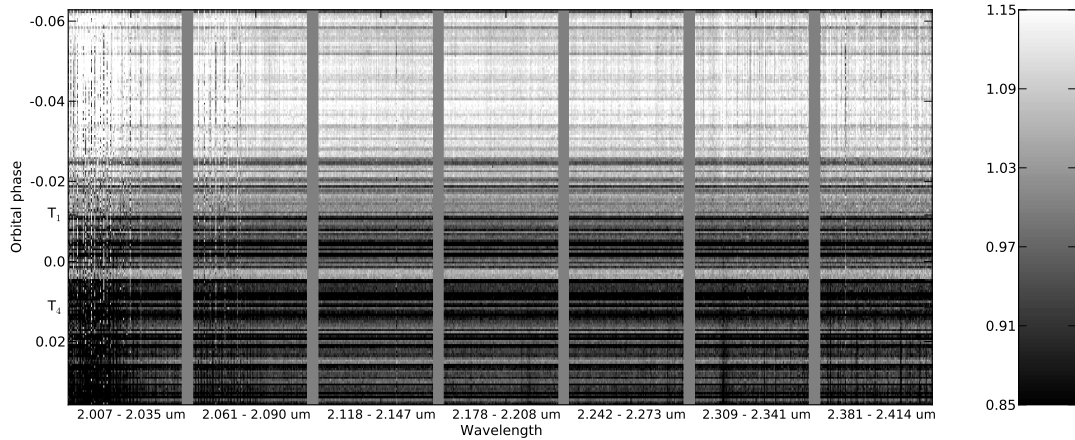


Figure 6.4 Spectrophotometric data $f_{i\lambda}$, normalized by the median value in each wavelength channel. The variations (due to a combination of airmass effects and instrumental slit loss) are of order 10% (which prevents us from directly seeing GJ 1214b’s transit) and are largely common mode. For display purposes the data from each echelle order are separated by a narrow gray region. T_1 and T_4 denote the beginning of transit ingress and the end of egress (Carter et al. 2011).

should only depend on (a) frame-to-frame changes in starlight entering the spectrograph slit, and (b) atmospheric continuum extinction. In each spectrum we add up the flux in these telluric-free regions, creating a time series representative of the slit losses suffered by the instrument. We denote this quantity as ℓ and refer to it as the slit loss, though it is actually a combination of instrumental slit losses and telluric continuum absorption due to changing airmass. The slit loss is plotted in Figure 6.5 with other (cleaned) spectrophotometric time series, and in Figure 6.6 along with other observable systematics.

Table 6.3. Telluric-free spectral regions from [Hinkle et al. \(2003\)](#)

Wavelength range (μm)
2.1264290 - 2.1265542
2.1297217 - 2.1299722
2.1304068 - 2.1305100
2.1313866 - 2.1317770
2.1320127 - 2.1322632
2.1326462 - 2.1327346
2.1332503 - 2.1333681
2.1334270 - 2.1336333
2.1344289 - 2.1349077
2.1350624 - 2.1355338
2.1364841 - 2.1367567
2.1370218 - 2.1371176
2.1378911 - 2.1382520
2.1386277 - 2.1388855
2.1390697 - 2.1391655
2.1397769 - 2.1398579
2.1400789 - 2.1409260
2.1410071 - 2.1413459
2.1414859 - 2.1418321
2.1438800 - 2.1439978
2.1798910 - 2.1801862
2.1804436 - 2.1808296
2.1809886 - 2.1824343
2.1856588 - 2.1869077
2.1873467 - 2.1874754
2.1884518 - 2.1885654
2.1886411 - 2.1887849
2.1889590 - 2.1891407
2.1898219 - 2.1902609
2.1907680 - 2.1924106
2.1924938 - 2.1927512
2.1928723 - 2.1940153
2.1940758 - 2.1943105

Table 6.3—Continued

Wavelength range (μm)
2.1953777 - 2.1955367
2.1959757 - 2.1961422
2.2077762 - 2.2078973
2.2447114 - 2.2450073
2.3109368 - 2.3111936
2.3125575 - 2.3127902
2.3128624 - 2.3129587
2.3132796 - 2.3134401
2.3138813 - 2.3140418
2.3140980 - 2.3145473
2.3147318 - 2.3148201

High-precision near-infrared photometry demonstrates that apparent photometric variations can be induced by motion of a star across the detector, changes in seeing, and other instrumental sources (e.g., [Rogers et al. 2009](#)). We expect the same to be true for high-precision spectrophotometry, and so we measure the motion of the spectral profiles in the raw echelleograms parallel to (x) and perpendicular to (y) the long axis of the spectrograph slit. We also measure the total amount of light coupled into the spectrograph slit, and the FWHM of the seeing profile. All these quantities are plotted in [Figure 6.6](#).

We measure the x motion of the spectra on the detector by spline-interpolating the spectrum in each echelle order and cross-correlating it at sub-pixel increments with a high signal to noise (S/N) template spectrum ([Deming et al. 2005a](#)). We construct our template by taking the temporal average, after removing outliers, of all our spectra. A parabolic fit to the peak of each spectrum’s cross correlation provides the optimal offset value, and we then spline-interpolate all the spectra to the template’s reference frame.

We measure the y motion of the star along the slit axis by tracing the locations of the spectral profiles using the IRAF `apa11` task. The locations of the spectra on the detector are not significantly affected by differential atmospheric refraction,

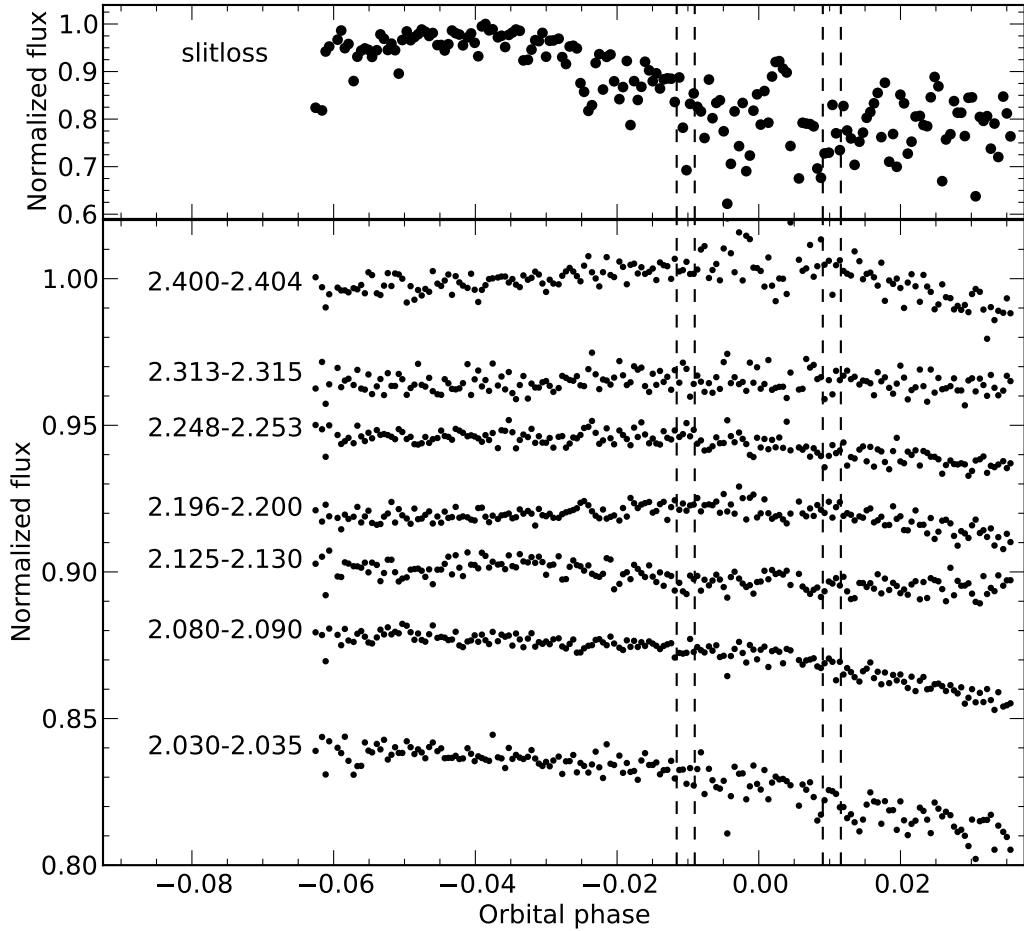


Figure 6.5 Representative spectrophotometric time series. The top panel shows the relative flux coupled into the spectrograph slit, as measured in regions free of telluric absorption lines; telluric continuum absorption and guiding errors combine to produce 10% variations, masking the 1.4% transit signature. The bottom panel shows one time series from each echelle order, after removal of the common mode slit loss term and binned over the wavelength range listed (in μm). After correcting for airmass effects these data have variations of order 0.5%, but the transit is still not visible: this is because dividing out the common-mode slit loss term removes a mean transit profile from all the data. The dashed lines indicate the times of first through fourth contact of the transit (Carter et al. 2011).

so we use the same set of relative positions for data at all wavelengths. Both x and y motions are plotted in Figure 6.6; though we see evidence that these motions affect our spectrophotometry (as we discuss in Section 6.4.4 below), this

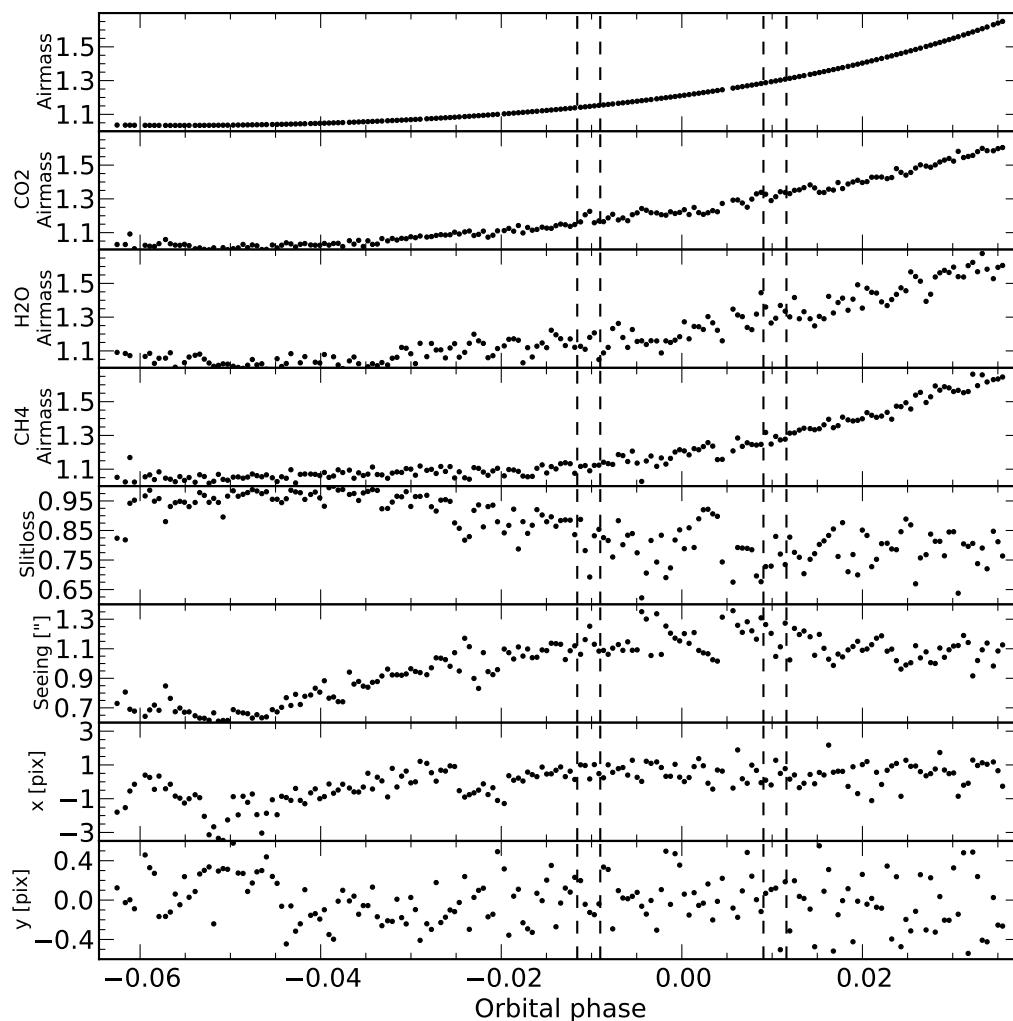


Figure 6.6 The various observable quantities (described in Section 6.4.2) measured during the course of our observations. As described in the text, we ultimately fit our data using the slitloss term, an empirical airmass quantity derived from the telluric CO₂ line flux, and several low-order polynomials. The dashed lines indicate the times of first through fourth contact of the transit (Carter et al. 2011).

is a low-amplitude effect.

Though we do not have a measure of the true astronomical seeing during the night, the width of the spectral profiles in the raw echelleograms provides a proxy for seeing. We fit a cubic spline to the mean spectral profile for each echelle order, and measure the average full width at half maximum in each frame. This

quantity depends on a combination of astronomical seeing, instrumental focus, and pointing jitter during an exposure, but we hereafter refer to it simply as seeing.

Previous studies (e.g., [Deming et al. 2005a](#)) report that an empirical measure of atmospheric absorption is preferable to the airmass value calculated from the telescope’s zenith angle when accounting for telluric extinction. To test this, we measure the flux in sets of telluric absorption lines caused by CO₂, CH₄, and H₂O. We select these lines, and verify that each is due to only a single absorber, by generating synthetic single-species telluric absorption spectra using the ATRAN code ([Lord 1992](#)). We fit the slitloss-corrected flux, f'_i , in these single-species telluric time series to the function $\ln f'_i = p + qa_i$, where a_i is the airmass at timestep i . We then define each species’ empirical airmass term as $a'_i = (\ln f'_i - p) / q$. These different airmass terms are all plotted in [Figure 6.6](#).

6.4.4 Identifying and Removing Systematic Effects

After extracting the spectra and quantifying observable systematic effects, our next step is to remove the large-scale flux variations caused by slit losses and (continuum) telluric absorption (note that this is the point in the analysis at which we inject synthetic model transit signals, as discussed later in [Section 6.5.3](#)). We divide the flux in every wavelength channel by the slit loss time series, viz.: $f'_{i\lambda} = f_{i\lambda} / \ell_\lambda$. This improves the S/N in regions clear of telluric absorption lines from roughly 10 pixel⁻¹ to roughly 50 pixel⁻¹ (cf. [Figures 6.4](#) and [6.7](#)) – this is still > 3 times worse than expected from photon noise. This step removes a mean transit profile from all wavelength channels, but the overall shape of the transmission spectrum should remain the same. We show a set of binned, slitloss-corrected spectrophotometric time series in [Figure 6.5](#), and show the full set of

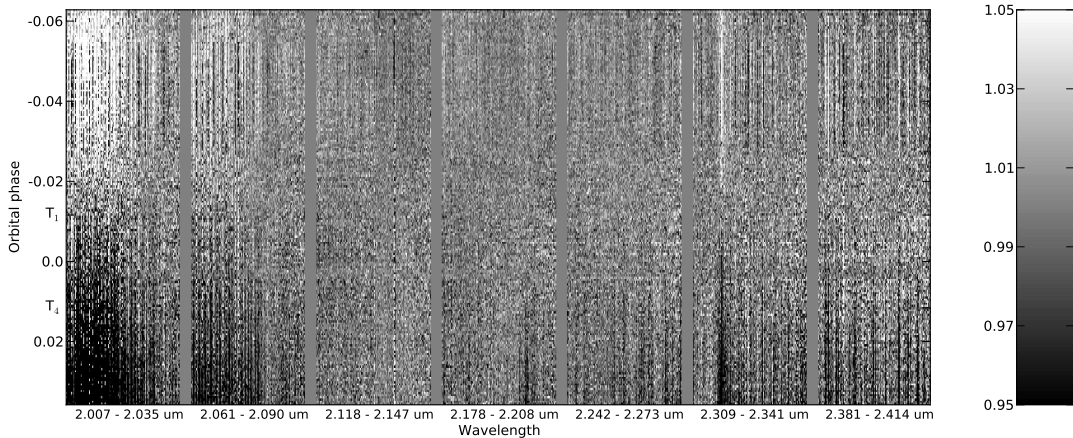


Figure 6.7 Spectrophotometric data $f'_{i\lambda}$ after dividing all wavelength channels by the common mode slit loss term (shown in Figure 6.5), and normalized by the median value in each wavelength channel. The data shown have variations of order 0.5% after correcting for residual airmass trends, but still no transit is visible because dividing by the slit loss term has removed the mean transit depth from all wavelength channels. T_1 and T_4 denote the beginning of transit ingress and the end of egress (Carter et al. 2011). For display purposes the the data from each echelle order are separated by a narrow gray region.

$f'_{i\lambda}$ in Figure 6.7.

The most obvious remaining variability is correlated with airmass. We identify other possible sources of variability using Principal Component Analysis (Jolliffe 1986). We compute the strongest several principal components (PCs) in our slit loss-corrected data set, and look for correlations between these PCs and our systematic observables: i.e., x and y motions, seeing, slit losses, sky line emission, and our several airmass proxies. We observe correlations between strong principal components and airmass, x , y , and slit losses, but not with other instrumental parameters. We attribute the x and y dependence to residual flat-field variations as each resolution element moves on the detector. The correlation of slit losses (which have already been removed to first order) with a principal component which is most prominent in regions of strong telluric absorption suggests flux variations in the core of telluric lines not well explained by a simple exponential

extinction relation. As described in Section 6.5.1, we ultimately detrend our data using only the slit loss term because our precision is not high enough to justify using additional correction terms..

6.5 Needle in a Haystack: Searching for Transit Signatures

We are unable to measure GJ 1214b’s transit light curve directly, because this signal is buried in the slit loss term we remove from all spectral time series. This removal has the effect of subtracting a constant offset value C from the transmission spectrum. The overall shape of the spectrum is therefore unchanged, and we can still hope to measure the modified transmission spectrum – i.e., $d_\lambda = (R_P/R_*)^2 - C$.

If GJ 1214b has a cloudless, H₂/He-dominated atmosphere we expect substantial variations in d_λ across the wavelength ranges we observe (cf. Figure 6.2; also Miller-Ricci & Fortney 2010); but if the planet has a denser atmosphere (and thus a smaller atmospheric scale height) we expect to see an essentially flat transit spectrum – in this case we might see no transit signature in any wavelength channel. Clouds would further suppress any spectral features occurring below a given altitude.

Photon noise alone precludes detection of the residual differential transit signal in any single spectral line. Even when examining time series that average over broad spectral regions (e.g., molecular bandheads) we are unable to detect any transit-like features. This agrees with our conclusion that, at our sensitivity, the spectrum is consistent with being featureless. To achieve our final sensitivity we must use our entire wavelength coverage. Our data do not permit us to search

for any individual spectral features (cf. [Redfield et al. 2008](#)), but they do allow us to test a given model against the entirety of our data.

Note that we cannot use exactly the same cross-correlation technique successfully used by [Snellen et al. \(2010\)](#) in their detection of CO on HD 189733b. This is because (a) GJ 1214b exhibits a much smaller change in velocity (12 km s⁻¹) during a transit than does HD 189733b, (b) our spectral resolution is much lower (17,000 with NIRSPEC vs. 100,000 with CRIFES), and (c) the signal to noise of our (fewer) spectra are substantially lower. For similar reasons, and because the most optimistic models of planetary emission predict planet-to-star contrast ratios of $\lesssim 10^{-4}$ for GJ 1214b, we cannot use the spectral deconvolution techniques used by [Barnes et al. \(2010\)](#) to search for planetary emission.

Instead, we search for residual transit signatures in our data by fitting a model (including telluric, systematic, and transit effects) to the time series in each wavelength channel, as described in Section [6.5.1](#). We then compare the extracted transmission spectrum to model spectra using both cross-correlation and linear least squares techniques, as described in Section [6.5.2](#).

6.5.1 Fitting to the data

We fit each spectral time series (i.e., the slitloss-corrected flux in each wavelength bin) with the following relation:

$$f'_{i\lambda} = f_{0\lambda} e^{b_\lambda a_i} (1 + d_\lambda r_i) \left(1 + \sum_{j=1}^J c_{j\lambda} v_{ji} \right) \quad (6.1)$$

This equation represents a transit light curve affected by systematic and telluric effects. In all cases the subscript i refers to the frame number and λ to the particular wavelength bin. The variables are: $f'_{i\lambda}$, the slitloss-corrected measured

flux; $f_{0\lambda}$, the out-of-transit flux that would be measured above the Earth’s atmosphere; r_i , the flux in a transit light curve scaled to equal zero out of transit and approximately -1 inside transit (i.e., $(F - 1)/(R_P/R_*)^2$, using the nomenclature of [Mandel & Agol 2002](#)); d_λ , the depth of transit; v_{ij} , the J state vectors expected to have a linearly perturbative effect on the instrumental sensitivity; $c_{j\lambda}$, the coefficients for each state vector; and a_i , the airmass, which has an exponential extinction effect on the measured flux modulated by an extinction coefficient b_λ . Since residual, low-amplitude drifts are common in this kind of observation (cf. [Swain et al. 2010](#); [Bean et al. 2010](#)) we account for and remove the effect of these drifts by including a series of polynomials in the set of vectors v_{ji} . For our polynomials we use the Chebychev polynomials of the first kind, which we compute as functions of orbital phase normalized to the domain $[-1, +1]$ to preserve the orthogonality of the set; as we describe below, we ultimately use the first three (linear through cubic) Chebychev polynomials in our analysis. After fitting we obtain a set of coefficients ($f_{0\lambda}, b_\lambda, c_{j\lambda}, d_\lambda$) from our full set of observations; the d_λ represent our measured transmission spectrum.

We use the parameters of [Carter et al. \(2011\)](#) for our model transit light curve and use a nonlinear limb-darkened light curve using the small-planet approximation from [Mandel & Agol \(2002\)](#). We take our near-infrared limb-darkening coefficients from [Claret \(2000\)](#) for a star with $T = 3000$ K and surface gravity 10^5 cm s^{-2} . In any case we are not especially sensitive to different limb-darkening models – even a uniform-disk transit curve leaves our results unchanged within their uncertainties.

We initially fit our data using many combinations of state vectors and low-order polynomials, and both calculated and empirical airmass quantities. We

use the Bayesian Information Criterion³ (BIC) to choose which of these many parameter sets best fit our data. Calculating the BIC involves computing χ^2 from each set of parameters, which in turn requires us to assign uncertainties to each data point. We estimate these uncertainties as follows. We first compute unweighted fits of Eq.6.1 (using no v_{ji} , and airmass as reported from the telescope control system) to the data using a multivariate minimization provided in the SciPy⁴ software distribution (the function `optimize.leastsq`), and compute the residuals for each time series. We then assign uncertainties to the individual data points by adding in quadrature the expected photon noise and the standard deviation of the residuals in each time series; this weights more heavily frames with the highest throughput, which are presumably those least affected by systematically lower telluric transmission and/or slit loss from guiding errors. Our next step is to globally scale down all uncertainties in each wavelength channel to give a χ^2 equal to the number of data points. We then use these scaled values as our per-point measurement uncertainties. Although this method of estimating uncertainties is not statistically valid inasmuch as it overestimates our goodness-of-fit (because we have artificially reduced χ^2 ; remember also that that even near-infrared photometry typically only comes within a factor of 3-5 of the photon noise limit) and underestimates parameter uncertainties (Andrae 2010), it provides a quantitative measure with which to compare the relative merit of various models.

The instrumental model which gives the lowest global BIC for our data include polynomials up to cubic order, the slit loss term described previously, and an empirical airmass calculated from the sum of flux in unsaturated telluric CO₂ lines from 2.0 – 2.1 μm . We confirmed that this result is not dominated by the

³Bayesian Information Criterion (BIC) = $\chi^2 + k \ln N$, where k is the number of free parameters and N the number of data points.

⁴Available at <http://www.scipy.org/>.

first two echelle orders (populated with the numerous telluric CO₂ lines from which we construct our empirical CO₂ airmass) by excluding these orders and repeating the BIC analysis; the same set of parameters still deliver the lowest BIC.

The relative transit depth spectrum d_λ that results from the fitting process represents a modified transmission spectrum of GJ 1214b; specifically, $d_\lambda = (R_P(\lambda)/R_*)^2 - C$. The constant C is the mean transit depth removed by our correction for slit loss variability. For display purposes, we show our extracted spectrum – averaged in wavelength – in Figure 6.8; note that we do not fit to the binned data shown there. Regions of strong telluric absorption (especially for $\lambda < 2.1 \mu\text{m}$) are notably biased, and we see a distinct tilt in all echelle orders. We suspect (but cannot independently confirm) that this tilt is some sort of detector artifact; we also see it in the spectra we extract after injecting model spectra into our data (cf. Section 6.5.3). We do not know the origin of this intra-order slope; though because we make an inherently relative transit fit in each wavelength channel we do not believe it could be due to spatial detector sensitivity variations. Removing this tilt from each order does not markedly increase our sensitivity, and to be conservative we do not remove it from our data. Our sensitivity tests demonstrate that we are still sensitive to plausible injected models in the presence of this slope.

We assess σ_{d_λ} , the uncertainties on d_λ , in two ways: using the residual permutation method (or prayer-bead method; Gillon et al. 2007), and by quantifying how our extracted parameters vary as we inject model transits at different times. The residual permutation technique fits fake data sets that are generated by adding temporally shifted copies of the residuals to the best-fit model. Thus it is similar to the bootstrap method, but has the advantage of preserving the proper-

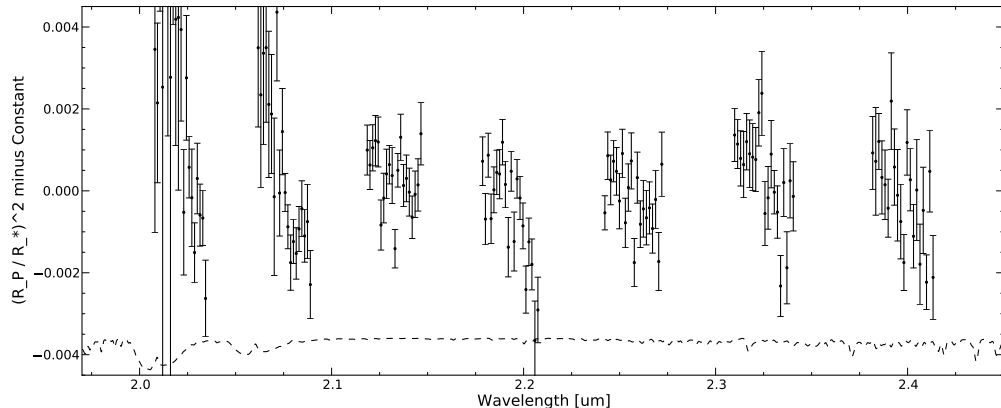


Figure 6.8 Extracted transmission spectrum of GJ 1214b, binned to 1.5 nm for display purposes; error bars here represent solely statistical (standard deviation on the mean) errors. Regions of strong telluric absorption (e.g., shortward of 2.1 μm) are notably biased. We do not know the source of the tilt in each echelle order. The dashed line at bottom represents the telluric transmission from [Hinkle et al. \(2003\)](#).

ties of correlated noise (present in our data). We estimate the 68.3% confidence interval on the d_λ by marginalizing over all other parameters and determining the parameter values that enclose the central 68.3% of the resulting one-dimensional parameter distributions.

Our second technique to determine parameter uncertainties injects model transit spectra into our data set (as described in Section 6.5.3) with varying ephemerides. We vary the injected transit ephemeris from 90 minutes before to 45 minutes after the expected time of transit, and we observe how the extracted transmission spectrum varies. These variations demonstrate the extent to which temporal evolution of systematic effects may limit our sensitivity.

We find that the σ_{d_λ} computed through this second technique are generally larger than the uncertainties from our residual-permutation analysis. To be conservative we assign the differential transit depth in each wavelength channel an uncertainty equal to the larger of the uncertainties from the two techniques.

6.5.2 Comparing models to data

We compare d_λ , the extracted transmission spectrum, to the spectral transmission models described in Section 6.3.2 in two ways. First, we cross-correlate our extracted spectrum with each model and measure the integrated signal centered at zero lag. Second, we fit our extracted spectrum to (a) each model spectrum and (b) a flat, featureless spectrum (representing a non-detection) and compare the BIC of each fit.

We require that a robust detection of a given model must satisfy several criteria. First, we require that d_λ is better fit (in a least-squares sense) by the tested model than by a flat spectrum. Second, we require that the integrated cross-correlation signal (i) is consistent with what we see when injecting synthetic models into our data and (ii) is significantly greater than zero. If a particular model meets these criteria with the injected signals but not with the unadulterated, observed data then we rule out the model as a plausible description of GJ 1214b’s atmosphere. A model is unconstrained if we are unable to reliably recover it when it has been injected into the data. Since we ultimately achieve no positive detections, our main result is our ability to rule out a large segment of atmospheric parameter space.

We do not use the entire set of extracted d_λ when comparing to models. We exclude wavelength channels with $S/N < 40$, which mainly affects spectral regions of low telluric or instrumental transmission. We also exclude all data from the first two echelle orders ($\lambda < 2.1\mu m$), because these wavelengths are heavily corrupted by numerous, strongly saturated absorption features from telluric CO_2 . Finally, we exclude the region $2.196\mu m < \lambda < 2.2\mu m$ because those portions of the data are visibly corrupted by detector anomalies. Because of the various models we inject we do not end up using the same set of wavelength channels in the analysis

of each real or synthetic data set, but in general we use 4200 ± 5 (out of 7,168 possible) wavelength channels in the tests that follow.

6.5.2.1 Template cross-correlation

We first compare our extracted transmission spectrum, d_λ , against atmospheric models by cross-correlating with the model spectra described in Section 6.3.2. We investigated the use of the Least-Squares Deconvolution algorithm (Donati et al. 1997; Barnes et al. 2007) to compare our measured transmission spectrum with model spectra, but we find this method to be less sensitive than straightforward cross-correlation.

Instead, we use the Discrete Correlation Function (DCF; Edelson & Krolik 1988) to perform a cross-correlation between d_λ and each spectral model. The DCF has several advantages over standard (linear-shift) methods for computing cross-correlations: it obviates the need for interpolation to a linear wavelength grid, and it allows us to compute the cross-correlation while excluding low S/N channels without the need for interpolating across the resulting gaps. In the case of regularly sampled data the DCF gives results identical to linear-shift cross-correlation.

For each model transmission spectrum, we cross-correlate our extracted transmission spectrum with the model over each echelle order. We then take the weighted average of these several cross-correlations, where the weights are proportional to the number of wavelength channels used to compute each echelle order's DCF.

In the limit of high S/N and perfect correspondence between our model and the observed transmission spectrum this analysis is equivalent to computing the transmission spectrum autocorrelation. We show the autocorrelation for each

echelle order, and the weighted average, in Figure 6.9 for the case of our solar abundance model. The mean autocorrelation shows features on two characteristic scales: a strong, narrow (tens of km s^{-1}) peak and a much broader (roughly 200 km s^{-1}) plateau of lower amplitude; we refer to these as the narrowband and broadband cross-correlation signals, respectively. The former results mainly from the individual, narrow spectral features while the latter results from broader variations of transit depth with wavelength. Integrating over these two correlation lag scales provides us with two measures of the cross-correlation signal, which we denote $\sum\text{DCF}$. By varying the range of summation we determine that we achieve the highest S/N with summation limits set at $|v_{lag}| \leq 10 \text{ km s}^{-1}$ and $|v_{lag}| \leq 200 \text{ km s}^{-1}$.

Examples of this cross-correlation process are shown in Figures 6.10–6.14 for several of our models. These cross-correlations do not closely resemble the noiseless autocorrelation shown in Figure 6.9 because of residual instrumental and telluric sources of measurement error. We verify that, on average, the expectation value for the effect of our noise sources on the cross-correlation values is zero and thus the expectation values for our integrated signals are unaffected.

We quantify the significance of a $\sum\text{DCF}$ measurement by first taking the standard deviation of the $\sum\text{DCF}$ values measured for the case of an injected signal at each of the several transit ephemerides (from 90 minutes earlier than, to 45 minutes later than, the true time of transit). We also simulate cross-correlation functions by resampling a smoothed fit to the mean power spectrum of the measured cross-correlation functions, and then examining the frequency with which peaks of a particular amplitude occur in this simulated data; these two techniques give comparable results, which give us confidence in our measurement uncertainty. We then estimate the expected $\sum\text{DCF}$ value in the presence of

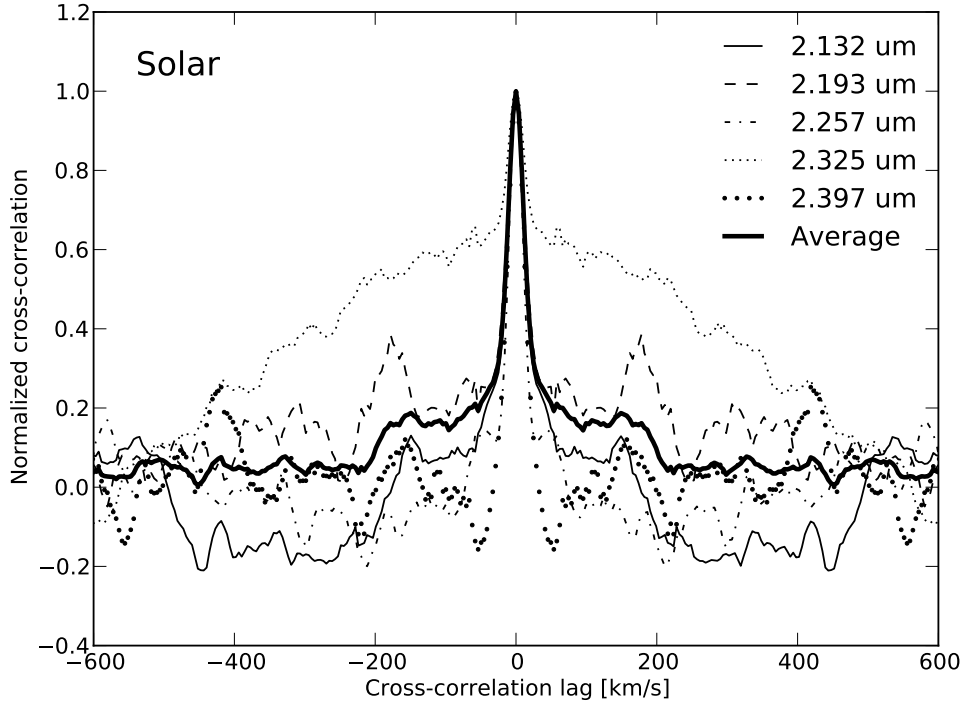


Figure 6.9 Autocorrelation of our solar abundance model computed in each echelle order (thin lines), and the average (thick solid line) weighted by the number of wavelength channels used in our analysis. All orders show a strong, narrow peak resulting from the narrow features in the model; broader structures (e.g. in the $2.325 \mu\text{m}$ order) result from broad spectral variations (cf. Figure 6.3). In the limit of infinite S/N, this figure shows our expected cross-correlation signal.

a known signal by injecting and re-extracting models into our data at varying ephemerides (as described in Section 6.5.3). We take the mean and standard error on the mean of the $\sum \text{DCF}_{\text{inj}}$ to be our best estimate of this quantity. We list all these values in Table 6.4. The agreement between the injected ($\sum \text{DCF}_{\text{inj}}$) and nominal ($\sum \text{DCF}_0$) values indicates the degree to which the model corresponds to our measurements; if they disagree at $> 3\sigma$ we rule out the model being tested. Detection of a model would require the two cross-correlation sums to be consistent and $\sum \text{DCF}_0$ to be significantly greater than zero.

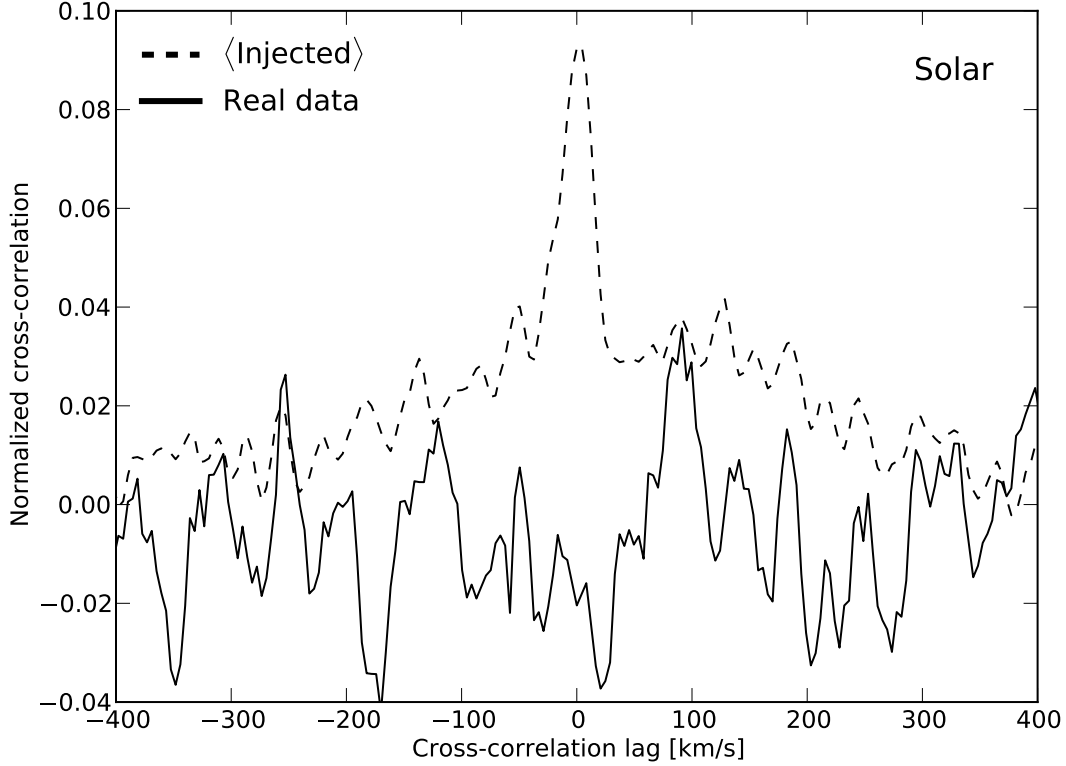


Figure 6.10 Template cross-correlation results. The solid line is the Discrete Correlation Function (DCF) of our solar-composition model with our extracted, unbinned transmission spectrum. The dashed line is the mean extracted DCF of the same model with data into which the transit signature of the model has been injected (cf. Section 6.5.3). The integrated signal over our narrowband ($|v_{lag}| \leq 10 \text{ km s}^{-1}$) and broadband ($|v_{lag}| \leq 200 \text{ km s}^{-1}$) apertures differ from the mean injected signal by 4.6σ and 5.6σ , respectively. This allows us to rule out this model as a good representation of the transmission spectrum of GJ 1214b.

6.5.2.2 Least-squares template matching

We also compare the extracted spectrum, d_λ , to the various spectral models using weighted linear least squares. We determine the offset value C necessary to give the best match between the measured and model spectra using $1/\sigma_{d_\lambda}^2$ as the weights – that is, we solve $d_\lambda = m_\lambda - C$ in a least squares sense, where

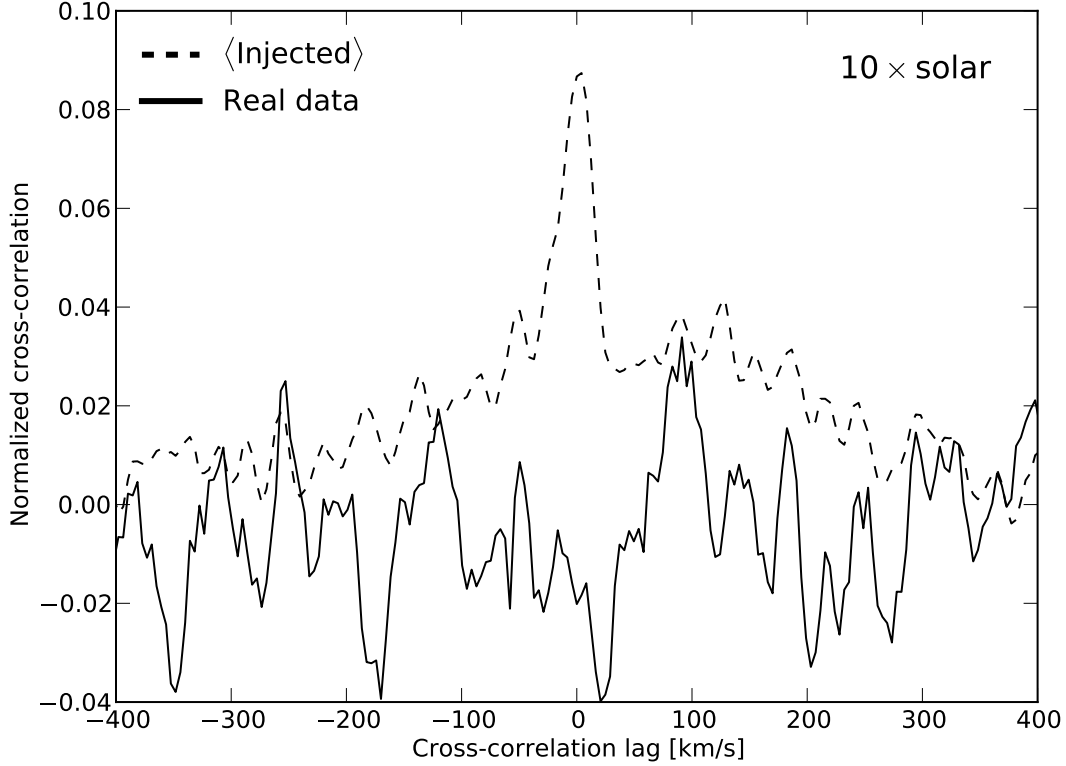


Figure 6.11 Same as Figure 6.10, but for our $10\times$ solar abundance model. The narrowband and broadband integrated signals differ from the mean injected signal by 4.4σ and 5.4σ , respectively. This allows us to rule out this model as a good representation of the transmission spectrum of GJ 1214b.

m_λ is the model spectrum being tested. The offset C results from our removal of the absolute transit depth by our correction for slit losses. We compute the statistic ΔBIC equal to the difference between the BIC for each model and the BIC resulting from a flat, featureless spectrum (i.e., a nondetection). Then, $\Delta\text{BIC} \leq 0$ implies the data are more consistent with a constant $R_P(\lambda)$ than with the tested atmospheric model, while $\Delta\text{BIC} > 0$ indicates we are justified in preferring the additional parameter – i.e., the model spectrum – to match our data. We list the ΔBIC from comparing each of our spectral models in Table 6.4.

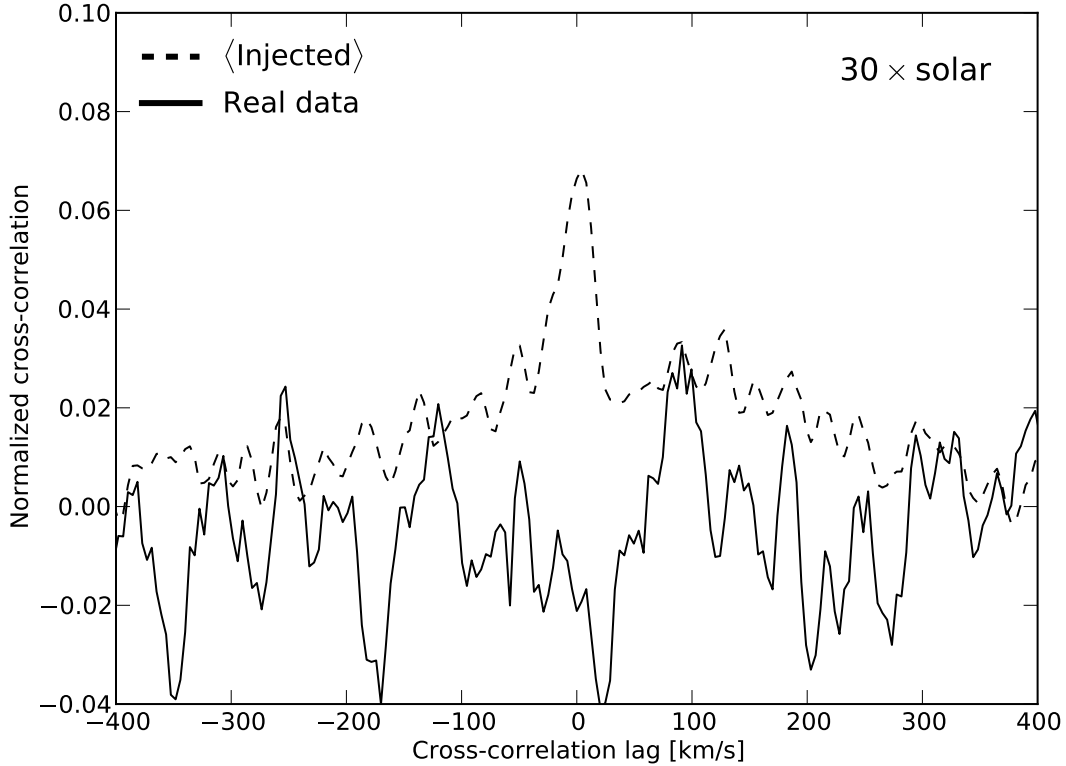


Figure 6.12 Same as Figure 6.10, but for our $30\times$ solar abundance model. The narrowband and broadband integrated signals differ from the mean injected signal by 3.6σ and 4.7σ , respectively. This allows us to rule out this model as a good representation of the transmission spectrum of GJ 1214b.

6.5.3 Sensitivity tests: injected models

As previously alluded to, we test the sensitivity of our analysis by inserting our model transmission spectra (cf. Section 6.3.2) into our extracted echelle spectra and attempting to recover the injected signal. We include both the time-dependent wavelength shift of the transmission spectrum due to the planet’s orbital motion and the overall transit light curve shape in each wavelength channel. Our ability to recover these velocity-shifted models justifies our decision to neglect the radial velocity shift when fitting each wavelength transit events. All

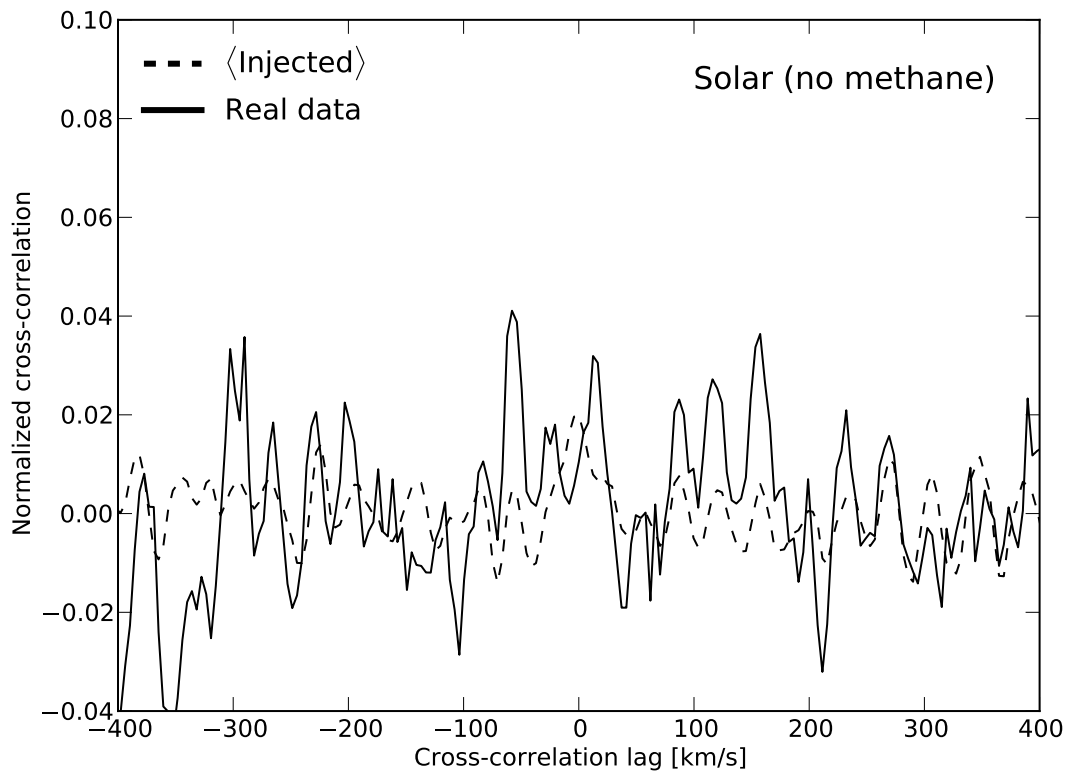


Figure 6.13 Same as Figure 6.10, but for our solar abundance, methane-free model. This model is quite flat and so we barely see a cross-correlation signal in the average, injected case; therefore our sensitivity does not allow us to state with confidence whether such a model represents the transmission spectrum of GJ 1214b.

data outside of the simulated transit are unaffected.

We inject these signals using ephemerides shifted by up to 90 minutes earlier than, and 45 minutes later than, the true transit ephemeris at intervals of 15 minutes. We inject each model spectrum immediately before the echelle spectra have been brought to a common wavelength frame (i.e., at the beginning of Section 6.4.4) and repeat the same analyses and tests as described in the preceding sections. The mean and error on the mean of the ensemble of the results of these injected and re-extracted spectra are listed in Table 6.4; these define our

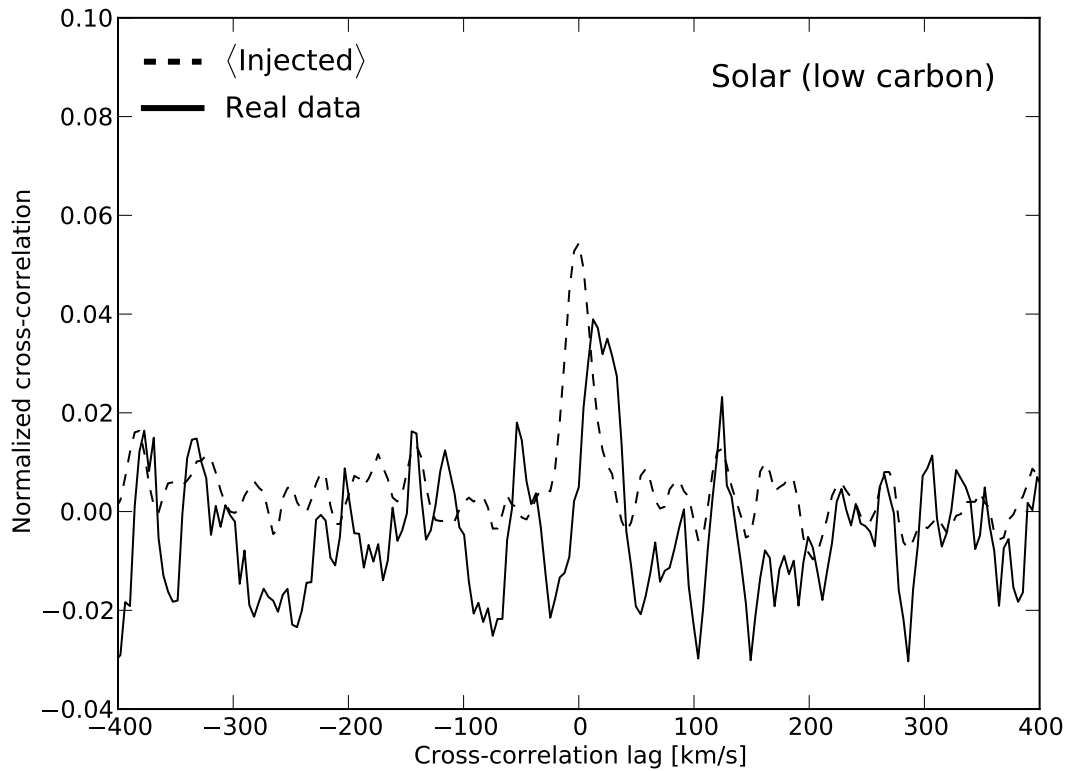


Figure 6.14 Same as Figure 6.10, but for our low carbon abundance solar model. The intriguing signal at $v \approx 20 \text{ km s}^{-1}$ has approximately the right shape and size as the expected signal but represents only a 1.9σ detection; in addition its offset from zero lag seems too large to result from uncertainties in either GJ 1214b’s orbit or in our wavelength calibration. We deem this feature a false positive, and otherwise our sensitivity does not allow us to state with confidence whether such a model represents the transmission spectrum of GJ 1214b.

sensitivity limits.

Table 6.4. GJ 1214b Cross-Correlation Results

Model	σ_{R_P} ^a	ΔBIC_0^b	$\langle \Delta\text{BIC}_{\text{inj}} \rangle^b$	$\sum_v \text{DCF}_0^c$	$\langle \sum_v \text{DCF}_{\text{inj}} \rangle^d$	$ v_{\text{lag}} \leq 10 \text{ km s}^{-1}$	$\sum_v \text{DCF}_0^c$	$\langle \sum_v \text{DCF}_{\text{inj}} \rangle^d$	$ v_{\text{lag}} \leq 200 \text{ km s}^{-1}$	Result ^e
30× solar	0.058	-180	177	-0.35(43)	1.33(17)	-0.35(43)	-2.0(2.4)	10.2(1.0)	Ruled out	
" ($\log_{10}(\text{CH}_4) \approx -3.0$)	0.052	-150	148	-0.35(43)	1.20(16)	-0.35(43)	-2.0(2.4)	9.4(1.0)	Ruled out	
" ($\log_{10}(\text{CH}_4) \approx -4.0$)	0.047	-124	122	-0.34(43)	1.07(16)	-0.34(43)	-1.9(2.5)	8.7(1.0)	Ruled out	
" ($\log_{10}(\text{CH}_4) \approx -5.1$)	0.041	-101	99	-0.34(43)	0.95(16)	-0.34(43)	-1.7(2.5)	7.9(1.0)	Unconstrained	
10× solar	0.076	-288	285	-0.33(43)	1.70(17)	-0.33(43)	-2.1(2.5)	12.5(1.1)	Ruled out	
" ($R_{\text{min}} = 2.85 R_{\oplus}$)	0.071	-255	234	-0.37(44)	1.58(18)	-0.37(44)	-2.5(2.7)	11.8(1.2)	Ruled out	
" ($R_{\text{min}} = 2.9 R_{\oplus}$)	0.064	-205	176	-0.44(47)	1.39(19)	-0.44(47)	-3.1(2.8)	10.7(1.2)	Ruled out	
" ($\log_{10}(\text{CH}_4) \approx -3.6$)	0.069	-238	237	-0.33(43)	1.54(17)	-0.33(43)	-2.0(2.5)	11.5(1.1)	Ruled out	
" ($\log_{10}(\text{CH}_4) \approx -4.6$)	0.061	-194	194	-0.32(43)	1.37(17)	-0.32(43)	-1.9(2.6)	10.5(1.1)	Ruled out	
" ($\log_{10}(\text{CH}_4) \approx -5.6$)	0.054	-155	156	-0.31(43)	1.21(16)	-0.31(43)	-1.8(2.6)	9.5(1.1)	Ruled out	
" ($\log_{10}(\text{CH}_4) \approx -6.6$)	0.047	-122	122	-0.30(43)	1.05(16)	-0.30(43)	-1.6(2.7)	8.4(1.1)	Unconstrained	
Solar	0.082	-329	315	-0.34(43)	1.81(18)	-0.34(43)	-2.4(2.5)	13.1(1.1)	Ruled out	
" ($R_{\text{min}} = 2.85 R_{\oplus}$)	0.081	-320	300	-0.34(43)	1.78(18)	-0.34(43)	-2.5(2.6)	12.9(1.1)	Ruled out	
" ($R_{\text{min}} = 2.9 R_{\oplus}$)	0.075	-291	193	-0.39(45)	1.46(19)	-0.39(45)	-2.9(2.7)	10.8(1.4)	Ruled out	
" ($\log_{10}(\text{CH}_4) \approx -3.8$)	0.074	-273	263	-0.33(43)	1.63(18)	-0.33(43)	-2.4(2.6)	12.1(1.1)	Ruled out	
" ($\log_{10}(\text{CH}_4) \approx -4.7$)	0.067	-224	216	-0.33(43)	1.45(17)	-0.33(43)	-2.3(2.6)	11.0(1.1)	Ruled out	

Table 6.4—Continued

Model	σ_{R_P} ^a	ΔBIC_0 ^b	$\langle \Delta\text{BIC}_{\text{inj}} \rangle$	$\sum_v \text{DCF}_0^c$	$\langle \sum_v \text{DCF}_{\text{inj}} \rangle^d$	$\sum_v \text{DCF}_0^c$	$\langle \sum_v \text{DCF}_{\text{inj}} \rangle^d$	$ v_{\text{lag}} \leq 200 \text{ km s}^{-1}$	Result ^e
" $(\log_{10}(\text{CH}_4) \approx -5.5)$	0.059	-179	174	-0.32(43)	1.28(17)	-2.3(2.7)	9.9(1.1)	Ruled out	
" $(\log_{10}(\text{CH}_4) \approx -6.4)$	0.052	-141	137	-0.31(43)	1.10(17)	-2.2(2.7)	8.8(1.1)	Ruled out	
" $(\log_{10}(\text{CH}_4) \approx -7.3)$	0.045	-107	104	-0.30(43)	0.93(16)	-2.0(2.8)	7.7(1.1)	Unconstrained	
" (low carbon)	0.050	-61	36	0.20(34)	0.99(13)	-1.5(1.7)	2.6(0.6)	Unconstrained	
" (low C; $v_0 = 20 \text{ km s}^{-1}$) ^f	0.050	-61	36	0.72(38)	0.99(13)	-1.6(1.6)	2.6(0.6)	Unconstrained	
" (no methane)	0.026	-14	6.1	0.22(49)	0.35(17)	2.1(3.1)	0.1(0.1)	Unconstrained	

^aStandard deviation of the model $R_P(\lambda)$, in Earth radii, over the wavelengths used in our analysis and at our model resolution.

^b $\Delta\text{BIC} = \text{BIC}_{\text{flat}} - \text{BIC}_{\text{model}}$; a positive value implies that the the extracted transmission spectrum is better fit by the given spectral model than by a flat, featureless spectrum; cf. Section 6.5.

^cCross-correlation sum for the nominal case – i.e., the true transit ephemeris and without any injected signal. The uncertainty quoted is the standard deviation of the quantities measured at alternate transit ephemerides.

^dExpectation value in the case of a positive signal, estimated by calculating the mean and standard deviation on the mean of the values measured for the injected cases.

^eTo rule out a model we require that $\Delta\text{BIC} > 0$ in the injected case and that $\sum_v \text{DCF}_0 < \langle \sum_v \text{DCF}_{\text{inj}} \rangle$ at greater than 3σ confidence for both the narrowband and broadband cross-correlation signals.

^fLow carbon model, but with the limits of cross-correlation integration shifted by 20 km s^{-1} to encompass the feature centered there (cf. Figure 6.14). The model is still unconstrained in this case because the narrowband $\sum \text{DCF}_0$ is still $< 2\sigma$ discrepant from zero.

6.6 Results and Discussion

6.6.1 Spectroscopic results

We see no evidence of a significant match between our extracted transmission spectrum and any of our various spectral models. These nondetections are significant because our sensitivity analysis described above demonstrates our ability to recover signals of comparable magnitude in our data, as demonstrated by the values of ΔBIC and $\sum\text{DCF}$ listed in Table 6.4 for each model. In this section we discuss the results of our spectroscopic analysis, and in the section that follows we discuss these results in the context of other observations.

We rule out cloud-free atmospheres in chemical equilibrium with solar, $10\times$ solar, and $30\times$ solar abundances. Additionally, we rule out clear atmospheres with CH_4 abundances reduced from that expected in chemical equilibrium: we constrain $\log_{10}(N_{\text{CH}_4})$, the CH_4 molar abundance, to be < -6.4 , < 5.6 , and < 4.0 in the case of solar, $10\times$ solar, and $30\times$ solar abundance, respectively. In general we have less ability to discriminate between variants of the $30\times$ solar model than of the solar abundance model. This is because the variations of transit depth with wavelength decrease with increasing atmospheric metallicity, as seen in Figure 6.3, because a greater mean molecular weight results in a smaller scale height and thus a general suppression of the amplitudes of all spectral features. A similar trend is also apparent in the models of Miller-Ricci & Fortney (2010) with atmospheres even more enriched in heavy elements. We demonstrate an ability to constrain the presence of clouds: in the case of an atmosphere with solar or $10\times$ solar abundance, an opaque cloud deck as high as $2.9 R_{\oplus}$ (roughly 100 mbar; cf. Figure 6.1) still allows us to detect the spectroscopic signature of the planet.

The closest we come to detecting any atmospheric model (i.e., those tests which result in the largest values of ΔBIC and $\sum\text{DCF}_0$) are our no-methane and low-carbon models. The no-methane model (cf. Figure 6.13) is the only model with a broadband ($|v_{lag} \leq 200 \text{ km s}^{-1}$) sum greater than zero, but it is still consistent with zero at the 0.7σ level. Cross-correlation with the low-carbon model (cf. Figure 6.14) produces a very interesting feature, similar in size and shape to the expected narrowband signal but offset by 20 km s^{-1} . However, this large cross-correlation lag seems too large to be explained by either uncertainties in GJ 1214b’s orbit or in our wavelength calibration. Since this feature is only discrepant from zero at the 1.9σ level, both these low-significance $\sum\text{DCF}$ measurements seem most likely to be simple false positives. Nonetheless, these low-methane models remain intriguing in light of the correspondence between their predicted planetary radii and recent photometric observations (as we describe below).

6.6.2 Constraints on GJ 1214b’s atmosphere

If GJ 1214b has a H_2/He -dominated atmosphere, our observations require a reduced methane abundance in order for the atmospheric signature to remain undetectable to our analysis. Such an atmosphere also resolves the tension between the recent claims of a high (Bean et al. 2010; Désert et al. 2011) and low (Croll et al. 2011a) mean molecular weight atmosphere on GJ 1214b. Zahnle et al. (2009) has suggested that the atmospheres of cooler (but still strongly irradiated) planets may be conducive to photochemistry and polymerization of CH_4 into more complex organic compounds, which may form a haze with significant optical opacity. An optical haze (as observed on HD 189733b; Sing et al. 2011b) formed from CH_4 reaction products provides a possible way to reconcile the nearly flat optical

([Bean et al. 2010](#)) transmission spectrum with the significantly larger Ks-band radius ([Croll et al. 2011a](#)).

Thus a methane-depleted, H₂/He-dominated atmosphere with an optical haze appears broadly consistent with all of the optical and infrared results for this system. Intriguingly, the only two atmospheric models to evince even a hint of a detected signal in our spectroscopic analysis have little or no methane; these are the models with low carbon and zero methane abundances (cf. [Table 6.4](#), and [Figures 6.13](#) and [6.14](#)); the correspondence is curious and warrants further consideration. As [Figure 6.15](#) demonstrates, both of these models are consistent (within 1.5σ) with the observed mid- and near-infrared planetary radius ratios ([Désert et al. 2011](#); [Croll et al. 2011a](#)) – compare this to the equilibrium-abundance models ruled out by our analysis, which are also discrepant (at $> 5\sigma$) from the photometric observations. Further observations are certainly needed. Fortunately, a methane-depleted atmosphere should be easy to characterize since it should still exhibit prominent absorption features from H₂O. To disentangle the effects of these exoplanetary absorption features from the telluric H₂O that defines the edges of ground-based observing bands, the atmosphere might best be characterized from space using the HST WFC3 grism in the J and H bands; ground-based narrowband infrared transit photometry (e.g., 2.1-2.3 μm) could also test the existence of such an atmosphere.

A number of possible interpretations consistent with our results and with other observations are excluded solely by the large Ks transit depth ([Croll et al. 2011a](#)). For example, our data alone are consistent with a dense molecular (non-H₂) atmosphere on GJ 1214b, which would reduce the atmospheric scale height such that the transmission spectrum would be essentially constant with wavelength. This is consistent with the near-constant optical and mid-infrared transit depth

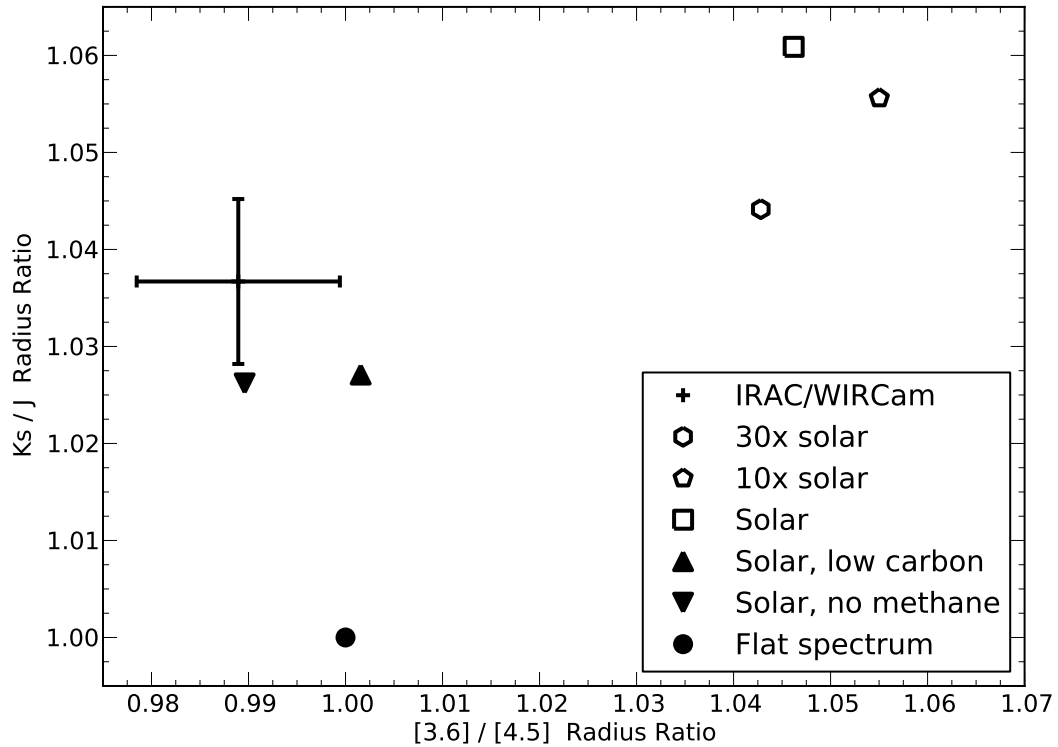


Figure 6.15 Near-infrared (K_s/J) and mid-infrared ($[3.6]/[4.5]$) planetary radius ratios for GJ 1214b. Values predicted by our atmospheric models, and the observed ratios and their uncertainties as measured with IRAC (Désert et al. 2011) and WIRCam (Croll et al. 2011a), are plotted. Solid symbols are models consistent with our analysis; open symbols are models that we rule out. Models substantially depleted in methane are consistent with our and prior observations, but equilibrium-abundance H_2/He -dominated models are strongly inconsistent with all observations. A flat transmission spectrum (due, e.g., to an atmosphere dominated by heavier molecular species), though consistent with our spectroscopic analysis, is inconsistent with photometric observations at $> 4\sigma$.

(Bean et al. 2010; Carter et al. 2011; Désert et al. 2011). This scenario would imply that GJ 1214b probably did not accrete much of its atmosphere from the gaseous protoplanetary disk in which it presumably formed, but instead formed largely from accretion of, and outgassing by, volatile-rich ices (Rogers & Seager 2010). Such an atmosphere would have features in transmission an order of

magnitude weaker than those expected for a H₂/He-dominated atmosphere, and so would be more amenable to characterization by looking for the $\lesssim 10^{-3}$ mid-infrared ($>5 \mu\text{m}$) secondary eclipse signature (Miller-Ricci & Fortney 2010). Such observations may have to wait for the James Webb Space Telescope, though perhaps dedicated observations with the Stratospheric Observatory for Infrared Astronomy (SOFIA) could make a contribution somewhat sooner.

GJ 1214b’s atmosphere would also be consistent with our observations if it were covered in high-altitude ($> 2.9 R_{\oplus}$ or < 100 mbar) clouds that would mask the spectroscopic signals to which we are sensitive. However, the effect of such a cloud layer would presumably extend to the optical, where observations demonstrate that the planet is significantly smaller than this. This discrepancy suggests that in a H₂/He-dominated atmosphere clouds could not consistently explain our (and prior) results.

In our calculations we have taken the larger stellar radius ($0.21 R_{\odot}$) proposed by Carter et al. (2011). It is possible that this overestimates the radius of the host star by as much as 15% (Charbonneau et al. 2009; Carter et al. 2011), making any planetary atmosphere more difficult for us to detect. A smaller radius would increase the surface gravity and decrease the atmospheric scale height, and a higher density would make the planet somewhat more consistent with denser interior models that may be less likely to host the extended, H₂/He-dominated envelopes to which our observations are most sensitive. This reduced radius would allow GJ 1214b’s mass and radius to be fit without any atmosphere whatsoever (even the larger radius is only 2σ discrepant from such a scenario; Rogers & Seager 2010). Though it may be difficult to motivate a formation and evolution scenario that leads to a composition wholly lacking an atmosphere, this would be consistent with most current observations – except, once again, for the Ks

band transit measurements (Croll et al. 2011a) which seems to argue against all scenarios but those with H₂/He-dominated atmospheres.

6.6.3 Lessons for future ground-based spectroscopy

High-resolution spectroscopy holds promise for the characterization of extrasolar atmospheres, as evidenced by the limits we set here with only half a night’s observations. Throughout this paper, we have noted that our analysis is sensitive to variations in transit depth with wavelength, and not to the absolute transit depth. A simple way to quantify our final sensitivity is in terms of the level of radius variability we can rule out, as measured by σ_{R_P} , the standard deviation of $R_P(\lambda)$ at our model resolution. Though the details of our sensitivity analysis depend on the shape of the spectrum being tested, a simple rule of thumb turns out to work fairly well: as seen from Table 6.4, we can reliably detect models with $\sigma_{R_P} \gtrsim 0.05 R_\oplus$. Equivalently, any tested model with wavelength-dependent transit depth variations $\gtrsim 5 \times 10^{-4}$ over our wavelength range should be detectable to our analysis. Successful characterization with NIRSPEC of a 100% H₂O atmosphere on a GJ 1214b-like planet would require roughly a factor of 5 better precision, which seems at the outer edge of what might be achieved with a dedicated spectroscopic campaign. The atmospheres of smaller, cooler, and more Earth-like planets will be even more challenging to detect. On the other hand, a GJ 436b-like Hot Neptune would have an atmospheric signal only a factor of two below our sensitivity, and so such an object might be amenable to high-resolution spectroscopic characterization in only a single observing season.

Our sensitivity is fundamentally limited by the spectrophotometric variability resulting from (a) variations in spectroscopic slit loss, (b) telluric-induced flux variations, and (c) slow drifts likely of instrumental or residual telluric origin. We

address the first by removing the common-mode slitloss term (removing the absolute transit depth from our data), the second by calibrating our data with various empirical airmass terms, and the third by including low-order polynomials in our fitting process; our ability to address these suggests that further observations with NIRSPEC or comparably instruments would probably allow us to probe a somewhat greater region of atmospheric parameter space and should not be discounted (we are aware of at least one other group which has obtained additional NIRSPEC K band observations of GJ 1214b during transit, and we look forward to seeing whether these can more tightly constrain the model parameter space we have explored).

That said, we note that concerns (a) and (b) above can be largely eliminated – without the penalties or tradeoffs incurred by our methods – by multi-object spectroscopy (Bean et al. 2010); this technique would at least partially mitigate limitation (c) as well, though there is some evidence that field-rotating multi-object spectrographs may suffer their own peculiar set of systematic effects (Moehler et al. 2010). There are a growing number of cryogenic, infrared multi-object spectrographs on large-aperture telescopes: MOIRCS at Subaru, and soon MOSFIRE at Keck and FLAMINGOS-2 at Gemini South. Combined with extant optical multi-object spectrographs these instruments may have a leading role to play in the future characterization of exoplanetary atmospheres.

A subset of exoplanet systems could be amenable to spectroscopic characterization in an alternate manner. If an exoplanet host star has another star of comparable brightness nearby, observations from a sufficiently precise slit-viewing camera or facility guiding camera could be used to calibrate out the (broadband) photometric variations resulting from telluric effects. With a sufficiently wide spectrograph slit (probably $\geq 3''$), good guiding, and no slit nodding the slit loss

term that limits our observations here could also be almost wholly compensated for. The independent photometric calibration offered by this technique would also be useful in refining the precise transit ephemeris of a given observation and of characterizing any spot crossings or other astrophysical “red noise” sources. This method could enable at least coarse spectroscopic characterization on even smaller (and hence, more accessible) telescopes, and we plan to test it in future observations.

6.7 Conclusions

Planets with GJ 1214b’s mass and radius have no solar system analogues, so *a priori* we know relatively little about the nature of their interiors or atmospheres. Here we report high-resolution near-infrared spectroscopy of the GJ 1214 system during GJ 1214b’s transit, taken to ascertain the nature of the planet’s atmosphere. Calibration using a common-mode flux variation time series (which removes the absolute transit depth, C , from the data) allows us to search for the relative change in transit depth with wavelength: that is, we measure the quantity $(R_P(\lambda)/R_*)^2 - C$.

Our spectroscopy rules out a clear, cloudless atmosphere in or near chemical equilibrium for GJ 1214b assuming solar, $10\times$ solar, and $30\times$ solar abundances, and in this sense we are consistent with previous results (Bean et al. 2010; Désert et al. 2011). Our data are consistent with any of the following: (i) a H_2/He -dominated atmosphere depleted in methane, (ii) an atmosphere dominated by heavier molecular species with a smaller atmospheric scale height, or (iii) almost any atmospheric composition if obscured by a high-altitude cloud layer. However, the large Ks band transit depth reported for this system (Croll et al. 2011a) argues against (ii) and (iii) above. GJ 1214b thus appears more likely to be a

scaled-down version of GJ 436b (another methane-depleted, H-dominated planet orbiting an M dwarf) than a rock- or ice-dominated body with a dense envelope. As the interpretation hinges largely on the near- and mid-infrared measurements, further observations of this system are needed to pin down the nature of its atmosphere.

Planet surveys suggest that objects of this mass and size may be quite common ([Howard et al. 2010](#); [Borucki et al. 2011](#)), so we expect similar planets to be confirmed in the future. Further observations of GJ 1214b during transit – both photometric and spectroscopic – will help refine our understanding of this object and future objects like it, and pave the way toward the characterization of ever more Earthlike planets. Because GJ 1214 is such a cool star, infrared wavelengths continue to offer the best prospects for these future observations. We suggest that infrared spectroscopy (especially from spectrographs such as Subaru/MOIRCS, Keck/MOSFIRE, and HST/WFC3) and narrowband photometry will be able place the tightest atmospheric constraints on this planet and those like it as yet undiscovered.

6.8 GJ 1214b: Post-publication Updates

A number of groups have made additional observations of GJ 1214b since the publication of the work discussed above ([Crossfield et al. 2011](#)). For completeness, below I discuss the recent progress and our current best understanding of this planet.

Two additional sets of multi-object transit spectroscopy have been acquired for this system ([Bean et al. 2011](#)), one blueward of the previous optical data (using VLT/FORS2) and the other simultaneously covering J, H, and K bands (using

Magellan/MMIRS). These data are all generally consistent with a flat transmission spectrum, though there is a hint of increasing transit depth at the shortest wavelengths (~ 650 nm) that could be interpreted as Rayleigh scattering in a H_2 -rich atmosphere. These observations disagree with the deeper K band transit depth measured previously (Croll et al. 2011a), so there is plenty of elbowroom for future study.

Eight transits of GJ 1214b were observed by de Mooij et al. (2012) using broadband filters spanning a wavelength range from g to K band. In these data all but the g band observations give a consistent transit depth. The g band transit appears to be $\sim 2\sigma$ deeper than the other planets, which (if confirmed at higher significance) would be evidence for Rayleigh scattering. Followup of this feature will be challenging, because GJ 1214 is very faint at optical wavelengths ($V \sim 15$), but could be a key probe of GJ 1214b's atmospheric scale height that would be independent of assumptions about detailed atmospheric chemistry.

Perhaps most impressive is the $1 - 1.7 \mu\text{m}$ transmission spectrum resulting from three transits observed by Wide Field Camera 3 on HST (Berta et al. 2012). This work demonstrates the highest-precision and highest-resolution direct measurement to date of GJ 1214b's transmission profile. The spectrum is, again, very nearly flat, but atmospheric models with H_2O opacity features evident are marginally preferred by the data. This could be interpreted either as an atmosphere with a high ($> 50\%$) H_2O concentrations or by an H_2 -dominated atmosphere with a nearly (but not entirely) opaque cloud deck.

Thus at the time of this writing the ultimate nature of GJ 1214b remains ambiguous. Two independent courses of study seem most likely to determine the ultimate nature of the planet's atmosphere. First, short-wavelength transit observations could confirm or rule out the Rayleigh scattering signature hinted at in

prior data (Bean et al. 2011; de Mooij et al. 2012). If detected, this would confirm that the atmosphere is dominated by H₂. Second, high-precision near-infrared (1 – 2.5 μm) spectroscopy of this system using MOSFIRE (McLean et al. 2008, 2010) or similar instruments could hope to discern the absorption signatures of heavier molecules, especially H₂O and CH₄ (though signs of the latter are lacking in analysis of Spitzer/IRAC data; cf. Désert et al. 2011, Fraine et al. in preparation). Such observations could potentially confirm the H₂O features reported previously (Berta et al. 2012) and distinguish between a H₂O-dominated and a cloudy, H₂-dominated atmospheric composition.

CHAPTER 7

Conclusion

7.1 Summary of Dissertation

My dissertation has primarily focused on developing the techniques necessary for ground-based infrared spectroscopy, which offers the promise of greatly enhanced science return over broadband photometric analyses such as those described in Chs. 2 and 3. In Ch. 4 I described observations of WASP-12b, the archetypal carbon-rich hot Jupiter (Madhusudhan et al. 2011a), to measure its emission spectrum at low resolution ($\lambda/\Delta\lambda \sim 80$). My analysis suggests warmer-than-predicted nighttime temperatures and reveals the planet's 3,000 K day side continuum emission. A further hint of strong emission from WASP-12b was provided by the wavelength-resolved narrow band photometry presented in Ch. 5. Finally, I probed the atmosphere of GJ 1214b, the first known low-density super Earth, with high-resolution ($\lambda/\Delta\lambda \sim 15,000$) infrared spectroscopy, as described in Ch. 6. By correcting for time-variable slit losses, normalizing spectra during transit by data out of transit, and cross-correlating with spectral templates I found no significant detection of a H₂-dominated atmosphere, consistent with other recent observations and suggesting that GJ 1214b hosts either a cloud-covered or an H₂O-dominated atmosphere.

For both WASP-12b and GJ 1214b, systematic variations restricted the spectroscopic precision that could be obtained. The NIRSPEC observations of GJ 1214b

were affected by detector inhomogeneities and by chromatic slit loss, which induced a spurious low-order spectral trend that substantially limited the utility of the extracted planetary spectrum. Similarly, the WASP-12b results are limited both by chromatic slit losses and by changes in telluric transparency. In both cases, the final spectrum lacked the precision necessary to resolve spectral features.

7.2 Toward Multi-Object Exoplanet Spectroscopy

These results suggest that we may be near the performance limit of single-slit spectrographs. As described in Secs. 4.8 and 6.6.3, the precision of such observations is limited because conventional spectrographs suffer from instrumental variations that fundamentally interfere with their calibration. Variations in pointing and seeing, and atmospheric dispersion, cause time-varying, chromatic slit losses that make even relative (e.g., $1.6\ \mu\text{m}$ vs. $2.2\ \mu\text{m}$) spectroscopic measurements difficult and preclude absolute measurements altogether. Variations in the Earth's atmosphere (especially its water content) severely limit the usable wavelength range to narrow regions almost entirely clear of any atmospheric absorption features (Figure 4.11 and Mandell et al. 2011).

Multi-object spectrographs (MOS) offer the potential to overcome these single-slit limitations, as has been demonstrated by the recent, pioneering work of Bean et al. (2010, 2011). A MOS allows the simultaneous observation of exoplanet host star and several calibrator stars to perform precise, relative spectrophotometry with extremely wide (> 8 arcsec) slits; this is essentially ground-based slitless spectroscopy. The comparison objects calibrate out the telluric and instrumental effects that have limited single-slit spectroscopy, enabling an observational precision surpassing that attainable from space (Bean et al. 2011). As an exam-

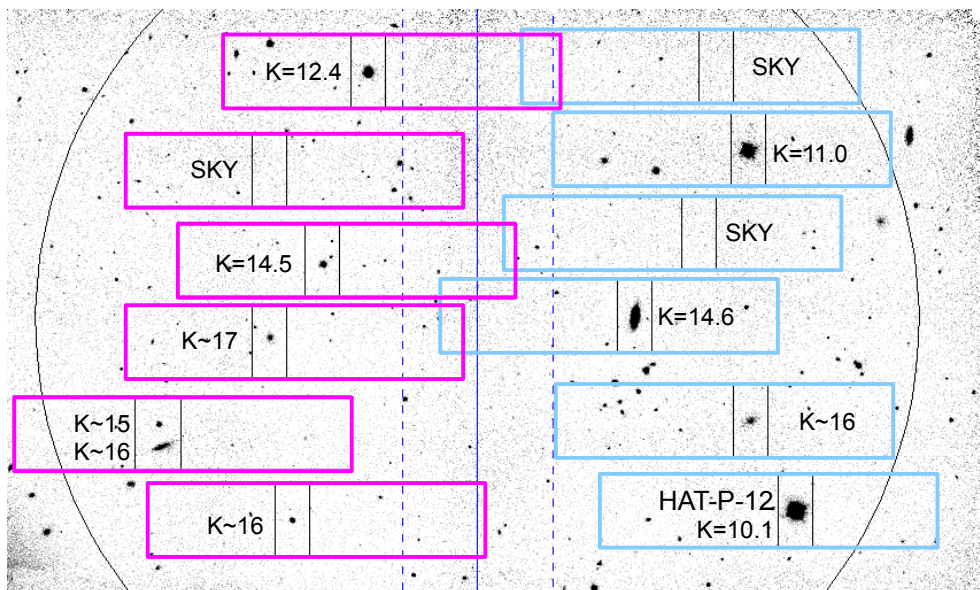


Figure 7.1 **Sample multi-object slit mask design** for my April 2012 transmission spectroscopy of the sub-Saturn mass planet HAT-P-12b on Subaru/MOIRCS. The large circle indicates the unvignetted 6'-diameter field of view, while the many narrow rectangles indicate the wide ($\sim 20''$) slits and the predicted locations of spectra on the two MOIRCS detectors. Magnitudes of the primary target and comparison objects are indicated, and are taken from either 2MASS K_S or NB2315 (cf. Ch. 5) photometry. Despite the appearance of the figure the spectra do not overlap: the detectors are physically separated by a rooftop mirror. Initial light curves for these observations are shown in Figure 7.3.

ple, I show in Figure 7.1 the multi-object slit mask for my recently completed Subaru/MOIRCS observations of the cool, sub-Saturn mass planet HAT-P-12b.

MOS instruments are poised to usher in a new era of exoplanetary characterization by allowing the detailed spectroscopic study of many planets for the first time. Optical MOS units may be of limited utility if the hazes seen on some exoplanets (e.g., Sing et al. 2011b) are common, but an MOS operating in the infrared should be less susceptible to haze. These NIR instruments are deployed on a growing number of large-aperture telescopes (6.5 m Magellan, 8 m Subaru

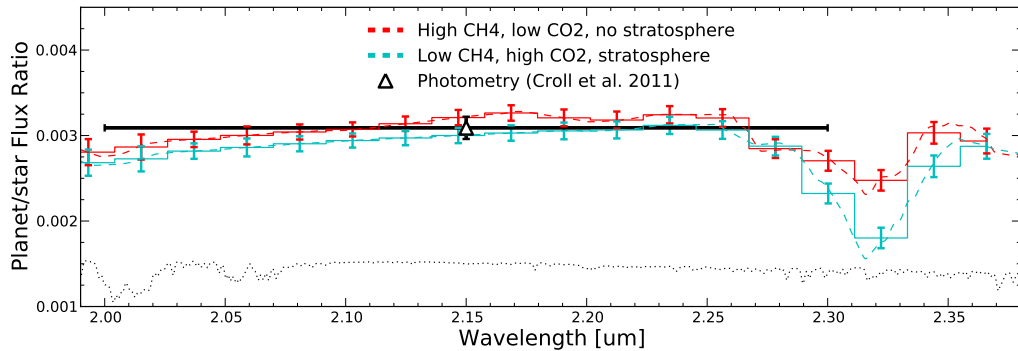


Figure 7.2 **Simulated MOS exoplanet spectroscopy: a single night with an 8 m-class telescope suffices to discriminate between different models of atmospheric carbon chemistry and of planet formation.** The dashed lines are models (adapted from Madhusudhan et al. 2011a) of the atmospheric emission of Hot Jupiter WASP-12b that fit current photometric data (Croll et al. 2011b; Campo et al. 2011) equally well. The simulated observations shown (recently proposed for Keck/MOSFIRE in semester 2012B) would discriminate between the models shown with high confidence and directly test the recent claim of an enhanced C/O ratio in this planet. Error bars are the predicted measurement uncertainties in each spectral channel ($\lambda/\Delta\lambda \approx 50$), scaled from the precision obtained with past, similar observations; note the dramatic improvement over what is possible with single-slit spectroscopy from a smaller telescope (cf. Figure 4.14). The dotted line at bottom represents the transmission of Earth’s atmosphere.

and LBT, and the 10 m Keck) and though until now MOS units have been little used for exoplanet observations, work presented at recent conferences suggests that the situation is rapidly changing. My own calculations, such as the simulated Subaru/MOIRCS spectrum of WASP-12b shown in Figure 7.2, demonstrate that just a single night with these facilities should be sufficient to discriminate between models with high confidence. In April 2012 I obtained 1.5 transits and 1.5 eclipses of four planets, thus beginning an extended campaign of spectroscopic exoatmospheric characterization. A quick reduction of the light curves from our first night (using the slit mask shown in Figure 7.1) is shown in Figure 7.3; the data quality looks good, and analysis is continuing.

Future ground-based MOS observations will be most useful when taken in

HAT-P-12b: Linear LD (no prior), variable T_0 allowed

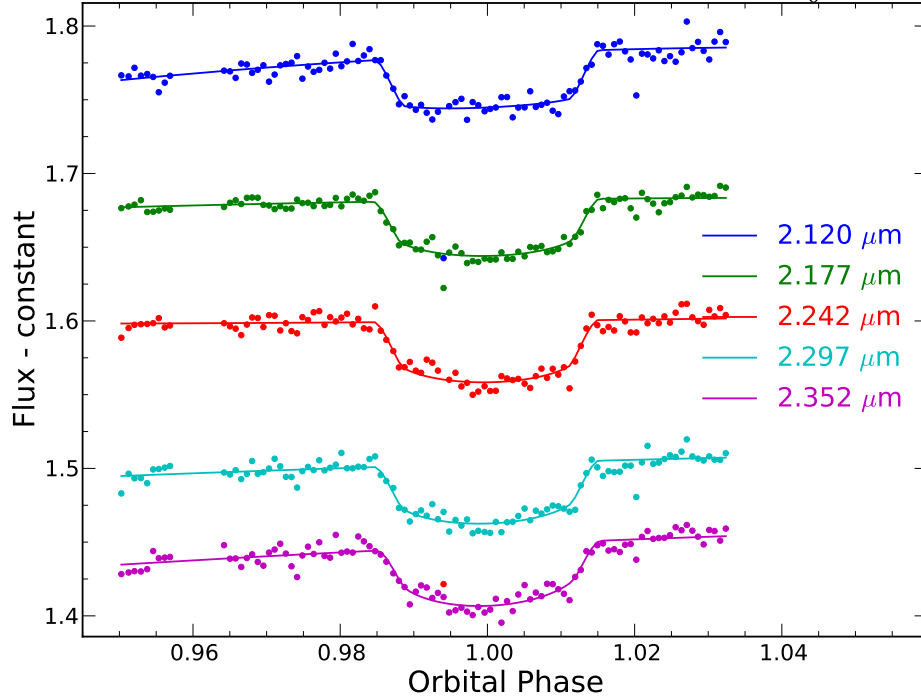


Figure 7.3 **Early spectrophotometric transit light curves from Subaru/MOIRCS multi-object spectroscopy of HAT-P-12b.** This early analysis breaks the K band into five wavelength bins and fits each light curve independently; current transit depths are measured with a precision of $\lesssim 0.1\%$. Subsequent refinements will correct for detector nonlinearity on a pixel-by-pixel basis, improve the precision by linking the time of transit center, orbital inclination, and a/R_* of all events, and impose a model prior on the limb-darkening coefficients derived from stellar atmosphere models.

K band ($2 - 2.4 \mu\text{m}$), where HST/WFC3 cannot observe and where carbon-bearing molecular signatures are especially pronounced (e.g., the $2.3 \mu\text{m}$ CO and CH_4 band heads). Hot Jupiters emit much of their flux in this wavelength range, making K band observations essential to understanding the energy budgets of these planets and to constraining their temperature-pressure structures. Measuring abundances of CH_4 and CO – whether via eclipse spectroscopy, as depicted in Figure 7.2, or via transmission spectroscopy – will constrain the dominant

atmospheric carbon reservoirs and test the claims of carbon-rich planetary atmospheres (Madhusudhan et al. 2011a,b). Spectroscopy of, and subsequent comparison of models with, these planets’ atmospheres near the edges of the K band may also constrain the H₂O abundance. H₂O acts as the dominant oxygen reservoir in carbon-poor planets, and of course its abundance in atmospheres of smaller, cooler planets has important implications for future studies of planetary habitability with JWST.

7.3 Selection of MOS Transit Targets

An optimal spectroscopic target must not just have a strong emission and/or transmission signal: one must also be able to observe the eclipse or transit with sufficient precision. In this section I briefly discuss considerations that enter into selection of optimal targets for a campaign of multi-object spectroscopy of transiting systems.

If spectroscopic precision is limited primarily by the statistical Poisson noise of the observations, then the precision will depend on the number of photons detected in each wavelength channel, $N_\lambda \propto F_{\lambda,*} T_{14}$, where $F_{\lambda,*}$ is the apparent stellar flux density and T_{14} is the transit/eclipse duration. Because observations to date seem to only come within a factor of 2-3 of this limit (Swain et al. 2010; Bean et al. 2011), and observations of the brightest systems may encounter a noise floor before doing even this well, I pessimistically scale each system’s predicted transmission or emission signal by $N^{1/3}$ (rather than the standard \sqrt{N}). I then set a minimum observability threshold by comparing to a detailed simulation of NIR spectroscopic observations (similar to that shown in Figure 7.2) and by extrapolating from recent observations (Bean et al. 2011).

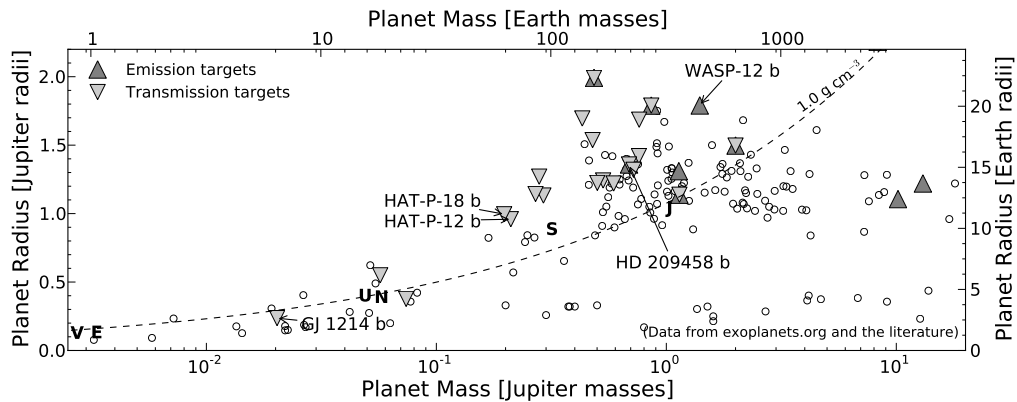


Figure 7.4 **The exoplanet systems suited to spectroscopic atmospheric characterization with a single night of observations.** Current ground-based instruments are capable of studying emission from the hottest, most massive planets (up-triangles) and can study smaller, cooler planetary atmospheres in transmission (down-triangles). Named systems are high-priority targets either because of their extreme mass, size, and/or temperature (GJ 1214b and WASP-12b), because they allow for near-homogeneous comparisons of pairs of objects (HAT-P-12b and -18b), or for comparison with past observations (HD 209458b). Open circles are exoplanets less well-suited for spectroscopy, and single letters indicate Solar System giant planets. The dash-dotted line is a fiducial line of constant density.

Figure 7.4 shows the mass and radius of all transiting exoplanets, with the systems most conducive to atmospheric study highlighted. This assumes a single night on an 8 – 10 m telescope, which allows these systems to be studied at $\lambda/\Delta\lambda \approx 50$ (sufficient to resolve molecular bandheads). A wide range of targets is available, from small, cool super-Earths to the hottest, most massive gas giants. Some compelling early targets are:

- **WASP-12.** This is the prototypical carbon-rich planet (Madhusudhan et al. 2011a), for which I have already measured a low-resolution emission spectrum (cf. Figure 7.2) and a higher-precision narrow band eclipse measurement (cf. Ch. 5). Additional eclipse observations will test this claim by resolving individual CO bands through NIR multi-object spectroscopy

(cf. Figure 7.2). My team has proposed for Keck/MOSFIRE observations of this system in semester 2012B.

- **HD 209458b** This is the first discovered transiting planet and the archetypal Hot Jupiter with a temperature inversion (Knutson et al. 2008), and is described in Ch. 3. Observing this touchstone system would provide a crucial verification of the observational technique. However, the system is very bright ($K_s = 6.3$) and so special methods (e.g., a custom neutral-density occulting spot) may be necessary to observe it with 8-10 m telescopes.
- **HAT-P-12b and 18b.** These apparently similar planets have recently been suggested to differ in their bulk metal content (Miller & Fortney 2011). I recently obtained Subaru/MOIRCS transmission spectroscopy of this planetary pair; the slit mask design and initial transit light curves are shown in Figures 7.1 and 7.3, respectively. Analysis of these data will ultimately allow a homogeneous comparison of atmospheric abundances (a) between the systems and (b) relative to their host stars, thus constraining formation theories and interior models.
- **GJ 1214b.** The first super-Earth with an atmosphere, which my and other recent observations suggest hosts either a cloud-covered or an H₂O-dominated atmosphere (Ch. 6 and Bean et al. 2010, 2011; Désert et al. 2011; Croll et al. 2011b; de Mooij et al. 2012; Berta et al. 2012). Dedicated, multi-epoch spectroscopy of this system will have sufficient precision to allow the first detection of a non-H₂-dominated exoplanet atmosphere.
- **Kepler-11.** A single system of six planets around a sun-like star with orbital periods from 10-118 days (Lissauer et al. 2011). This system offers a unique opportunity to perform a comparative study of planets with a closely linked formational history. Planets d and e are most amenable to ground-based spectroscopic characterization; multiple observations will be needed

to build up the necessary precision, but the insight into the formation and interiors will be well worth it.

The first systems listed above are mostly the low-hanging fruit ideal for refining observational techniques and data analysis algorithms. Other systems, more interesting but more challenging to characterize (e.g. the multiple-planet Kepler-11 system), will be studied once the technique's limitations are well understood. In addition, new planets continue to be announced by the Kepler mission and by ground-based transit surveys. A fraction of these systems will be bright enough to enable ground-based spectroscopic followup for atmospheric characterization, and I will adjust my target list accordingly.

7.4 Final Thoughts

The study of extrasolar planets with multi-object spectrographs is poised to revolutionize the field of exoplanet atmospheres by providing the first precise, reliable spectra for dozens of these systems. My work with single-slit, near-infrared spectrographs has laid the groundwork necessary to continue this work in future campaigns. These observations will help to pin down the atmospheric structure and composition of Hot Jupiters and of progressively smaller bodies, providing a solid theoretical foundation for future studies. The results will provide an essential complement to shorter-wavelength HST/WFC3 grism spectra and will inform the next generation of models in preparation for future JWST spectroscopy of even smaller, cooler, and more Earthlike planets.

BIBLIOGRAPHY

- Agol, E., Cowan, N. B., Knutson, H. A., Deming, D., Steffen, J. H., Henry, G. W., & Charbonneau, D. 2010, *ApJ*, 721, 1861, [ADS, 1007.4378](#)
- Allard, F., Homeier, D., & Freytag, B. 2010, ArXiv e-prints, [ADS, 1011.5405](#)
- Andrae, R. 2010, ArXiv e-prints, [ADS, 1009.2755](#)
- Asplund, M. 2005, *ARAA*, 43, 481, [ADS](#)
- Asplund, M., Grevesse, N., Sauval, A. J., & Scott, P. 2009, *ARAA*, 47, 481, [ADS, 0909.0948](#)
- Assef, R. J. et al. 2010, *ApJ*, 713, 970, [ADS, 0909.3849](#)
- Atreya, S. K., Mahaffy, P. R., Niemann, H. B., Wong, M. H., & Owen, T. C. 2003, *PSSci*, 51, 105, [ADS](#)
- Baines, E. K., McAlister, H. A., ten Brummelaar, T. A., Turner, N. H., Sturmann, J., Sturmann, L., Goldfinger, P. J., & Ridgway, S. T. 2008, *ApJ*, 680, 728, [ADS, 0803.1411](#)
- Barman, T. 2007, *ApJL*, 661, L191, [ADS, 0704.1114](#)
- Barman, T. S., Hauschildt, P. H., & Allard, F. 2005, *ApJ*, 632, 1132, [ADS, arXiv:astro-ph/0507136](#)
- Barnes, J. R. et al. 2010, *MNRAS*, 401, 445, [ADS, 0909.2510](#)
- Barnes, J. R., Leigh, C. J., Jones, H. R. A., Barman, T. S., Pinfield, D. J., Collier Cameron, A., & Jenkins, J. S. 2007, *MNRAS*, 379, 1097, [ADS, 0705.0272](#)
- Batalha, N. M. et al. 2011, *ApJ*, 729, 27, [ADS, 1102.0605](#)

- Bean, J. L. et al. 2011, ApJ, 743, 92, [ADS](#), [1109.0582](#)
- Bean, J. L., Miller-Ricci Kempton, E., & Homeier, D. 2010, Nature, 468, 669, [ADS](#), [1012.0331](#)
- Beaulieu, J. P. et al. 2010, MNRAS, 409, 963, [ADS](#), [0909.0185](#)
- Beichman, C. A., Neugebauer, G., Habing, H. J., Clegg, P. E., & Chester, T. J., eds. 1988, Infrared astronomical satellite (IRAS) catalogs and atlases. Volume 1: Explanatory supplement, Vol. 1, [ADS](#)
- Berdyugina, S. V., Berdyugin, A. V., & Piirola, V. 2011, ArXiv e-prints, [ADS](#), [1109.3116](#)
- Bergfors, C., Brandner, W., Henning, T., & Daemgen, S. 2011, in IAU Symposium, Vol. 276, IAU Symposium, ed. A. Sozzetti, M. G. Lattanzi, & A. P. Boss, 397–398, [ADS](#)
- Berta, Z. K., Charbonneau, D., Bean, J., Irwin, J., Burke, C. J., Désert, J., Nutzman, P., & Falco, E. E. 2011, ApJ, 736, 12, [ADS](#), [1012.0518](#)
- Berta, Z. K. et al. 2012, ApJ, 747, 35, [ADS](#), [1111.5621](#)
- Bodenheimer, P., Lin, D. N. C., & Mardling, R. A. 2001, ApJ, 548, 466, [ADS](#)
- Boensch, G., & Potulski, E. 1998, Metrologia, 35, 133, [ADS](#)
- Bolton, S. J., & Bolton. 2010, in IAU Symposium, Vol. 269, IAU Symposium, 92–100, [ADS](#)
- Borucki, W. J. et al. 2011, ApJ, 736, 19, [ADS](#), [1102.0541](#)
- Bouchy, F. et al. 2005, A&A, 444, L15, [ADS](#), [arXiv:astro-ph/0510119](#)

- Brown, T. M., Charbonneau, D., Gilliland, R. L., Noyes, R. W., & Burrows, A. 2001, ApJ, 552, 699, [ADS](#), [arXiv:astro-ph/0101336](#)
- Brown, T. M., Libbrecht, K. G., & Charbonneau, D. 2002, PASP, 114, 826, [ADS](#), [arXiv:astro-ph/0205246](#)
- Burke, C. J. et al. 2007, ApJ, 671, 2115, [ADS](#), [0705.0003](#)
- Burrows, A., Budaj, J., & Hubeny, I. 2008, ApJ, 678, 1436, [ADS](#), [0709.4080](#)
- Burrows, A., Hubeny, I., Budaj, J., & Hubbard, W. B. 2007, ApJ, 661, 502, [ADS](#), [arXiv:astro-ph/0612703](#)
- Burrows, A., Rauscher, E., Spiegel, D. S., & Menou, K. 2010, ApJ, 719, 341, [ADS](#), [1005.0346](#)
- Butler, R. P., Marcy, G. W., Williams, E., Hauser, H., & Shirts, P. 1997, ApJL, 474, L115+, [ADS](#)
- Butler, R. P. et al. 2006, ApJ, 646, 505, [ADS](#), [arXiv:astro-ph/0607493](#)
- Campo, C. J. et al. 2011, ApJ, 727, 125, [ADS](#), [1003.2763](#)
- Carpenter, J. M. 2001, AJ, 121, 2851, [ADS](#), [arXiv:astro-ph/0101463](#)
- Carter, J. A., Winn, J. N., Holman, M. J., Fabrycky, D., Berta, Z. K., Burke, C. J., & Nutzman, P. 2011, ApJ, 730, 82, [ADS](#), [1012.0376](#)
- Castelli, F., & Kurucz, R. L. 2004, ArXiv Astrophysics e-prints, [ADS](#), [arXiv:astro-ph/0405087](#)
- Chan, T., Ingemyr, M., Winn, J. N., Holman, M. J., Sanchis-Ojeda, R., Esquerdo, G., & Everett, M. 2011, AJ, 141, 179, [ADS](#), [1103.3078](#)

- Charbonneau, D. et al. 2005, ApJ, 626, 523, [ADS](#), [arXiv:astro-ph/0503457](#)
- . 2009, Nature, 462, 891, [ADS](#), [0912.3229](#)
- Charbonneau, D., Brown, T. M., Latham, D. W., & Mayor, M. 2000, ApJL, 529, L45, [ADS](#), [arXiv:astro-ph/9911436](#)
- Charbonneau, D., Brown, T. M., Noyes, R. W., & Gilliland, R. L. 2002, ApJ, 568, 377, [ADS](#), [arXiv:astro-ph/0111544](#)
- Charbonneau, D., Knutson, H. A., Barman, T., Allen, L. E., Mayor, M., Megeath, S. T., Queloz, D., & Udry, S. 2008, ApJ, 686, 1341, [ADS](#), [0802.0845](#)
- Cho, J., Menou, K., Hansen, B. M. S., & Seager, S. 2008, ApJ, 675, 817, [ADS](#)
- Cho, J. Y.-K., Menou, K., Hansen, B. M. S., & Seager, S. 2003, ApJL, 587, L117, [ADS](#), [arXiv:astro-ph/0209227](#)
- Claret, A. 2000, A&A, 363, 1081, [ADS](#)
- Clough, S., Shephard, M., Mlawer, E., Delamere, J., Iacono, M., Cady-Pereira, K., Boukabara, S., & Brown, P. 2005, Journal of Quantitative Spectroscopy and Radiative Transfer, 91, 233 , [ADS](#)
- Colbert, J., ed. 2011, MIPS Instrument Handbook, v3.0
- Cooper, C. S., & Showman, A. P. 2005, ApJL, 629, L45, [ADS](#), [arXiv:astro-ph/0502476](#)
- . 2006, ApJ, 649, 1048, [ADS](#), [arXiv:astro-ph/0602477](#)
- Cowan, N. B., & Agol, E. 2008, ApJL, 678, L129, [ADS](#), [0803.3622](#)
- . 2011a, ApJ, 726, 82, [ADS](#), [1011.0428](#)

- . 2011b, ApJ, 729, 54, [ADS, 1001.0012](#)
- Cowan, N. B., Agol, E., & Charbonneau, D. 2007, MNRAS, 379, 641, [ADS, 0705.1189](#)
- Cowan, N. B., Machalek, P., Croll, B., Shekhtman, L. M., Burrows, A., Deming, D., Greene, T., & Hora, J. L. 2012, ApJ, 747, 82, [ADS, 1112.0574](#)
- Croll, B., Albert, L., Jayawardhana, R., Miller-Ricci Kempton, E., Fortney, J. J., Murray, N., & Neilson, H. 2011a, ApJ, 736, 78, [ADS, 1104.0011](#)
- Croll, B., Lafreniere, D., Albert, L., Jayawardhana, R., Fortney, J. J., & Murray, N. 2011b, AJ, 141, 30, [ADS, 1009.0071](#)
- Crossfield, I. J. M., Barman, T., & Hansen, B. M. S. 2011, ApJ, 736, 132, [ADS, 1104.1173](#)
- Crossfield, I. J. M., Hansen, B. M. S., & Barman, T. 2012a, ApJ, 746, 46, [ADS, 1201.1023](#)
- Crossfield, I. J. M., Hansen, B. M. S., Harrington, J., Cho, J. Y.-K., Deming, D., Menou, K., & Seager, S. 2010, ApJ, 723, 1436, [ADS, 1008.0393](#)
- Crossfield, I. J. M., Knutson, H., Fortney, J., Showman, A., Cowan, N. B., & Deming, D. 2012b, ArXiv e-prints, [ADS, 1202.1562](#)
- Cushing, M. C., Rayner, J. T., & Vacca, W. D. 2005, ApJ, 623, 1115, [ADS, arXiv:astro-ph/0412313](#)
- Cushing, M. C., Vacca, W. D., & Rayner, J. T. 2004, PASP, 116, 362, [ADS](#)
- Daemgen, S., Hormuth, F., Brandner, W., Bergfors, C., Janson, M., Hippler, S., & Henning, T. 2009, A&A, 498, 567, [ADS, 0902.2179](#)

- de Mooij, E. J. W. et al. 2012, A&A, 538, A46, [ADS](#), [1111.2628](#)
- de Mooij, E. J. W., & Snellen, I. A. G. 2009, A&A, 493, L35, [ADS](#), [0901.1878](#)
- Deming, D., Brown, T. M., Charbonneau, D., Harrington, J., & Richardson, L. J. 2005a, ApJ, 622, 1149, [ADS](#), [arXiv:astro-ph/0412436](#)
- Deming, D., Harrington, J., Seager, S., & Richardson, L. J. 2006, ApJ, 644, 560, [ADS](#), [arXiv:astro-ph/0602443](#)
- Deming, D., Seager, S., Richardson, L. J., & Harrington, J. 2005b, Nature, 434, 740, [ADS](#), [arXiv:astro-ph/0503554](#)
- Deming, D. et al. 2009, PASP, 121, 952, [ADS](#), [0903.4880](#)
- Demory, B.-O. et al. 2011, ApJL, 735, L12, [ADS](#), [1105.5143](#)
- Deroo, P., Swain, M. R., & Vasisht, G. 2010, ArXiv e-prints, [ADS](#), [1011.0476](#)
- Désert, J.-M. et al. 2011, ApJL, 731, L40+, [ADS](#), [1103.2370](#)
- Désert, J.-M., Vidal-Madjar, A., Lecavelier Des Etangs, A., Sing, D., Ehrenreich, D., Hébrard, G., & Ferlet, R. 2008, A&A, 492, 585, [ADS](#), [0809.1865](#)
- Dlugokencky, E. J., Lang, P. M., & Masarie, K. A. 2011, Methane Dry Air Mole Fractions from quasi-continuous measurements at Barrow, Alaska and Mauna Loa, Hawaii, 1986-2010, <ftp://ftp.cmdl.noaa.gov/ccg/ch4/in-situ/>
- Dobbs-Dixon, I., Cumming, A., & Lin, D. N. C. 2010, ApJ, 710, 1395, [ADS](#), [1001.0982](#)
- Donati, J., Semel, M., Carter, B. D., Rees, D. E., & Collier Cameron, A. 1997, MNRAS, 291, 658, [ADS](#)

- Eastman, J., Siverd, R., & Gaudi, B. S. 2010, *PASP*, 122, 935, [ADS](#), [1005.4415](#)
- Edelson, R. A., & Krolik, J. H. 1988, *ApJ*, 333, 646, [ADS](#)
- Eggenberger, A., Udry, S., Chauvin, G., Beuzit, J.-L., Lagrange, A.-M., Ségransan, D., & Mayor, M. 2007, *A&A*, 474, 273, [ADS](#)
- Encrenaz, T. 2005, *SpSciRev*, 116, 99, [ADS](#)
- Engelbracht, C. W. et al. 2007, *PASP*, 119, 994, [ADS](#), [0704.2195](#)
- Fabrycky, D., & Tremaine, S. 2007, *ApJ*, 669, 1298, [ADS](#), [0705.4285](#)
- Ferraz-Mello, S., Tadeu Dos Santos, M., Beaugé, C., Michtchenko, T. A., & Rodríguez, A. 2011, *A&A*, 531, A161+, [ADS](#), [1011.2144](#)
- Filippenko, A. V. 1982, *PASP*, 94, 715, [ADS](#)
- Ford, E. B., Rasio, F. A., & Sills, A. 1999, *ApJ*, 514, 411, [ADS](#), [arXiv:astro-ph/9807085](#)
- Foreman-Mackey, D., Hogg, D. W., Lang, D., & Goodman, J. 2012, *ArXiv e-prints*, [ADS](#), [1202.3665](#)
- Fortney, J. J., Cooper, C. S., Showman, A. P., Marley, M. S., & Freedman, R. S. 2006, *ApJ*, 652, 746, [ADS](#), [arXiv:astro-ph/0608235](#)
- Fortney, J. J., Lodders, K., Marley, M. S., & Freedman, R. S. 2008, *ApJ*, 678, 1419, [ADS](#), [0710.2558](#)
- Fortney, J. J., Marley, M. S., & Barnes, J. W. 2007, *ApJ*, 659, 1661, [arXiv:astro-ph/0612671](#)
- Fortney, J. J., Shabram, M., Showman, A. P., Lian, Y., Freedman, R. S., Marley, M. S., & Lewis, N. K. 2010, *ApJ*, 709, 1396, [ADS](#), [0912.2350](#)

- Fossati, L. et al. 2010, ApJL, 714, L222, [ADS](#), [1005.3656](#)
- Fressin, F., Knutson, H. A., Charbonneau, D., O'Donovan, F. T., Burrows, A., Deming, D., Mandushev, G., & Spiegel, D. 2010, ApJ, 711, 374, [ADS](#), [0909.5221](#)
- Fuhrmann, K., Pfeiffer, M. J., & Bernkopf, J. 1998, A&A, 336, 942, [ADS](#)
- Gibson, N. P., Pont, F., & Aigrain, S. 2011, MNRAS, 411, 2199, [ADS](#), [1010.1753](#)
- Gillon, M. et al. 2007, A&A, 471, L51, [ADS](#), [0707.2261](#)
- Green, R. M. 1985, Spherical astronomy, ed. Green, R. M., [ADS](#)
- Gu, P.-G., Lin, D. N. C., & Bodenheimer, P. H. 2003, ApJ, 588, 509, [ADS](#), [arXiv:astro-ph/0303362](#)
- Gulbis, A. A. S. et al. 2011, PASP, 123, 461, [ADS](#), [1102.5248](#)
- Hansen, B. M. S. 2008, ApJS, 179, 484, [ADS](#), [0801.2972](#)
- Harrington, J., Hansen, B. M., Luszcz, S. H., Seager, S., Deming, D., Menou, K., Cho, J., & Richardson, L. J. 2006, Science, 314, 623, [ADS](#)
- Hebb, L. et al. 2009, ApJ, 693, 1920, [ADS](#), [0812.3240](#)
- Heim, G. B. et al. 1998, 3356, 985, [ADS](#)
- Heng, K., Frierson, D. M. W., & Phillipps, P. J. 2011a, MNRAS, 418, 2669, [ADS](#), [1105.4065](#)
- Heng, K., Menou, K., & Phillipps, P. J. 2011b, MNRAS, 413, 2380, [ADS](#), [1010.1257](#)

- Henry, G. W., Fekel, F. C., Henry, S. M., & Hall, D. S. 2000a, *ApJS*, 130, 201, [ADS](#)
- Henry, G. W., Marcy, G. W., Butler, R. P., & Vogt, S. S. 2000b, *ApJL*, 529, L41, [ADS](#)
- Hinkle, K. H., Wallace, L., & Livingston, W. 2003, 35, 1260, [ADS](#)
- Høg, E. et al. 2000, *A&A*, 355, L27, [ADS](#)
- Howard, A. W. et al. 2011, ArXiv e-prints, [ADS](#), [1103.2541](#)
- . 2010, *Science*, 330, 653, [ADS](#), [1011.0143](#)
- Howell, S. B., Everett, M. E., Sherry, W., Horch, E., & Ciardi, D. R. 2011, *AJ*, 142, 19, [ADS](#)
- Hubeny, I., Burrows, A., & Sudarsky, D. 2003, *ApJ*, 594, 1011, [ADS](#), [arXiv:astro-ph/0305349](#)
- Husnoo, N. et al. 2011, *MNRAS*, 413, 2500, [ADS](#), [1004.1809](#)
- Ibgui, L., Spiegel, D. S., & Burrows, A. 2011, *ApJ*, 727, 75, [ADS](#), [0910.5928](#)
- Ichikawa, T. et al. 2006, in Society of Photo-Optical Instrumentation Engineers (SPIE) Conference Series, Vol. 6269, Society of Photo-Optical Instrumentation Engineers (SPIE) Conference Series, [ADS](#)
- Irwin, J., Charbonneau, D., Nutzman, P., & Falco, E. 2009, in IAU Symposium, Vol. 253, IAU Symposium, 37–43, [0807.1316](#), [ADS](#)
- Jefferies, S. M., & Christou, J. C. 1993, *ApJ*, 415, 862, [ADS](#)
- Johnson, J. A. et al. 2011, *ApJ*, 730, 79, [ADS](#), [1008.4141](#)

- Joliffe, I. T. 1986, *Principal Component Analysis*, ed. Joliffe, I. T.
- Kaltenegger, L., & Traub, W. A. 2009, *ApJ*, 698, 519, [ADS, 0903.3371](#)
- Kipping, D. M., & Spiegel, D. S. 2011, *MNRAS*, 417, L88, [ADS, 1108.2297](#)
- Kleinmann, S. G., & Hall, D. N. B. 1986, *ApJS*, 62, 501, [ADS](#)
- Knutson, H. A., Charbonneau, D., Allen, L. E., Burrows, A., & Megeath, S. T. 2008, *ApJ*, 673, 526, [ADS, 0709.3984](#)
- Knutson, H. A. et al. 2007a, *Nature*, 447, 183, [ADS, 0705.0993](#)
- Knutson, H. A., Charbonneau, D., Cowan, N. B., Fortney, J. J., Showman, A. P., Agol, E., & Henry, G. W. 2009a, *ApJ*, 703, 769, [ADS, 0908.1977](#)
- Knutson, H. A. et al. 2009b, *ApJ*, 690, 822, [ADS, 0802.1705](#)
- Knutson, H. A., Charbonneau, D., Deming, D., & Richardson, L. J. 2007b, *PASP*, 119, 616, [0705.4288](#)
- Knutson, H. A., Howard, A. W., & Isaacson, H. 2010, *ApJ*, 720, 1569, [ADS, 1004.2702](#)
- Knutson, H. A. et al. 2011, *ApJ*, 735, 27, [ADS, 1104.2901](#)
- Kraus, A. L., & Hillenbrand, L. A. 2007, *AJ*, 134, 2340, [ADS, 0708.2719](#)
- Kurucz, R. L. 1979, *ApJS*, 40, 1, [ADS](#)
- Lecavelier Des Etangs, A., Pont, F., Vidal-Madjar, A., & Sing, D. 2008a, *A&A*, 481, L83, [ADS, 0802.3228](#)
- Lecavelier Des Etangs, A., Vidal-Madjar, A., Désert, J., & Sing, D. 2008b, *A&A*, 485, 865, [ADS, 0805.0595](#)

- . 2008c, *A&A*, 485, 865, [ADS, 0805.0595](#)
- Li, S.-L., Miller, N., Lin, D. N. C., & Fortney, J. J. 2010, *Nature*, 463, 1054, [ADS, 1002.4608](#)
- Lissauer, J. J. et al. 2011, *Nature*, 470, 53, [ADS, 1102.0291](#)
- Lopez, E. D., Fortney, J. J., & Miller, N. K. 2012, ArXiv e-prints, [ADS, 1205.0010](#)
- López-Morales, M., Coughlin, J. L., Sing, D. K., Burrows, A., Apai, D., Rogers, J. C., Spiegel, D. S., & Adams, E. R. 2010, *ApJL*, 716, L36, [ADS, 0912.2359](#)
- Lord, S. D. 1992, A new software tool for computing Earth's atmospheric transmission of near- and far-infrared radiation, Tech. rep., [ADS](#)
- Luhman, K. L., & Mamajek, E. E. 2010, *ApJL*, 716, L120, [ADS, 1005.2675](#)
- Maciejewski, G., Errmann, R., Raetz, S., Seeliger, M., Spaleniak, I., & Neuhäuser, R. 2011, *A&A*, 528, A65, [ADS, 1102.2421](#)
- Madhusudhan, N. et al. 2011a, *Nature*, 469, 64, [ADS, 1012.1603](#)
- Madhusudhan, N., Mousis, O., Johnson, T. V., & Lunine, J. I. 2011b, *ApJ*, 743, 191, [ADS, 1109.3183](#)
- Madhusudhan, N., & Seager, S. 2009, *ApJ*, 707, 24, [ADS, 0910.1347](#)
- . 2010, *ApJ*, 725, 261, [ADS, 1010.4585](#)
- Majeau, C., Agol, E., & Cowan, N. B. 2012, *ApJL*, 747, L20, [ADS, 1202.1883](#)
- Mandel, K., & Agol, E. 2002, *ApJL*, 580, L171, [ADS](#)
- Mandell, A. M., Drake Deming, L., Blake, G. A., Knutson, H. A., Mumma, M. J., Villanueva, G. L., & Salyk, C. 2011, *ApJ*, 728, 18, [ADS, 1011.5507](#)

- Masci, F. J., Laher, R., Fang, F., Fowler, J. W., Lee, W., Stolovy, S., Padgett, D., & Moshir, M. 2005, in *Astronomical Society of the Pacific Conference Series*, Vol. 347, *Astronomical Data Analysis Software and Systems XIV*, ed. P. Shopbell, M. Britton, & R. Ebert, 468–+, [ADS](#)
- Mason, B. D., Wycoff, G. L., Hartkopf, W. I., Douglass, G. G., & Worley, C. E. 2001, *AJ*, 122, 3466, [ADS](#)
- Maurin, A. S., Selsis, F., Hersant, F., & Belu, A. 2012, *A&A*, 538, A95, [ADS](#), [1110.3087](#)
- Mayor, M., & Queloz, D. 1995, *Nature*, 378, 355, [ADS](#)
- Mazeh, T. et al. 2000, *ApJL*, 532, L55, [ADS](#), [arXiv:astro-ph/0001284](#)
- McArthur, B. E., Fritz. Benedict, G., Barnes, R., Martioli, E., Korzennik, S., Nelan, E., & Butler, R. P. 2010, *ApJ*, 715, 1203, [ADS](#)
- McLean, I. S. et al. 1998, in *SPIE Conference Series*, ed. A. M. Fowler, Vol. 3354, 566–578, [ADS](#)
- McLean, I. S. et al. 2010, in *Society of Photo-Optical Instrumentation Engineers (SPIE) Conference Series*, Vol. 7735, *Society of Photo-Optical Instrumentation Engineers (SPIE) Conference Series*, [ADS](#)
- McLean, I. S., Steidel, C. C., Matthews, K., Epps, H., & Adkins, S. M. 2008, in *Society of Photo-Optical Instrumentation Engineers (SPIE) Conference Series*, Vol. 7014, *Society of Photo-Optical Instrumentation Engineers (SPIE) Conference Series*, [ADS](#)
- Mérand, A., Bordé, P., & Coudé du Foresto, V. 2005, *A&A*, 433, 1155, [ADS](#), [arXiv:astro-ph/0412251](#)

- Meschiari, S., Wolf, A. S., Rivera, E., Laughlin, G., Vogt, S., & Butler, P. 2009, PASP, 121, 1016, [ADS, 0907.1675](#)
- Miller, N., & Fortney, J. J. 2011, ApJL, 736, L29+, [ADS, 1105.0024](#)
- Miller-Ricci, E., & Fortney, J. J. 2010, ApJL, 716, L74, [ADS, 1001.0976](#)
- Miller-Ricci, E., Seager, S., & Sasselov, D. 2009, ApJ, 690, 1056, [ADS, 0808.1902](#)
- Miller-Ricci Kempton, E., & Rauscher, E. 2011, ArXiv e-prints, [ADS, 1109.2270](#)
- Moehler, S., Freudling, W., Møller, P., Patat, F., Rupprecht, G., & O'Brien, K. 2010, PASP, 122, 93, [ADS, 1001.1099](#)
- Montalto, M., Santos, N. C., Boisse, I., Boué, G., Figueira, P., & Sousa, S. 2011, A&A, 528, L17, [ADS, 1102.0464](#)
- Moór, A. et al. 2011, ApJS, 193, 4, [ADS, 1012.3631](#)
- Moses, J. I. et al. 2011, ApJ, 737, 15, [ADS, 1102.0063](#)
- Moshir, M. 1989, IRAS Faint Source Survey, Explanatory supplement version 1 and tape, ed. Moshir, M., [ADS](#)
- Naef, D., Mayor, M., Beuzit, J. L., Perrier, C., Queloz, D., Sivan, J. P., & Udry, S. 2004, A&A, 414, 351, [ADS, arXiv:astro-ph/0310261](#)
- Nagasawa, M., Ida, S., & Bessho, T. 2008, ApJ, 678, 498, [ADS, 0801.1368](#)
- Narita, N. et al. 2010, PASJ, 62, 779, [ADS, 1004.2458](#)
- Nettelmann, N., Fortney, J. J., Kramm, U., & Redmer, R. 2011, ApJ, 733, 2, [ADS, 1010.0277](#)

- Öberg, K. I., Murray-Clay, R., & Bergin, E. A. 2011, *ApJL*, 743, L16, [ADS](#), [1110.5567](#)
- Pollack, J. B., Hubickyj, O., Bodenheimer, P., Lissauer, J. J., Podolak, M., & Greenzweig, Y. 1996, *Icarus*, 124, 62, [ADS](#)
- Pont, F., Zucker, S., & Queloz, D. 2006, *MNRAS*, 373, 231, [ADS](#), [arXiv:astro-ph/0608597](#)
- Powell, M. J. D. 1964, *The Computer Journal*, 7, 155
- Press, W. H. 2002, *Numerical recipes in C++ : the art of scientific computing*, ed. Press, W. H., [ADS](#)
- Quirrenbach, A. 2000, in *Principles of Long Baseline Stellar Interferometry*, ed. P. R. Lawson, 71–+, [ADS](#)
- Rauscher, E., & Menou, K. 2010, *ApJ*, 714, 1334, [ADS](#), [0907.2692](#)
- . 2012, *ApJ*, 745, 78, [ADS](#), [1105.2321](#)
- Rauscher, E., Menou, K., Cho, J., Seager, S., & Hansen, B. M. S. 2008, *ApJ*, 681, 1646, [ADS](#), [0712.2242](#)
- Rauscher, E., Menou, K., Seager, S., Deming, D., Cho, J. Y.-K., & Hansen, B. M. S. 2007, *ApJ*, 664, 1199, [ADS](#), [arXiv:astro-ph/0612412](#)
- Rayner, J. T., Cushing, M. C., & Vacca, W. D. 2009, *ApJS*, 185, 289, [ADS](#), [0909.0818](#)
- Rayner, J. T., Toomey, D. W., Onaka, P. M., Denault, A. J., Stahlberger, W. E., Vacca, W. D., Cushing, M. C., & Wang, S. 2003, *PASP*, 115, 362, [ADS](#)
- Reach, W. T. et al. 2005, *PASP*, 117, 978, [ADS](#), [arXiv:astro-ph/0507139](#)

- Redfield, S., Endl, M., Cochran, W. D., & Koesterke, L. 2008, *ApJL*, 673, L87, [ADS, 0712.0761](#)
- Richardson, L. J., Deming, D., & Seager, S. 2003a, *ApJ*, 597, 581, [arXiv:astro-ph/0307297](#)
- Richardson, L. J., Deming, D., Wiedemann, G., Goukenleuque, C., Steyert, D., Harrington, J., & Esposito, L. W. 2003b, *ApJ*, 584, 1053, [ADS](#)
- Richardson, L. J., Harrington, J., Seager, S., & Deming, D. 2006, *ApJ*, 649, 1043, [ADS, arXiv:astro-ph/0606096](#)
- Rieke, G. H. et al. 2004, in Presented at the Society of Photo-Optical Instrumentation Engineers (SPIE) Conference, Vol. 5487, Society of Photo-Optical Instrumentation Engineers (SPIE) Conference Series, ed. J. C. Mather, 50–61, [ADS](#)
- Rogers, J. C., Apai, D., López-Morales, M., Sing, D. K., & Burrows, A. 2009, *ApJ*, 707, 1707, [ADS, 0910.1257](#)
- Rogers, L. A., & Seager, S. 2010, *ApJ*, 716, 1208, [ADS, 0912.3243](#)
- Rojas-Ayala, B., Covey, K. R., Muirhead, P. S., & Lloyd, J. P. 2010, *ApJL*, 720, L113, [ADS](#)
- Rowe, J. F. et al. 2008, *ApJ*, 689, 1345, [ADS, 0711.4111](#)
- Santos, N. C., Israelian, G., & Mayor, M. 2004, *A&A*, 415, 1153, [ADS](#)
- Schaefer, L., & Fegley, B. 2009, *ApJL*, 703, L113, [ADS, 0906.1204](#)
- Schlaufman, K. C., & Laughlin, G. 2010, *A&A*, 519, A105+, [ADS, 1006.2850](#)

- Schoedel, R., Yelda, S., Ghez, A., Girard, J. H. V., Labadie, L., Rebolo, R., & Perez-Garrido, A. 2011, ArXiv e-prints, [ADS, 1110.2261](#)
- Schuler, S. C., Flateau, D., Cunha, K., King, J. R., Ghezzi, L., & Smith, V. V. 2011, *ApJ*, 732, 55, [ADS, 1103.0757](#)
- Seager, S. 2011, *Exoplanets*, ed. Piper, S., [ADS](#)
- Seager, S., & Deming, D. 2009, *ApJ*, 703, 1884, [ADS, 0910.1505](#)
- Seager, S., & Sasselov, D. D. 2000, *ApJ*, 537, 916, [ADS, arXiv:astro-ph/9912241](#)
- Selsis, F., Wordsworth, R. D., & Forget, F. 2011, *A&A*, 532, A1+, [ADS, 1104.4763](#)
- Shabram, M., Fortney, J. J., Greene, T. P., & Freedman, R. S. 2011, *ApJ*, 727, 65, [ADS, 1010.2451](#)
- Shkolnik, E., Bohlender, D. A., Walker, G. A. H., & Collier Cameron, A. 2008, *ApJ*, 676, 628, [ADS, 0712.0004](#)
- Shkolnik, E., Walker, G. A. H., Bohlender, D. A., Gu, P., & Kürster, M. 2005, *ApJ*, 622, 1075, [ADS, arXiv:astro-ph/0411655](#)
- Showman, A. P., Fortney, J. J., Lian, Y., Marley, M. S., Freedman, R. S., Knutson, H. A., & Charbonneau, D. 2009, *ApJ*, 699, 564, [ADS](#)
- Showman, A. P., & Guillot, T. 2002, *A&A*, 385, 166, [ADS, arXiv:astro-ph/0202236](#)
- Sing, D. K., Désert, J., Lecavelier Des Etangs, A., Ballester, G. E., Vidal-Madjar, A., Parmentier, V., Hebrard, G., & Henry, G. W. 2009, *A&A*, 505, 891, [ADS, 0907.4991](#)

- Sing, D. K. et al. 2011a, *A&A*, 527, A73+, [ADS](#), [1008.4795](#)
- Sing, D. K., & López-Morales, M. 2009, *A&A*, 493, L31, [ADS](#)
- Sing, D. K. et al. 2011b, *MNRAS*, 416, 1443, [ADS](#), [1103.0026](#)
- Sing, D. K., Vidal-Madjar, A., Lecavelier des Etangs, A., Désert, J., Ballester, G., & Ehrenreich, D. 2008, *ApJ*, 686, 667, [ADS](#), [0803.1054](#)
- Skrutskie, M. F. et al. 2006, *AJ*, 131, 1163, [ADS](#)
- Smith, G. J., Naylor, D. A., & Feldman, P. A. 2001, *International Journal of Infrared and Millimeter Waves*, 22, 661, 10.1023/A:1010689508585
- Snellen, I. A. G., Albrecht, S., de Mooij, E. J. W., & Le Poole, R. S. 2008, *A&A*, 487, 357, [ADS](#), [0805.0789](#)
- Snellen, I. A. G., de Kok, R. J., de Mooij, E. J. W., & Albrecht, S. 2010, *Nature*, 465, 1049, [ADS](#), [1006.4364](#)
- Southworth, J. 2008, *MNRAS*, 386, 1644, [ADS](#), [0802.3764](#)
- Spiegel, D. S., Silverio, K., & Burrows, A. 2009, *ApJ*, 699, 1487, [ADS](#), [0902.3995](#)
- Stevenson, K. B. et al. 2010, *Nature*, 464, 1161, [ADS](#), [1010.4591](#)
- Suzuki, R. et al. 2008, *PASJ*, 60, 1347, [ADS](#)
- Swain, M. R. 2010, in *Bulletin of the American Astronomical Society*, Vol. 42, AAS/Division for Planetary Sciences Meeting Abstracts #42, 1064, [ADS](#)
- Swain, M. R., Bouwman, J., Akeson, R. L., Lawler, S., & Beichman, C. A. 2008, *ApJ*, 674, 482, [arXiv:astro-ph/0702593](#)
- Swain, M. R. et al. 2010, *Nature*, 463, 637, [ADS](#), [1002.2453](#)

- Takeda, G., Ford, E. B., Sills, A., Rasio, F. A., Fischer, D. A., & Valenti, J. A. 2007, *ApJS*, 168, 297, [ADS](#), [arXiv:astro-ph/0607235](#)
- Thoning, K. W., Kitzis, D. R., & Crotwell, A. 2010, Carbon Dioxide Dry Air Mole Fractions from quasi-continuous measurements at Barrow, Alaska; Mauna Loa, Hawaii; American Samoa; and South Pole, 1973-2009, <ftp://ftp.cmdl.noaa.gov/ccg/co2/in-situ/>
- Thrastarson, H. T., & Cho, J. Y. 2010, *ApJ*, 716, 144, [ADS](#), [1004.2871](#)
- Tokunaga, A. T., Simons, D. A., & Vacca, W. D. 2002, *PASP*, 114, 180, [ADS](#), [arXiv:astro-ph/0110593](#)
- Torres, G., Andersen, J., & Giménez, A. 2010, *A&ARv*, 18, 67, [ADS](#), [0908.2624](#)
- Torres, G., Konacki, M., Sasselov, D. D., & Jha, S. 2004, *ApJ*, 614, 979, [ADS](#), [arXiv:astro-ph/0406627](#)
- . 2005, *ApJ*, 619, 558, [ADS](#), [arXiv:astro-ph/0410157](#)
- Torres, G., Winn, J. N., & Holman, M. J. 2008, *ApJ*, 677, 1324, [ADS](#), [0801.1841](#)
- Vacca, W. D., Cushing, M. C., & Rayner, J. T. 2003, *PASP*, 115, 389, [arXiv:astro-ph/0211255](#)
- Valencia, D. 2011, in *IAU Symposium*, Vol. 276, *IAU Symposium*, ed. A. Sozzetti, M. G. Lattanzi, & A. P. Boss, 181–188, [1103.3725](#), [ADS](#)
- Valenti, J. A., & Fischer, D. A. 2005, *ApJS*, 159, 141, [ADS](#)
- Vasisht, G., Swain, M. R., Akeson, R. L., Burrows, A., Deming, D., Grillmair, C. J., & Greene, T. P. 2008, in *Society of Photo-Optical Instrumentation Engineers (SPIE) Conference Series*, Vol. 7010, *Society of Photo-Optical Instrumentation Engineers (SPIE) Conference Series*, [ADS](#)

- von Braun, K., van Belle, G. T., Ciardi, D. R., López-Morales, M., Hoard, D. W., & Wachter, S. 2008, *ApJ*, 677, 545, [ADS](#), [0712.3822](#)
- Waldmann, I. P., Tinetti, G., Drossart, P., Swain, M. R., Deroo, P., & Griffith, C. A. 2012, *ApJ*, 744, 35, [ADS](#), [1104.0570](#)
- Watkins, C., & Cho, J. Y.-K. 2010, *ApJ*, 714, 904, [ADS](#), [1003.4818](#)
- Welsh, W. F., Orosz, J. A., Seager, S., Fortney, J. J., Jenkins, J., Rowe, J. F., Koch, D., & Borucki, W. J. 2010, *ApJL*, 713, L145, [ADS](#), [1001.0413](#)
- Winn, J. N. 2010, ArXiv e-prints, [ADS](#), [1001.2010](#)
- Wittenmyer, R. A., Endl, M., & Cochran, W. D. 2007, *ApJ*, 654, 625, [ADS](#), [arXiv:astro-ph/0609117](#)
- Wolfgang, A., & Laughlin, G. 2011, ArXiv e-prints, [ADS](#), [1108.5842](#)
- Wright, E. L. et al. 2010, *AJ*, 140, 1868, [ADS](#), [1008.0031](#)
- Yelda, S., Lu, J. R., Ghez, A. M., Clarkson, W., Anderson, J., Do, T., & Matthews, K. 2010, *ApJ*, 725, 331, [ADS](#), [1010.0064](#)
- Young, E. T. et al. 2003, in Society of Photo-Optical Instrumentation Engineers (SPIE) Conference Series, Vol. 4850, Society of Photo-Optical Instrumentation Engineers (SPIE) Conference Series, ed. J. C. Mather, 98–107, [ADS](#)
- Zacharias, N., Urban, S. E., Zacharias, M. I., Wycoff, G. L., Hall, D. M., Monet, D. G., & Rafferty, T. J. 2004, *AJ*, 127, 3043, [ADS](#), [arXiv:astro-ph/0403060](#)
- Zahnle, K., Marley, M. S., & Fortney, J. J. 2009, ArXiv e-prints, [ADS](#), [0911.0728](#)
- Zhao, M., Monnier, J. D., Swain, M. R., Barman, T., & Hinkley, S. 2012, *ApJ*, 744, 122, [ADS](#), [1109.5179](#)